学位論文

A Study of Near-infrared Diffuse Interstellar Bands

(近赤外 DIB 吸収バンドの研究)

平成 26 年 12 月博士（理学）申請

東京大学大学院理学系研究科

天文学専攻

濱野　哲史

ABSTRACT

In this thesis, we present a first comprehensive survey of diffuse interstellar bands (DIBs) in $0.91 - 1.32\mu$m with the newly developed near-infrared (NIR) spectrograph, WINERED, mounted on the Araki 1.3 m Telescope in Japan. The DIBs in the NIR wavelength range are expected to be electronic transitions of ionized large-sized carbon molecules, such as polycyclic aromatic hydrocarbons (PAH) and fullerenes. The NIR wavelength range is also useful in exploring the DIBs toward the stars with heavy interstellar extinction because of its higher transmittance in interstellar clouds compared with the optical wavelength range. Despite the potential importance of the DIBs in the NIR wavelength range, there has been no systematic search while exceeding 500 DIBs have been detected mainly in the optical wavelength range. WINERED offers a high resolution of $R \equiv \lambda/\Delta\lambda = 28,300$ with high sensitivity in a wide wavelength coverage of $0.91 - 1.36\mu$m, where only five DIBs have been identified till now. With the survey, we aimed to extensively search for NIR DIBs and to reveal their properties. We present following three studies of NIR DIBs in this thesis.

The search for NIR DIBs

We obtained high-resolution ($R = 28,300$) spectra of 25 early-type stars with color excesses of $0.07 < E(B-V) < 3.4$. We searched for the absorption lines originating from interstellar gas clouds by comparing the obtained spectra with the stellar model spectra. Consequently, in addition to the five DIBs previously identified in the wavelength coverage of WINERED, we identified 15 new DIBs, seven of which were reported as DIB "candidates" by Cox.

The properties of NIR DIBs

We analyzed the correlations among NIR DIBs, strong optical DIBs, and the reddening of the stars. Consequently, we found that all NIR DIBs show weaker correlations with the reddening rather than the strong optical DIBs, suggesting that the equivalent widths of NIR DIBs depend on some physical conditions of the interstellar clouds, such as UV flux. Three NIR DIBs, $\lambda\lambda$10780, 10792, and 11797, are found to be classifiable as a "family," in which the DIBs are well correlated with each other, suggesting that the carriers of these DIBs are connected with some chemical reactions and/or have similar physical properties such as ionization potential. We also found that the three strongest NIR DIBs $\lambda\lambda$10780, 11797, and 13175 are well correlated with the optical DIB λ5780.5, whose carrier is proposed to be a cation molecule with high ionization potential, indicating that the carriers of the NIR DIBs could be cation molecules.

The environmental dependence of NIR DIBs in the Cyg OB2 association

In order to reveal the environmental dependence of NIR DIBs, we obtained the NIR high-resolution spectra of seven early-type stars in the Cyg OB2 association, toward which the gas clouds are known to have complex gaseous structures exposed to the strong flux of ionizing photons. We detected all 18 NIR DIBs with large EWs toward all the observed stars. We examined the relations between the DIBs and the column densities of C_2 molecules in the literature. Consequently, we could not find any clear relations between DIBs and C2 column densities toward the Cyg OB2 association, suggesting that NIR DIB carriers are distributed mainly in the diffuse component rather than in the dense component. Such properties of NIR DIBs are common to those of "classical" strong DIBs in the optical wavelength range. It is also found that the EW ratios of DIBs $\lambda\lambda$10504 and 5780.5 to DIBs $\lambda\lambda$10780, 10792, 11797, 12623, and 13175 in the Cyg OB2 association are lower than those in the diffuse interstellar environment by a factor of two. We suggest that the environmental dependence of DIB ratios illustrates some difference in the properties of the DIB carriers, such as the stability to the high-energy photons and the ionization potential.

Contents

List of Figures

List of Tables

Chapter 1

Introduction

1.1 Diffuse interstellar bands

Diffuse interstellar bands (DIBs) are ubiquitous absorption lines in optical wavelength range detected in the spectra of reddened stars, which originate from foreground interstellar clouds. DIBs were discovered in the observation at Lick Observatory by Heger (1919) (Fig. 1.1). After her first study, four DIBs at $\lambda = 5780$, 5797, 6284, and 6614Å were proved to originate from the interstellar clouds in the lines of sight of the stars by Merrill (1936). The DIBs are intrinsically broader than the interstellar atomic transitions (e.g., sodium D lines), which is the reason why they are named "diffuse" interstellar bands.

Since the first studies about a century ago, the most important question arising from the DIB studies has been "What are the DIB carriers?" Now, DIBs are thought to be the electronic transitions of free carbon-based molecules. The broadness of DIBs can be explained by the unresolved rotational contour of large molecules with small rotational constant B. In fact, two DIBs $\lambda\lambda$5797 and 6614 were found to exhibit profiles with three components, which are reminiscent of P, Q, R branches of molecular rotational transitions (Fig. 1.2). Recently, the carriers of a few weak DIBs were possibly identified as carbon chain molecules (see §1.2.3 for detail). However, the main contributor to DIBs are not unveiled at all (see next section for the specific proposed candidates).

The observations of DIBs with high-resolution spectrographs have revealed their complex-

ity and ubiquitousness in the Universe. Recent spectroscopic surveys have identified about 500 DIBs mainly in optical wavelength region (see Fig. 1.3; Jenniskens & Desert, 1994; Tuairisg et al., 2000; Hobbs et al., 2008, 2009). The correlations among some strong DIBs have been investigated in search of the pairs of DIBs originating from an identical molecule (Cami et al., 1997; Moutou et al., 1999; Friedman et al., 2011). However, no perfect correlations have been found, except for $\lambda\lambda$6196.0 and 6613.6 (McCall et al., 2010), which led to the proposal "one DIB - one molecule". Therefore, the large number of DIBs illustrates the richness of the molecules in the Universe. However, note that some vibrational progressions of a large molecule were found in the DIB spectrum recently, suggesting thatthe DIBs consisting of the progressions originate from an identical molecule (Fig. 1.4; Duley & Kuzmin, 2010). DIBs have also been investigated in extragalactic objects, such as the Magellanic clouds (Welty et al., 2006; Cox et al., 2007), M31 (Cordiner et al., 2011), and high$-z$ dumped Lyα systems (Lawton et al., 2008). The understanding of the molecular chemistry and evolution in the Universe is one of the central topic in the field of Astrochemistry and Astrobiology. DIBs will play an important role to reveal the formation and destruction processes of organic material in interstellar clouds, ultimately the seeds of life in the Universe.

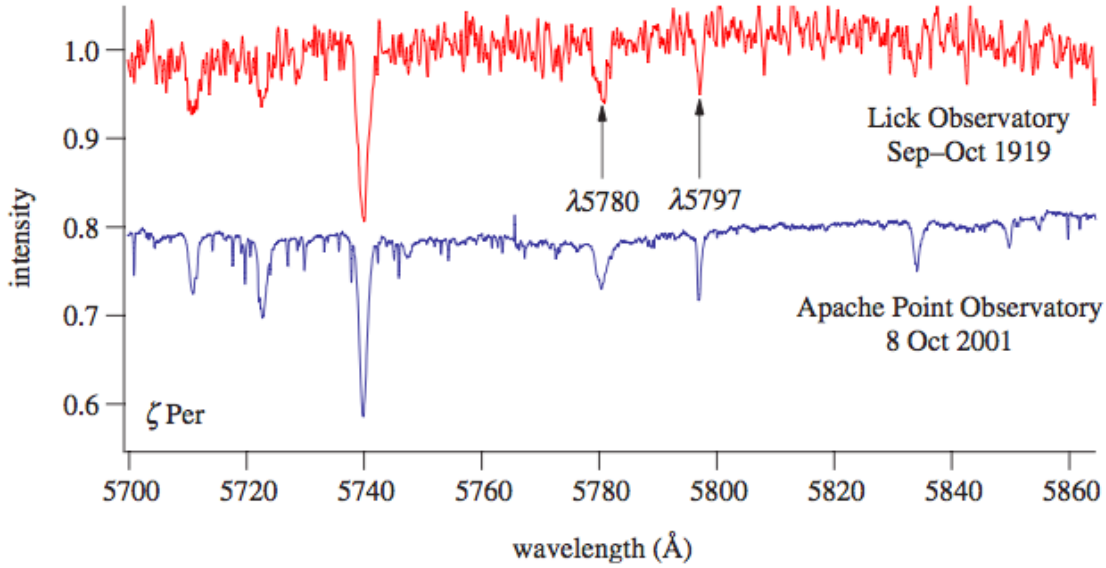

Figure 1.1: The first DIB spectrum of ζ Per obtained by Mary Lea Heger at Lick Observatory (red line) and the recent spectrum of the same star obtained at Apache Point Observatory (blue line). This figure is reproduced from the review of DIB history by McCall & Griffin (2013).

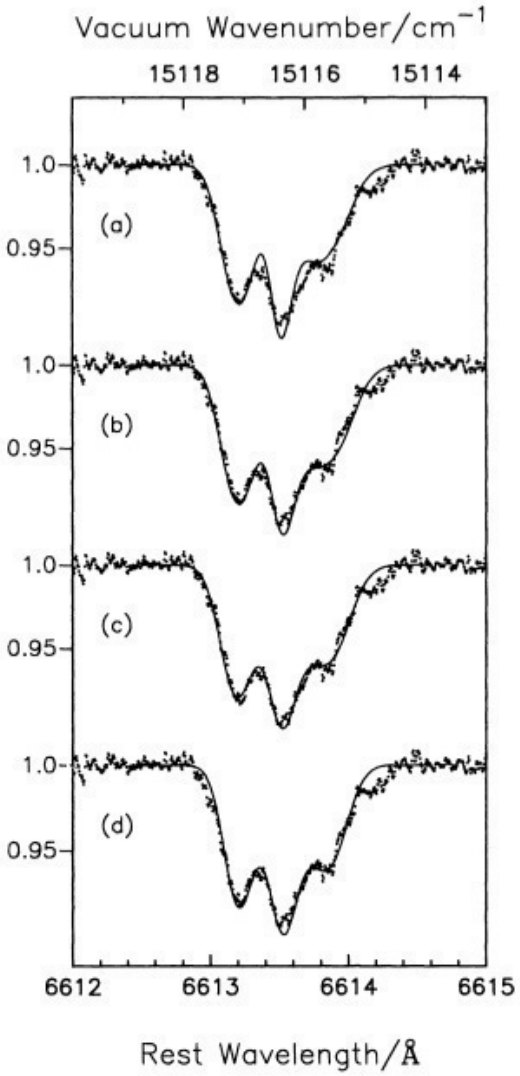

Figure 1.2: The ultra-high-resolution ($R = 600,000$) profile of DIB λ6614 toward μ Sgr and four fitted molecular rotational contours ((a) - (d)). This figure is reproduced from Kerr et al. (1996).

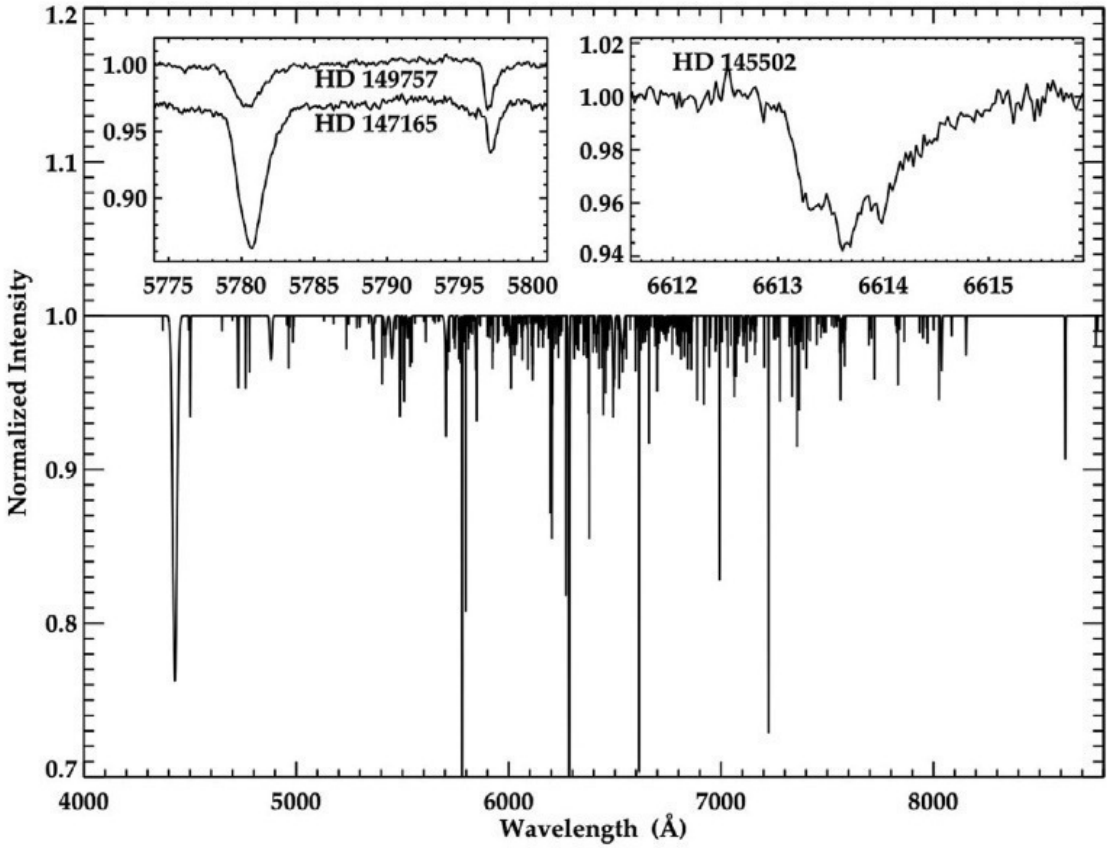

Figure 1.3: The spectrum of about 400 DIBs in optical wavelength range. The left insert shows the large variation of the strengths of two DIBs $\lambda\lambda$5780 and 5797 toward HD 149757 and HD 147165. The right insert shows the detailed profile of λ6614. This figure is reproduced from Tielens (2014).

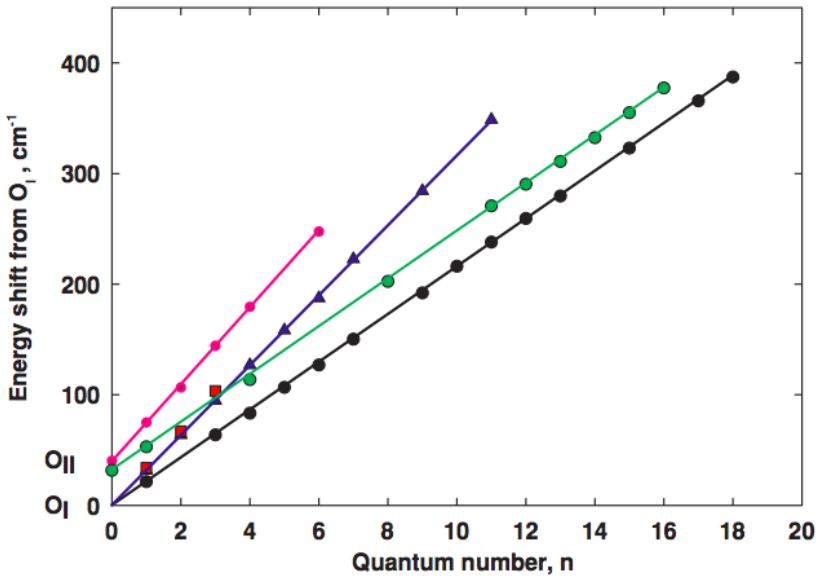

Figure 1.4: The vibrational progressions found in the DIB spectrum. The vertical axis shows the energy shift from the band origins $O_I = 6862.61$Å and $O_{II} = 6843.64$Å. The horizontal axis shows the vibrational quantum numbers. This figure is reproduced from Duley & Kuzmin (2010).

1.2 Proposed carriers

Recent enormous progresses in the laboratory experiments to measure the absorption spectra of specific gas-phase molecules have been stimulating the researchers to directly identify the DIB carriers. However, contrary to expectations, the DIB carriers could not be identified at all except for very few instances. Here, we summarize some proposed carrier molecules and its status. The molecules shown here are just popular candidates frequently referred. There are some proposals that are not summarized here (e.g., see Jones, 2014)

1.2.1 Polycyclic aromatic hydrocarbon

Because polycyclic aromatic hydrocarbons (PAHs) are known to be abundant and ubiquitous in the Universe from the observations of the UIR bands in mid-infrared, the class of PAH molecules are proposed to be the DIB carriers (Tielens, 2008). The large number of DIBs exceeding 500 can be explained by the many possible species of PAHs, which are estimated

to contain $\sim$ 50 C atoms per molecule on average. Though the properties of the "mixture" of PAHs, such as the abundance and the ionization state, can be constrained by the UIR emission bands, it is still hard to constrain their structures and sizes of specific PAHs just by the emission bands. If the DIB carriers are identified as PAHs, we can better understand the variety and abundance of specific PAHs in interstellar clouds, which will eventually allow us to study the formation and destruction processes of such organic material in the Universe.

The measurement of the absorption bands of PAHs in the laboratory is a laborious and difficult work. It is difficult to make the gas-phase PAHs and control their ionization state. In addition, the possible patterns of the molecular structures of PAHs are numerous. The first laboratory spectra of PAHs in near-UV to near infrared wavelength range have been obtained in the last decade. At first, the absorption spectra of PAHs have been obtained with matrix isolation technique (Salama et al., 1999; Clayton et al., 2003; Mattioda et al., 2005). However, the possible shifts and broadening of the absorption bands by the solid matrix prevented us from the firm identification of DIB carriers as PAH molecules. The gas-phase spectra of some PAHs, which can be compared to DIBs, were obtained quite recently by Gredel et al. (2011) and Salama et al. (2011). They could not detect the absorption lines of some neutral PAHs in near-UV spectra of stars and derived the upper limits of the abundances of some specific neutral PAHs. Because the examined size and ionization states of PAHs are still limited, it is expected that the further progress of the laboratory experimental studies will settle the proposal that DIBs originate from interstellar PAHs.

Along with the non-detection of the electronic transitions of interstellar PAHs, some issues have also been proposed for the PAH-DIB hypothesis. The number of possible structures of PAHs ($\sim$ several million) is much larger than the number of DIBs detected so far ($\sim$ 500) (Steglich et al., 2011). If the PAH-DIB hypothesis is correct, a few selected PAHs must be abundant enough to be detected in interstellar medium. Furthermore, the electronic transitions of PAH cations are much broader than DIBs (Biennier et al., 2003). As a possible solution for the proposed issues, Rouillé et al. (2012) suggested that the polyynyl-substituted PAH molecules can be the carries of DIBs because they have transitions in optical wavelength range with widths as narrow as those of DIBs and higher oscillator strengths than their parent

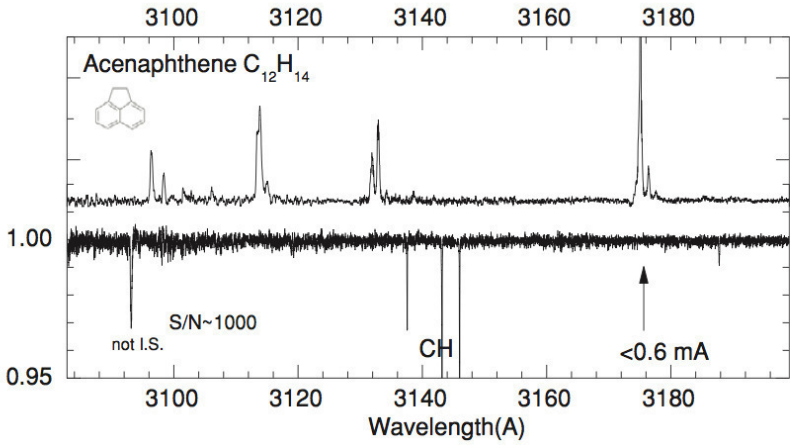

Figure 1.5: An example of the comparison between the PAH absorption spectrum (upper line: aceneaphthene) and the DIB spectrum (lower line) (Salama et al., 2011). The absorption bands could not be detected in the stellar spectrum and the upper limit for the equivalent width of the strongest band was derived. This figure is reproduced from Salama et al. (2011).

PAHs. Although this proposal is still controversial, interstellar PAHs are thought to be the most attractive candidates of the DIB carriers.

1.2.2 Fullerenes

Fullerenes (e.g., C_{60} and C_{70}) are also fascinating candidates of the DIB carriers. Foing & Ehrenfreund (1994) detected two DIBs at $\lambda = 9577$ and 9632Å, which are similar to the wavelengths of main electronic transitions of ionized buckminsterfullerene (C_{60}^{+}). However, the identification has not been confirmed yet because the compared absorption spectrum of C_{60}^{+} is obtained by the matrix isolation technique, which can shift and broaden the transitions. Misawa et al. (2009) reported the detection of the candidates of weaker sub-bands of C_{60}^{+} at $\lambda \sim$9017, 9210, 9258Å. Recently, the mid-infrared emission bands of fullerenes C_{60} and C_{70} in a young planetary nebulae Tc 1 were reported by Cami et al. (2010). However, the transitions of neutral C_{60} molecules at $\lambda \sim 3760, 3980,$ and 4024 Å could not be detected in the fullerene-rich planetary nebulae yet (García-Hernández & Díaz-Luis, 2013). Though the number of possible structures of fullerenes and its derivatives cannot explain all the over 500 DIBs, it is expected that some DIBs will be identified as the absorption band of the interstellar fullerenes.

1.2.3 Carbon chains

Three diatomic molecules, CH, CH^+, and CN, are known to have the absorption lines in the optical wavelength range (Snow & McCall, 2006). The Phillips band system of C_2 molecule is also detected in far red and near-infrared wavelength range: the (1,0), (2,0), and (3,0) bands at $\lambda \sim 10140$, 8765, and 7720 Å, respectively. Note that the fundamental (0,0) band of C_2 at $\lambda \sim 12070$ Å had not been detected in interstellar medium yet. Maier et al. (2001) detected the transition of the simplest polyatomic carbon chain molecule C_3 at 4051.6 Å. On the analogy of such simple molecules, the longer carbon chain molecules are expected to be distributed in interstellar medium and detectable as DIBs. Motylewski et al. (2000) reported a possible detection of a weak band of $HCCCCCN^+$ at 5819.27Å. Maier et al. (2004) searched for the transitions of bare carbon chains C_4 and C_5 in interstellar medium, but could not detect. Krełowski et al. (2010) and Maier et al. (2011a) possibly identified the carriers of some DIBs as HC_4H^+ and $l-C_3H_2$, respectively (Fig. 1.6). Note that Maier et al. (2011b) suggested that the assignment of HC_4H^+ as the carrier of a DIB at 5069Å by Krełowski et al. (2010) is unlikely because of the slight difference of the band shape and wavelength between the DIB and the laboratory absorption spectrum of HC_4H^+. However, the absorption bands of carbon chains cannot be a main contributor of DIBs because all of the identified absorption bands are quite weak.

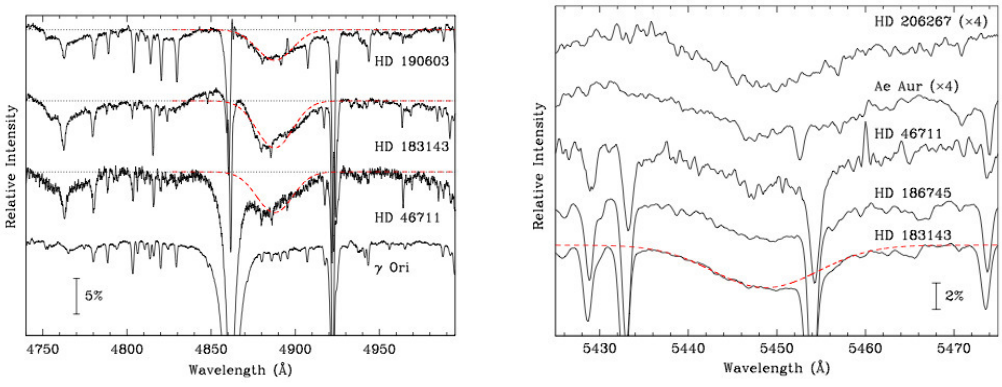

Figure 1.6: The comparison between the DIB spectra (black lines) and the laboratory absorption spectrum of $l-C_3H_2$ (dashed red lines). The DIBs at 4887Å and 5450Å seem to agree with the absorption lines of $l-C_3H_2$. This figure is reproduced from Maier et al. (2011a).

1.3 Near-infrared DIBs

The DIBs in the near-infrared (NIR) wavelength range are of great interest in search of the transitions of ionized large-sized PAHs (Salama et al., 1996; Mattioda et al., 2005; Ruiterkamp et al., 2005). Salama et al. (1996) illustrated the transitions of the electrons in neutral and ionized PAHs (Fig. 1.7). While only the $\pi \rightarrow \pi^*$ transitions are possible in neutral PAHs, the transitions within the π or the π^* levels are possible in the cation and anion of PAHs. The energy of the $\pi \rightarrow \pi$ or the $\pi^* \rightarrow \pi^*$ transitions are lower than that of the $\pi \rightarrow \pi^*$ transitions. Therefore, the transitions of ionized PAHs appear in the longer wavelength range compared to those of neutral PAHs. Because the π and π^* levels are mirror images in the first order approximaiton, the transitions of cation and anion of PAHs appear at similar wavelengths. Fig. 1.8 shows the transitions of the specific PAHs (neutral, cations, and anions) from the theoretical calculation (Ruiterkamp et al., 2005) and laboratory measurements (Mattioda et al., 2005; Gredel et al., 2011; Salama et al., 2011). The transitions of ionized PAHs are distributed from the optical to NIR wavelength range, suggesting that they can be the carriers of DIBs. In general, larger PAH molecules have transitions at longer wavelength (Salama et al., 1996; Ruiterkamp et al., 2005). Therefore, the ionized large-sized PAHs would have the electronic transitions in the NIR wavelength range, which are detectable as DIBs.

The NIR wavelength range is also useful in exploring the DIBs toward the stars with heavy interstellar extinction because of its higher transmittance in interstellar clouds compared to the optical wavelength range. The environmental dependences of DIBs can be investigated by observing the NIR DIBs toward, for example, the stars embedded in the dense clouds and the distant stars in the inner and outer regions of our Galaxy (Adamson et al., 1994; Geballe et al., 2011; Rawlings et al., 2014). The properties of NIR DIBs can also be used as the new diagnostics of interstellar clouds (Zasowski et al., 2015).

Despite the potential importance of the DIBs in the NIR wavelength range, they have not been searched extensively while exceeding 500 DIBs have been detected mainly in optical wavelength range. Only two DIBs at λ = 11797 and 13175Å discovered by Joblin et al. (1990) were known at $\lambda > 1\mu$m until recently (Fig. 1.8). This is because the power of NIR spectrograph is much weaker than that of optical in view of the sensitivity and the spectral

resolution. Many telluric absorption lines in the NIR wavelength range due to water vapor and oxygen in the atmosphere also veil weak DIBs. Owing to the recent progress in NIR high-resolution spectroscopy, the number of NIR DIBs has increased. Geballe et al. (2011) detected 11 new DIBs in the $H-$band toward the Galactic center. Cox et al. (2014) reported 12 NIR DIB "candidates" in $0.9 < \lambda < 2.5\mu$m detected in their spectral survey of NIR DIBs with the X-shooter spectrograph on the Very Large Telescope (VLT). However, the weak DIBs in the NIR wavelength range have not been searched comprehensively yet in the earlier studies. Even their basic properties, such as the line profile, the EW variations, and the correlations, have not been fully examined. Independently of the PAH-DIB hypothesis, revealing their properties in various environments would contribute to the identification of the DIB carriers.

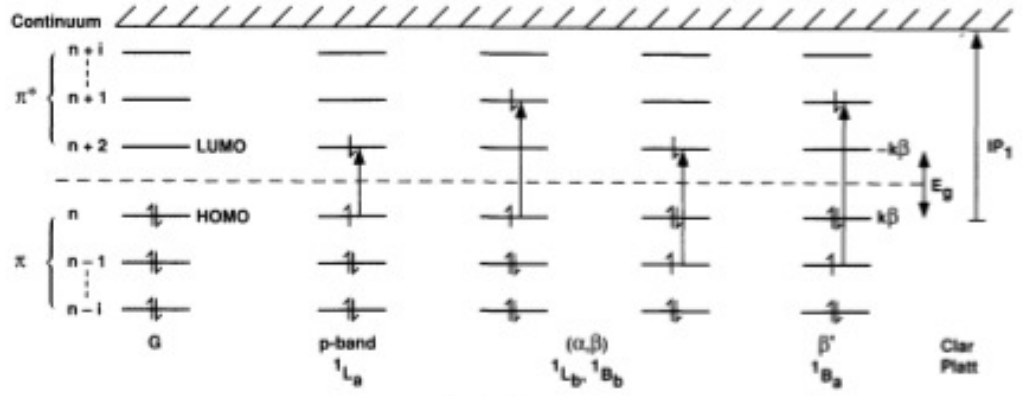

FIG. 7*a*

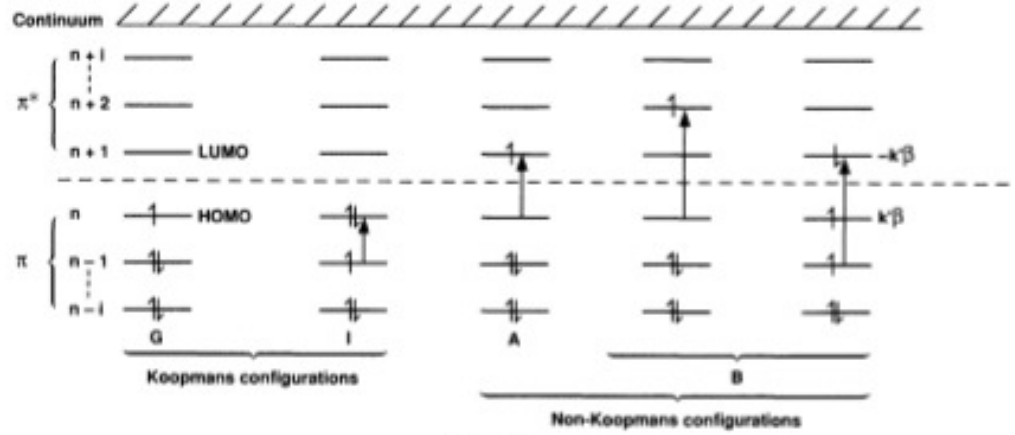

FIG. 7*b*

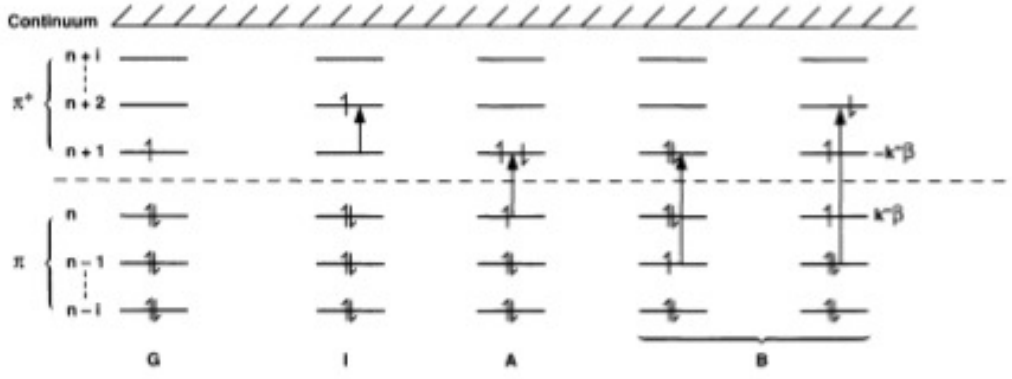

FIG. 7*c*

Figure 1.7: Hückel π molecular orbital energy level diagrams for (a) neutral, (b) cation, and (c) anion PAHs. This figure is reproduced from Salama et al. (1996).

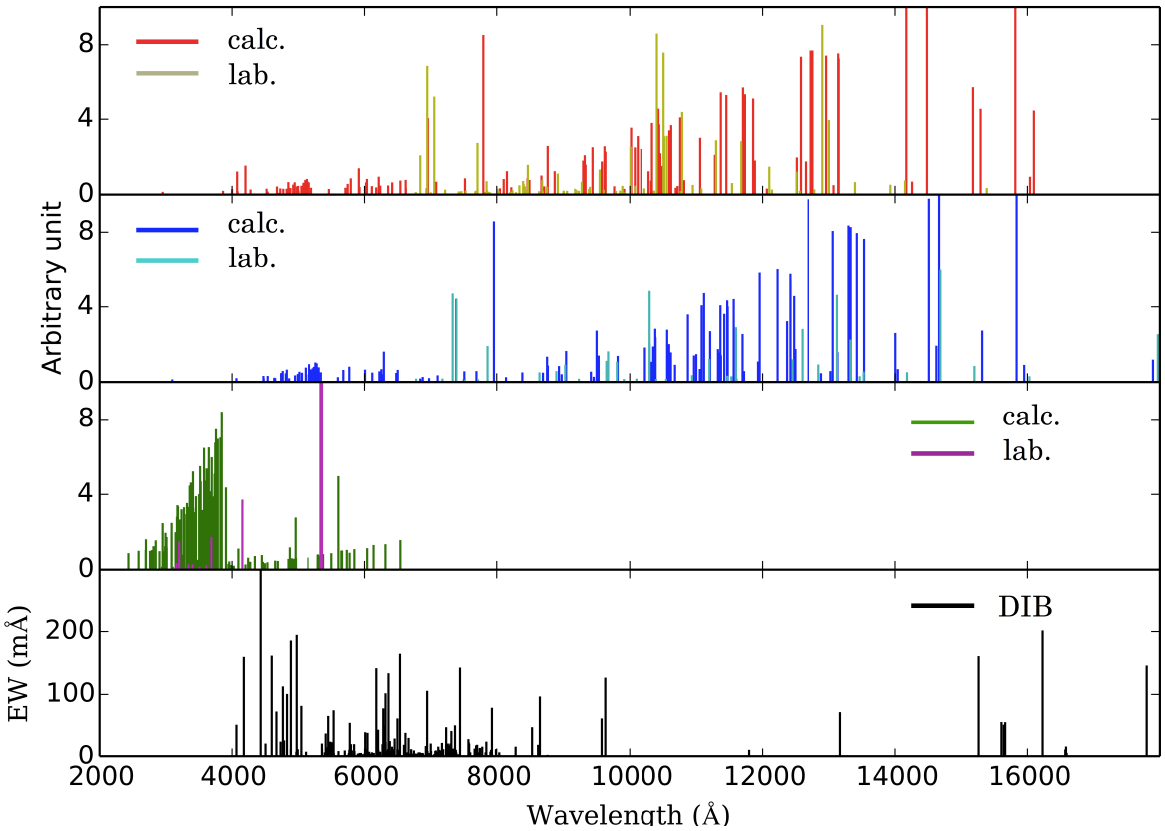

Figure 1.8: The absorption spectra of the specific neutral, cation, and anion PAHs in the literature (three upper panels) and DIB spectrum (lower panel). The DIB spectrum is synthesized from Jenniskens & Desert (1994) and Geballe et al. (2011). The PAH spectra are from the theoretical calculation by Ruiterkamp et al. (2005) (green, red, and blue lines for neutral, cation, and anion PAHs, respectively) and the laboratory experiments by Gredel et al. (2011) and Salama et al. (2011) for neutral PAHs (magenta lines) and Mattioda et al. (2005) for ionized PAHs (yellow and cyan lines for cation, and anion PAHs, respectively).

1.4 The purpose of this thesis

In this thesis, we present a first comprehensive survey of NIR DIBs in $z-$, $Y-$ and $J-$bands with newly developed NIR echelle WINERED spectrograph (Ikeda et al., 2006; Yasui et al., 2006, 2008; Kondo et al., 2015) mounted on the Araki 1.3 m Telescope in Koyama Astronomical Observatory in Japan. WINERED offers a high resolution of $R \sim 28,300$ with high sensitivity in wide wavelength coverage of $0.91 - 1.36\mu$m, where only four DIBs have been confirmed till now (see Fig. 1.8). With the survey, we aimed to extensively search for NIR DIBs and to reveal their properties. Because WINERED is newly developed and the data reduction pipeline is critical for an extensive survey work, we started from the development of the automatic data reduction pipeline customized for the WINERED data. All the data obtained in our survey were reduced with this pipeline. We present the following three studies on NIR DIBs in this thesis.

1.4.1 The search for NIR DIBs

First, we obtained high-resolution spectra of 25 early-type stars with color excesses of $0.07 < E(B-V) < 3.4$. We searched for the DIB features originating from the interstellar medium in the obtained spectra. Consequently, in addition to the four DIBs previously detected in the wavelength coverage of WINERED, we identified 16 new DIBs, eight of which were reported as DIB "candidates" by Cox et al. (2014).

1.4.2 The properties of NIR DIBs

Subsequently, we investigated the basic properties of the identified NIR DIBs by examining their correlations. The correlations among the strength of DIBs and the amount of other atomic or molecule species in the gas clouds have been extensively investigated for the DIBs in the optical wavelength range to reveal their properties (Krełowski & Walker, 1987; Cami et al., 1997; McCall et al., 2010; Friedman et al., 2011). Regarding the NIR DIBs, although earlier studies succeeded in detecting new DIBs, their properties in the interstellar clouds have not been investigated owing to small sample size (Joblin et al., 1990; Cox et al., 2014). We analyzed the correlations among NIR DIBs, "classical" strong optical DIBs, and the reddening

of the stars.

1.4.3 The environmental dependence of NIR DIBs in the Cyg OB2 association

In order to reveal the environmental dependence of DIBs, we obtained the NIR high-resolution spectra of seven early-type stars in the Cyg OB2 association, which contains a number of bright early-type stars with large extinction. The observation of the stars in the Cyg OB2 association allow us to study the correlations of DIBs including weak ones more confidently owing to the large EWs. In addition, the lines of sight toward the Cyg OB2 association, in particular the Cyg OB2 No.12, have received much attention because of the detection of large amount of H_3^+ molecules by McCall et al. (1998). Several small-sized molecules (e.g., C_2, CN, HCO^+, and CO) are also detected toward the Cyg OB2 association (Gredel et al., 2001; Casu et al., 2005). The models reproducing the abundances of H_3^+ toward the Cyg OB2 association suggested that the lines of sight contain the diffuse clouds ($n = 100$ cm^{-3}) and embedded dense clouds ($n = 10^4$ cm^{-3}) (Cecchi-Pestellini & Dalgarno, 2000). Such density structure of the gas clouds was supported by the observations of C_2 and CO (Gredel et al., 2001; Casu et al., 2005). Gredel et al. (2001) showed that the abundances of C_2 and CN can be explained by the chemistry induced by the high X-ray flux from the early-type stars in the association. As such, the clouds of the Cyg OB2 association have complex density structure and are exposed to the strong flux of the high-energy photons from nearby OB stars. The environment is quite different from the interstellar environment. By revealing the environmental dependence of DIBs in the Cyg OB2 association, we could peer into the characteristics of the DIB carriers. We obtained the NIR high-resolution spectra of the seven brightest stars in $J-$band, and investigated the DIBs toward their lines of sight in comparison with those in the diffuse interstellar environment.

1.5 Outline

This thesis is composed as follows. In Chapter 2, we describe the specifications and the status of WINERED, and our whole observations. In Chapter 3, we describe the data reduction

pipeline originally developed for the WINERED data. In the following Chapters, three studies of NIR DIBs are presented: 1) the search for NIR DIBs (Chapter 4), 2) the properties of NIR DIBs (Chapters 5, 6, and 7), and 3) the environmental dependences of NIR DIBs in the Cyg OB2 association (Chapter 8). In Chapter 9, the summary of this thesis and the future prospect are presented.

Chapter 2

Observation

2.1 WINERED

In this thesis, we used the newly developed high-resolution spectrograph, WINERED (Fig. 2.1; Ikeda et al., 2006; Yasui et al., 2006, 2008; Kondo et al., 2015), which is mounted on the F/10 Nasmyth focus of the Araki 1.3 m telescope (Fig. 2.2) at Koyama Astronomical Observatory, Kyoto-Sangyo University, Japan (Yoshikawa et al., 2012). The primary objective of WINERED is to realize NIR high-resolution spectrograph with high sensitivity by achieving high optical throughput ($> 40\%$), which is about twice as high as those of conventional high resolution spectrographs. WINERED has three observational modes, one is the normal grating mode ($N-$mode) covering $0.91 - 1.36\mu$m in one exposure with $R = 28,300$ using a reflective echelle grating. The others are two immersion grating modes, $Y-$ and $J-$modes, which cover $0.96 - 1.13\mu$m and $1.12 - 1.35\mu$m, respectively, with $R = 103,000$. These modes are now under development. Table 2.1 summarizes the basic specifications of WINERED.

We have completed the development of WINERED in $N-$mode, and started engineering observations. Figure 2.3 shows the Echellogram of an astronomical object and a flat lamp. Figure 2.4 and 2.5 show the measured spectral resolution and throughput of WINERED as a function of wavelength. The achieved spectral resolution is comparable to those of many IR high resolution spectrographs, but the high throughput and wide wavelength coverage allowed us an efficient search of weak DIBs for the first time.

Table 2.1: The basic specifications of WINERED.

Wavelength Coverage	0.91-1.36 μm
Spectral Resolution	$R = 28,300$ ($\Delta v = 11$ km s^{-1})
Throughput	~ 40 %
Pixel Scale[1]	$0''.8$ / pix
Slit Width[1]	$1''.6$ (2 pix)
Slit Length[1]	48"
Array	HAWAII-2RG 2048 $\times$ 2048

[1] Calculated for the Araki 1.3 m telescope.

WINERED looked the first light in May 2012, and we started engineering observations with an engineering grade array. The detection limit of WINERED was estimated as J =11.4 mag for the total integration time of 8 hrs (1,800sec $\times$ 16) and S/N = 30. The scientific grade array was installed in Aug 2013 and the detection limit was improved by about 1 mag in $J-$band. In the engineering observations, the ambient background was found to be about 50 times higher than expected because of a thermal leak in $1.7-1.8\mu$m. To reduce the thermal leak, we installed an $H-$band blocking filter in Mar 2014, to achieve the originally specified detection-limit J =13.5 mag. However, the filter was slightly distorted due to a mechanical failure and caused a slight bluring of the light. Consequently, the resultant spectral resolution became $R =\sim 20,000$ for the observing runs during summer of 2014. This problem is now being solved with an overhaul of the instrument in winter of 2014.

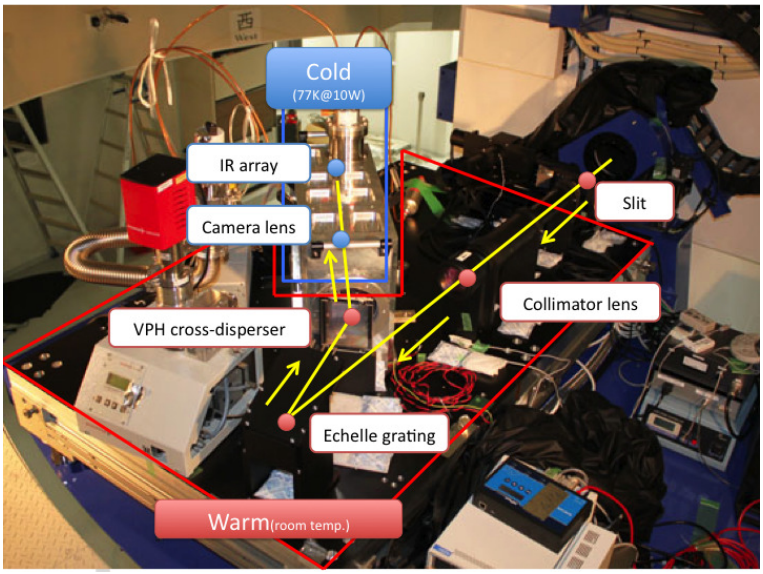

Figure 2.1: WINERED mounted on the Nasmyth focus of the Araki 1.3m telescope. Warm optics, including the echelle grating and the cross-disperser (VPH), are exposed for viewing purpose.

Figure 2.2: The picture of the Araki 1.3m telescope.

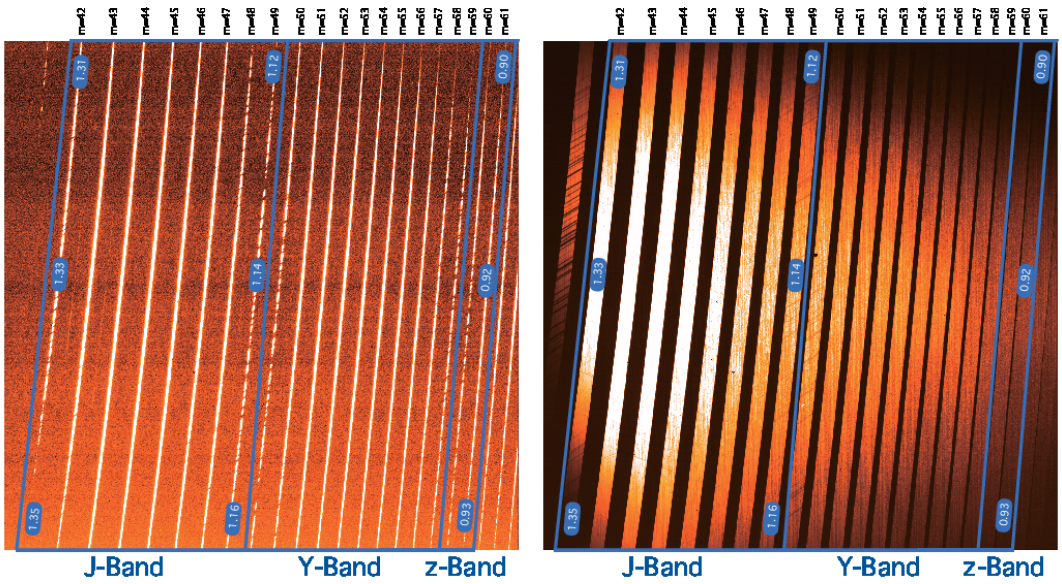

Figure 2.3: Echellogram of an astronomical object (left) and a flat-lamp (right) obtained with WINERED.

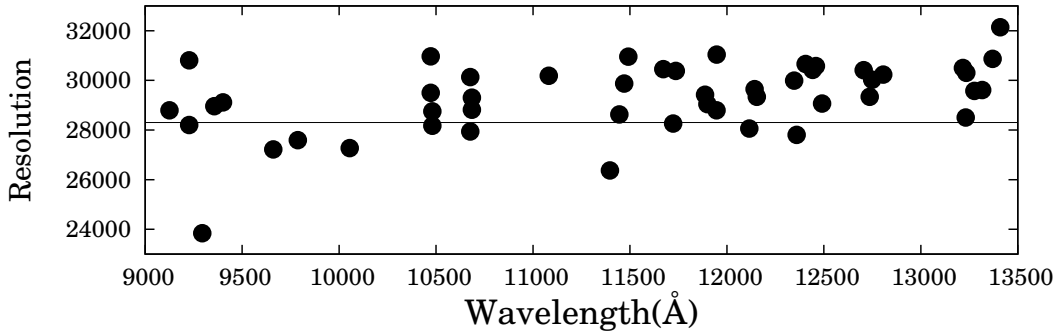

Figure 2.4: Measured spectral resolution of WINERED. The black points show the measured values. The solid line shows the designed spectral resolution, which is defined by 2-pixel sampling.

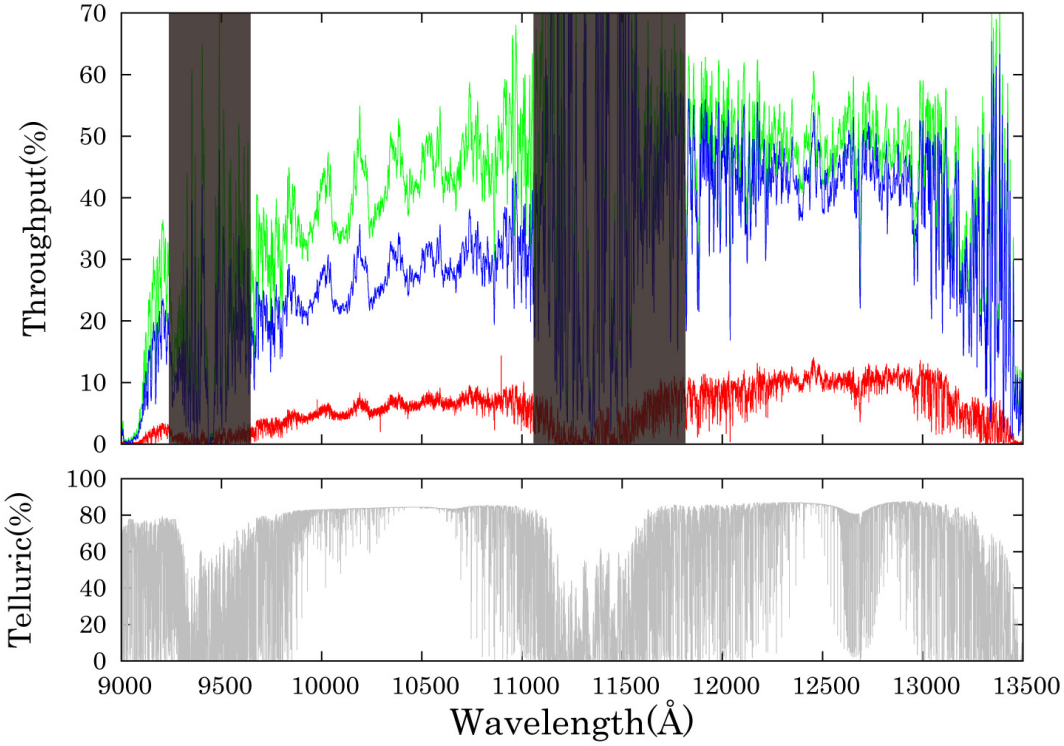

Figure 2.5: Estimated throughput of WINERED. The top panel shows the throughput (Green: WINERED optics only, Blue: WINERED optics times QE of the SG array, Red: as observed with the EG array). The bottom panel shows the assumed telluric absorption spectrum for estimating the throughput.

2.2 Targets and Observations

2.2.1 The survey of NIR DIBs

We selected bright early-type (O, B, A) stars with $J < 6.2$ mag from the literatures as targets of our initial survey (Table 2.2). The color excesses of the targets are in the range $0.07 < E(B-V) < 0.85$ except for Cyg OB2 No.12 ($E(B-V) = 3.4$). We also obtained the spectra of Rigel ($E(B-V) = 0.0$) as a reference, which should not show any absorption features due to interstellar dust. Observations of almost all targets were conducted from November 2013 to January 2014. Only two stars (Cyg OB2 No.12 and HD190603) were observed in July 2012 when we used an engineering array with worse sensitivity, in particular at shorter wavelength ($\lambda < 1\mu$m), compared to that of the currently used scientific array. Therefore, the signal-to-noise ratio (S/N) and quality of the spectra of these stars are not as good as the other data. The telescope was nodded by about 30 arcsec along the direction of the slit length between alternating frames to offset the sky emission. Only for HD 37043, which is embedded in the Orion Nebulae, were the frames obtained without nodding, and corresponding sky frames were obtained in a field far from the star to avoid the emission from the Orion Nebulae. Note that the telluric absorption lines by water are stronger for two stars, HD190603 and Cyg OB2 No.12, than for the other stars because these two stars were observed in July, when the humidity is very high in Japan.

2.2.2 Cyg OB2 association

We observed seven stars in the Cyg OB2 association, which are the brightest in the $J-$band. The observations were conducted with WINERED mounted on the Araki 1.3 m telescope during Sep and Oct in 2014. Owing to the distortion in the newly installed thermal cut filter, the spectral resolution became $R =\sim 20,000$, which is lower than the designed value of WINERED, $R = 28,300$ (see §2.1). Because we do not focus on the profiles of DIBs, the lower resolution does not affect our results and discussion. Table 2.3 summarizes the observation of the Cyg OB2 association. We observed the telluric standard stars of A0V type at similar airmass as those of the targets.

Table 2.2: Summary of Observations and Targets for the DIB survey

Star	Spectral Type	J (mag)	$E(B-V)$ (mag)	Obs. Date	Integration Time (sec)	S/N[1] Raw	S/N[2] Corrected	Telluric [3]
HD2905	B1Iae	4.141	0.33	2014/1/22	720	600	600	50 Cas
HD12953	A1Iae	4.062	0.62	2014/1/22	960	700	600	50 Cas
HD14489	A2Ia	4.528	0.40	2014/1/22	1,800	750	650	50 Cas
HD20041	A0Ia	4.057	0.73	2014/1/21	1,200	750	750	50 Cas
HD21291	B9Ia	2.712	0.42	2013/12/25	1,200	400	300	50 Cas
HD21389	A0Iab	3.050	0.55	2013/12/25	1,500	500	500	50 Cas
HD23180	B1III	3.610	0.31	2014/1/22	1,300	600	500	7 Cam
HD24398	B1Ib	2.650	0.32	2013/12/25	400	450	300	50 Cas
HD24912	O7.5IIIe	3.987	0.33	2013/12/25	1,200	400	300	50 Cas
HD25204	B3V+A4IV	3.572	0.30	2014/1/23	720	650	400	7 Cam
HD30614	O9.5Ia	4.243	0.30	2014/1/22	960	550	400	7 Cam
HD36371	B4Ib	4.246	0.43	2014/1/23	720	700	550	7 Cam
HD36486	B0III+O9V	2.744	0.07	2014/1/23	240	750	400	21 Lyn
HD36822	B0III	4.807	0.11	2014/1/23	1,200	600	450	7 Cam
HD37043	O9III	3.490	0.07	2014/1/23	600	600	350	7 Cam
HD37128	B0Iab	2.191	0.08	2013/12/8	240	700	450	HR1483
HD37742	O9Iab	2.210	0.08	2014/1/23	240	850	400	7 Cam
HD38771	B0Iab	2.469	0.07	2013/12/8	240	600	350	HR1483
HD41117	B2Iaev	4.186	0.44	2014/1/23	720	500	400	21 Lyn
HD43384	B3Iab	5.187	0.57	2014/1/23	1,440	500	400	21 Lyn
HD50064	B6:Ia	6.175	0.85	2014/1/24	1,200	300	300	omi Aur
HD190603	B1.5Ia+	4.416	0.70	2012/6/28	800	200	200	HIP87108
HD202850	B9Iab	3.973	0.13	2013/12/25	180	170	170	50 Cas
HD223385	A3Iae	3.500	0.59	2014/1/22	720	650	550	50 Cas
Cyg OB2 No.12	B3-4Ia+	4.667	3.4	2012/6/28	800	100	100	HIP87108
Rigel	B8Iab	0.206	0.00	2013/12/8	8	650	300	HR1483

[1] The signal-to-noise ratio of the spectrum at $\lambda \sim 10400$Å.
[2] The signal-to-noise ratio of the spectrum at $\lambda \sim 10400$Å after the correction of telluric absorption lines.
[3] Telluric standard stars used for the correction of the telluric absorption lines.

Table 2.3: Summary of Observations and Targets in the Cyg OB2 Association

Stars	Spectral Type	J (mag)	$E(B-V)$ (mag)	Obs. Date	Integration Time (sec)	S/N[1] Raw	S/N[2] Corrected	Telluric [3]	λ5780.5[4] (mÅ)
No.3	O9	6.498	2.01	2014/9/11	1,800	300	250	ρ Peg	—
No.5	O7Ia	5.187	1.99	2014/9/20	1,200	400	300	c And	787.4
No.8A	O6Ib+O4.5III	6.123	1.55	2014/9/16	2,400	300	300	35 Vul	—
No.9	O5If	6.468	2.25	2014/9/13	1,800	300	300	29 Vul	1004.3
No.10	O9.5Ia	6.294	1.83	2014/9/11	1,800	250	250	ρ Peg	1021.4
No.11	O5.5Ifc	6.650	1.75	2014/9/14	2,400	300	250	HR 8844	—
No.12	B3-4Ia	4.667	3.4	2014/10/17	3.600	500	500	HR 196	929.1

[1] The signal-to-noise ratio of the spectrum at $\lambda \sim 10400$Å.
[2] The signal-to-noise ratio of the spectrum at $\lambda \sim 10400$Å after the correction of telluric absorption lines.
[3] Telluric standard stars used for the correction of the telluric absorption lines.
[4] The EWs of DIB λ5780.5 from Chlewicki et al. (1986).

Chapter 3

Data Reduction

3.1 Data reduction pipeline

We developed the data reduction pipeline for WINERED data. The pipeline includes the interpolation of bad pixels, the subtraction of scattered light and sky, the flat fielding, the transformation, the extraction of one dimensional spectra, and the application of dispersion solution. All of the data obtained with WINERED are automatically reduced with this pipeline. Here, we briefly summarize the pipeline procedures, which mainly uses the tasks in IRAF[1].

First, the bad pixels in the raw data are interpolated by the counts of the surrounding good pixels. The map of bad pixels are prepared for each observational runs. The scattered light and bias are removed by fitting two dimensional polynomial function to the counts of inter-order regions using an IRAF task, *apscatter*. These procedures are also applied to the flat images, which are obtained by observing the dome flat. Then, the object images are divided by the flat image and the corresponding nodded frames are subtracted to offset the sky emission.

Subsequently, the one dimensional spectra are extracted from the two dimensional images. Because the slit direction is tilted from the axes of the array coordinate (Fig. 3.1), the array

[1]IRAF is distributed by the National Optical Astronomy Observatory, which is operated by the Association of Universities for Research in Astronomy, Inc., under cooperative agreement with the National Science Foundation.

coordinate must be transformed to the coordinate whose axis is in the slit direction. An IRAF task, *transform*, which transform the images from the long-slit spectroscopy, cannot be used for the Echelle imaga. Therefore, we made a custom software to transform the coordinate for WINERED data. The detailed procedure of the transformation will be described in the next section. From the transformed images, one dimensional spectra of astronomical objects are extracted by an IRAF task, *apall*, and dispersion solution is applied to the spectra. The dispersion solution is prepared for each run using about 200 emission lines of ThAr lamp as a comparison. After the automatic reduction with the pipeline, we manually removed the telluric absorption lines in the object spectra by dividing them by the telluric standard spectra using an IRAF task, *telluric*. Note that we did not remove the hydrogen and metal absorption lines in standard stars, because the profile fitting and removal of those features is difficult in many cases due to contamination of atmospheric absorption lines. Therefore, emission-like features appear in the divided spectra. The spectra are normalized by a low-order Legendre function using the IRAF task, *continuum*, for each order of Echelle spectra.

3.2 Transformation

Fig. 3.1 shows the combined image of a flat frame and a comparison frame (ThAr lamp) obtained by WINERED. The slit direction, which is shown with the emission lines of Th or Ar, is tilted from the axes of the array coordinate. Because the extraction of one-dimensional spectra with an IRAF task, *apall*, are conducted by integrating the spectra in the direction of the axes of the array coordinate, the image must be transformed to align the slit direction to the axes of the array coordinate. Here, we define (X, Y) and (U, V) as the array coordinates and the transformed array coordinates, respectively. Because the slit image can be regarded as a straight line, the coordinate transformation matrix can be expressed by very simple formulas. Fig. 3.2 shows the schematic image of the transformation. In this case, the

coordinate transformation matrix is expressed as:

$$U = X, \tag{3.1}$$

$$V = Y - X \tan\theta, \tag{3.2}$$

where θ is the angle between the slit direction and X axis. As for the WINRED data, the angle θ is not constant but a function of the array coordinates, ranging from about 29 degree to 35 degree. Fig. 3.3 shows the θ - Y plot made by measuring the angles of the slit to the array coordinate Y at the center of the emission lines of a comparison frame. From this plot, the angle θ is found to be expressed as a linear function of Y. Therefore, $\theta(X, Y)$ can be written as:

$$\theta(X, Y) = aY + b. \tag{3.3}$$

Using this relation, the coordinate transformation matrix (Eq. (3.1) and (3.2)) can be expressed as:

$$U = X, \tag{3.4}$$

$$V = Y - X \tan(aY + b). \tag{3.5}$$

This coordinate transformation matrix must be prepared for all strips of the cross-dispersed order because the angle is not constant throughout the array. The same matrix can be used for the transformation of each strip of the cross-dispersed order only when the matrix is a linear function of the array coordinates (X, Y). As for the WINERED data, the transformation is conducted as shown in Fig. 3.4. In this case, the coordinate transformation matrix of cross-dispersed order i can be expressed as:

$$U_i = X, \tag{3.6}$$

$$V_i = Y - (X - f_i(Y)) \tan(aY + b), \tag{3.7}$$

where (U_i, V_i) is the array coordinate of order i after the transformation, and $f_i(Y)$ is the X value at the center of the strip of order i as a function of Y (see the caption of Fig. 3.4

for the detailed explanation of the formulas). By determining the parameters, a and b, and the function, $f_i(Y)$, from the obtained WINERED data, we could obtain the matrix formulas of the transformation for each order. The parameters a and b are obtained by the fitting shown in Fig. 3.3 and $f_i(Y)$ is obtained by an IRAF task, *aptrace*. Consequently, we could obtain the transformed images of each order by using the matrix as an input for an IRAF task,*transform* (Fig. 3.5).

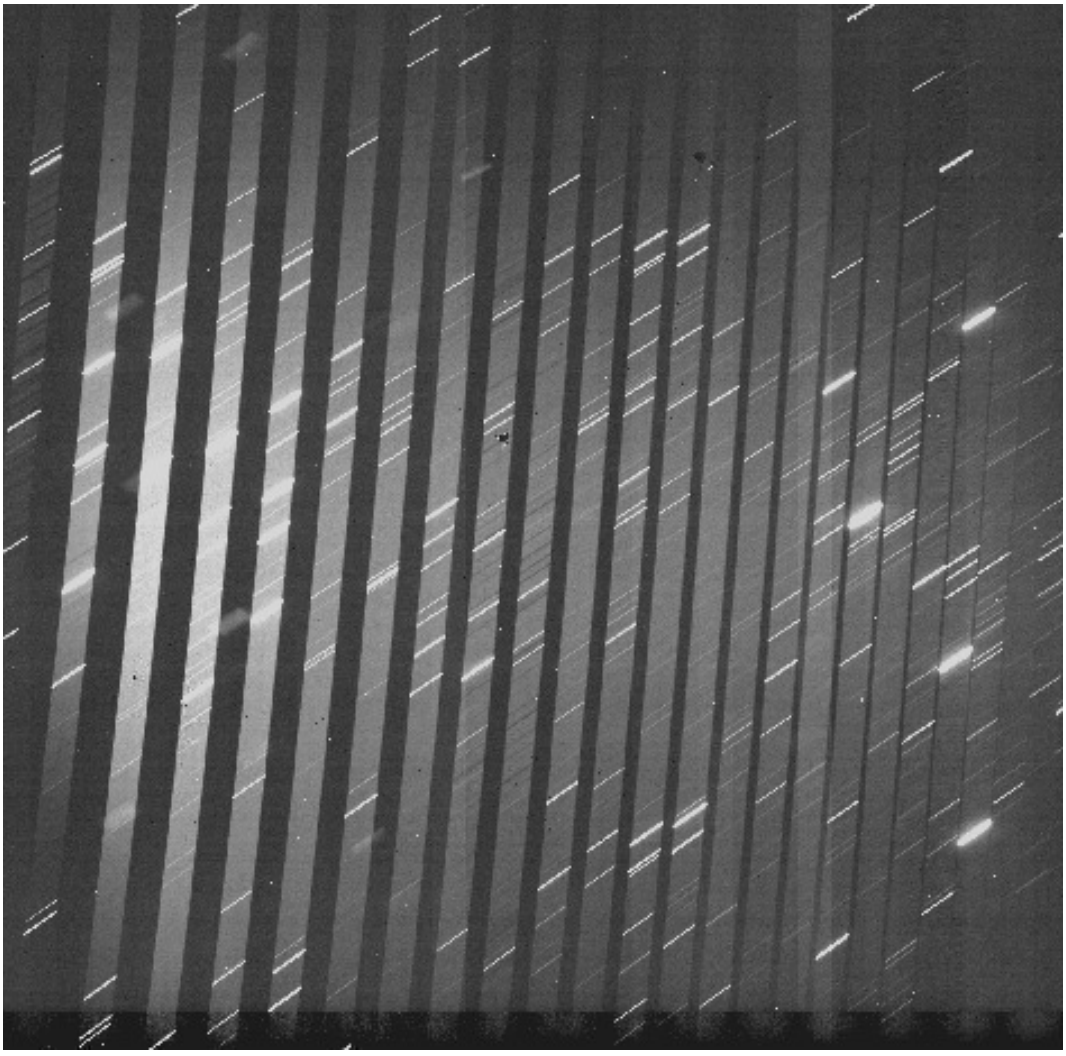

Figure 3.1: A combined image of a flat frame and a comparison frame obtained by WINERED. The slit direction is tilted to the array coordinates.

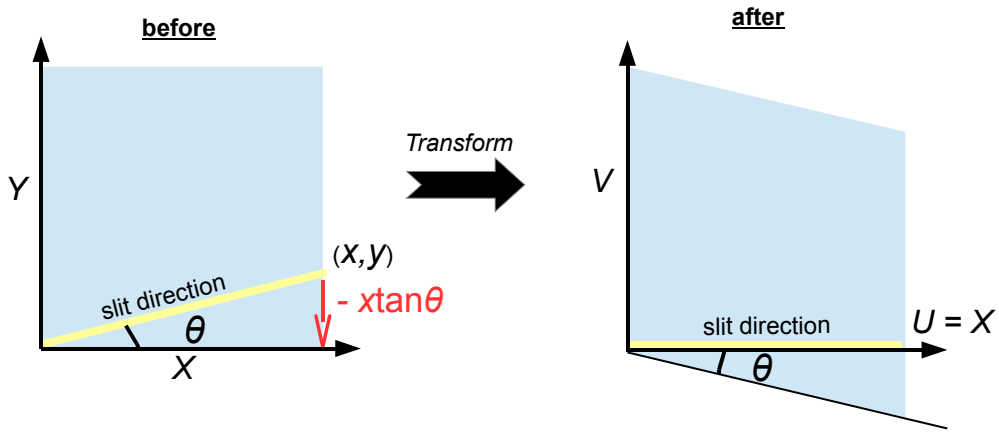

Figure 3.2: A schematic image of the coordinate transformation.

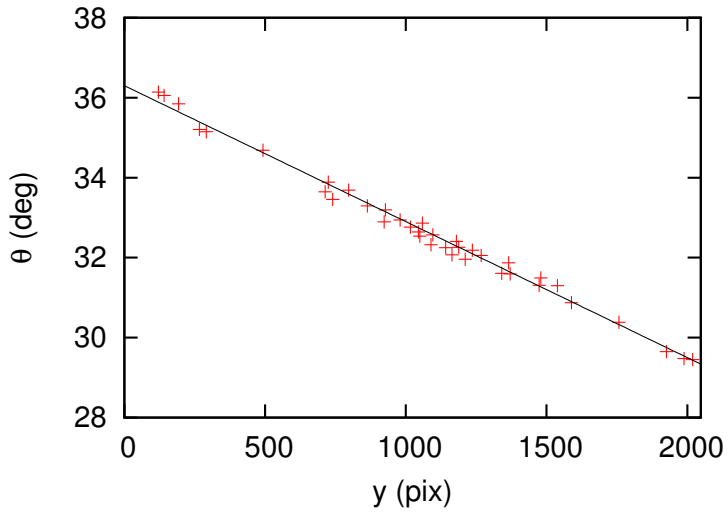

Figure 3.3: The plot of the angle of the slit direction to the X axis (θ) veraus Y. The red crosses show the measured angles and the central Y value of the emission lines in the comparison frame. The black line is a linear function fitted to the red crosses.

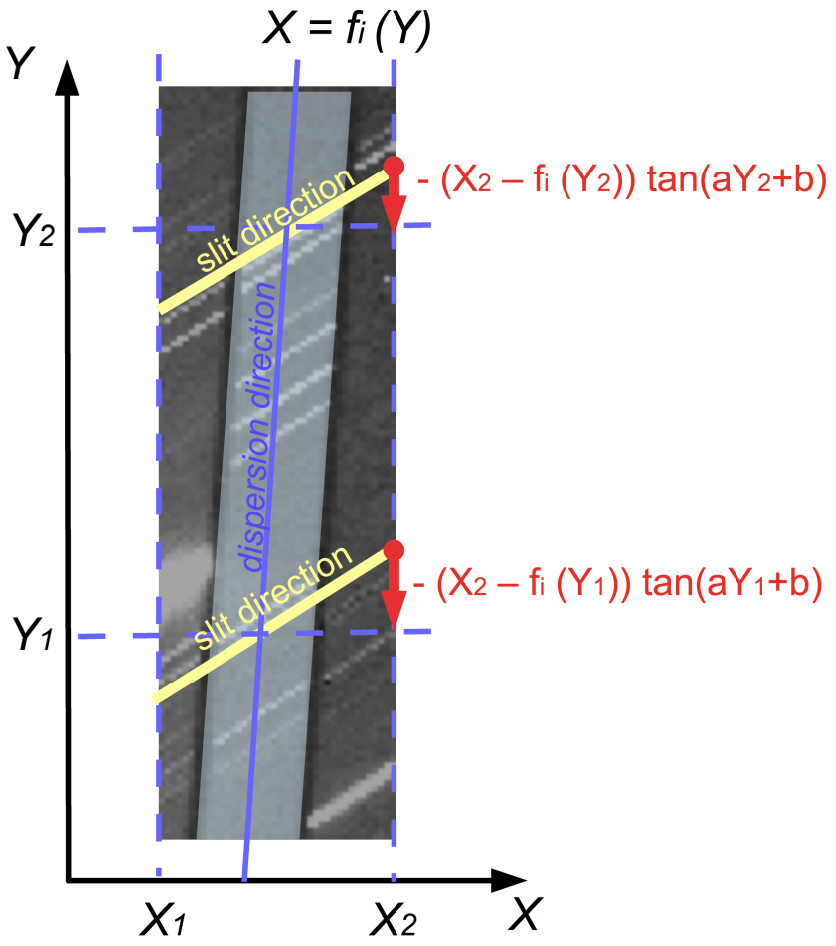

Figure 3.4: The image of a comparison frame and the formulation of the transformation procedure. The shaded area (a gray parallelogram at the center) shows the spectrum of $i-$th order. The image must be transformed to align the silt direction (yellow) to an axis of the array coordinate. First, we set the center line of the order (a blue thick line) as a standard, whose Y value does not change by the transformation. Because the true center line is tilted and curved slightly, it should be expressed with a relation $X = f_i(Y)$, where the function $f_i(Y)$ is a polynomial function of Y obtained by the fitting procedure for an object frame. For example, at $Y = Y_1$, the slit direction is tilted from the $X-$axis by $\theta = aY_1 + b$. Therefore, for example, the point (X_2, Y_1) is shifted by $-(X_2 - f_i(Y_1))\tan(aY_1 + b)$ by the transformation. Consequently, the coordinate transformation matrix required here is expressed as Eq. 3.6 and 3.7.

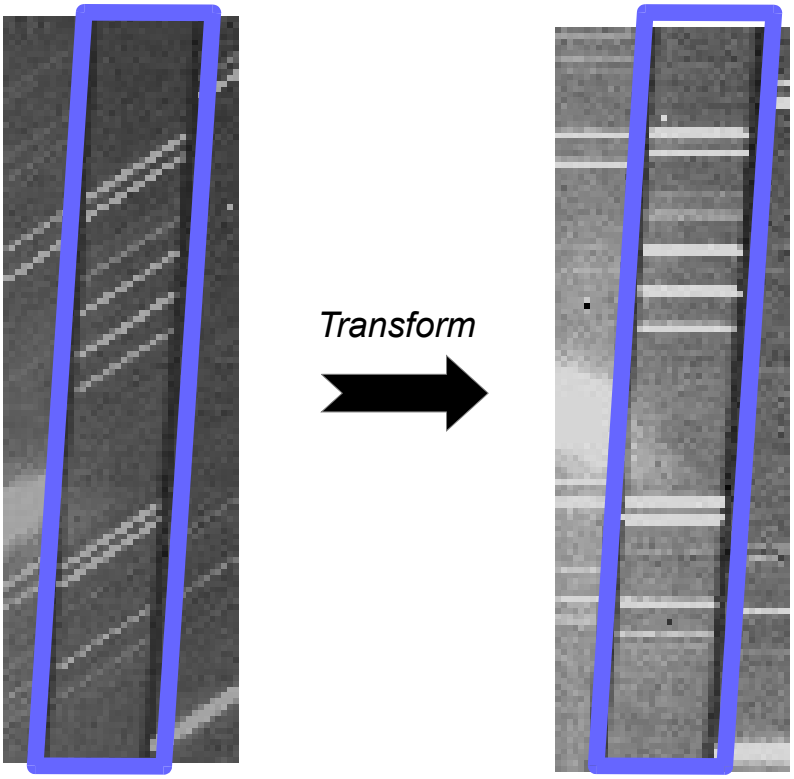

Figure 3.5: The image of the coordinate transformation of the WINERED data. The tilted slit images are aligned to the direction of the array coordinate after the transformation.

Chapter 4

The Search for DIBs

In our wavelength range, four major DIBs are known at $\lambda = 9577, 9633, 11797,$ and 13175Å (Joblin et al., 1990; Foing & Ehrenfreund, 1994). In addition, Groh et al. (2007) found a DIB at λ =10780Å, which is correlated with $E(B-V)$. We first searched for these five DIBs in the target spectra. Although $\lambda\lambda$9577 and 9633, which are proposed to be the electronic transitions of the fullerene cation (C_{60}^{+}; Foing & Ehrenfreund, 1994; Jenniskens et al., 1997; Galazutdinov et al., 2000), are detected toward some reddened stars, their EWs cannot be estimated confidently because of heavy telluric absorption lines. Conversely, the fairly strong DIBs, $\lambda\lambda$10780, 11797 and 13175, are detected toward many lines of sight. In addition to these five major DIBs, three weak DIBs at $\lambda = 9017, 9210,$ and 9258Å were reported in the Orion Nebulae by Misawa et al. (2009), who suggested that these DIBs are additional features of C_{60}^{+}. Because the DIBs, $\lambda\lambda$9210and 9258, which fall in our wavelength range, are blended with stellar absorption lines, it was difficult to evaluate their EWs without modeling the stellar spectra. The "C_{60}^{+}" DIBs in the wavelength range of WINERED, $\lambda\lambda 9210, 9258, 9577,$ and 9633, will be discussed in a separate study after a complete evaluation of the contamination by the overlapped telluric and stellar absorption lines.

Subsequently, we searched for new DIBs in the wavelength range of $0.91 < \lambda < 1.32\mu$m. Note that the wavelength ranges $0.93 < \lambda < 0.96\mu$m, $1.11 < \lambda < 1.16\mu$m, and $\lambda > 1.32\mu$m were not usable in searching for DIBs owing to heavy telluric absorption lines. We searched for the absorption lines satisfying the following two criteria: 1) the absorption lines are detected

with a 5σ level in the spectra of reddened stars, and 2) the absorption lines do not exist in the spectra of the reference star Rigel or the model stellar spectra of the A0Ia, A0V, B5Ia, and B5III stars. We synthesized model spectra using the SPTOOL program (Takeda, 1995), which employs ATLAS9 model atmospheres (Kurucz, 1993).[1] We first searched for such absorption lines in the spectrum of HD20041, because even weak DIBs are expected to be detectable toward HD20041 in view of the high S/N of the spectrum and the large EWs of $\lambda\lambda$11797 and 13175. Then, we searched for absorption lines in the spectra of other stars that are detected near the wavelength of the absorption lines detected toward HD20041. Consequently, 15 absorption features were detected toward multiple lines of sight as new DIB candidates.

To confirm that the candidate absorption features are DIBs originating from the interstellar clouds, we checked the consistency between the velocity of the intervening gas clouds and those of the detected absorption features. The rest-frame wavelengths of the absorption features were determined by fitting Gaussian profiles to the absorption features detected toward HD20041 (see the next section for details). As for the stars toward which the interstellar atomic absorption lines (K I, Na I, and Ca I) have been reported in the literature (see the Table 4.1 footnote for references), we compare the velocities of the detected absorption lines we detected with those of the atomic absorption lines. Regarding the other stars without known interstellar atomic lines, we compare the velocities of the candidate absorption lines with those of the confirmed DIB λ11797. The absorption lines whose velocities are inconsistent with those of the interstellar clouds should be categorized as non-DIBs. However, no absorption features were rejected by checking their velocities. Because their EWs do not show any dependence on the stellar spectral types but exhibit positive correlations with $E(B-V)$ (see §6.1), we conclude that all of the absorption features are truly DIBs.

In summary, we identified 15 new DIBs in addition to five DIBs previously identified in this wavelength range. Table 4.2 summarizes all the DIBs detected. The table also shows the

[1]The atomic line data was adopted from the Vienna Atomic Line Database (VALD; Kupka et al., 1999). The effective temperatures and surface gravities are as follows : $(T_{\rm eff}, \log g) = (9900, 2.1)$ for A0Ia, (9727,4.27) for A0V, (13600,2.5) for B5Ia, and (15000,4.22) for B5III. These values are adopted from Gray (1992) ($T_{\rm eff}$ of A0V and $\log g$ of A0V and B5V), Gray & Corbally (2009) ($T_{\rm eff}$ of A0Ia and B5V), and Cox (2000) ($\log g$ of A0Ia and B5Ia).

effect of the stellar and telluric absorption lines on the DIBs. Figures 4.1- 4.5 show the DIB spectra for all observed stars. The EWs of all DIBs toward all observed stars are summarized in Table 4.3. We calculated the EWs by a simple integration because the DIB profiles are not well established. Only for DIB λ10504, whose EWs cannot be evaluated by simple integration because of blending with stellar lines (see §4.3.1 for details), we fit Gaussian profiles to the DIB profile to estimate the EWs. The wavelength range used for the integration is arbitrarily set to include the whole DIB region (see Figures 4.1-4.5). The uncertainties of the EWs ($\sigma_{\rm err}$) or 5σ upper limits ($\mathrm{EW}^{5\sigma}_{\rm upp}$) are estimated from the S/N of the neighboring continuum using the following equations:

$$\sigma_{\rm err} = \Delta\lambda\sqrt{w}(\mathrm{S/N})^{-1}, \tag{4.1}$$

$$EW^{5\sigma}_{\rm upp} = 5\Delta\lambda\sqrt{w_{\rm inst}}(\mathrm{S/N})^{-1}, \tag{4.2}$$

where $\Delta\lambda$ is the wavelength interval per pixel ($\sim$ 0.2 Å), w, and $w_{\rm inst}$ are the widths of the DIB and the instrumental profile in pixels, respectively. Here, $w_{\rm inst}$ is defined as $2J+1$ pixel, where $J(=2\mathrm{pixels})$ is the slit width used in our observation. We did not consider additional systematic uncertainties due to continuum fitting, telluric absorption lines, and stellar lines. Several concerns on the systematic uncertainties in the EWs of each DIB will be discussed in §4.3.

Recently, Cox et al. (2014) reported 11 new NIR DIB candidates with their NIR DIB survey with VLT/X-shooter, 8 of which fall in our wavelength range, although they could not confirm that the candidates are truly DIBs because they detected the candidates only toward 3 stars at most. Of their candidates, 7 are included in our newly identified 15 DIBs for which we confirmed that they are truly DIBs by detecting them toward many lines of sight. Note that a line at λ $\sim$10507Å, which is reported as a DIB candidate by Cox, is identified as a stellar absorption line of N Roman1 in this study. The DIB λ10792 was originally reported as an unidentified line by Groh et al. (2007).

Table 4.1: The Line-of-sight Velocities of Intervening Interstellar Clouds

Star	$E(B-V)$ (mag)	$v_\odot$ [1] (km s^{-1})	Ref.[2]
HD2905	0.33	-21	1, 2
HD12953	0.62	–	–, –
HD14489	0.40	–	–, –
HD20041	0.73	-5	1, 3
HD21291	0.42	0	–, 2
HD21389	0.55	-10	1, 3
HD23180	0.31	13	1, 2
HD24398	0.32	15	1, 2
HD24912	0.33	7	1, 2
HD25204	0.30	–	–, –
HD30614	0.30	-3	1, 4
HD36371	0.43	–	1, –
HD36486	0.07	24	1, 5
HD36822	0.11	25	1, 6
HD37043	0.07	8	1, 5
HD37128	0.08	25	1, 2
HD37742	0.08	23	1, 6
HD38771	0.07	20	1, 2
HD41117	0.44	15	1, 2
HD43384	0.57	–	1, –
HD50064	0.85	–	1, –
HD190603	0.70	–	–, –
HD202850	0.13	–	1, –
HD223385	0.59	-28	–, 2
Cyg OB2 No.12	3.4	–	1, –
Rigel	0.00	–	–, –

[1] The heliocentric velocity of the strongest velocity component of the interstellar clouds.

[2] Left: References for DIBs in the optical wavelength range. Right: References for atomic absorption lines to define the velocities of interstellar clouds: (1) Friedman et al. (2011), (2) Welty & Hobbs (2001) (K I), (3) on-line catalog by Dan Welty (http://astro.uchicago.edu/ dwelty/gal.html), (4) Welty et al. (2003) (Ca I), (5) Welty et al. (1994) (Na I), (6) Price et al. (2001) (Na I, Ca II)

Table 4.2: Summary of the Identified DIBs

DIB [1]	λ_0 (Å)[2]	EW (mÅ)[3]	FWHM[4](Å)	Ref. [5]	Stellar Line [6]	Telluric Effect [7]
λ9880	9880.34 ±0.10	18.2 ± 1.9	1.25 ±0.12	This study	–	Slightly affected
λ10360	10360.69 ±0.10	17.5 ± 1.2	1.63 ±0.11	2	–	None
λ10393	10393.17 ±0.10	25.6 ± 1.6	2.62 ±0.18	2	Mg II	None
λ10438	10438.00 ±0.21	21.6 ± 1.6	6.06 ±0.52	2	–	None
λ10504	10504.52 ±0.10	36.2 ± 0.9	1.46 ±0.25	2	N I, Fe II	None
λ10697	10696.71 ±0.05	120.3 ± 5.3	4.73 ±0.12	2	Many C I, Si I	Slightly affected
λ10780	10780.46 ±0.10	57.1 ± 2.1	1.64 ±0.07	3	–	Slightly affected
λ10792	10792.15 ±0.18	17.3 ± 2.0	2.52 ±0.43	3	–	Slightly affected
λ11797	11797.53 ±0.10	61.0 ± 3.5	1.51 ±0.04	1	–	Overlapped
λ12293[8]	12293.69 ±0.10	–	1.76 ±0.24	This study	N I	Overlapped
λ12337	12337.32 ±0.23	25.5 ± 2.0	5.08 ±0.53	2	–	Slightly affected
λ12518	12518.69 ±0.18	9.7 ± 1.6	2.32 ±0.42	This study	–	Slightly affected
λ12536	12536.69 ±0.13	13.1 ± 1.8	1.72 ±0.31	This study	–	Slightly affected
λ12623	12623.86 ±0.11	38.1 ± 4.1	2.16 ±0.25	This study	–	Overlapped
λ12799	12799.13 ±0.09	50.8 ± 3.1	2.22 ±0.20	This study	He I, H I(Pa β)	Slightly affected
λ12861	12861.62 ±0.22	24.4 ± 2.3	4.36 ±0.51	This study	–	Slightly affected
λ13027	13027.68 ±0.35	37.6 ± 2.2	3.36 ±0.81	2	–	Overlapped
λ13175	13175.55 ±0.10	285.2 ± 5.6	4.07 ±0.19	1	–	Overlapped

[1] The rest-frame wavelength in air.
[2] The center wavelength measured for the profile of DIBs toward HD20041. The 1 σ uncertainties are shown.
[3] The equivalent widths of DIBs toward HD20041. The 1 σ uncertainties are shown.
[4] The 1 σ uncertainties are shown.
[5] References, in which the DIB was reported for the first time: (1) Joblin et al. (1990), (2) Cox et al. (2014), (3) Groh et al. (2007)
[6] Contaminated stellar absorption lines.
[7] How heavily the DIB is affected by the contamination of telluric absorption lines.
[8] λ_0 and FWHM of this DIB are measured for HD21389. See §5.2 for detail.

Table 4.3: EWs of DIBs

Stars	$E(B-V)$	λ9980	λ10360	λ10393	λ10438	λ10504	λ10697	λ10780	λ10792	λ11797
HD2905	0.33	10.9 ± 2.2	6.0 ± 0.9	5.8 ± 0.9	4.6 ± 0.9	8.3 ± 1.2	93.7 ± 5.3	47.8 ± 2.0	7.5 ± 1.5	38.3 ± 2.7
HD12953	0.62	13.0 ± 1.6	19.4 ± 1.6	11.4 ± 0.9	< 3.3	–	90.5 ± 5.5	71.2 ± 2.6	25.3 ± 2.9	78.7 ± 3.2
HD14489	0.40	11.8 ± 1.8	14.1 ± 1.0	–	< 3.0	30.8 ± 0.7	86.1 ± 4.9	66.4 ± 1.5	19.4 ± 2.0	70.1 ± 2.8
HD20041	0.73	18.2 ± 1.9	17.5 ± 1.2	25.6 ± 1.6	21.6 ± 1.6	36.2 ± 0.9	120.3 ± 5.3	57.1 ± 2.1	17.3 ± 2.0	61.0 ± 3.5
HD21291	0.42	< 8.4	8.3 ± 1.3	< 4.2	16.9 ± 2.2	18.4 ± 1.5	102.9 ± 9.2	22.7 ± 3.3	11.5 ± 3.0	18.0 ± 4.6
HD21389	0.55	16.8 ± 2.0	15.5 ± 1.2	–	13.2 ± 1.5	45.9 ± 1.1	217.3 ± 9.2	123.9 ± 3.3	36.3 ± 2.8	103.6 ± 3.5
HD23180	0.31	< 5.3	< 2.5	< 2.8	10.8 ± 1.3	< 4.3	–	11.8 ± 1.3	< 4.1	10.9 ± 1.4
HD24398	0.32	< 8.1	< 4.0	< 3.6	< 4.4	< 6.2	–	9.2 ± 2.3	< 7.9	< 19.8
HD24912	0.33	< 7.5	< 4.9	< 4.2	10.7 ± 1.9	18.6 ± 2.0	55.4 ± 5.6	44.5 ± 3.4	17.7 ± 2.8	33.8 ± 4.6
HD25204	0.30	< 5.2	< 2.2	< 2.3	< 2.4	< 4.6	–	< 6.9	< 6.5	< 9.6
HD30614	0.30	< 5.0	< 2.7	6.3 ± 0.9	< 3.1	10.4 ± 1.2	–	6.7 ± 1.0	–	24.9 ± 3.2
HD36371	0.43	9.3 ± 1.6	9.1 ± 1.1	9.2 ± 1.0	18.3 ± 1.4	29.1 ± 1.1	139.4 ± 7.4	58.0 ± 2.6	15.4 ± 1.0	67.4 ± 3.3
HD36486	0.07	< 5.1	< 2.3	< 2.2	< 2.7	< 3.7	–	9.6 ± 1.6	< 5.4	< 7.2
HD36822	0.11	< 5.6	< 2.4	< 2.8	< 3.2	< 4.5	–	11.9 ± 1.5	< 5.3	17.1 ± 3.5
HD37043	0.07	< 6.1	< 3.3	< 2.5	< 2.4	< 4.4	–	< 6.1	< 6.1	< 14.4
HD37128	0.08	< 7.7	< 2.5	< 2.0	< 2.4	< 3.4	–	9.5 ± 1.7	< 4.9	< 7.2
HD37742	0.08	< 6.2	< 2.0	< 1.9	< 2.2	< 3.3	–	< 6.0	< 6.0	< 9.6
HD38771	0.07	< 8.4	< 2.5	< 2.3	< 2.6	< 3.8	–	13.0 ± 2.0	< 6.2	–
HD41117	0.44	16.0 ± 1.7	8.2 ± 1.0	6.5 ± 0.9	16.5 ± 1.4	18.1 ± 1.0	85.6 ± 5.8	47.2 ± 2.0	20.6 ± 2.0	47.2 ± 2.3
HD43384	0.57	15.2 ± 1.9	14.4 ± 1.5	< 3.9	11.5 ± 1.3	26.9 ± 1.1	117.7 ± 4.6	54.3 ± 2.3	14.5 ± 2.2	70.5 ± 3.1
HD50064	0.85	< 18.3	< 6.4	< 6.5	40.9 ± 2.9	–	171.6 ± 9.6	96.3 ± 4.2	36.0 ± 4.3	105.1 ± 6.6
HD190603	0.70	18.2 ± 5.2	18.2 ± 2.7	< 15.8	< 13.0	45.5 ± 6.6	233.8 ± 12.8	136.2 ± 5.2	50.9 ± 3.7	139.2 ± 7.8
HD202850	0.13	< 14.1	< 10.9	< 10.7	< 12.8	–	–	43.2 ± 4.1	–	46.2 ± 8.5
HD223385	0.59	22.1 ± 2.5	27.5 ± 1.4	–	24.6 ± 1.5	–	169.1 ± 6.3	156.3 ± 3.3	57.3 ± 3.4	170.4 ± 4.1
Cyg OB2 No.12	3.4	92.6 ± 10.2	72.7 ± 5.9	37.7 ± 5.3	< 27.8	99.0 ± 3.5	434.6 ± 16.5	322.9 ± 6.1	72.8 ± 6.5	300.5 ± 14.5
Rigel	0.0	< 11.0	< 2.2	< 2.4	< 2.5	–	–	< 5.7	< 5.8	< 9.3

The EWs are given in units of mÅ. The bars mean that the EW or upper limit of the DIB could not be evaluated due to the overlapped stellar absorption lines and/or the residual features of the telluric correction.

Table 4.3: Continued.

Stars	$E(B-V)$	λ12293	λ12337	λ12518	λ12536	λ12623	λ12799	λ12861	λ13027	λ13175
HD2905	0.33	5.9 ± 1.1	7.4 ± 1.1	< 5.0	< 4.3	10.1 ± 2.1	12.3 ± 1.6	< 5.5	28.2 ± 2.2	99.2 ± 5.0
HD12953	0.62	7.9 ± 1.1	13.7 ± 1.5	< 3.2	10.9 ± 1.3	20.1 ± 2.5	22.3 ± 1.4	27.3 ± 2.3	18.2 ± 1.8	294.0 ± 5.3
HD14489	0.40	14.5 ± 1.4	16.1 ± 2.0	8.1 ± 1.4	27.0 ± 2.4	37.5 ± 3.8	30.1 ± 2.3	21.4 ± 1.9	< 5.7	307.0 ± 6.1
HD20041	0.73	–	25.5 ± 2.0	9.7 ± 1.6	13.1 ± 1.8	38.1 ± 4.1	50.8 ± 3.1	24.4 ± 2.3	37.6 ± 2.2	285.2 ± 5.6
HD21291	0.42	< 9.0	17.9 ± 2.7	< 10.5	< 12.5	< 13.8	38.8 ± 4.8	< 9.2	< 12.5	–
HD21389	0.55	19.4 ± 2.0	15.2 ± 1.7	7.4 ± 1.5	29.8 ± 2.3	53.9 ± 3.6	43.4 ± 2.7	58.4 ± 3.3	17.3 ± 2.5	479.4 ± 9.1
HD23180	0.31	7.9 ± 1.6	< 5.0	< 6.3	< 6.3	< 5.7	< 7.3	< 4.0	< 4.5	13.8 ± 3.1
HD24398	0.32	< 10.0	< 8.5	< 10.3	< 11.3	< 9.6	< 13.0	< 10.3	< 13.0	< 17.5
HD24912	0.33	11.9 ± 2.4	19.7 ± 2.9	< 9.2	< 11.5	< 15.1	25.1 ± 3.5	< 11.1	< 11.9	199.2 ± 13.7
HD25204	0.30	< 5.5	< 5.4	< 6.1	< 7.4	–	< 9.1	< 7.0	< 6.9	< 16.7
HD30614	0.30	< 5.0	< 4.9	< 5.0	< 4.7	< 6.4	< 7.0	< 5.5	< 5.4	< 13.2
HD36371	0.43	12.1 ± 1.8	< 5.1	12.8 ± 1.9	< 7.0	–	10.0 ± 2.8	16.2 ± 2.7	14.3 ± 2.5	219.0 ± 7.7
HD36486	0.07	< 8.3	< 7.0	< 7.0	< 6.7	< 7.8	16.9 ± 2.9	15.7 ± 2.2	< 6.9	< 13.7
HD36822	0.11	< 5.2	< 5.8	< 6.5	< 6.5	< 11.9	< 10.9	< 7.4	< 8.4	< 14.2
HD37043	0.07	< 8.0	< 7.5	< 8.9	< 11.6	< 13.3	–	< 8.7	< 9.0	< 13.4
HD37128	0.08	< 5.3	< 4.4	< 6.1	< 7.3	< 7.1	–	10.4 ± 2.0	< 7.4	–
HD37742	0.08	< 6.2	< 6.1	< 6.6	< 6.5	< 8.6	< 8.4	11.0 ± 1.9	< 8.4	< 14.4
HD38771	0.07	< 5.6	–	< 7.6	< 9.8	< 11.1	–	< 7.7	< 8.0	–
HD41117	0.44	< 5.1	11.9 ± 1.6	< 6.8	9.3 ± 1.8	18.6 ± 2.2	21.4 ± 1.9	18.7 ± 2.3	36.1 ± 2.7	155.3 ± 4.7
HD43384	0.57	8.2 ± 1.6	39.0 ± 3.0	< 7.4	11.1 ± 2.2	29.8 ± 2.9	32.4 ± 2.3	32.5 ± 3.2	19.0 ± 2.5	241.8 ± 6.6
HD50064	0.85	14.2 ± 3.4	< 9.6	< 10.3	55.7 ± 4.9	65.3 ± 5.9	56.0 ± 3.8	< 15.8	43.2 ± 4.4	386.5 ± 14.8
HD190603	0.70	21.5 ± 2.9	76.5 ± 5.6	31.5 ± 4.1	< 9.8	48.9 ± 3.7	21.6 ± 3.6	24.4 ± 4.0	–	493.8 ± 11.6
HD202850	0.13	< 16.2	< 15.6	< 14.8	< 15.8	< 23.5	–	< 14.8	< 16.2	–
HD223385	0.59	12.5 ± 1.7	37.1 ± 2.8	24.3 ± 1.7	22.2 ± 1.6	41.3 ± 3.1	34.9 ± 2.2	27.4 ± 3.2	–	436.6 ± 6.5
Cyg OB2 No.12	3.4	–	162.3 ± 10.9	42.7 ± 5.5	48.7 ± 4.7	141.2 ± 6.5	87.7 ± 6.0	73.6 ± 4.2	–	982.3 ± 12.5
Rigel	0.0	< 7.5	–	< 9.0	< 7.6	< 9.0	–	< 7.6	< 9.4	–

The EWs are given in units of mÅ. The bars mean that the EW or upper limit of the DIB could not be evaluated due to the overlapped stellar absorption lines and/or the residual features of the telluric correction.

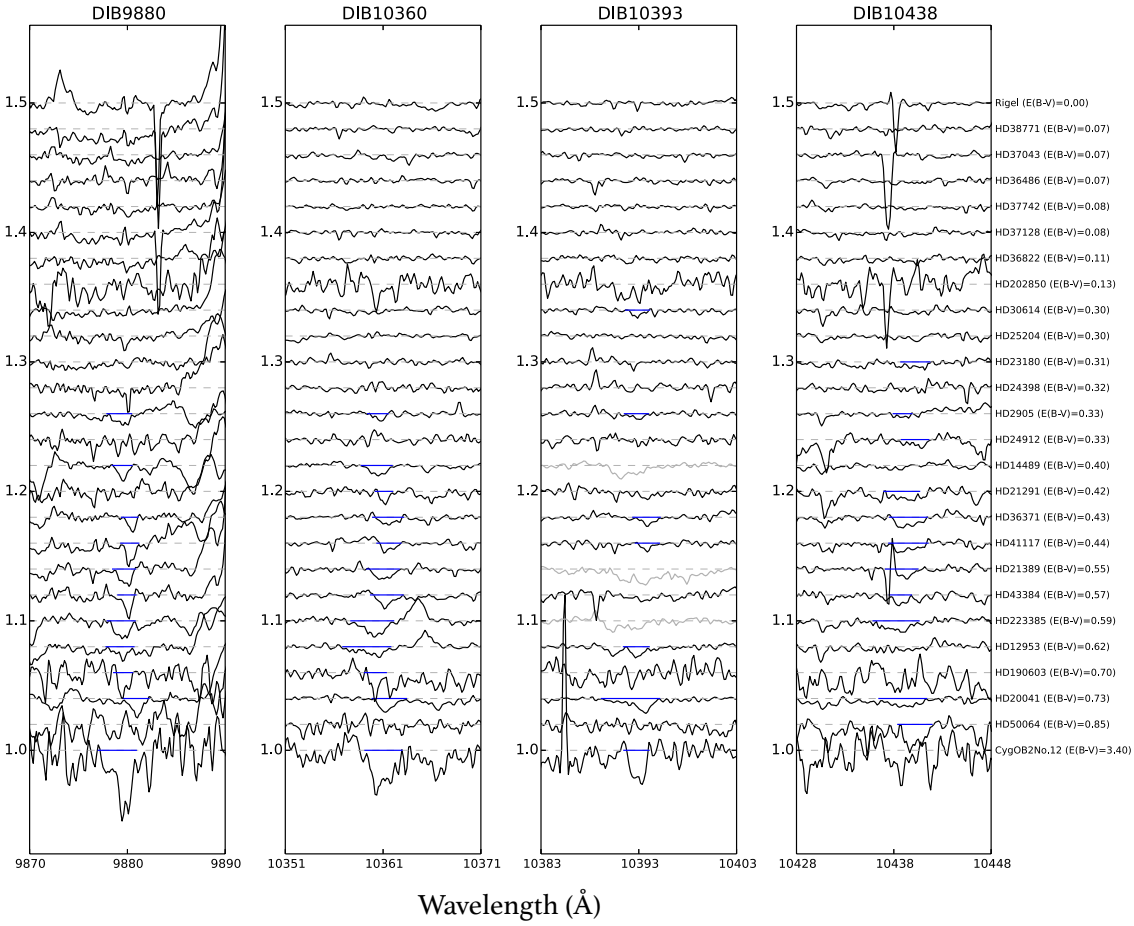

Figure 4.1: Spectra of four DIBs, $\lambda\lambda 9880, 10360, 10393,$ and 10438, for all targets plotted in increasing order of $E(B-V)$ from top to bottom. The spectra are normalized and plotted with arbitrary offsets. The continuum level of each star is shown by a dashed thin line. The spectra of the stars, in which the EWs or upper limits of the DIBs cannot be evaluated due to overlapped stellar and/or telluric absorption lines, are plotted with gray lines. The integrated ranges used in the calculation of the EWs are shown as thick blue lines.

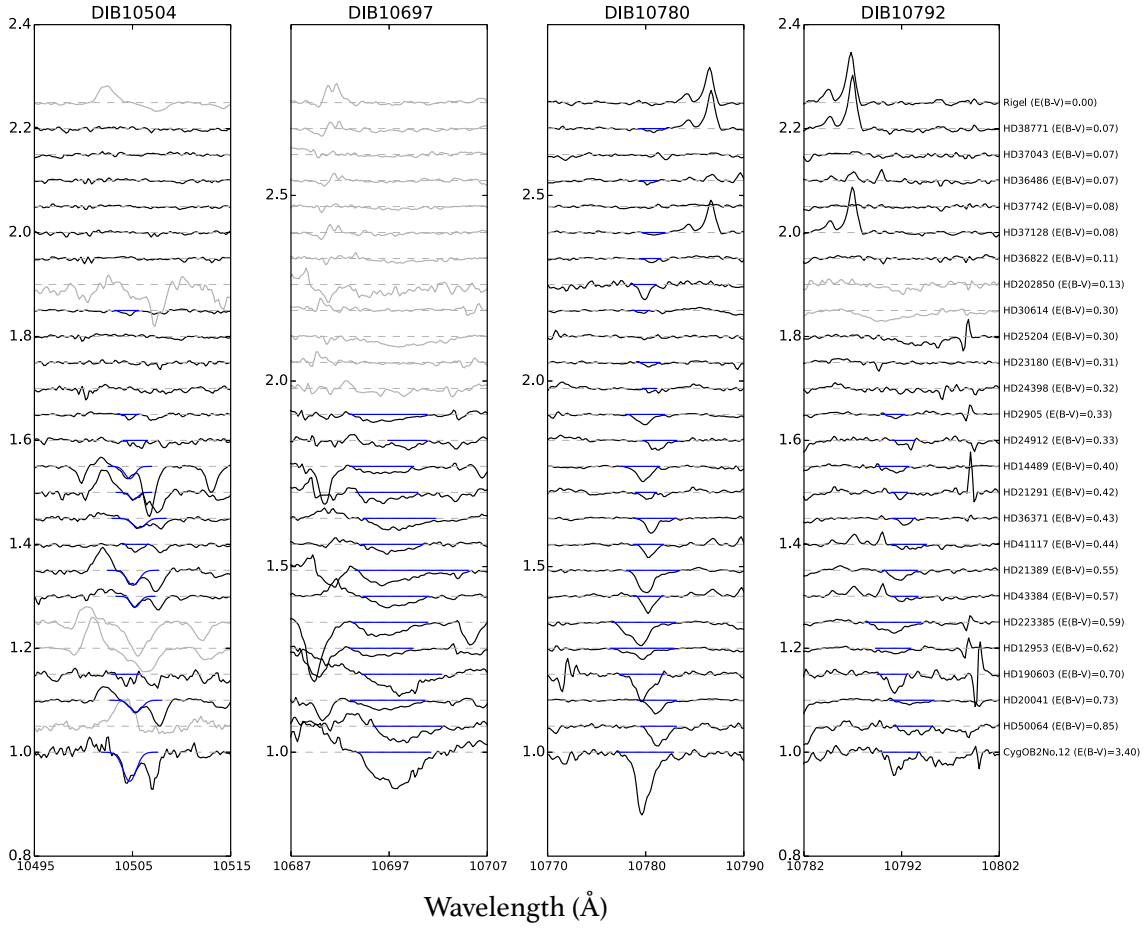

Figure 4.2: Spectra of four DIBs $\lambda\lambda 10504, 10697, 10780,$ and 10792 for all targets. The notations are the same as those in Figure 4.1 except for DIB $\lambda 10504$, for which the EWs are estimated by fitting Gaussian profiles (shown as blue lines) to avoid the blending of the stellar absorption lines (see §5.3.1 for detail). The spectra of $\lambda 10697$ were divided by the spectra of telluric standard stars, from which overlapped C I and Si I stellar absorption lines were removed (see §5.3.2 for details).

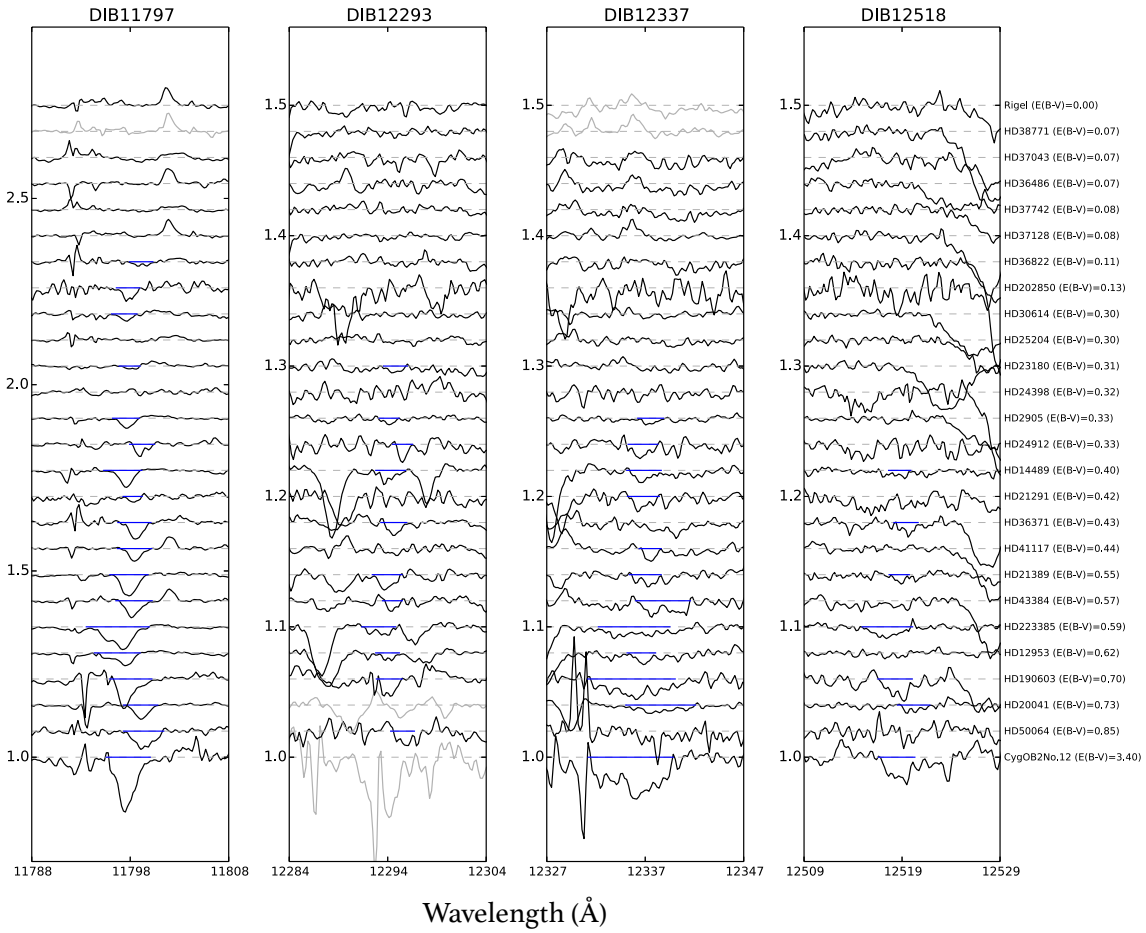

Figure 4.3: Spectra of DIBs $\lambda\lambda 11797, 12293, 12337,$ and 12518 for all targets. The notations are the same as those in Figure 4.1.

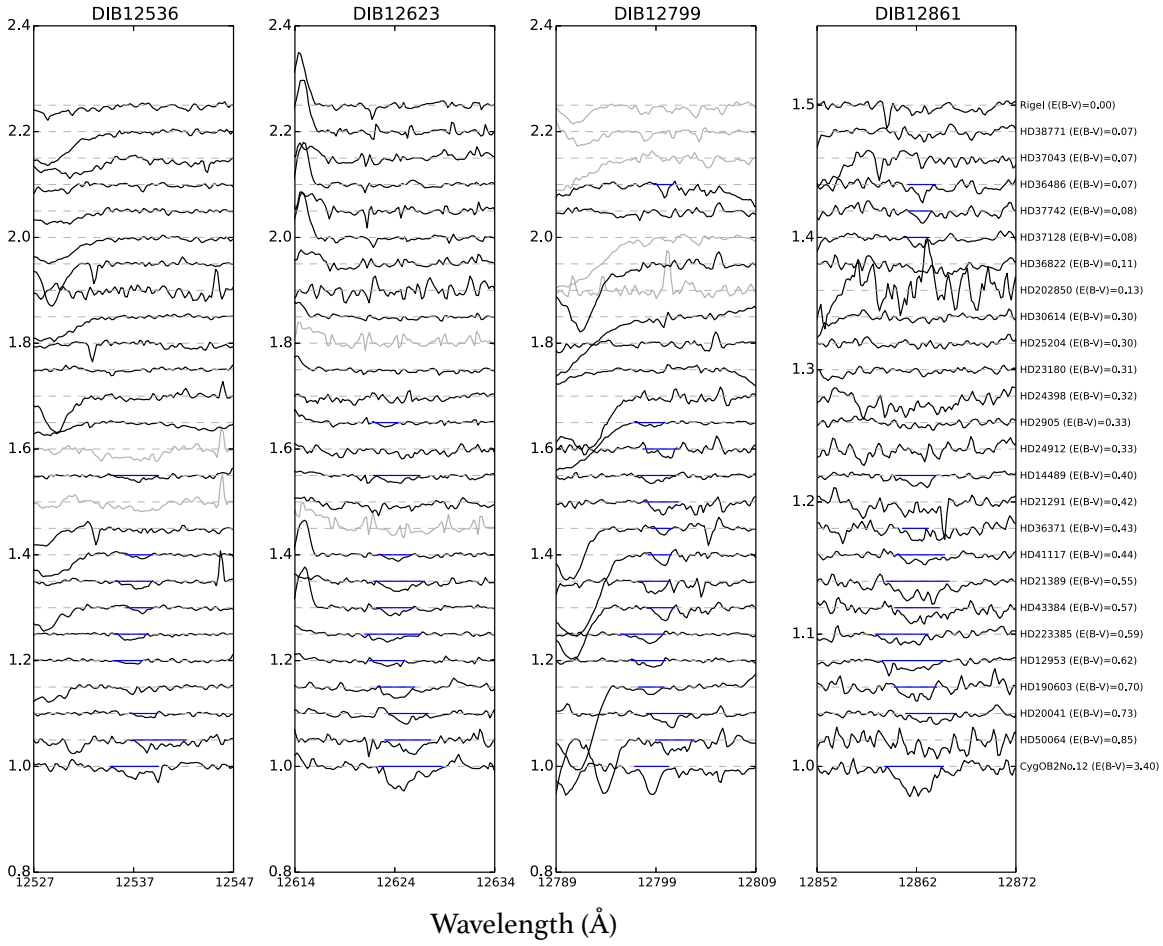

Figure 4.4: Spectra of DIBs $\lambda\lambda 12536, 12623, 12799,$ and 12861 for all targets. The notations are the same as those in Figure 4.1. The spectra of $\lambda 12799$ were normalized with a high-order polynomial function to remove the overlapped He I and H I stellar absorption lines (see §5.3.5 for details)).

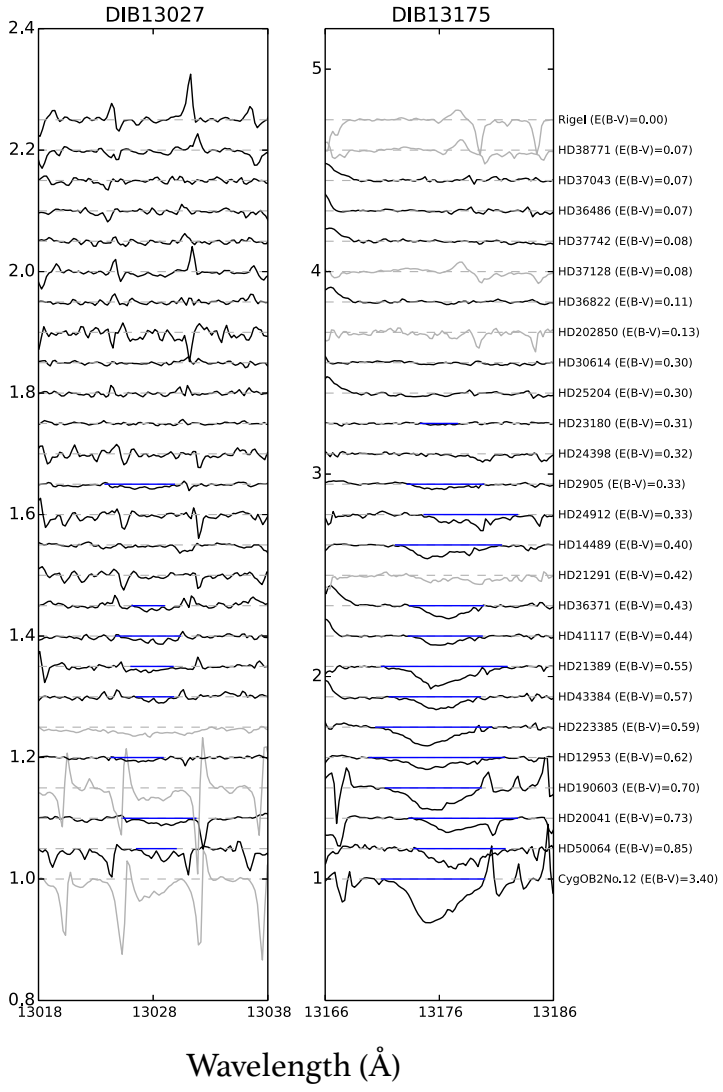

Figure 4.5: Spectra of DIBs $\lambda\lambda$13027and 13175 for all targets. The notations are the same as those in Figure 4.1.

Chapter 5

Properties of NIR DIBs

5.1 EW distribution

Figure 5.1 shows the distribution of the ratios of the EWs to $E(B-V)$ for DIBs in 4000Å$<\lambda<$ 18000 Å. The data for optical DIBs in the wavelength range 4000Å$<\lambda<$ 10000Å are adopted from the catalog published on the Web[1] by P. Jenniskens. The catalog is primarily based on the studies by Jenniskens & Desert (1994) and Krełowski et al. (1995) (see the Web site for other references). We do not include the recent surveys of DIBs in the optical wavelength range such as Tuairisg et al. (2000); Hobbs et al. (2008, 2009) in this figure, because most of the DIBs found in these surveys are weak. The data for $H-$band DIBs are adopted from Cox et al. (2014). Because the authors do not show the ratios of EWs to $E(B-V)$, we roughly estimated them by dividing the EWs toward 4U 1907+09 by the color excess, $E(B-V)=3.48$. Regarding the DIBs identified in this study, we determine the ratios of EWs to $E(B-V)$ by fitting linear functions ($EW = a \times E(B-V) + b$) to EW$-E(B-V)$ plots (see §6.1 and Table 6.1). From Fig. 5.1, we found that the NIR DIB λ13175 is one of the strongest DIBs ever detected. We also found that there are many DIBs in the range $0.91 < \lambda < 1.32\mu$m, in which only four DIBs were previously confirmed. All of the DIBs detected herein are stronger than 10 mÅ, below which the majority of optical DIBs are distributed. Assuming a similar distribution as that of the optical DIBs, we expect that the

[1] http://leonid.arc.nasa.gov/DIBcatalog.html

number of weak NIR DIBs increases by an order of magnitude through deeper spectroscopic observations.

5.2 Wavelength and FWHM

We measured the rest-frame wavelengths in air (λ_0) and full width at half maximum (FWHM) of all identified DIBs by fitting Gaussian functions to profiles. We fitted the Gaussian functions to the profiles of HD20041, toward which almost all DIBs are detected with high S/N. Because the DIB λ12293 toward HD20041 is blended with two N I stellar absorption lines, we used the spectrum of HD21389 only for this DIB. Table 4.2 summarizes the fitting results, and Figure. 5.2 shows the spectra of the DIBs and fitted Gaussian profiles. We shift the measured wavelength to the rest-frame wavelength using the heliocentric velocities of the strongest velocity component of the interstellar clouds toward these stars (Table 4.1). The systematic uncertainties may remain in the measured λ_0 and FWHMs of the DIBs because of the possible velocity dispersion of multiple velocity components toward these two stars.

5.3 Comments on individual DIBs

5.3.1 $\lambda\lambda$10360, 10393, 10438, and 10504

These DIBs fall in the wavelength ranges without any telluric absorption lines. Because the S/N of raw spectra is higher compared with the S/N of spectra divided by that of telluric standard stars, their EWs are calculated from the undivided spectra. DIB λ10504 is contaminated by two stellar lines: Fe II λ10501.5 emission line of supergiant stars of early A-type and late B-type and N I λ10507.0 absorption line of stars earlier than late B-type (Figure. 5.2). In the case when the relative velocity between the background star and the interstellar clouds is large, the observed DIB is blended by the lines. A relative velocity of only $\sim$ 30 km s^{-1}, which produces a wavelength shift of $\sim$ 1Å, can affect the calculation of EWs of the DIB. In this study, we do not calculate the EWs of the DIB toward HD50064 and HD223385, which are clearly detected but significantly blended by the stellar lines (see Figure 4.2). When the DIB is separately detected with slight blending, we calculate the EWs by fitting two Gaussian

profiles to the blended DIB profile and N I absorption line (Figure 4.2). We do not estimate systematic uncertainties from the fitting procedure. For a more precise analysis of this DIB, a model spectrum that reproduces both the absorption and emission lines for each star is required.

5.3.2 λ10697

The DIB λ10697 is surrounded by strong stellar absorption lines of C I and Si I as well as telluric absorption lines (Figure 5.2). Because these stellar metal absorption lines are also detected in the A0V telluric standard stars, many false emission-like features appear in all telluric-corrected spectra. These artificial features significantly affect the continuum fitting and evaluation of EWs or upper limits. Therefore, we attempted to remove from the telluric standard spectra the C I lines at $10689.72, 10683.03, 10691.24,$ and 10707.32Å and the Si I lines at 10685.34 and 10694.25Å.

First, we define the instrumental profile of stellar metal absorption lines using the absorption profile of S I 10459.41Å and Si I 10827.09Å lines, which are free from any blending of telluric absorption lines and show a clear line profile. The profiles of S I 10459.41Å and Si I 10827.09Å lines are used for the removal of C I and Si I lines, respectively. We then fit the instrumental profiles to the C I and Si I lines by shifting the wavelength and scaling the intensity on the basis of the intensity ratios of the metal absorption lines in the model spectra of A0V stars. We construct a spectrum containing only C I and Si I absorption lines by synthesizing the profiles of each absorption line. These stellar metal lines are removed from the telluric standard spectra by dividing them by the synthetic spectra of C I and Si I lines. Note that the slight residuals appear to remain in the resultant spectra for some telluric standard stars probably because the S I line profile is slightly different from the C I lines. Finally, telluric absorptions are corrected using the C I and Si I corrected spectra of telluric standard stars. Consequently, the continuum fitting is improved except for Cyg OB2 No.12 and HD190603, for which the data were obtained in 2012 July (when the climate is humid in Japan), and the metal absorption lines of the telluric standard star HIP87108 could not be removed well because of the low S/N and quite strong telluric absorption lines. Figure 4.2

shows the spectra of λ10697 divided by the spectra of telluric standard stars, from which the C I and Si I absorption lines were removed. The EWs of λ10697 are estimated, but the upper limit of the EW is not evaluated because of the possible residual of stellar metal lines when the DIB is not detected.

5.3.3 λ12293

The DIB is located between two N I absorption lines, $\lambda\lambda$12289.18 and 12298.54 (Figure 5.2). Because of the relatively large wavelength offset $\sim$ 5Å ($\sim$ 120 km s^{-1}), it is unusual that they are blended significantly. However, these stellar lines affect the determination of the continuum level around the DIB. In particular, the DIB of HD20041 is surrounded by both the N I absorption lines and false emission-like features from the N I absorption lines in the telluric standard star. Although the DIB itself is clearly detected toward HD20041, we cannot estimate its EW.

5.3.4 λ12799

Because the DIB is located in the wings of the strong and broad He I and H I (Pa β) absorption lines, we remove these broad lines by fitting a high-order polynomial function with an IRAF task (i.e., *continuum*) for telluric-corrected spectra (Figures. 4.4 and 5.2). Although we do not consider various possible systematic uncertainties, we can identify this absorption as a DIB because of a clear positive correlation with $E(B-V)$ (see §6.1). Note that the upper limit of the EWs for the DIB cannot be evaluated for Rigel, HD38771, and HD37043 because the telluric absorption lines cannot be removed sufficiently well.

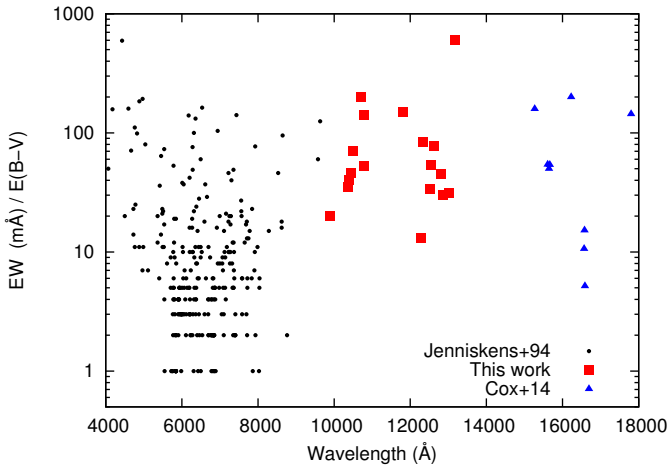

Figure 5.1: Distribution of the ratios of the EWs to $E(B-V)$ as a function of the wavelength for all DIBs in optical and near-infrared. Black circles, red squares, and blue triangles represent the points of optical DIBs from Jenniskens & Desert (1994), NIR DIBs found in this study, and DIBs in the $H-$band from Cox et al. (2014), respectively.

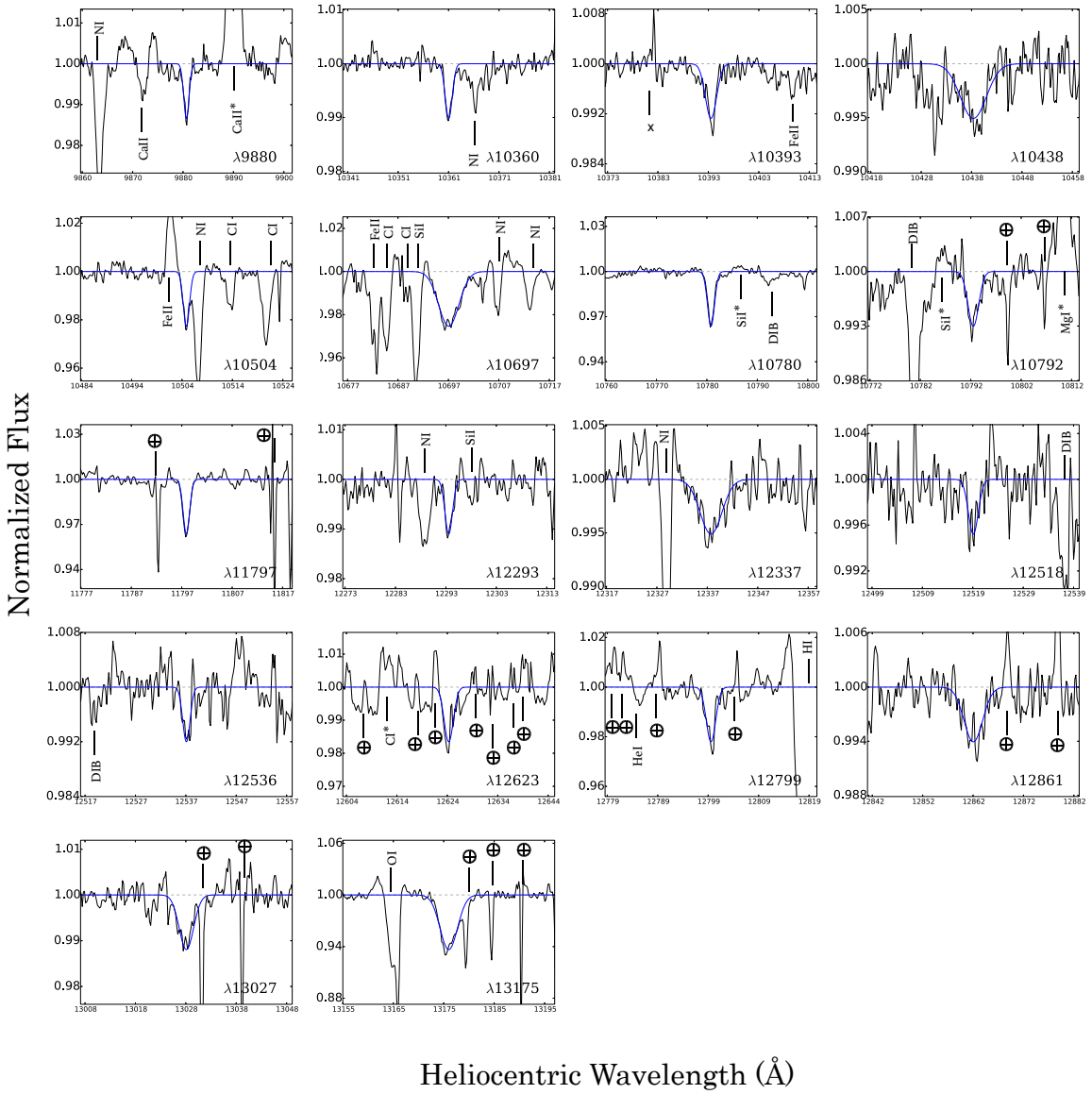

Figure 5.2: Profiles of identified DIBs toward HD20041 ($E(B-V) = 0.73$). The spectrum of HD21389 ($E(B-V) = 0.55$) is shown only for λ12293 because λ12293 toward HD20041 is blended by the stellar absorption lines (see the main text for details). The black line shows the observed spectrum, while the blue line shows the Gaussian profile fitted to the DIB. The stellar absorption and emission lines are marked with vertical lines and the species names (emission lines with asterisk: artificial emission-like features from the absorption lines of telluric standard stars). The residuals of corrected telluric absorption lines are marked with "⊕". The spurious features are marked with x's.

Chapter 6

Correlations

To reveal the properties of the DIB carriers in an astronomical environment, it is a first step to investigate the correlations among DIBs as well as the correlations of DIBs with the parameters of interstellar clouds, such as reddening (Herbig, 1993; Cami et al., 1997; Friedman et al., 2011). The correlations of the NIR DIBs at $\lambda > 1\mu$m have been discussed for a limited number of lines of sight (Joblin et al., 1990; Geballe et al., 2011; Cox et al., 2014) except for the strongest DIB in the $H-$band, λ15272, which was examined by Zasowski et al. (2015) for about 60,000 lines of sight in the SDSS-III/APOGEE survey. Here, we analyze the correlations among the NIR DIBs that we identified at $0.91 < \lambda < 1.32\mu$m, $E(B-V)$, and optical DIBs, with a significant number of lines of sight (i.e., 25) for the first time. The EWs of the optical DIBs are adopted from Friedman et al. (2011), who investigated the correlations among eight strong optical DIBs ($\lambda\lambda$5487.7, 5705.1, 5780.5, 5797.1, 6196.0, 6204.5, 6283.8, and 6613.6). Among the 25 stars that we observed, the optical spectra of 19 stars were also obtained in Friedman et al. (2011). Therefore, it is possible that the correlation between optical and NIR DIBs can be investigated using a significant number of lines of sight.

6.1 Correlations with $E(B-V)$

Figure 6.1 show the EW$-E(B-V)$ plot. We also plot the data of Cox et al. (2014) for the DIBs that they detected. However, we do not include their data in the calculation of the

correlation coefficients in order to preserve the uniformity of data. We fit the linear functions ($EW = a \times E(B-V) + b$) to each EW$-E(B-V)$ plot. The results are summarized in Table 6.1. In the calculation of the correlation coefficients, we exclude the data point of Cyg OB2 No.12, for which the EWs of the optical DIBs are known to be much lower than that expected from the correlation with $E(B-V)$ (Chlewicki et al., 1986). To compare the correlation coefficients with those of the optical DIBs, we also show the correlation coefficients between $E(B-V)$ and the EWs of the eight optical DIBs taken from Friedman et al. (2011) (Table 6.1). To eliminate the bias effect and the difference in sample size, we calculate the correlation coefficients using only the 19 stars observed in both NIR (our data) and optical wavelength ranges (Friedman et al., 2011). As an example, Figure 6.2 shows the correlations of the optical DIB λ5780.5 and the NIR DIB λ11797 with $E(B-V)$.

All NIR DIBs are found to have a positive correlation with $E(B-V)$, which is expected for DIBs. We focus on the DIBs detected toward more than 10 lines of sight, whose correlation coefficients appear to be reliable. The correlation coefficients of all the NIR DIBs are found to be lower than those of the eight strong optical DIBs calculated for the same sample ($r \sim 0.9$). When discussing the difference between two correlation coefficients, we must consider the attenuation of the correlations due to measurement errors and the statistical significance of the difference between correlation coefficients. Here, we will consider whether the differences in the correlation coefficients between optical and NIR DIBs are statistically significant. We focus on the correlation coefficients of three NIR DIBs, $\lambda\lambda 10780, 11797,$ and 13175, because they are detected toward many lines of sight (> 10) and the uncertainties of their EWs are expected to be low owing to their large EWs and the smaller effect of contamination by stellar lines. Regarding the other DIBs, statistical tests are not meaningful because of the limited sample size and/or large systematic uncertainties.

We conduct a statistical test for the pairs of the three NIR DIBs and eight optical DIBs to clarify the difference between the correlation coefficients using the Fisher z-transformation. Consequently, the correlation coefficients of the five optical DIBs with $r > 0.91$ are found to be different from those of the three NIR DIBs, with a 95% significance level. Therefore, the difference in the correlation coefficients with $E(B-V)$ between the optical and NIR DIBs

are suggested to be statistically significant for some pairs. As for the other pairs and NIR DIBs, further observations are necessary.

The high correlation coefficients of optical DIBs show that the abundances of their carriers are simply in proportion to the amount of gas in the lines of sight. Considering the lower correlation coefficients of NIR DIBs, we infer that the abundance of the NIR DIB carriers is more sensitive to other physical parameters of the interstellar clouds (such as ionization UV flux) as well as to the amount of gas in the line of sight.

6.2 Correlations among NIR DIBs: A family of NIR DIBs?

We also examine the correlations between all pairs of NIR DIBs except for 5 weak DIBs, which are detected toward fewer than 10 stars, and 2 DIBs $\lambda\lambda$12293 and 12799, whose EWs have large systematic uncertainties owing to a blending of neighboring stellar absorption lines. From the NIR DIB set identified, we search for so-called families, in which DIBs are well correlated with each other. DIBs in a family are expected to arise from molecules having similar physical and/or chemical properties (Moutou et al., 1999; McCall et al., 2010).

The correlation coefficients for all 55 pairs consisting of 11 DIBs are shown in Table 6.2. As in the previous section, we do not include the EWs of DIBs toward Cyg OB2 No.12 in the calculation. All pairs are found to have positive correlation coefficients. In particular, three pairs consisting of $\lambda\lambda 10780, 10792,$ and 11797 have the highest correlation coefficients with $r \sim 0.95$, suggesting that these DIBs can be classified as a family (Figure 6.3). Because all three DIBs are fairly strong and detected toward over 10 lines of sight, the correlation coefficients should be reliable. Note that λ13175 is also well correlated with the three DIBs $\lambda\lambda 10780, 10792,$ and 11797, but the correlation coefficients ($r \sim 0.9$) are slightly lower than those among the three DIBs. Because there are several points that do not quite fit the correlation, carriers of these three DIBs would not be the same molecule. Note that λ10792 toward Cyg OB2 No.12 is considerably weaker than that expected from the correlations (Figure 6.3), suggesting that the carrier of this DIB may become less abundant due to some chemical processes, which would be efficient in a dense cloud with $n_{\rm H} \sim 10^3 {\rm cm}^{-3}$ (Casu et al., 2005). Alternatively, the high X-ray flux from many massive stars in the Cygnus OB2

association including Cyg OB2 No.12 may affect the abundance of the λ10792 carrier (Gredel et al., 2001).

Two pairs, $\lambda10504 - \lambda12623$ and $\lambda10504 - \lambda13175$, are also found to have high correlation coefficients of $r > 0.95$ (Figure 6.4). However, the correlation coefficient of the remaining pair, $\lambda12623 - \lambda13175$, is lower ($r = 0.84$). This is because the EWs of $\lambda\lambda$12623 and 13175 toward HD50064, whose EW of λ10504 cannot be measured owing to the blending of the stellar absorption lines (see §6.3.1), do not match the correlation. As the number of lines of sight used for the calculation of the correlation coefficients is small for these pairs (e.g., seven stars for the $\lambda10504 - \lambda12623$ pair), the correlation coefficients could be affected by the sample selection. Although these DIBs may form another family in view of the high correlation coefficients, it is necessary to increase the data points to confirm this from more solid correlations.

6.3 Correlations of NIR DIBs with optical DIBs

Finally, we examine the correlations between the optical and NIR DIBs. We focus on four NIR DIBs, $\lambda\lambda10438, 10780, 11797,$ and 13175, whose correlation coefficients with optical DIBs can be calculated with over 10 data points. Regarding the other DIBs, the number of data points available for the calculation of the correlation coefficients is too small for a statistical discussion. As in the previous two sections, we exclude Cyg OB2 No.12 from the calculation of the correlation coefficients. Table 6.3 shows the correlation coefficients of 32 pairs consisting of 8 optical DIBs and 4 NIR DIBs. As a reference, we also calculate the correlation coefficients among optical DIBs using only the stars observed by us and Friedman et al. (2011).

Friedman et al. (2011) showed that the correlation coefficients of all pairs consisting of eight optical DIBs have $r > 0.9$, except for the two pairs $\lambda5487.7 - \lambda5797.1$ ($r = 0.87$) and $\lambda5797.1 - \lambda6283.8$ ($r = 0.86$). The correlation coefficients calculated in this study for the optical DIBs are as high as theirs for all pairs. However, none of the correlation coefficients between NIR and optical DIBs are found to be as high as those among optical DIBs, suggesting that these NIR DIBs do not form a family with the optical DIBs. This is consistent with the discussion in §6.1, in which a clear difference in the correlation coefficients with $E(B - V)$

between optical and NIR DIBs is shown.

In addition, we find that the three strongest NIR DIBs, $\lambda\lambda 10780, 11797,$ and 13175 are better correlated with $\lambda\lambda 5705.1, 5780.5, 6204.5,$ and 6283.8 ($r = 0.8-0.9$) than with $\lambda\lambda 5797.1$, 6196.0, and 6613.6 ($r = 0.6-0.7$) although there are a few exceptions such as $\lambda 5705.1-\lambda 13175$ ($r = 0.75, N = 10$), whose correlation coefficient is lower compared to those of $\lambda 5705.1 - \lambda 10780$ and $\lambda 5705.1 - \lambda 11797$. Figure 6.5 shows the correlations between four NIR DIBs and two representative optical DIBs in the two groups, $\lambda\lambda 5780.5$ and 5797.1. The DIB $\lambda 10438$ is moderately well correlated with the eight optical DIBs (correlation coefficients are $\sim$0.7-0.8). Because the DIB $\lambda 10438$ is weaker than the other three DIBs, the correlation coefficients could be affected by the relatively large uncertainty of the EWs.

These two groups of optical DIBs classified by their correlation with NIR DIBs are consistent with the previous studies on the correlations among optical DIBs. Cami et al. (1997) showed that two pairs of $\lambda\lambda 5780.5, 6204.5$ and $\lambda\lambda 5797.1, 6613.6$, which are members of the groups, are well correlated. $\lambda\lambda 6196.0, 6613.6$ is the only pair that is proposed to have a perfect correlation (Moutou et al., 1999; McCall et al., 2010). However, the differences in the correlation coefficients between the two groups are not statistically significant. For all pairs, we cannot exclude the null hypothesis that the correlation coefficients are not truly different. For example, the probability that the two correlation coefficients of $\lambda 5780.5 - \lambda 10780$ ($r = 0.85, N = 17$) and $\lambda 5797.1 - \lambda 10780$ ($r = 0.70, N = 15$) are not different is estimated to be $p = 0.32$, which is too high to reject the null hypothesis. Therefore, it is necessary to increase the number of samples to clarify the difference in correlation coefficients.

Table 6.1: Correlation Coefficients between EWs and $E(B-V)$ and the Results of Linear Least-square Fit

DIB	N[1]	r[2]	a	b
λ9880	10	0.68	20±8	4±4
λ10360	11	0.73	35±11	-4±6
λ10393	6	0.88	40±11	-8±5
λ10438	11	0.83	46±10	-6±5
λ10504	11	0.80	71±18	-8±8
λ10697	13	0.60	202±81	21±43
λ10780	21	0.73	141±30	-4±12
λ10792	13	0.56	53±24	-3±13
λ11797	17	0.69	149±41	-4±19
λ12293	11	0.45	13±8	6±4
λ12337	11	0.60	84±37	-18±19
λ12518	6	0.46	34±33	-4±18
λ12536	8	0.50	54±38	-10±22
λ12623	10	0.71	77±27	-8±16
λ12799	14	0.65	45±15	7±8
λ12861	12	0.56	30±14	11±6
λ13027	8	0.48	31±23	9±13
λ13175	13	0.70	601±182	-39±96
λ5487.7	13	0.91	194±26	-8±11
λ5705.1	14	0.85	181±32	0±14
λ5780.5	19	0.94	809±70	-34±23
λ5797.1	15	0.94	298±31	-9±12
λ6196.0	19	0.96	82±6	-3±2
λ6204.5	18	0.93	305±31	-2±11
λ6283.8	17	0.89	1662±221	19±81
λ6613.6	18	0.98	358±18	-22±6

[1] Number of stars with DIB detection (5σ), which are used for the calculation of the correlation coefficients. The data of Cyg OB2 No.12 is not included in the calculations of correlation coefficients and the fitting of linear functions ($EW = a \times E(B-V) + b$). See §6.1 for detail.

[2] Correlation coefficients ($E(B-V)$ - EW)

Table 6.2: Correlation Coefficients among NIR DIBs

	λ9880	λ10360	λ10438	λ10504	λ10697	λ10780	λ10792	λ11797	λ12337	λ12623	λ13175
λ9880	–	0.75 (10)	0.62 (7)	0.57 (8)	0.52 (10)	0.70 (10)	0.76 (10)	0.71 (10)	0.54 (9)	0.61 (9)	0.63 (10)
λ10360	–	–	0.66 (8)	0.89 (9)	0.45 (11)	0.78 (11)	0.80 (11)	0.85 (11)	0.47 (10)	0.57 (9)	0.75 (10)
λ10438	–	–	–	0.47 (8)	0.46 (10)	0.46 (11)	0.56 (10)	0.55 (11)	0.51 (8)	0.77 (7)	0.57 (10)
λ10504	–	–	–	–	0.82 (10)	0.88 (11)	0.81 (10)	0.90 (11)	0.58 (9)	0.99 (7)	0.95 (9)
λ10697	–	–	–	–	–	0.82 (13)	0.75 (13)	0.77 (13)	0.66 (11)	0.77 (10)	0.85 (12)
λ10780	–	–	–	–	–	–	0.96 (13)	0.97 (17)	0.50 (12)	0.65 (10)	0.92 (13)
λ10792	–	–	–	–	–	–	–	0.94 (13)	0.63 (11)	0.63 (10)	0.87 (12)
λ11797	–	–	–	–	–	–	–	–	0.63 (11)	0.63 (10)	0.90 (13)
λ12337	–	–	–	–	–	–	–	–	–	0.54 (9)	0.60 (10)
λ12623	–	–	–	–	–	–	–	–	–	–	0.84 (10)
λ13175	–	–	–	–	–	–	–	–	–	–	–

The number in parentheses denotes the number of stars used for the calculation of the correlation coefficients. The data of Cyg OB2 No.12 is not included in the calculations of the correlation coefficients.

Table 6.3: Correlations Coefficients among Optical DIBs and those between Optical and NIR DIBs

	λ5705.1	λ5780.5	λ6204.5	λ6283.8	λ5487.7	λ5797.1	λ6196.0	λ6613.6
λ5705.1	–	0.95 (14)	0.94 (14)	0.93 (14)	0.94 (13)	0.89 (14)	0.80 (14)	0.87 (14)
λ5780.5	–	–	0.99 (18)	0.97 (17)	0.97 (13)	0.94 (15)	0.95 (19)	0.96 (18)
λ6204.5	–	–	–	0.99 (16)	0.95 (13)	0.93 (15)	0.93 (18)	0.95 (18)
λ6283.8	–	–	–	–	0.88 (13)	0.89 (15)	0.89 (17)	0.91 (16)
λ5487.7	–	–	–	–	–	0.97 (13)	0.96 (13)	0.94 (13)
λ5797.1	–	–	–	–	–	–	0.94 (15)	0.94 (15)
λ6196.0	–	–	–	–	–	–	–	0.98 (18)
λ6613.6	–	–	–	–	–	–	–	–
λ10438	0.39 (8)	0.61 (9)	0.64 (9)	0.60 (9)	0.54 (8)	0.58 (9)	0.40 (9)	0.61 (9)
λ10780	0.75 (13)	0.81 (15)	0.86 (14)	0.91 (15)	0.61 (12)	0.71 (13)	0.74 (15)	0.68 (14)
λ11797	0.86 (12)	0.83 (11)	0.90 (11)	0.95 (11)	0.73 (11)	0.77 (11)	0.74 (11)	0.70 (11)
λ13175	0.68 (9)	0.78 (9)	0.87 (9)	0.92 (9)	0.49 (8)	0.63 (9)	0.48 (9)	0.60 (9)

The number in parentheses denotes the number of stars used for the calculation of the correlation coefficients. The data of Cyg OB2 No.12 is not included in the calculations of the correlation coefficients.

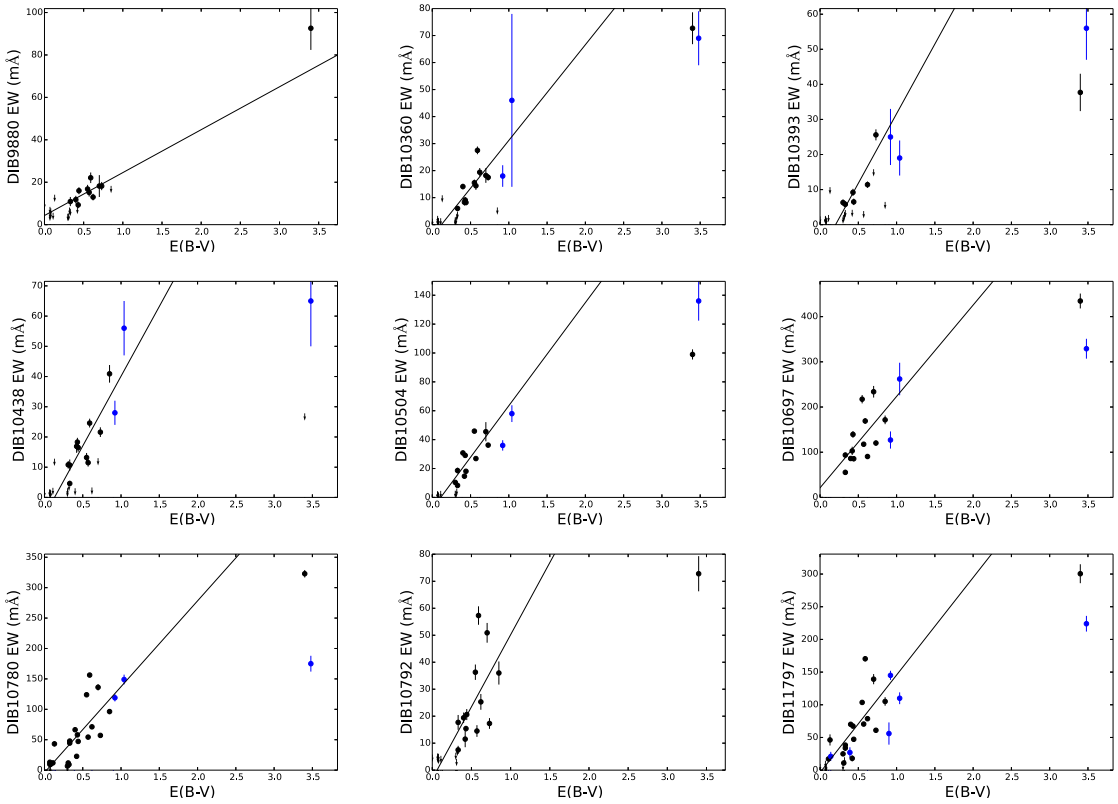

Figure 6.1: Correlations of NIR DIBs with $E(B-V)$. The black points show the EWs obtained by us, while the blue points show the EWs obtained by Cox et al. (2014). The lines in each panel show the linear functions fitted to each plot. The blue points and the points of Cyg OB2 No.12 at $E(B-V) = 3.4$ are not included in the fitting.

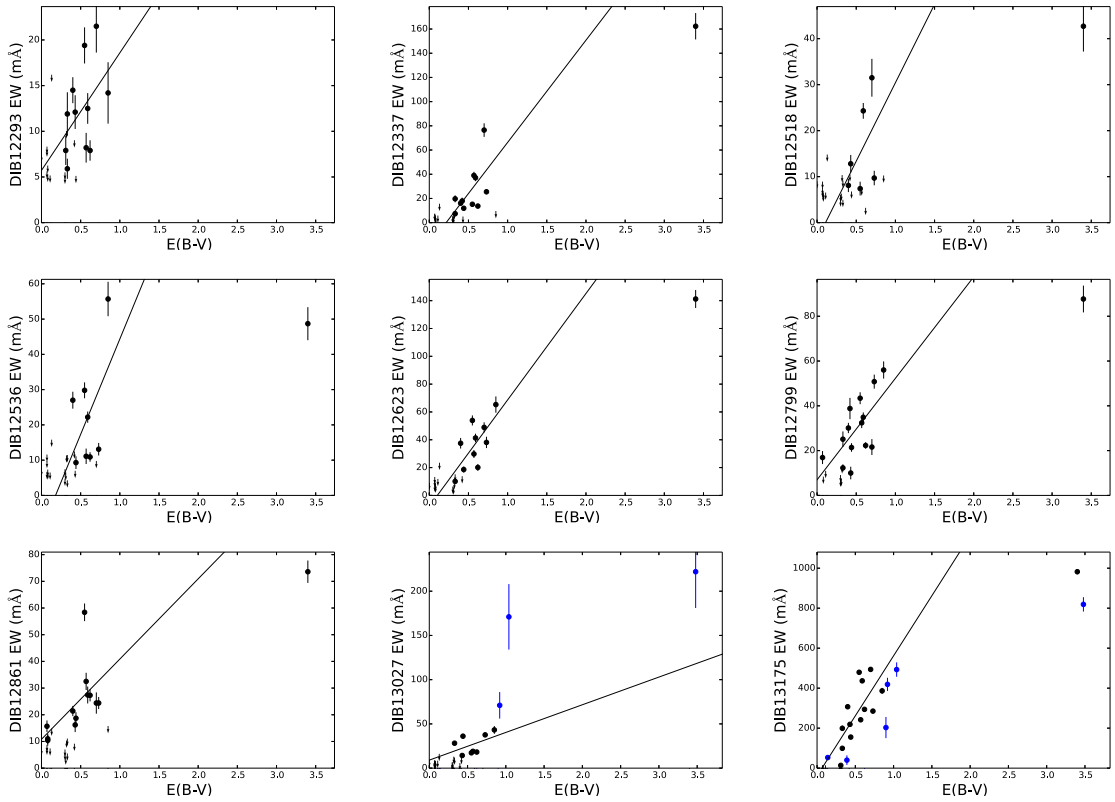

Figure 6.1: *Continued.*

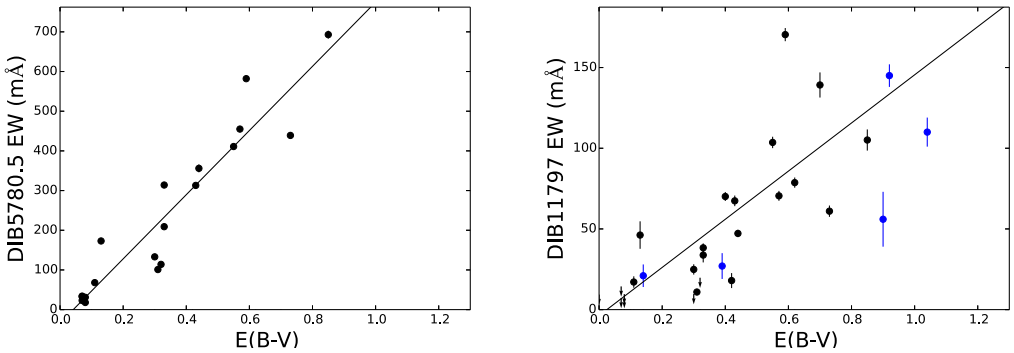

Figure 6.2: Comparison of correlations of optical DIB λ5780.5 (left panel) and NIR DIB λ11797 (right panel) with $E(B-V)$ for the range of $E(B-V) < 1.1$. For the right panel, the black points show the EWs obtained by us, while the blue points show the EWs obtained by Cox et al. (2014). For the left panel, the black points are from Friedman et al. (2011). The lines in each panel show the linear functions fitted to each plot. The blue points are not included in the fitting.

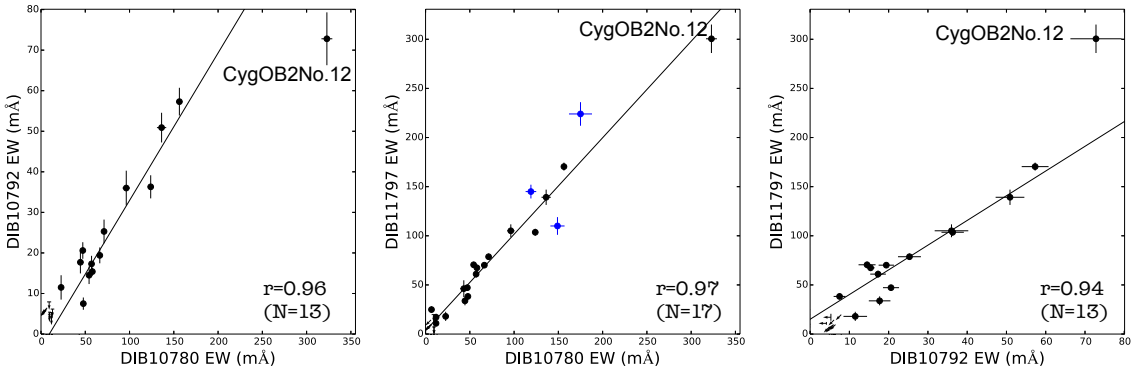

Figure 6.3: Correlations among three NIR DIBs, $\lambda\lambda 10780, 10792,$ and 11797. The black points show our data, while the blue points are from Cox et al. (2014). The lines in each panel show the linear functions fitted to each plot. The correlation coefficients (r) and the number of stars used in the calculation (N) are shown in each panel. The blue points and the points of Cyg OB2 No.12 are not included in the fitting.

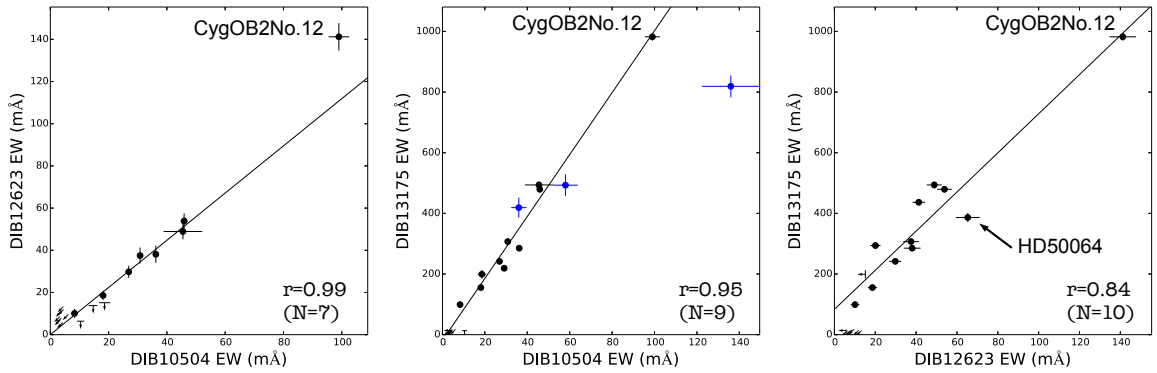

Figure 6.4: Correlations among three NIR DIBs, $\lambda\lambda 10504, 12623,$ and 13175. The notations are the same as those Figure 6.3.

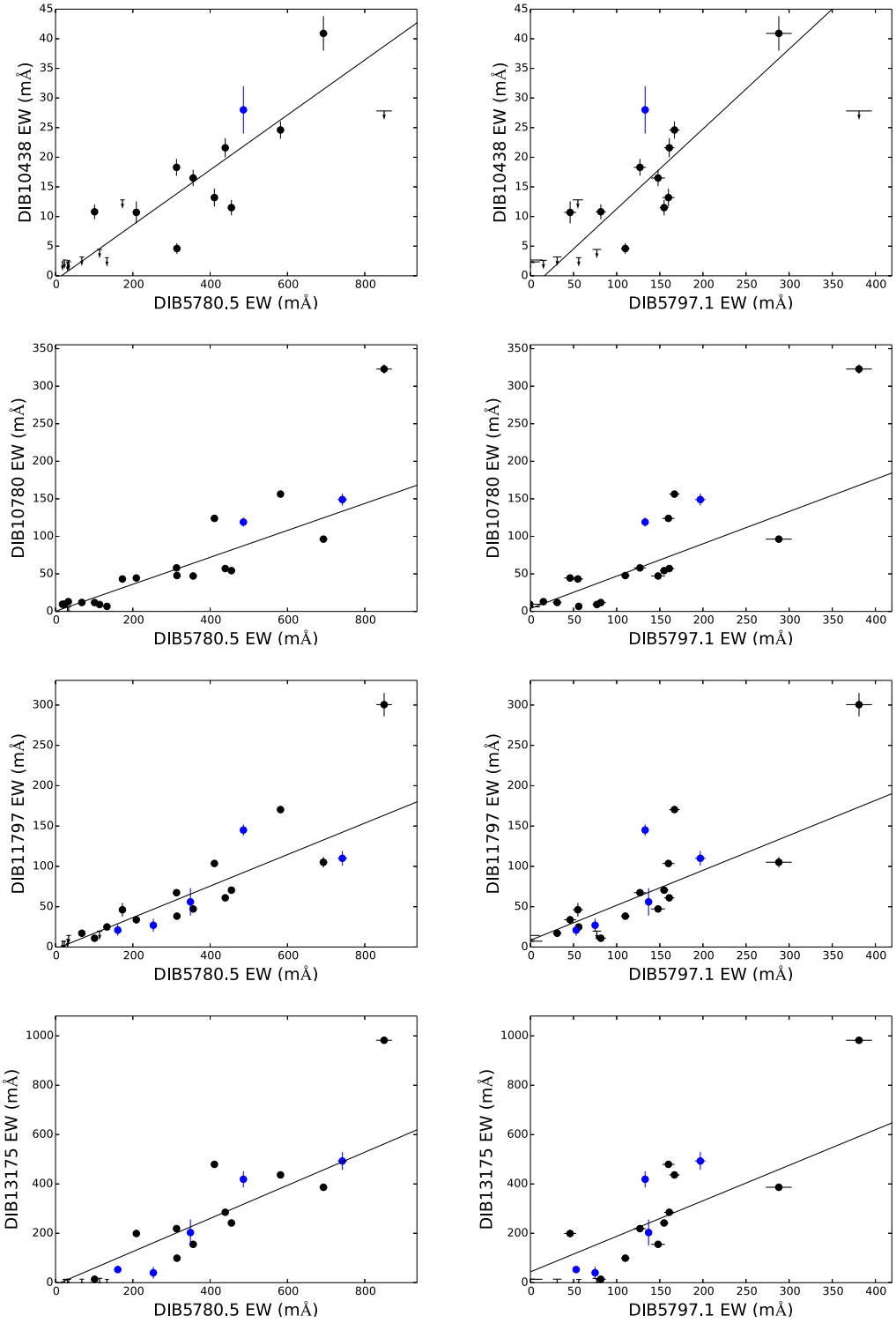

Figure 6.5: Correlations of four NIR DIBs, $\lambda\lambda 10438, 10780, 11797$, and 13175, with two optical DIBs, $\lambda\lambda 5780.5, 5797.1$. The black points show our data, while the blue points are from Cox et al. (2014). The lines in each panel show the linear functions fitted to each plot. The blue points and the points of Cyg OB2 No.12 are not included in the fitting.

Chapter 7

The Carriers of NIR DIBs

7.1 Cation molecules

In §6.3, we suggested that $\lambda\lambda 10780, 11797,$ and 13175 are better correlated with $\lambda\lambda$5705.1, 5780.5, 6204.5, and 6283.8 ($r = 0.8 - 0.9$) than with $\lambda\lambda$5797.1, 6196.0, and 6613.6 ($r = 0.6 - 0.7$). Among the optical DIBs, the environmental dependencies of two representative DIBs in the two groups, $\lambda\lambda$5780.5 and 5797.1, have been extensively investigated (Krełowski & Walker, 1987; Cami et al., 1997; Vos et al., 2011; Friedman et al., 2011). The ratio λ5797.1/λ5780.5 depends on the local UV intensities of the clouds because of the different ionization potentials of the DIB carriers (Cami et al., 1997; Vos et al., 2011). Cami et al. (1997) suggested that the ionization potential of the λ5791.1 carrier is lower than that of the λ5780.5 carrier. On the basis of modeling of the photoionization equilibrium, Sonnentrucker et al. (1997) estimated the ionization potential of the λ5797.1 carrier as $\sim$ 11 eV, whereas they suggested that the λ5780.5 carrier is a cation molecule according to its high ionization potential. The stronger correlations of the three NIR DIBs with λ5780.5 rather than with λ5797.1 may show that their carriers are also cation molecules with ionization potentials as high as the λ5780.5 carrier, probably ionized PAHs. It is also suggested that the other weaker NIR DIBs that are well correlated with the three strongest DIBs $\lambda\lambda 10780, 11797,$ and 13175, such as $\lambda\lambda 10504, 10792,$ and 12623, are also from cation molecules (see §6.2).

In our sample, HD23180 ($E(B-V) = 0.31$) and HD24398 ($E(B-V) = 0.32$) have

high λ5797.1/λ5780.5 ratios of $\sim$0.7-0.8, suggesting that the clouds toward these stars are $\zeta-$type, meaning that the UV intensity is weak relative to the cloud density (Vos et al., 2011). We compare the EWs of NIR DIBs in the $\zeta-$type clouds with those toward two stars with similar $E(B-V)$, HD2905 ($E(B-V)=0.33$) and HD24912 ($E(B-V)=0.33$), whose λ5797.1/λ5780.5 ratios are $\sim$ 0.3, which is near the threshold for the classification of $\zeta-,\sigma-$type clouds. λ5780.5 in $\zeta-$type clouds is weaker than those toward HD2905 and HD24912 by a factor of two to three although their color excesses are almost the same. This can be interpreted as the results of the λ5780.5 carrier decreasing in $\zeta-$type clouds, where the molecules are shielded from the UV flux. From our results, the NIR DIBs, $\lambda\lambda 10780, 11797,$ and 13175, in $\zeta-$type clouds are also found to be weaker than those toward HD2905 and HD24912 by a factor of three to four, which is similar to the factor of λ5780.5. This similar dependence on the UV intensity also illustrates that the carriers of $\lambda\lambda 10780, 11797,$ and 13175 and λ5780.5 may have similar ionization potentials.

7.2 Carrier candidates

We showed that a considerable number of DIBs are widely distributed in the NIR wavelength range as in the optical wavelength range. A number of ionized large-sized carbon molecules are proposed to have the transitions in the NIR wavelength range, which is consistent with our suggestion that the carriers of some NIR DIBs are cation molecules. First, ionized buckminsterfullerenes (C_{60}^+ and C_{60}^-) are also suggested to have transitions in the NIR wavelength range from the laboratory experiment (Fulara et al., 1993). In fact, DIBs $\lambda\lambda$9577 and 9633 are expected to be the transitions of C_{60}^+ (Foing & Ehrenfreund, 1994). Next, ionized PAHs (cation and anion) are theoretically suggested to have lower-energy transitions in the NIR wavelength range (Salama et al., 1996; Ruiterkamp et al., 2005). Mattioda et al. (2005) obtained the absorption spectra of some ionized PAH molecules in the NIR wavelength range. Recently, Jones (2013) proposed that heteroatom-doped (e.g., Si, O, N, and S) hydrogenated amorphous carbons (a-C: H: X) can be the DIB carriers. However, there is no strong evidence of any of those candidates of NIR DIB carriers. Further observational constraints on DIB properties as well as the identification with NIR absorption spectra of the proposed molecules

in the laboratory are necessary to reveal the carriers of NIR DIBs.

The NIR absorption spectra of 27 ionized PAHs (cations and anions) are obtained by Mattioda et al. (2005) using the matrix-isolation technique. Cox et al. (2014), who explored the DIBs in the NIR wavelength range, compared their newly detected DIB candidates and the electronic transitions of ionized PAHs. They found that some of the NIR DIBs are detected within a few tens of angstroms from the wavelengths of the strong electronic transitions of ionized PAHs reported by Mattioda et al. (2005). Among the eight NIR DIB candidates that are confirmed as DIBs in this study, they suggested that the wavelengths of $\lambda\lambda 10393, 10438, 10504, 10780,$ and 13027 are near those of strong bands of singly ionized PAHs. Among the eight NIR DIBs newly detected in this study, the DIB $\lambda 10792$ is detected close to the wavelength of the strong electronic transition of $C_{42}H_{22}^{+}$ ($\lambda = 10790$Å), but the wavelength of the other DIBs do not correspond to the strong electronic transitions of ionized PAHs. However, as Cox et al. (2014) pointed out, the pure gas-phase spectra of ionized PAHs are required for the firm identification of NIR DIBs with ionized PAHs.

Chapter 8

NIR DIBs toward the Cygnus OB2 association

In this chapter, we present a study of the NIR DIBs toward the Cyg OB2 association. Cyg OB2 association contains a number of bright early-type stars with large extinction, toward which strong DIBs can be detected (Chlewicki et al., 1986). By making use of the large EWs, we investigated more correlations of NIR DIBs including weak ones with much improved confidence. The gas clouds toward the Cyg OB2 association have complex gaseous structures and are exposed to the strong flux of ionizing photons from the early-type stars in the association, thus it is a good laboratory to investigate the environmental dependence of NIR DIBs. More detailed introduction of this study is given in §1.4.3. The summary of the observations is given in §2.2.2.

8.1 DIBs toward the Cyg OB2 association

We searched for all NIR DIBs identified in Chapter 4 in the spectra of seven stars in the Cyg OB2 association. Note that we do not evaluate the EWs of DIB λ10697 toward the Cyg OB2 association because of the overlapped stellar absorption lines (see §5.3.2 for detail). The EWs of DIBs are calculated with the same procedure as in Chapter 4. Table 8.1 summarizes the EWs and the uncertainties of NIR DIBs. Figures 8.1 − 8.5 show the DIB spectra of all

the observed stars. Owing to the large EWs and high S/N of the spectra, all NIR DIBs are clearly detected toward all the observed stars. The EWs of λ10780, 10792, and 12518 toward Cyg OB2 No.5 could not be estimated because the stellar absorption lines are overlapped on the DIBs. Note that the EWs of λ12518 toward No. 10 and λ13027 toward No. 8A could not be estimated due to the residual of the telluric absorption lines.

8.2 DIBs and C_2

Thorburn et al. (2003) show that some DIBs are well correlated with C_2 molecules, suggesting that those "C_2 DIBs" are chemically related to C_2. Ádámkovics et al. (2005) show that the C_2 DIBs are detected in the diffuse cloud core, where the typical strong DIBs (e.g., $\lambda\lambda$4430, 5797, and 5780) are quite weak. They suggested that the C_2 DIB carriers are distinct from the carriers of the typical strong DIBs, and occupy the denser regions of clouds than the strong DIBs. Because the column densities of C_2 molecules were obtained toward No. 5, 7, 8A, 9, 11, and 12 by Gredel et al. (2001), we can refer to the relations between C_2 and DIBs for the first time. The column densities of C_2 toward No. 5, 7, 8A, 9, 11, and 12 were estimated as $10^{+3.5}_{-1.5}$, < 3.3, 3.3, 5.2 ± 1, < 3.3 and 20^{+4}_{-2} $\times 10^{13}$ cm^{-2}, respectively, from the C_2 (2,0) Phillips band around $\lambda = 7720$Å (Gredel et al., 2001). Figure 8.6 shows the correlations between NIR DIBs and C_2 column densities toward the Cyg OB2 association. Although the number of the lines of sight is only five at most, no clear relations are found between all NIR DIBs and C_2 in the Cyg OB2 association. The column densities of C_2 toward the Cyg OB2 association are of wide range while all NIR DIBs are fairly strong toward all observed lines of sight.

The model of Cecchi-Pestellini & Dalgarno (2000), which reproduced the abundances of H_3^+, C_2 and CO toward No. 12 (McCall et al., 1998), suggests that the H_3^+ absorption originates from the diffuse component with $n_{\rm H} = 100$ cm^{-3}, while C_2 and CO are formed in the embedded denser component with $n_{\rm H} = 7 \times 10^3$ cm^{-3}. The lack of clear relations between NIR DIBs and C_2 suggests that the NIR DIBs may be mainly contributed from the diffuse component rather than the dense component. Such properties are common to the optical strong DIBs (Adamson et al., 1991; Ádámkovics et al., 2005). It is found that the NIR DIBs

identified here are distinct from "C_2 DIBs".

8.3 Environmental dependence of DIBs

In Chapter 6, we investigated the correlations among NIR DIBs, strong optical DIBs, and the reddening of stars. Consequently, we found some groups of DIBs that are well correlated. DIBs $\lambda\lambda 10780, 10792$ and 11797 were found to be classifiable as a DIB family, in which the DIBs are well correlated. The strongest NIR DIB $\lambda 13175$ is also well correlated with the three NIR DIBs though the number of the detected $\lambda 13175$ was not as large as the other three DIBs. DIBs $\lambda\lambda 10504, 12623$ and 13175 were also found to be well correlated though the statistics was relatively poor. The representative optical DIB $\lambda 5780.5$ is relatively better correlated with NIR DIBs $\lambda\lambda 10780, 11797$, and 13175 than $\lambda 5797.1$. Here, we investigate the correlations of those DIBs toward the Cyg OB2 association to assess their environmental dependence of DIBs. Because of the lack of clear relations between DIBs and C_2, all of the NIR DIBs are suggested to originate mainly from the diffuse component, which is exposed to the flux of high-energy photons from the early-type stars in the association. By revealing the dependence of DIBs on the environments, such as the UV-flux, the properties of the DIB carries could be constrained.

Figure 8.7 shows the correlations among four DIBs $\lambda\lambda 10780, 10792, 11797$, and 13175. It is found that the tight correlations of those DIBs seen in the diffuse interstellar environment also continue even in the harsh environment of the Cyg OB2 association. Note that only $\lambda 10792$ toward No. 8A is weaker than expected from the correlations.

Figure 8.8 shows the correlations among $\lambda\lambda 10504, 12623$, and 13175. Two DIBs, $\lambda\lambda 12623$ and 13175, are well correlated also in the Cyg OB2 association, but the correlation coefficient is not as high as those among the four DIBs $\lambda\lambda 10780$, 10792, 11797 and 13175. Note that $\lambda 12623$ is also well correlated with $\lambda\lambda 10780$, 10792, and 11797, which are tightly correlated with $\lambda 13175$ (see Figure 8.9). The correlation is consistent with the extrapolation of the correlation from the survey data (see the fitted line in the right panel of Figure 8.8). However, the correlations between $\lambda 10504$ and $\lambda\lambda 12623$ and 13175 in the Cyg OB2 association are quite different from the correlations from the survey data, suggesting that the ratios of $\lambda 10504$ to

the other two DIBs, $\lambda\lambda$12623 and 13175, in the Cyg OB2 association become smaller than those in the diffuse interstellar environment. Figure 8.10 shows the EW ratios among the three DIBs as functions of the color excesses. The ratios of λ10504 to $\lambda\lambda$12623 and 13175 in the Cyg OB2 association are lower than the ratios in the diffuse interstellar environment by a factor of about two. We suggest that the difference of the ratios between the Cyg OB2 association and the survey data is caused by the environmental dependence of the DIBs.

Figure 8.11 shows the ratios between the optical DIB λ5780.5 and $\lambda\lambda$10504 and 13175. The EWs of λ5780.5 for No.5, 9, 10, and 12 are adopted from Chlewicki et al. (1986), while there are no observations of DIBs in the optical wavelength range toward No. 3, 8A, and 11. The ratios of λ5780.5 to $\lambda\lambda$12623 and 13175 are also found to be lower in the Cyg OB2 association than those in the diffuse interstellar environment, while the ratios of λ10504 to λ5780.5 in the Cyg OB2 association are consistent with those in the interstellar environment. Although the correlation between λ10504 and λ5780.5 was not discussed in Chapter 6 because of the small number of the data points (i.e., 8), these DIBs are expected to be well correlated because the two pairs of $\lambda10504 - \lambda13175$ and $\lambda5780.5 - \lambda13175$ are well correlated, which is confirmed in the top panel of Figure 8.11.

In summary, it is found that 1) $\lambda\lambda$10780, 10792, 11797, and 13175 are tightly correlated in the Cyg OB2 association as well as in the interstellar environment (Figure 8.7), 2) λ12623 and λ13175 are also well correlated in the Cyg OB2 association as well as in the interstellar environment (Figure 8.10), and 3) the ratios of $\lambda\lambda$10504 and 5780.5 to λ13175 are lower than those in interstellar environment by a factor of about two (Figures 8.10 and 8.11). Consequently, the DIBs can be classified into two groups from the perspective of the environmental dependence in the Cyg OB2 association: Group 1) $\lambda\lambda$10780, 10792, 11797, 12623, and 13175 and Group 2) $\lambda\lambda$5780.5 and 10504. The ratios of the DIBs in Group 1 to the DIBs in Group 2 becomes larger in the Cyg OB2 association than in the interstellar environment by a factor of about two.

The environmental dependence of the DIBs may be attributed to the strong flux of the ionizing photons from the early-type stars in the Cyg OB2 association. Gredel et al. (2001) suggest that the abundances of light molecules (C_2, CN, CO, CH, and H_3^+) toward No. 12

can be explained by a chemistry induced by X-ray from the early-type stars. The high-energy ionizing photons would cause the destruction and/or ionization of the carrier molecules. If the carriers of the DIBs in Group 1 are more stable than those in Group 2 against to the flux of the ionizing photons, the carriers of DIBs in Group 2 would be destroyed and the abundances would become lower than in the interstellar environment as observed. The ionizing photon flux can affect the ionization state of the carrier molecules. If the carriers of some NIR DIBs are truly cation molecules as suggested in Chapter 7, the strong flux of ionizing photons in the Cyg OB2 association would increase the ionizing fraction of the DIB carriers. The difference of ionization potentials between the DIB carriers in Group 1 and 2 could result in the environmental dependence of the DIB ratios.

8.4 Correlations among weak DIBs

We also investigated the correlations among weak DIBs, which could not be discussed in Chapter 6 owing to their low detection rates and large uncertainties for weak absorption lines. The large EWs of weak DIBs toward the Cyg OB2 association allow us to examine the correlations confidently. Figure 8.12 shows the correlations among two weak DIBs $\lambda\lambda$12861 and 13027 and a strong DIB λ10780. It is found that these weak DIBs are well correlated with λ10780 as well as with $\lambda\lambda$10792, 11797, and 13175. Although the statistics is still poor to assess the significance of the correlations of these weak DIBs, their carriers could be chemically related to the carriers of the strong NIR DIBs. As for the other weak DIBs, we could not find good correlations in the Cyg OB2 association.

8.5 The C_2 Phillips bands

Besides the NIR DIBs, we detected the C_2 (0,0) and (1,0) Phillips bands around $\lambda = 12070$ and 10130 Å, respectively, toward some of the observed stars in the Cyg OB2 association. This is the first detection of the C_2 (0,0) bands, which is the most fundamental band of C_2 molecules, in interstellar medium, while the (1,0) bands were previously detected by Gredel & Muench (1994) only for No. 5 and No. 12. Here, we report the detection of these bands.

We do not discuss the density and rotational temperature of the intervening clouds, which can be analyzed with these (0,0) and (1,0) bands, because it is out of the scope of this thesis. The interstellar C_2 molecules have been observed mainly with the (2,0) and (3,0) bands around $\lambda = 8765$ and 7720 Å, respectively. The C_2 Phillips bands can be used as the thermometer and densitometer of interstellar clouds because the population distribution of each rotational level is the function of rotational excitation temperature and the density of the clouds (Snow & McCall, 2006). Because the (0,0) and (1,0) bands are intrinsically stronger than the (2,0) and (3,0) bands, the former bands are expected to be superior to the latter bands as the thermometer and densitometer of interstellar clouds. In addition, the (0,0) and (1,0) bands in the NIR wavelength range will be powerful tracers of C_2 molecules toward the stars obscured by the interstellar dust because of the higher transmittance of the starlight in the NIR wavelength range in interstellar clouds compared to the optical wavelength range.

8.5.1 First detection of the (0,0) bands

Figure 8.13 shows the C_2 (0,0) band spectra of the seven stars in the Cyg OB2 association around $\lambda = 12070$ Å. The most reddened star, No. 12, has the strongest absorption bands among the observed stars (Figure 8.14). The EWs of the C_2 bands toward No. 12 were measured by fitting Gaussian functions (Table 8.2). Because the (0,0) bands are the strongest compared to the other (1,0), (2,0), and (3,0) bands, the transitions with higher rotational levels, such as $Q(20)$, $R(20)$, and $Q(22)$, are clearly detected. Some of the $R-$branch lines are blended with the other transitions of the (0,0) bands because our spectral resolution ($R = 20,000$) is not enough to resolve them. The (0,0) bands toward No. 3, 5, 8A, and 9 are also clearly detected. As for No. 10 and 11, which are located in the outskirts of the Cyg OB2 association, even the strongest transitions, $Q(2)$ and $Q(4)$, could not be detected.

8.5.2 The (1,0) bands

Figure 8.15 shows the C_2 (1,0) band spectra of the seven stars in Cyg OB2 association around $\lambda = 10135$ Å. The (1,0) bands were clearly detected toward No. 3, 5, 9, and 12 while the bands could not be detected toward No. 10 and 11. The $Q(4)$ line was marginally detected

toward No. 8A. As seen in the (0,0) band spectra, No. 12 has the strongest (1,0) bands in the observed seven stars (see Figure 8.16). Gredel & Muench (1994) detected three transitions of the (1,0) bands ($R(0)$, $Q(2)$, and $Q(4)$) toward Cyg OB2 No. 5 and 12 with higher spectral resolution, $R = 65,000$, than ours ($R =\sim 20,000$). They detected four velocity components of the C_2 bands toward both stars, which could not be resolved in our spectra with the lower spectral resolution. The EWs measured for our WINERED spectra of No. 12 (Table 8.2) are consistent with the total EWs reported by Gredel & Muench (1994) within the uncertainties (36±15, 65±12, and 53±10 mÅ for $R(0)$, $Q(2)$, and $Q(4)$ lines, respectively).

Table 8.1: EWs of DIBs

Stars	$E(B-V)$	λ9980	λ10360	λ10393	λ10438	λ10504	λ10780
CygOB2No3	2.01	85.3 ± 4.3	77.0 ± 3.5	74.7 ± 4.6	83.6 ± 5.5	85.2 ± 1.7	403.2 ± 6.2
CygOB2No5	1.99	59.5 ± 3.7	77.2 ± 2.7	46.3 ± 2.5	78.0 ± 3.2	75.0 ± 3.2	–
CygOB2No8A	1.55	52.9 ± 3.0	94.8 ± 4.4	47.5 ± 3.4	125.8 ± 5.5	75.1 ± 1.9	279.0 ± 6.7
CygOB2No9	2.25	53.8 ± 3.2	76.5 ± 3.8	48.6 ± 3.3	75.9 ± 4.1	84.2 ± 1.8	347.8 ± 4.2
CygOB2No10	1.83	71.6 ± 4.9	97.9 ± 3.8	47.8 ± 3.0	201.4 ± 5.8	80.0 ± 2.7	486.3 ± 5.5
CygOB2No11	1.75	77.0 ± 5.8	104.2 ± 4.2	48.6 ± 3.0	81.8 ± 4.6	76.9 ± 4.4	387.9 ± 6.1
CygOB2No12	3.4	59.3 ± 3.0	96.2 ± 3.3	51.8 ± 3.2	93.2 ± 4.3	78.0 ± 1.7	322.0 ± 3.5

Stars	$E(B-V)$	λ10792	λ11797	λ12293	λ12337	λ12518	λ12536
CygOB2No3	2.01	115.2 ± 4.2	347.8 ± 6.8	65.1 ± 4.0	239.1 ± 8.3	33.4 ± 3.8	78.1 ± 4.2
CygOB2No5	1.99	–	213.6 ± 5.9	51.1 ± 3.1	203.9 ± 4.4	–	57.9 ± 4.5
CygOB2No8A	1.55	115.2 ± 5.4	220.6 ± 5.3	49.2 ± 3.5	129.1 ± 8.1	33.9 ± 3.4	73.5 ± 4.3
CygOB2No9	2.25	85.9 ± 2.8	290.2 ± 4.8	54.1 ± 2.8	255.9 ± 5.2	29.2 ± 2.6	89.7 ± 3.9
CygOB2No10	1.83	140.7 ± 5.7	401.3 ± 7.4	93.5 ± 4.2	208.2 ± 6.5	–	92.7 ± 5.1
CygOB2No11	1.75	95.6 ± 6.8	279.3 ± 7.3	60.8 ± 4.8	276.2 ± 13.6	29.2 ± 4.2	74.4 ± 5.5
CygOB2No12	3.4	82.5 ± 4.4	277.5 ± 4.1	75.2 ± 4.1	291.8 ± 3.9	49.3 ± 3.4	62.3 ± 2.7

Stars	$E(B-V)$	λ12623	λ12799	λ12861	λ13027	λ13175
CygOB2No3	2.01	245.5 ± 7.1	158.0 ± 4.4	97.1 ± 6.2	179.2 ± 5.5	1374.8 ± 11.9
CygOB2No5	1.99	135.0 ± 7.5	118.6 ± 4.8	56.6 ± 3.4	84.9 ± 5.6	949.8 ± 10.3
CygOB2No8A	1.55	110.7 ± 5.0	62.3 ± 5.3	73.4 ± 6.5	–	905.9 ± 9.1
CygOB2No9	2.25	185.7 ± 5.4	89.0 ± 3.2	97.0 ± 4.0	131.3 ± 4.0	1197.3 ± 9.9
CygOB2No10	1.83	183.4 ± 7.3	78.5 ± 3.2	130.5 ± 7.0	263.9 ± 6.7	1475.7 ± 11.2
CygOB2No11	1.75	140.9 ± 7.9	122.1 ± 6.5	109.6 ± 5.9	115.9 ± 5.9	1270.0 ± 13.1
CygOB2No12	3.4	140.4 ± 6.3	120.7 ± 3.1	98.2 ± 2.5	108.4 ± 4.8	1148.4 ± 7.6

The EWs are given in units of mÅ. The bars mean that the EW or upper limit of the DIB could not be evaluated due to the overlapped stellar absorption lines and/or the residual features of the telluric correction.

Table 8.2: EWs of the C_2 Phillips bands toward No. 12.

Transition	$(0,0)^2$ (mÅ)	$(1,0)^3$ (mÅ)	$(2,0)^4$ (mÅ)	$(3,0)^5$ (mÅ)
P(2)	5.0	9.2	5.0	6.5
P(4)	31.0	23.9	7.7	-
P(6)	22.4	22.9	8.7	-
P(8)	15.3	10.9	4.8	-
P(10)	-	12.4	< 3	-
P(12)	-	9.1	1.5	-
P(14)	6.6	-	1.5	-
P(16)	-	bl.	-	-
Q(2)	93.8	59.7	26.9	10.0
Q(4)	92.1	53.7	27.0	5.3
Q(6)	52.4	43.3	16.6	8.8
Q(8)	59.3	32.7	14.3	-
Q(10)	27.4	14.7	14.0	-
Q(12)	23.7	12.7	6.3	-
Q(14)	20.4	11.0	5.2	-
Q(16)	-	16.6	4.3	-
Q(18)	-	7.3	3.0	-
Q(20)	14.8	-	-	-
Q(22)	7.5	bl.	-	-
Q(24)	-	30.1	-	-
R(0)	71.4	47.2	14.0	7.1
R(2)	78.1	bl.	21.1	5.0
R(4)	36.3	bl.	18.9	-
R(6)	bl.	bl.	14.7	-
R(8)	bl.	bl.	-	-
R(10)	4.4	bl.	5.6	-
R(12)	bl.	bl.	2.5	-
R(14)	bl.	8.6	< 1.5	-
R(16)	bl.	-	< 1.5	-
R(18)	bl.	12.6	< 1.5	-
R(20)	5.6	-	-	-
R(22)	-	5	-	-
R(24)	-	4.4	-	-

[1] The transitions that cannot be detected within uncertainties are shown with bars ("-"). The transitions that appear to be detected but blended with the other transitions are shown with "bl.".

[2] The EWs of the (0,0) bands measured for the WINERED spectra of No.12.

[3] The EWs of the (1,0) bands measured for the WINERED spectra of No.12.

[4] The EWs of the (2,0) bands adopted from Gredel et al. (2001).

[5] The EWs of the (3,0) bands adopted from Gredel et al. (2001).

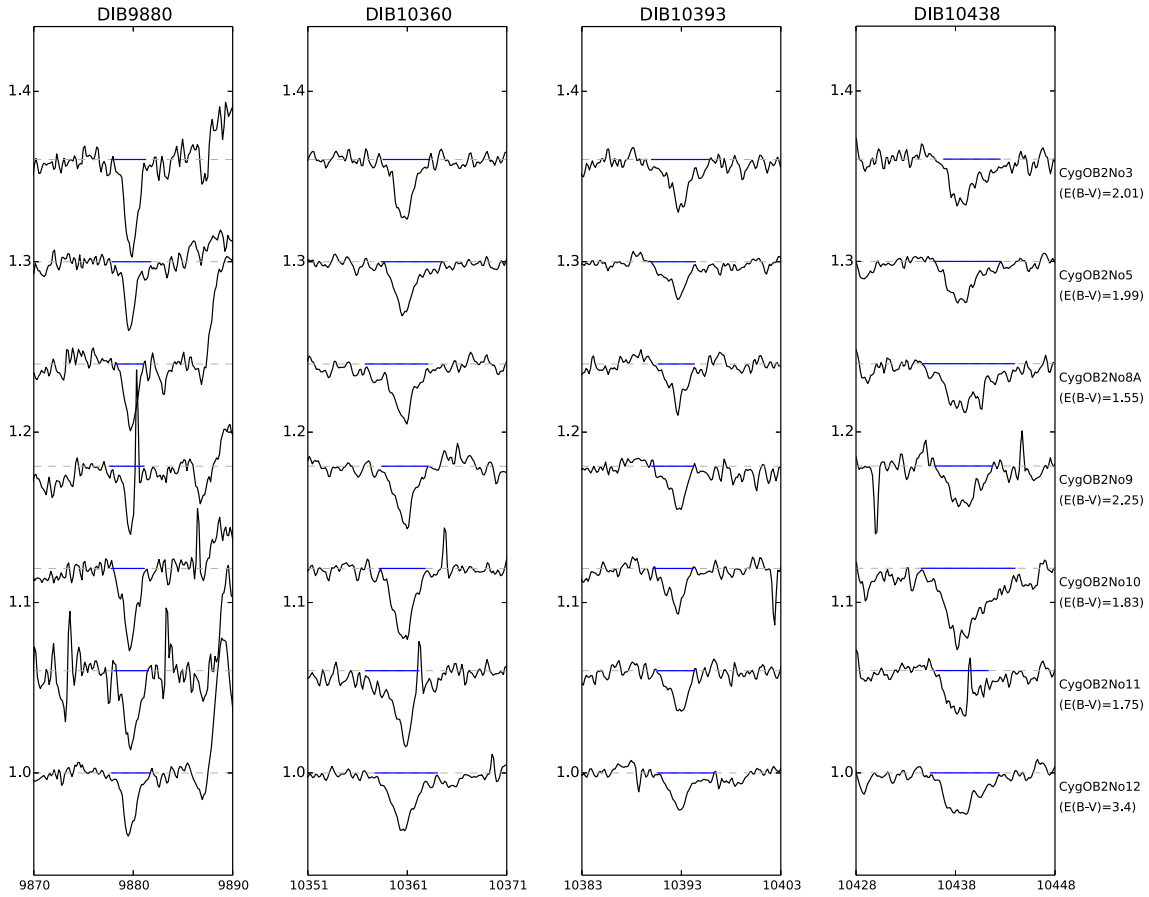

Figure 8.1: Spectra of four DIBs, $\lambda\lambda 9880, 10360, 10393,$ and 10438, for all targets plotted in increasing order of $E(B-V)$ from top to bottom. The spectra are normalized and plotted with arbitrary offsets. The continuum level of each stars is shown by a dashed thin line. The spectra of the stars, in which the EWs or upper limits of the DIBs cannot be evaluated due to overlapped stellar and/or telluric absorption lines, are plotted with gray lines. The integrated ranges used in the calculation of the EWs are shown as thick blue lines.

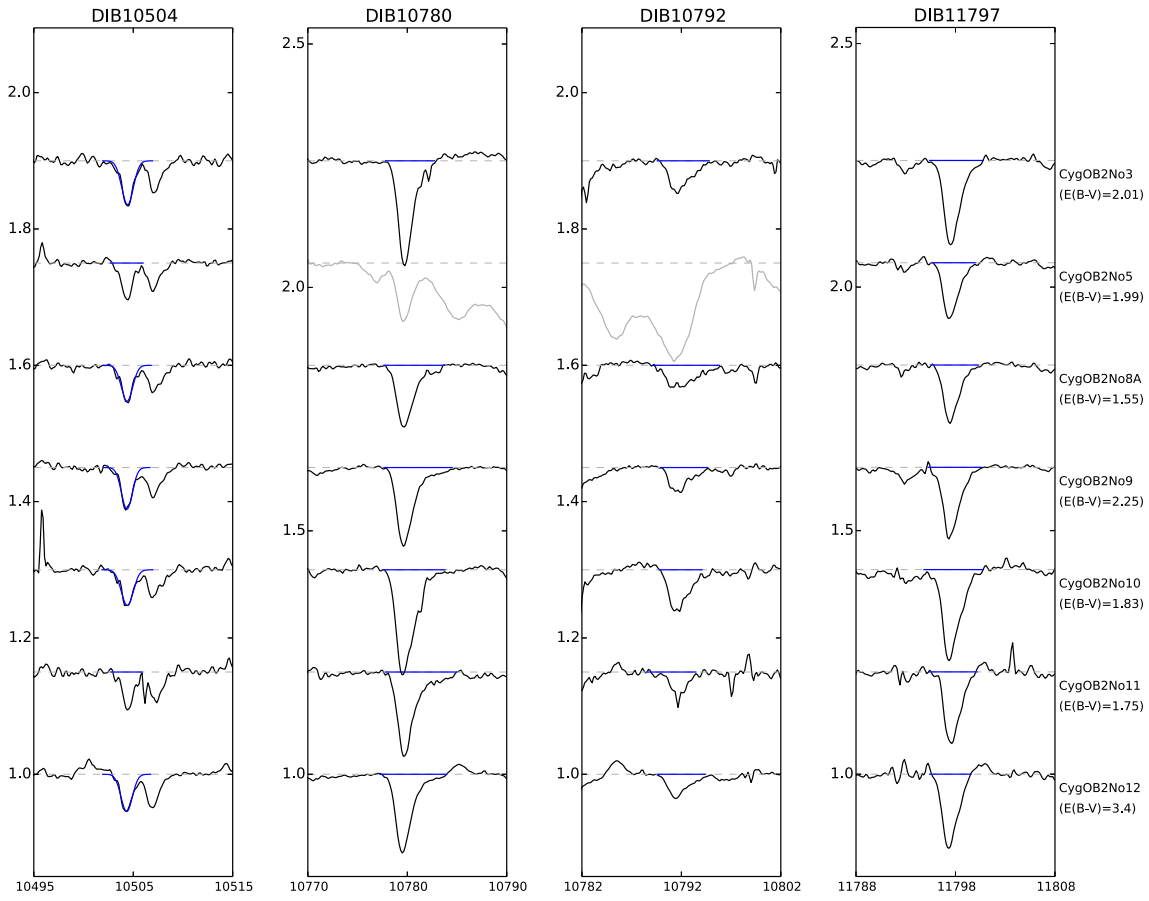

Figure 8.2: Spectra of four DIBs $\lambda\lambda$10504, 10780, 10792, and 11797 for all targets. The notations are the same as those in Figure 8.1 except for DIB λ10504, for which the EWs are estimated by fitting Gaussian profiles (shown as blue lines) to avoid the blending of the stellar absorption lines (see §5.3.1 for detail).

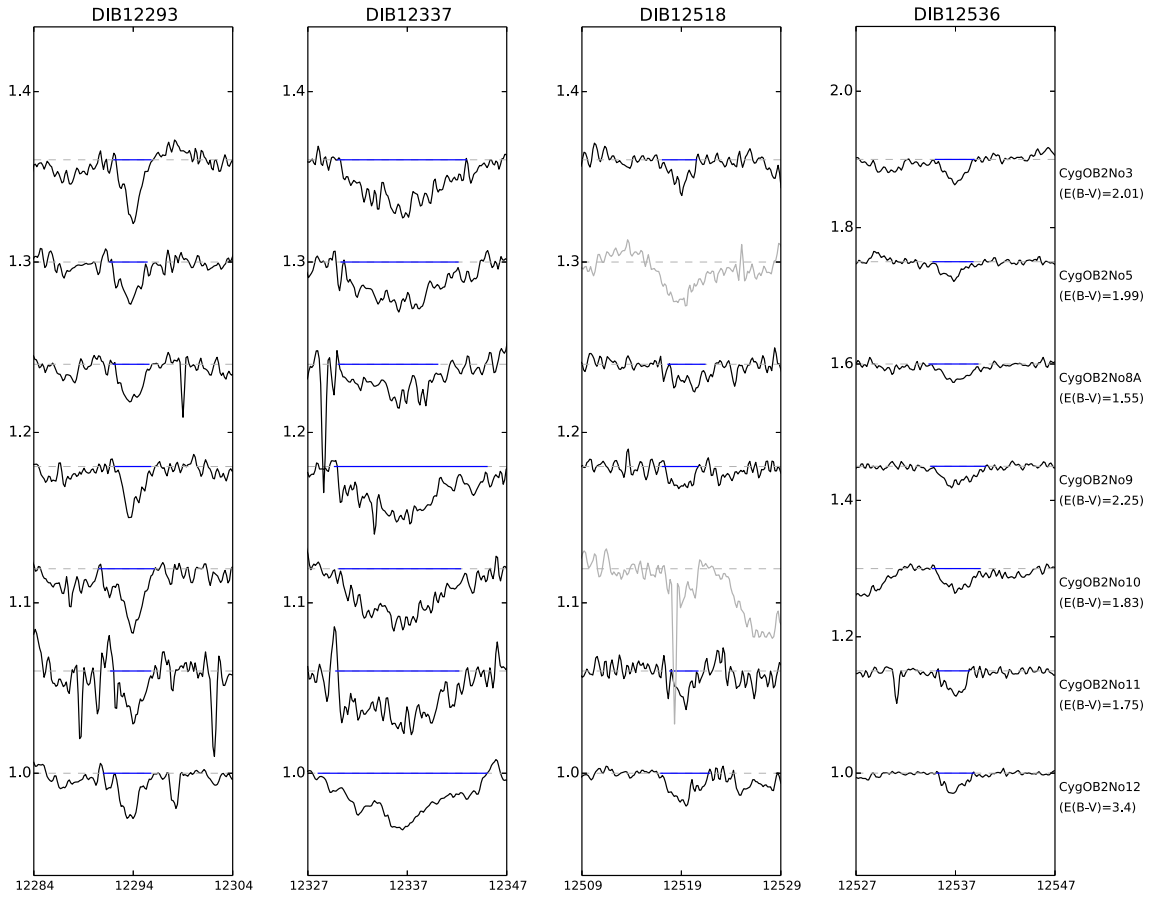

Figure 8.3: Spectra of DIBs $\lambda\lambda$12293, 12337, 12518, and 12536 for all targets. The notations are the same as those in Figure 8.1.

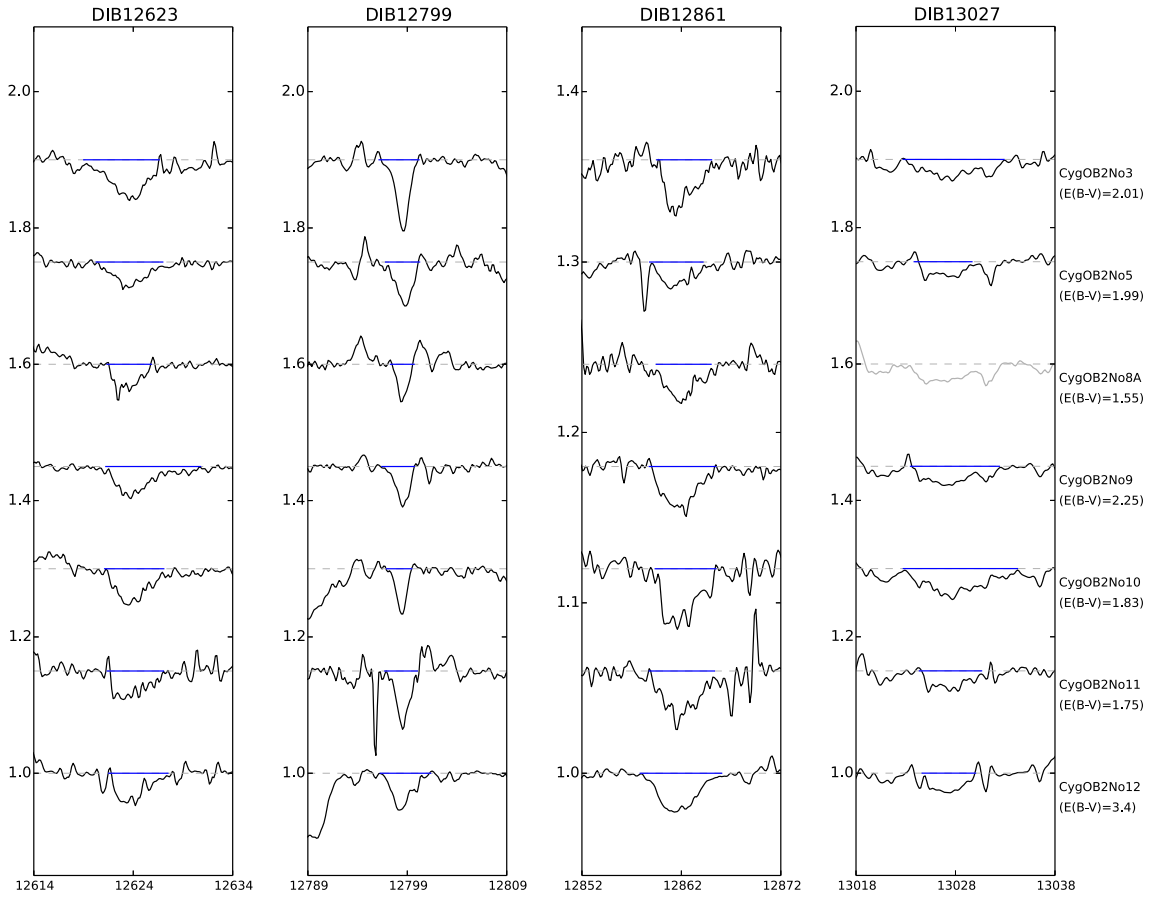

Figure 8.4: Spectra of DIBs $\lambda\lambda$12623, 12799, 12861, and 13027 for all targets. The notations are the same as those in Figure 8.1.

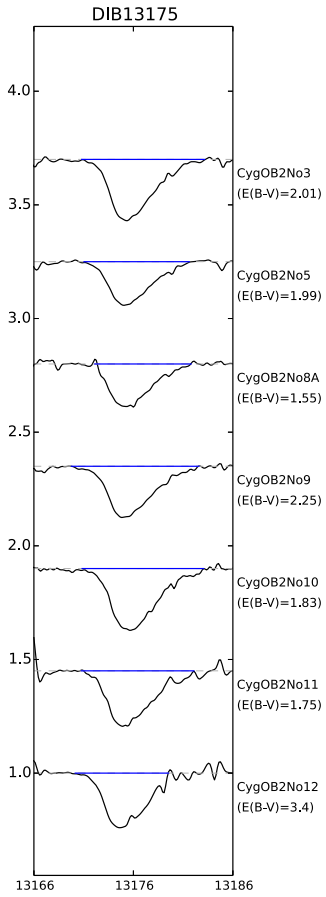

Figure 8.5: Spectra of a DIB λ13175 for all targets. The notations are the same as those in Figure 8.1.

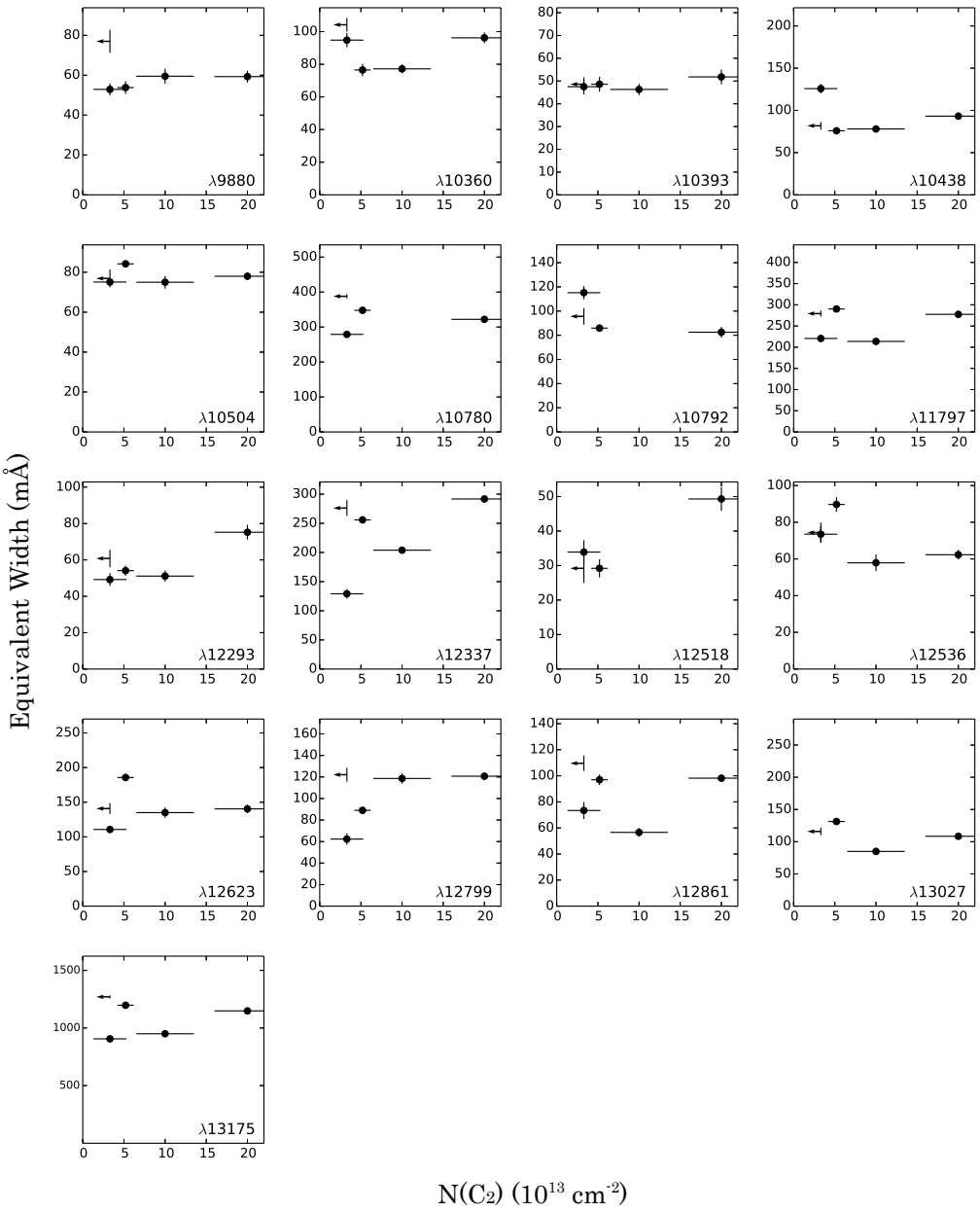

Figure 8.6: The EWs of 19 NIR DIBs as a function of the column densities of C_2 molecules. The C_2 column densities are adopted from Gredel et al. (2001), who obtained the spectra of the absorption lines of the C_2 $(2,0)$ Phillips bands toward the Cyg OB2 No. 5, 8A, 9, 11, and 12.

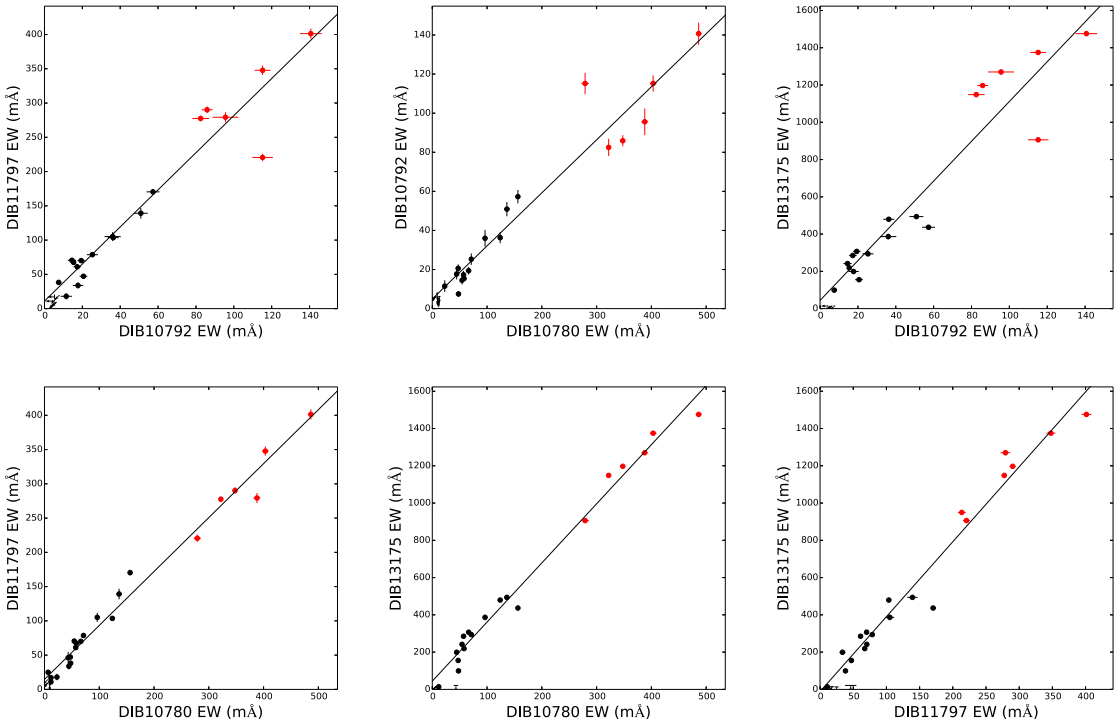

Figure 8.7: Correlations among four NIR DIBs, $\lambda\lambda$10780, 10792, 11797 and 13175. The black points show the survey data from the previous chapters, while the red points show the data points of the stars in the Cyg OB2 association. The lines in each panel show the linear functions fitted to all data points in each plot.

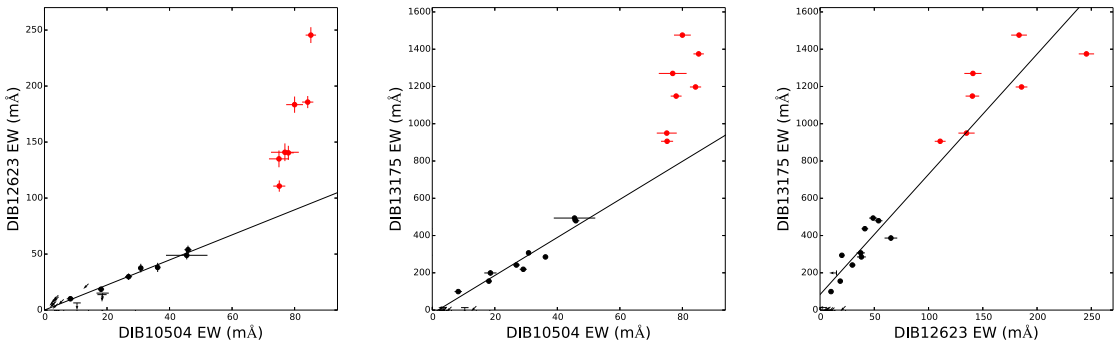

Figure 8.8: Correlations among three NIR DIBs, $\lambda\lambda$10504, 12623, and 13175. The lines in each panel show the linear functions fitted to the black points in each plot. The notations are the same as those in Figure 8.7.

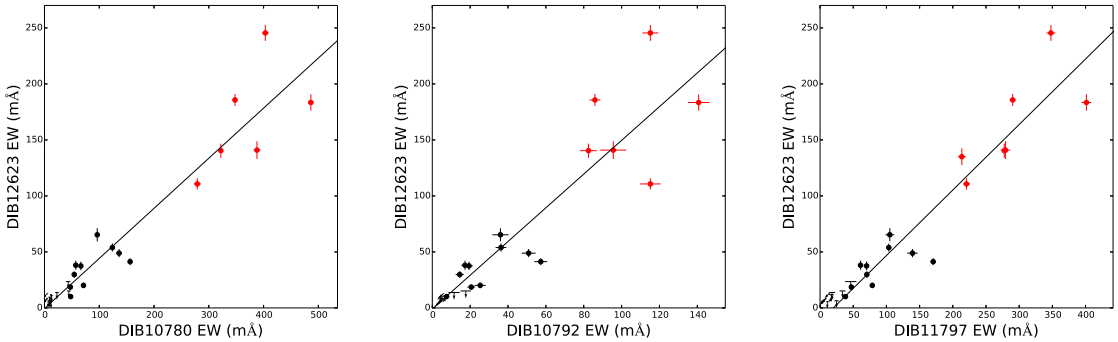

Figure 8.9: Correlations among of λ12623 with three NIR DIBs, $\lambda\lambda$10780, 10792, and 11797. The notations are the same as those in Figure 8.7.

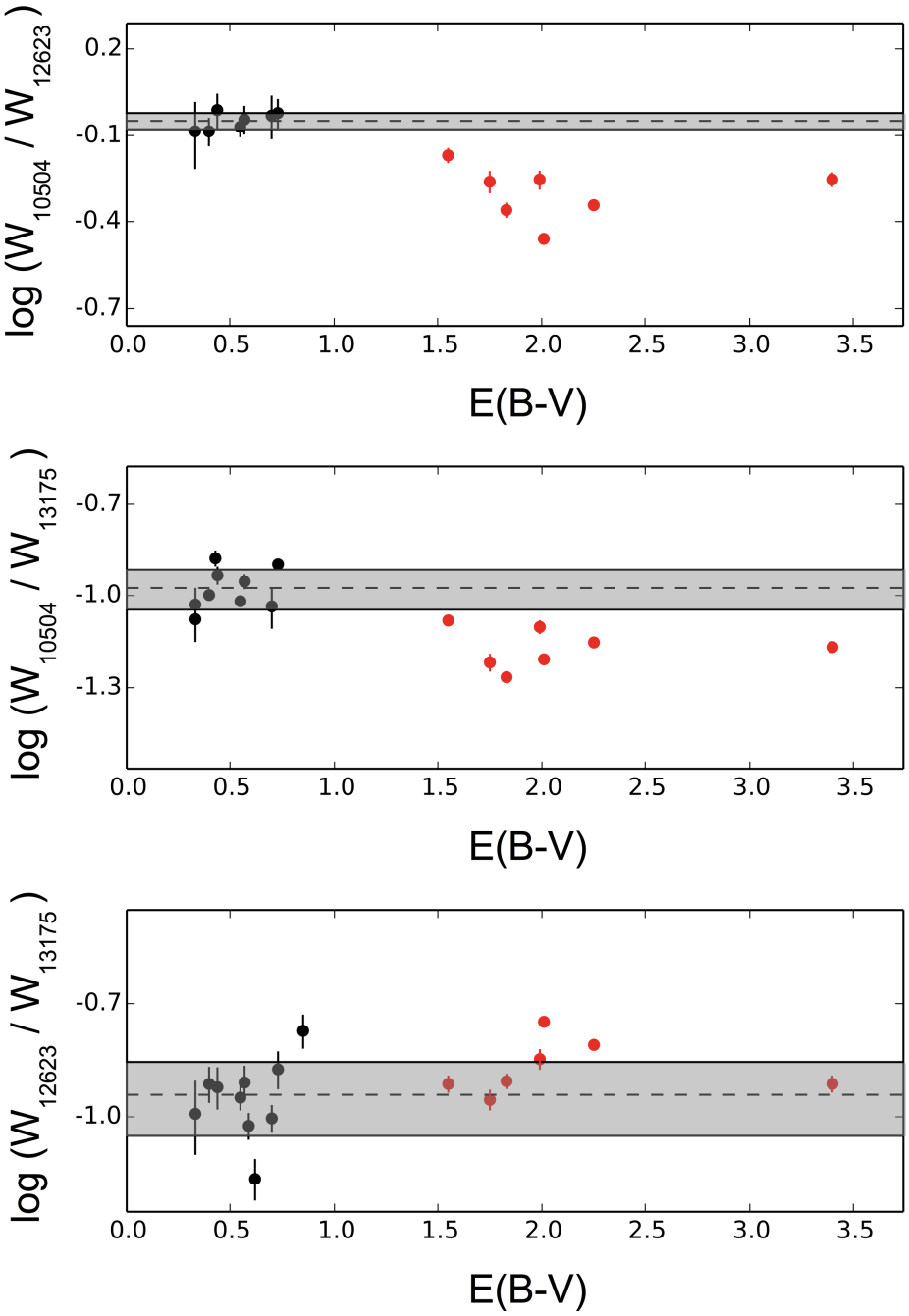

Figure 8.10: The EW ratios among three NIR DIBs $\lambda\lambda$10504, 12623 and 13175 as a function of $E(B-V)$. The dashed lines show the average of the ratios calculated from the survey data. The shaded areas show the standard deviations of the ratios.

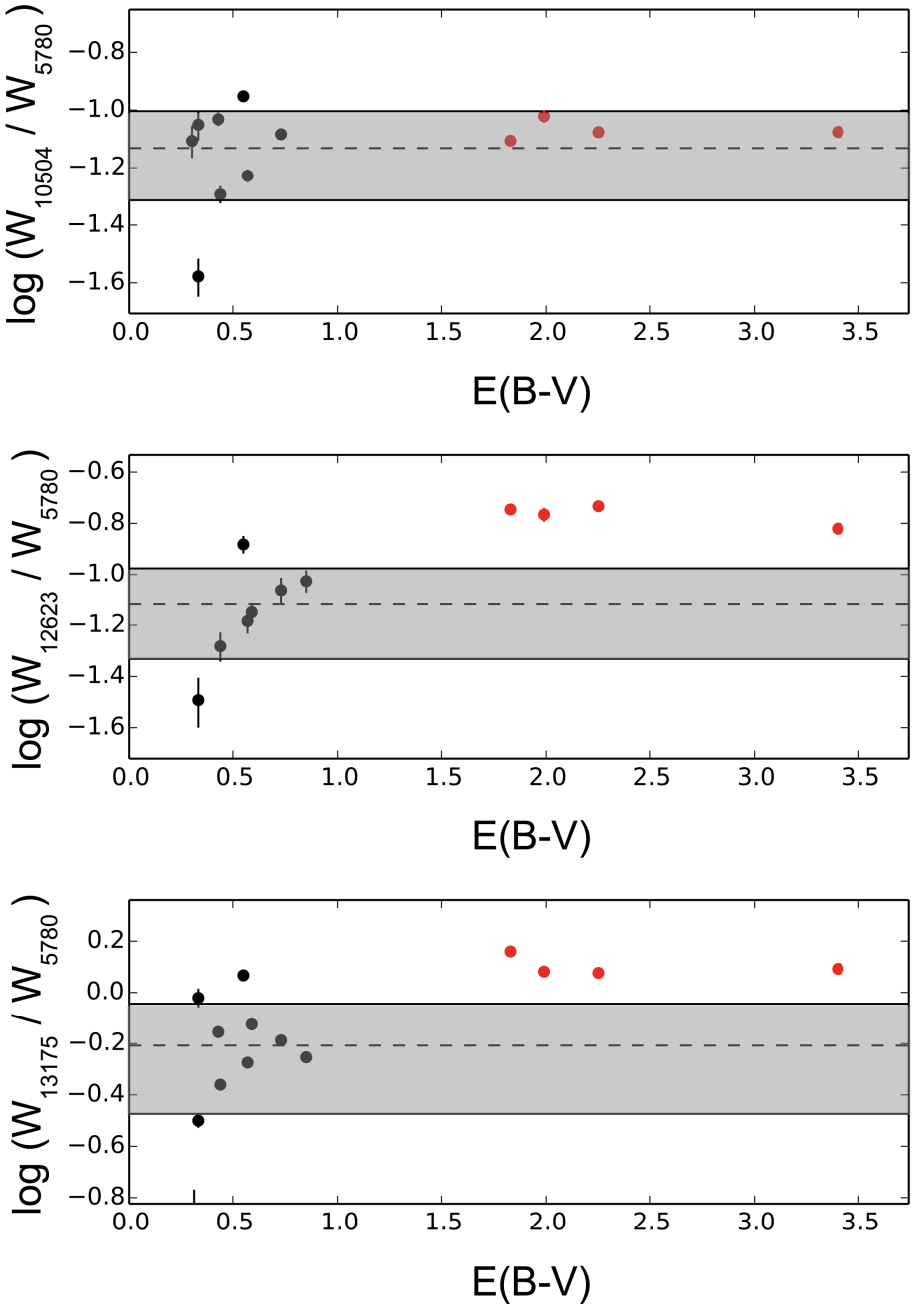

Figure 8.11: The EW ratios of NIR DIBs $\lambda\lambda$10504 and 13175 to λ5780.5 as a function of $E(B-V)$. The notations are the same as those in Figure 8.10.

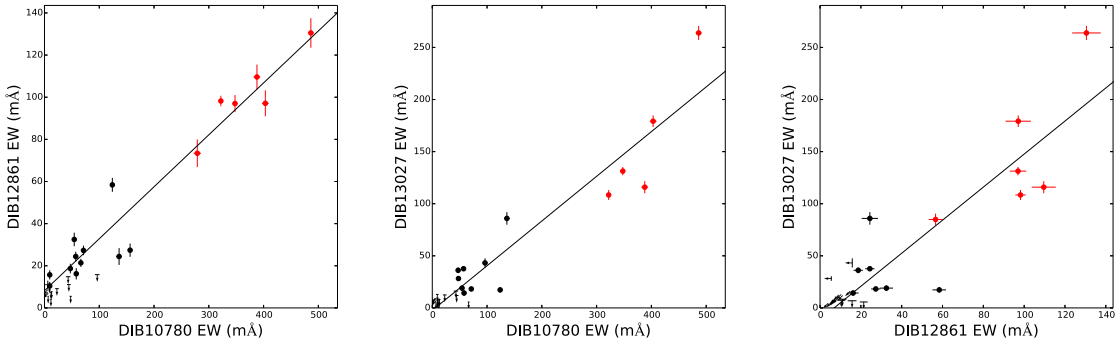

Figure 8.12: Correlations among four NIR DIBs, $\lambda\lambda$10780, 12861, and 13027. The notations are the same as those in Figure 8.7.

Figure 8.13: The WINERED spectra of C_2 (0,0) Phillips bands toward all the stars observed in the Cyg OB2 association (upper panel) and the spectrum of an A0V telluric standard star (lower panel). The positions of the C_2 (0,0) Phillips bands are shown by the blue vertical lines.

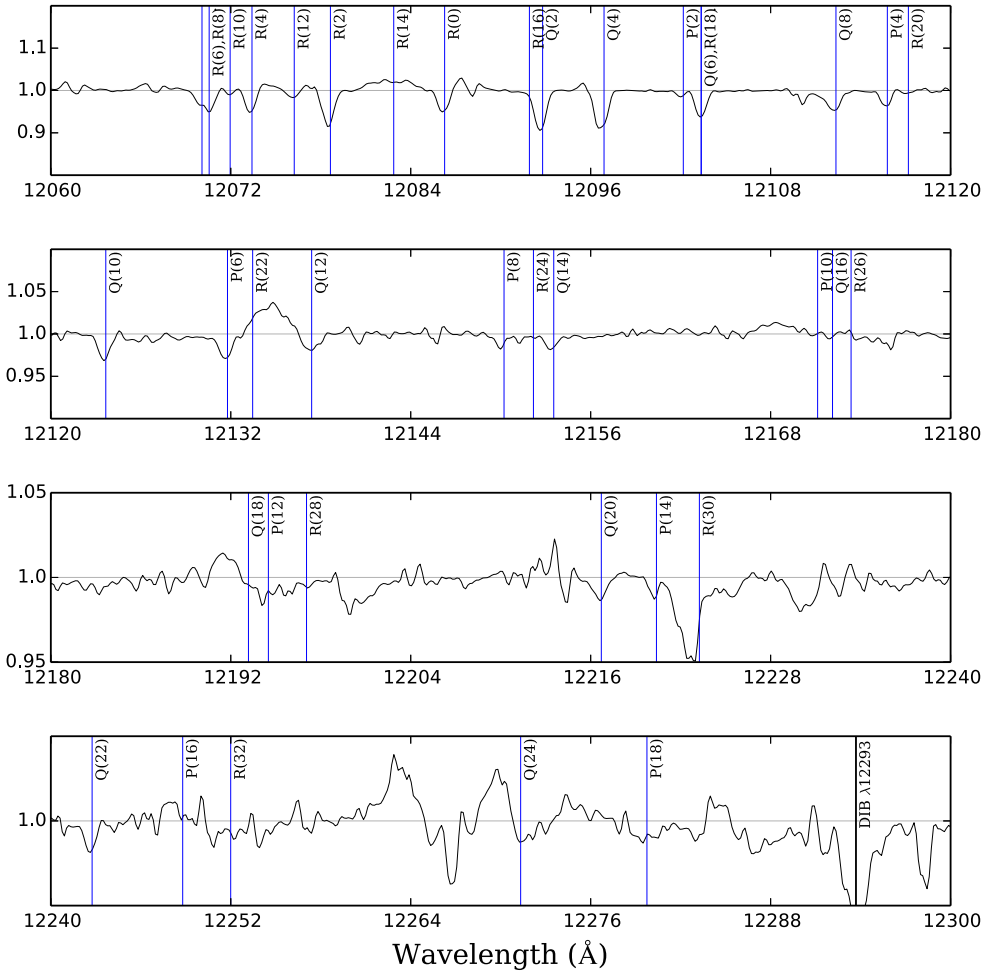

Figure 8.14: The WINERED spectra of the C_2 (0,0) Phillips bands of Cyg OB2 No.12.

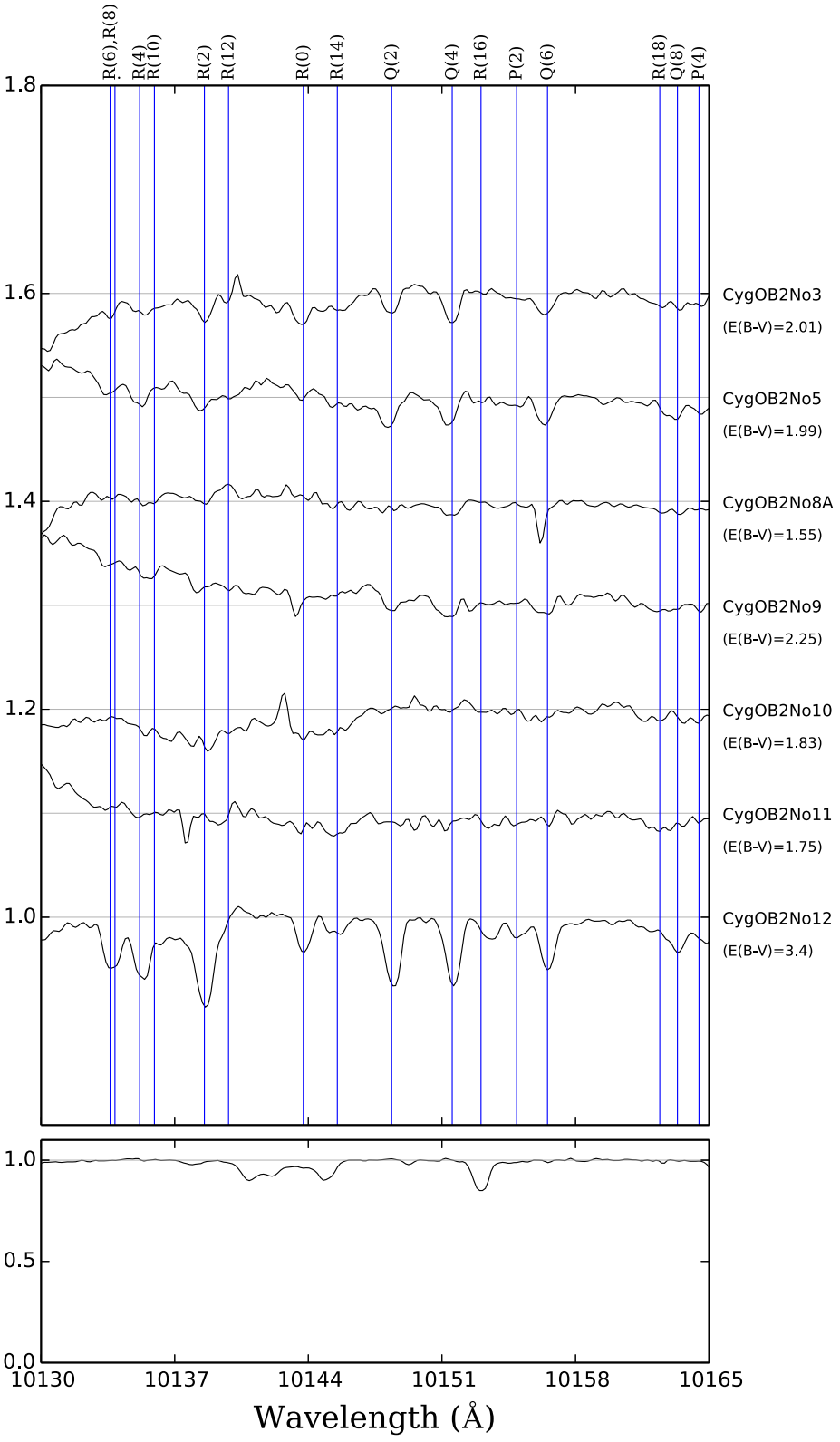

Figure 8.15: The WINERED spectra of C_2 (1,0) Phillips bands toward all the stars observed in the Cyg OB2 association (upper panel) and the spectrum of an A0V telluric standard star (lower panel). The positions of the C_2 (0,0) Phillips bands are shown by the blue vertical lines.

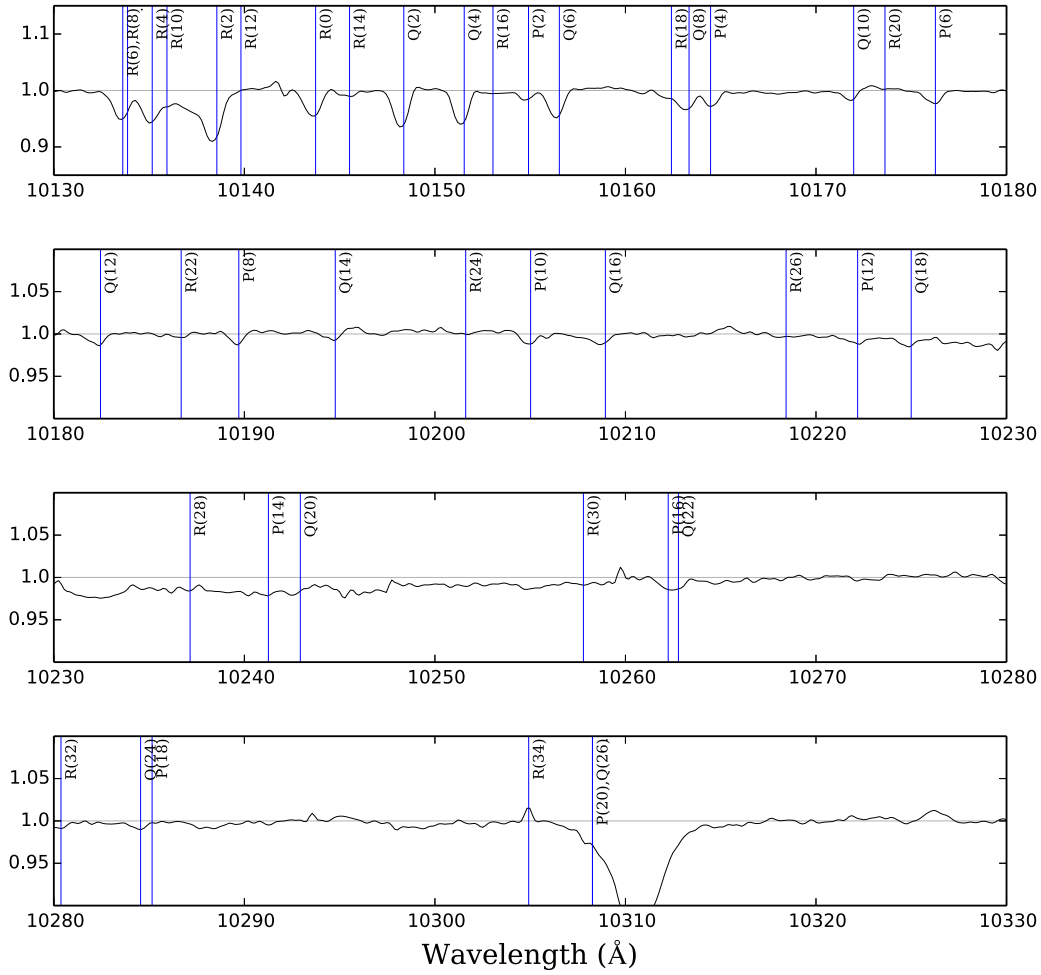

Figure 8.16: The WINERED spectra of the C_2 (1,0) Phillips bands of Cyg OB2 No.12.

Chapter 9

SUMMARY

In this thesis, we presented a first comprehensive survey of DIBs in the NIR wavelength range with the newly developed NIR Echelle spectrograph WINERED. We obtained the NIR high-resolution spectra of 25 early-type stars with color excesses of $0.07 < E(B-V) < 3.4$. We searched for NIR DIBs in the wavelength coverage of WINERED, $0.91 < \lambda < 1.32$ μm. Consequently, we identified 15 new DIBs in addition to five DIBs previously detected in this wavelength range. All of the DIBs detected herein are stronger than 10 mÅ, below which the majority of optical DIBs are distributed. Assuming a similar distribution as that of the optical DIBs, we expect that the number of weak NIR DIBs increase by an order of magnitude through deeper spectroscopic observations.

Using the largest data set so far of NIR high-resolution spectra for 25 reddened early-type stars, we investigated the correlations among NIR DIBs, eight strong optical DIBs investigated by Friedman et al. (2011) ($\lambda\lambda$5487.7, 5705.1, 5780.5, 5797.1, 6196.0, 6204.5, 6283.8, and 6613.6), and the reddening of stars. Our findings are summarized as follows:

1. All identified NIR DIBs are found to have correlation coefficients with $E(B-V)$ that are not as high as those of the strong optical DIBs. The lower correlation coefficients of NIR DIBs with $E(B-V)$ show that the abundance of the NIR DIB carriers depends on some physical properties of gas clouds, such as UV flux, as well as on the amount of gas in the line of sight.

2. Three NIR DIBs, $\lambda\lambda 10780, 10792,$ and 11797, are found to be well correlated with each other, suggesting that these three DIBs consist of a "family," wherein the carrier molecules share similar physical and chemical properties. Because some data points do not quite fit the correlation, these DIBs would appear to originate from a different molecule.

3. The three strongest NIR DIBs, $\lambda\lambda 10780, 11797,$ and 13175, are found to be correlated better with $\lambda\lambda 5705.1, 5780.5, 6204.5,$ and 6283.8 ($r = 0.8 - 0.9$) than with $\lambda\lambda 5797.1$, 6196.0, and 6613.6 ($r = 0.6 - 0.7$). Moreover, those NIR DIBs are found to be relatively weaker in $\zeta-$type clouds, where the molecules are shielded from UV flux, in the same manner as $\lambda 5780.5$, whose carrier is proposed to be a cation molecule with high ionization potential. Considering the similarity between the strongest NIR DIBs as well as some other NIR DIBs with $\lambda 5780.5$, we suggest that the carriers of these three NIR DIBs are also cation molecules.

4. We compared the wavelengths of newly identified NIR DIBs with the transitions of some specific ionized PAHs measured by Mattioda et al. (2005) with the matrix isolation technique. DIB $\lambda 10792$ is detected close to the wavelength of the strong electronic transition of $C_{42}H_{22}^{+}$ ($\lambda = 10790$Å), but the wavelength of the other DIBs do not correspond to the strong electronic transitions of ionized PAHs. However, the pure gas-phase spectra of ionized PAHs are required for firm identification of NIR DIBs with ionized PAHs. The DIBs in the NIR wavelength range have been expected to be the electronic transitions of the ionized large-sized carbon molecules, such as polycyclic aromatic hydrocarbons (PAH) and fullerenes, which is consistent with our suggestion that the carriers of some NIR DIBs are cation molecules. However, any candidates of the carriers of NIR DIBs do not have strong evidences yet. Further observational constraints on the DIB properties as well as the identification with NIR absorption spectra of the proposed molecules in the laboratory are necessary to reveal the carriers of the NIR DIBs.

We investigated the environmental dependence of DIBs toward the Cyg OB2 association. Cyg OB2 association contains a number of bright early-type stars with large extinction,

toward which strong DIBs can be detected (Chlewicki et al., 1986). The gas clouds toward the Cyg OB2 association are known to have complex gaseous structures exposed to the strong flux of ionizing photons from the ambient early-type stars. We observed the seven brightest stars in $J-$band in the Cyg OB2 association and detected all NIR DIBs with large EWs toward all the observed stars. We obtained the following results.

5 We could not confirm any clear relations between DIBs and C_2 column densities, which were estimated by Gredel et al. (2001) using the C_2 (2,0) and (3,0) Phillips bands. This suggests that the DIB carriers are distributed mainly in the diffuse component with $n_{\rm H} \sim 100{\rm cm}^{-3}$ rather than in the dense component with $n_{\rm H} > 10^4{\rm cm}^{-3}$, where C_2 molecules are distributed. Such properties of NIR DIBs are common to those of "classical" strong DIBs in the optical wavelength range.

6 Subsequently, we investigated the environmental dependence of DIBs that are well correlated. Consequently, we found that the EW ratios of DIBs $\lambda\lambda$10504 and 5780.5 to DIBs $\lambda\lambda$10780, 10792, 11797, 12623, and 13175 in the Cyg OB2 association are lower than those in the interstellar environment by a factor of two. We suggest that the environmental dependence of DIB ratios illustrates some difference in the properties of the DIB carriers, such as the stability to the high-energy photons.

7 The large EWs of weak DIBs toward the Cyg OB2 association allow us to examine the correlations confidently. The DIBs $\lambda\lambda$10780, 12861, and 13027 are found to be well correlated, suggesting that their carriers could be chemically related to the carriers of the strong NIR DIBs.

8 In the observation of the Cyg OB2 association, we could also detect the C_2 (0,0) and (1,0) Phillips bands around $\lambda = 12070$ and 10130Å, respectively. This is the first detection of the C_2 (0,0) Phillips bands in the interstellar medium, which is the most fundamental band of C_2 molecules. Compared to the (2,0) and (3,0) bands in the far red wavelength range, which have been mainly used as the tracer of interstellar C_2 molecules, the (0,0) and (1,0) bands in the NIR wavelength range will be powerful tracers of C_2 molecules toward the stars obscured by the interstellar dust because of the higher transmittance

of the starlight in the NIR wavelength range in interstellar clouds.

In summary, as a result of our survey of NIR DIBs, we could extend the DIB studies to the NIR wavelength range, where few detection of strong DIBs have been reported. The NIR wavelength range is of great advantage to investigate DIBs toward the stars with heavy interstellar extinction, such as the stars in inner and outer Galaxy and the stars embedded in the dense molecular clouds. By revealing the properties of DIBs in such various environment, the properties of the DIB carriers are expected to be constrained more strongly, which will contribute to the firm identification of the DIB carriers in the future.

ACKNOWLEDGEMENTS

First of all, I would like to express the deepest appreciation to my supervisor, Professor Naoto Kobayashi, for encouraging me through my graduate course. Without his supervision and constant help, this thesis would not have been finished. I am also very grateful to my collaborators, Professor Hideyo Kawakita, Dr. Yuji Ikeda, and Dr. Sohei Kondo, for their valuable comments on my thesis work. The discussion with Professor Hideyo Kawakita about the interstellar molecules inspired me. Dr. Yuji Ikeda gave me his in-depth knowledge on the stellar spectra of early-type stars. Dr. Sohei Kondo helped me with the observations and the development of the data reduction pipeline. I am also greatly benefited from the discussion with Dr. Noriyuki Matsunaga and Dr. Chikako Yasui. I would like to thank Professor Alan T. Tokunaga and Professor Setsuko Wada for their valuable comments. I also thank all of the students and staffs of WINERED project at Koyama Astronomical Observatory for their cooperation for my observations and data reduction. Especially, I thank Mr. Takafumi Kawanishi, Mr. Tetsuya Nakaoka, Mr. Shogo Otsubo, and Ms. Ayaka Kitano for their cooperation for my observations. I am also grateful to my colleagues, Mr. Kei Fukue, Ms. Natsuko Izumi, Mr. Ryo Yamamoto, Mr. Misaki Mizumoto, and Ms. Haruka Takahashi.

I was financially supported by the Japan Society for the Promotion of Science (JSPS) for Young Scientists.

Finally, I would like to extend my indebtedness to my wife for her understanding, support, encouragement and sacrifice throughout my study.

Bibliography

Ádámkovics, M., Blake, G. A., & McCall, B. J. 2005, ApJ, 625, 857

Adamson, A. J., Whittet, D. C. B., & Duley, W. W. 1991, MNRAS, 252, 234

Adamson, A. J., Kerr, T. H., Whittet, D. C. B., & Duley, W. W. 1994, MNRAS, 268, 705

Biennier, L., Salama, F., Allamandola, L. J., & Scherer, J. J. 2003, J. Chem. Phys., 118, 7863

Cami, J., Sonnentrucker, P., Ehrenfreund, P., & Foing, B. H. 1997, A&A, 326, 822

Cami, J., Bernard-Salas, J., Peeters, E., & Malek, S. E. 2010, Science, 329, 1180

Casu, S., Scappini, F., Cecchi-Pestellini, C., & Olberg, M. 2005, MNRAS, 359, 73

Cecchi-Pestellini, C., & Dalgarno, A. 2000, MNRAS, 313, L6

Chlewicki, G., van der Zwet, G. P., van Ijzendoorn, L. J., Greenberg, J. M., & Alvarez, P. P. 1986, ApJ, 305, 455

Chlewicki, G., van der Zwet, G. P., van Ijzendoorn, L. J., Greenberg, J. M., & Alvarez, P. P. 1986, ApJ, 305, 455

Clayton, G. C., Gordon, K. D., Salama, F., et al. 2003, ApJ, 592, 947

Cordiner, M. A., Cox, N. L. J., Evans, C. J., et al. 2011, ApJ, 726, 39

Cox, A. N. 2000, Allen ' s Astrophysical Quantities (London: The Athlone Press)

Cox, N. L. J., Cordiner, M. A., Ehrenfreund, P., et al. 2007, A&A, 470, 941

Cox, N. L. J., Cami, J., Kaper, L., et al. 2014, A&A, 569, A117

Duley, W. W., & Kuzmin, S. 2010, ApJ, 712, L165

Foing, B. H., & Ehrenfreund, P. 1994, Nature, 369, 296

Friedman, S. D., York, D. G., McCall, B. J., et al. 2011, ApJ, 727, 33

Fulara, J., Jakobi, M., & Maier, J. P. 1993, Chemical Physics Letters, 211, 227

Galazutdinov, G. A., Krełowski, J., Musaev, F. A., Ehrenfreund, P., & Foing, B. H. 2000, MNRAS, 317, 750

García-Hernández, D. A., & Díaz-Luis, J. J. 2013, A&A, 550, LL6

Geballe, T. R., Najarro, F., Figer, D. F., Schlegelmilch, B. W., & de La Fuente, D. 2011, Nature, 479, 200

Gray, D. F. 1992, Camb. Astrophys. Ser., Vol. 20,,

Gray, R. O., & Corbally, C., J. 2009, Stellar Spectral Classification (Princeton University Press)

Gredel, R., & Muench, G. 1994, A&A, 285, 640

Gredel, R., Black, J. H., & Yan, M. 2001, A&A, 375, 553

Gredel, R., Carpentier, Y., Rouillé, G., et al. 2011, A&A, 530, A26

Groh, J. H., Damineli, A., & Jablonski, F. 2007, A&A, 465, 993

Heger, M. L. 1919, Lick Observatory Bulletin, 10, 59

Herbig, G. H. 1993, ApJ, 407, 142

Hobbs, L. M., York, D. G., Snow, T. P., et al. 2008, ApJ, 680, 1256

Hobbs, L. M., York, D. G., Thorburn, J. A., et al. 2009, ApJ, 705, 32

Ikeda, Y., Kobayashi, N., Kondo, S., et al. 2006, Proc. SPIE, 6269,

Jenniskens, P., & Desert, F.-X. 1994, A&AS, 106, 39

Jenniskens, P., Mulas, G., Porceddu, I., & Benvenuti, P. 1997, A&A, 327, 337

Joblin, C., D'Hendecourt, L., Leger, A., & Maillard, J. P. 1990, Nature, 346, 729

Jones, A. P. 2013, A&A, 555, AA39

Jones, A. P. 2014, Planet. Space Sci., 100, 26

Kerr, T. H., Hibbins, R. E., Miles, J. R., et al. 1996, MNRAS, 283, L105

Kondo, S., Ikeda, Y., & Kobayashi, N., et al. 2015, arXiv:1501.03403

Krelowski, J., & Walker, G. A. H. 1987, ApJ, 312, 860

Krełowski, J., Sneden, C., & Hittgen, D. 1995, Planet. Space Sci., 43, 1195

Krełowski, J., Beletsky, Y., Galazutdinov, G. A., et al. 2010, ApJ, 714, L64

Kupka, F., Piskunov, N., Ryabchikova, T. A., Stempels, H. C., & Weiss, W. W. 1999, A&AS, 138, 119

Kurucz, R. L. 1993, ATLAS9 Stellar Atmosphere Programs and 2 km/s Grid, Kurucz CD-ROM No. 13. (Cambridge, MA: Smithsonian Astrophysical Observatory), 13

Lawton, B., Churchill, C. W., York, B. A., et al. 2008, AJ, 136, 994

Maier, J. P., Lakin, N. M., Walker, G. A. H., & Bohlender, D. A. 2001, ApJ, 553, 267

Maier, J. P., Walker, G. A. H., & Bohlender, D. A. 2004, ApJ, 602, 286

Maier, J. P., Walker, G. A. H., Bohlender, D. A., et al. 2011, ApJ, 726, 41

Maier, J. P., Chakrabarty, S., Mazzotti, F. J., et al. 2011, ApJ, 729, LL20

Mattioda, A. L., Hudgins, D. M., & Allamandola, L. J. 2005, ApJ, 629, 1188

McCall, B. J., Geballe, T. R., Hinkle, K. H., & Oka, T. 1998, Science, 279, 1910

McCall, B. J., Drosback, M. M., Thorburn, J. A., et al. 2010, ApJ, 708, 1628

McCall, B. J, & Griffin, R.E. 2013, Proc. R. Soc. A, 469,2151

Merrill, P. W. 1936, ApJ, 83, 126

Misawa, T., Gandhi, P., Hida, A., Tamagawa, T., & Yamaguchi, T. 2009, ApJ, 700, 1988

Motylewski, T., Linnartz, H., Vaizert, O., et al. 2000, ApJ, 531, 312

Moutou, C., Krełowski, J., D'Hendecourt, L., & Jamroszczak, J. 1999, A&A, 351, 680

Price, R. J., Crawford, I. A., Barlow, M. J., & Howarth, I. D. 2001, MNRAS, 328, 555

Rawlings, M. G., Adamson, A. J., & Kerr, T. H. 2014, ApJ, 796, 58

Rouillé, G., Steglich, M., Carpentier, Y., et al. 2012, ApJ, 752, 25

Ruiterkamp, R., Cox, N. L. J., Spaans, M., et al. 2005, A&A, 432, 515

Salama, F., Bakes, E. L. O., Allamandola, L. J., & Tielens, A. G. G. M. 1996, ApJ, 458, 621

Salama, F., Galazutdinov, G. A., Krełowski, J., Allamandola, L. J., & Musaev, F. A. 1999, ApJ, 526, 265

Salama, F., Galazutdinov, G. A., Krełowski, J., et al. 2011, ApJ, 728, 154

Sarre, P. J. 2008, IAU Symposium, 251, 49

Scappini, F., Cecchi-Pestellini, C., Codella, C., & Dalgarno, A. 2000, MNRAS, 317, L6

Scappini, F., Casu, S., Cecchi-Pestellini, C., & Olberg, M. 2002, MNRAS, 337, 495

Thorburn, J. A., Hobbs, L. M., McCall, B. J., et al. 2003, ApJ, 584, 339

Sonnentrucker, P., Cami, J., Ehrenfreund, P., & Foing, B. H. 1997, A&A, 327, 1215

Snow, T. P., & McCall, B. J. 2006, ARA&A, 44, 367

Steglich, M., Bouwman, J., Huisken, F., & Henning, T. 2011, ApJ, 742, 2

Takeda, Y. 1995, PASJ, 47, 287

Tielens, A. G. G. M. 2008, ARA&A, 46, 289

Tielens, A. G. G. M. 2014, IAU Symposium, 297, 399

Tuairisg, S. Ó., Cami, J., Foing, B. H., Sonnentrucker, P., & Ehrenfreund, P. 2000, A&AS, 142, 225

Vos, D. A. I., Cox, N. L. J., Kaper, L., Spaans, M., & Ehrenfreund, P. 2011, A&A, 533, A129

Welty, D. E., Hobbs, L. M., & Kulkarni, V. P. 1994, ApJ, 436, 152

Welty, D. E., & Hobbs, L. M. 2001, ApJS, 133, 345

Welty, D. E., Hobbs, L. M., & Morton, D. C. 2003, ApJS, 147, 61

Welty, D. E., Federman, S. R., Gredel, R., Thorburn, J. A., & Lambert, D. L. 2006, ApJS, 165, 138

Yasui, C., Ikeda, Y., Kondo, S., Motohara, K., & Kobayashi, N. 2006, Proc. SPIE, 6269, 62694P

Yasui, C., Kondo, S., Ikeda, Y., et al. 2008, Proc. SPIE, 7014,

Yoshikawa, T., Ikeda, Y., Fujishiro, N., et al. 2012, Proc. SPIE, 8444,

Zasowski, G., Ménard, B., Bizyaev, D., et al. 2015, ApJ, 798, 35

Appendix A

WINERED spectra

The WINERED spectra of the target stars in the DIB survey are shown in this appendix. In the upper panels, the obtained spectra of all targets are shown. The spectra are plotted in a sequence of $E(B-V)$ of the stars. The spectra of stars with larger $E(B-V)$ are plotted lower in the panel. The wavelength of DIBs and stellar lines are shown with green and thin black vertical lines, respectively. The quite noisy range of the spectra are not shown in this figure. In the lower panels, a spectrum of telluric standard star 50 Cas is shown.

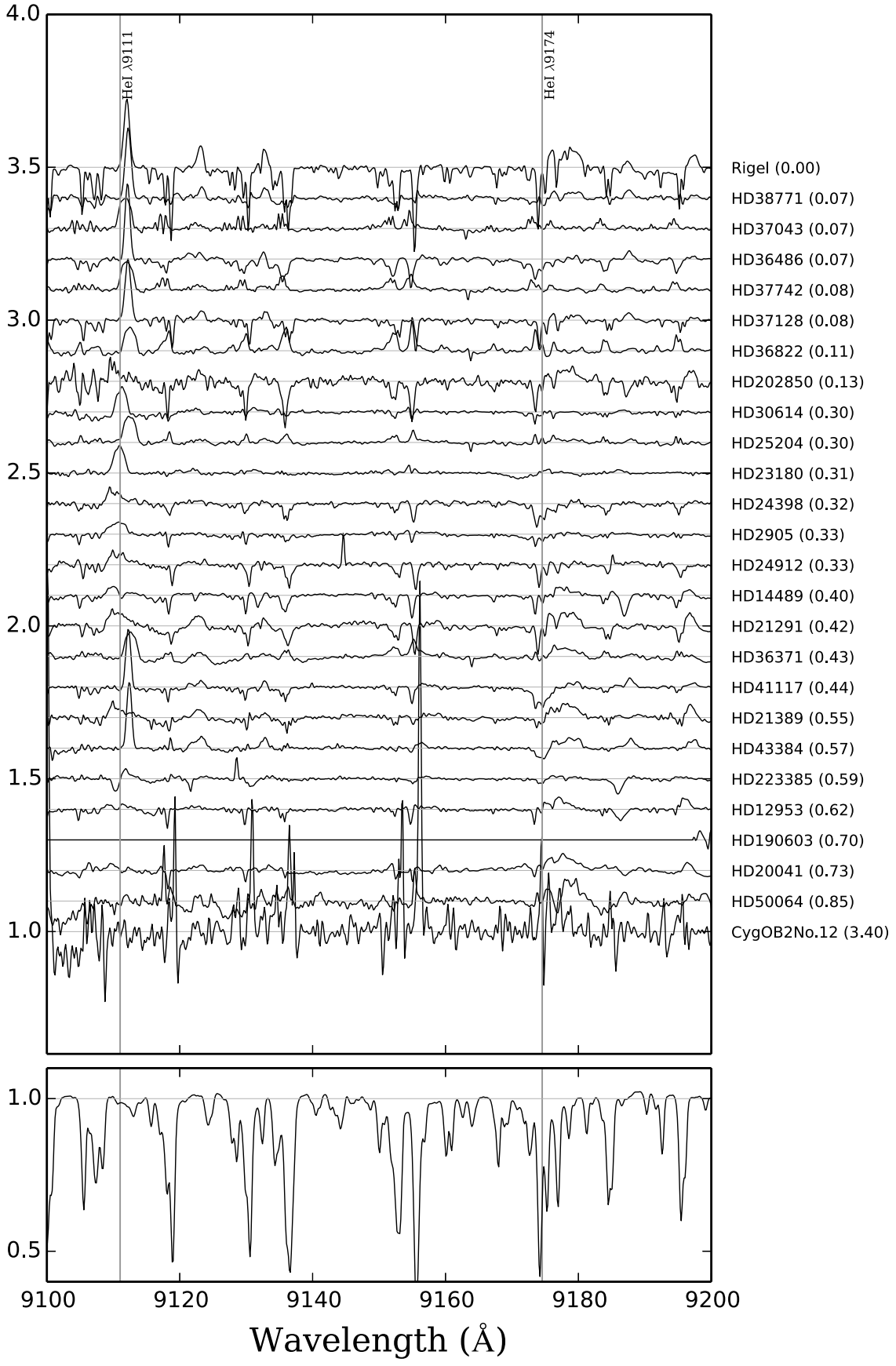
HeI λ9111
HeI λ9174
Rigel (0.00)
HD38771 (0.07)
HD37043 (0.07)
HD36486 (0.07)
HD37742 (0.08)
HD37128 (0.08)
HD36822 (0.11)
HD202850 (0.13)
HD30614 (0.30)
HD25204 (0.30)
HD23180 (0.31)
HD24398 (0.32)
HD2905 (0.33)
HD24912 (0.33)
HD14489 (0.40)
HD21291 (0.42)
HD36371 (0.43)
HD41117 (0.44)
HD21389 (0.55)
HD43384 (0.57)
HD223385 (0.59)
HD12953 (0.62)
HD190603 (0.70)
HD20041 (0.73)
HD50064 (0.85)
CygOB2No.12 (3.40)
4.0
3.5
3.0
2.5
2.0
1.5
1.0
1.0
0.5
9100
9120
9140
9160
9180
9200
Wavelength (Å)

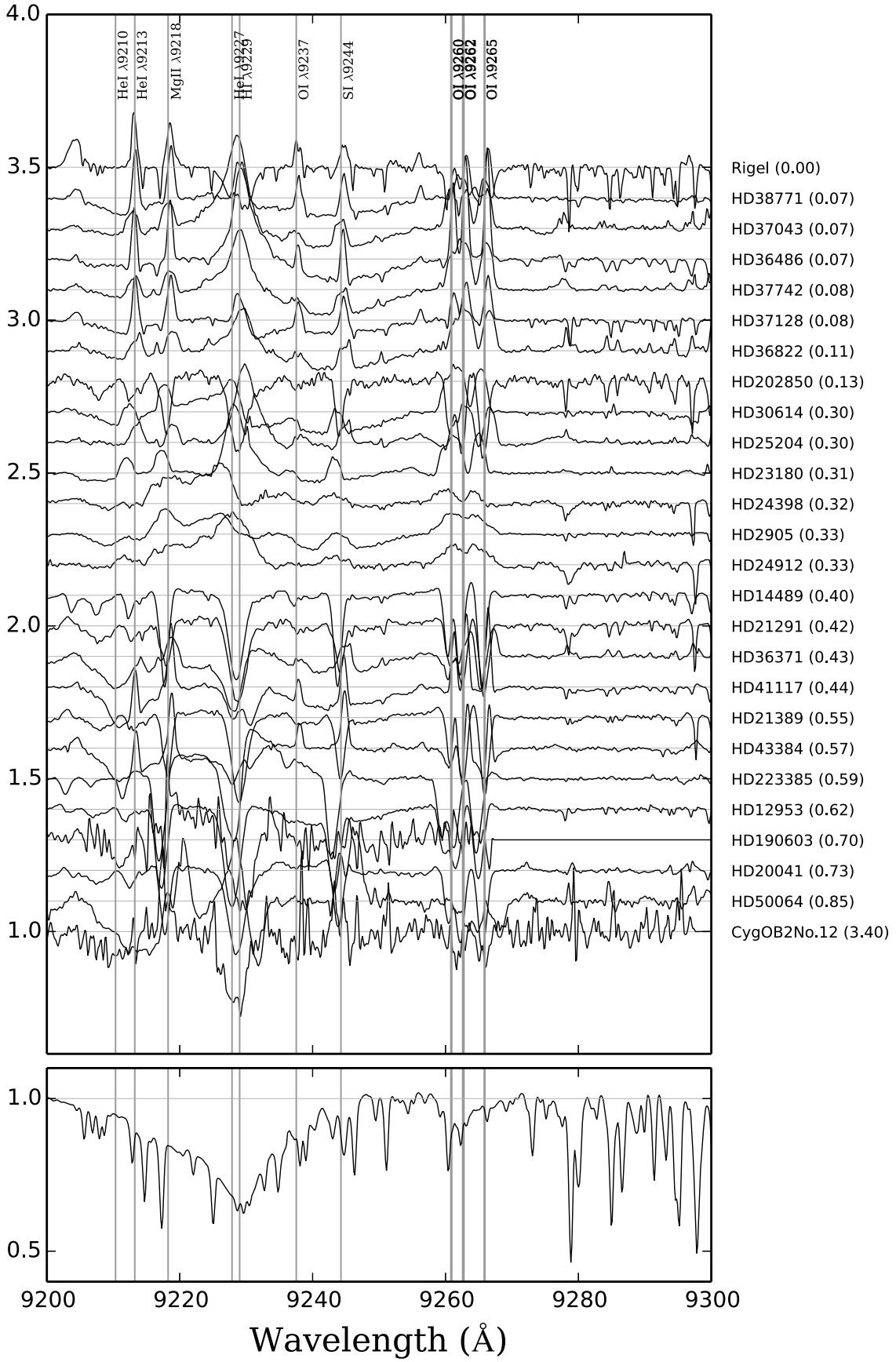
HeI λ9210
HeI λ9213
MgII λ9218
HeI λ9227
HI λ9229
OI λ9237
SI λ9244
OI λ9260
OI λ9262
OI λ9265
Rigel (0.00)
HD38771 (0.07)
HD37043 (0.07)
HD36486 (0.07)
HD37742 (0.08)
HD37128 (0.08)
HD36822 (0.11)
HD202850 (0.13)
HD30614 (0.30)
HD25204 (0.30)
HD23180 (0.31)
HD24398 (0.32)
HD2905 (0.33)
HD24912 (0.33)
HD14489 (0.40)
HD21291 (0.42)
HD36371 (0.43)
HD41117 (0.44)
HD21389 (0.55)
HD43384 (0.57)
HD223385 (0.59)
HD12953 (0.62)
HD190603 (0.70)
HD20041 (0.73)
HD50064 (0.85)
CygOB2No.12 (3.40)
4.0
3.5
3.0
2.5
2.0
1.5
1.0
1.0
0.5
9200
9220
9240
9260
9280
9300
Wavelength (Å)

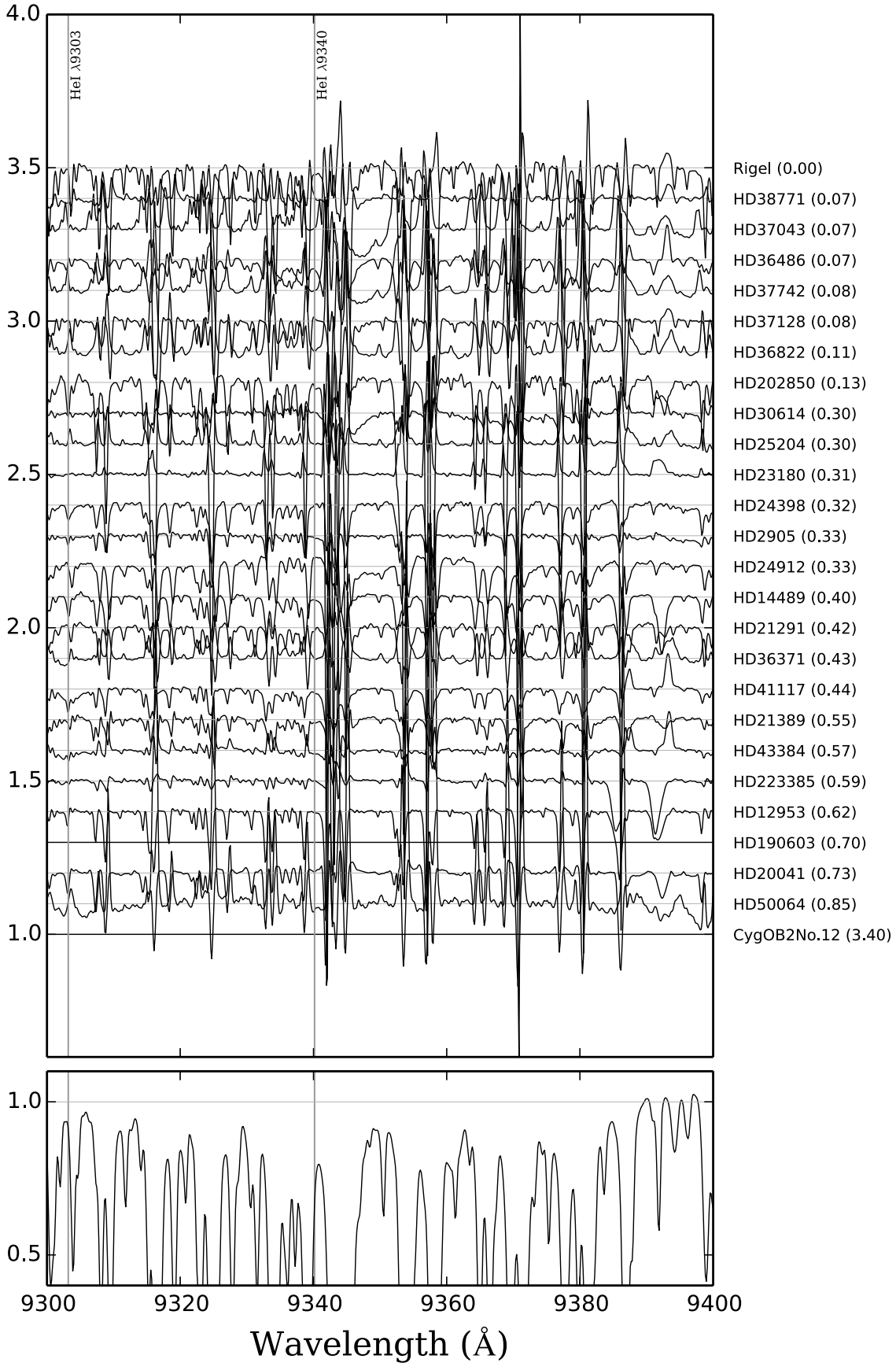
HeI λ9303
HeI λ9340
Rigel (0.00)
HD38771 (0.07)
HD37043 (0.07)
HD36486 (0.07)
HD37742 (0.08)
HD37128 (0.08)
HD36822 (0.11)
HD202850 (0.13)
HD30614 (0.30)
HD25204 (0.30)
HD23180 (0.31)
HD24398 (0.32)
HD2905 (0.33)
HD24912 (0.33)
HD14489 (0.40)
HD21291 (0.42)
HD36371 (0.43)
HD41117 (0.44)
HD21389 (0.55)
HD43384 (0.57)
HD223385 (0.59)
HD12953 (0.62)
HD190603 (0.70)
HD20041 (0.73)
HD50064 (0.85)
CygOB2No.12 (3.40)
4.0
3.5
3.0
2.5
2.0
1.5
1.0
1.0
0.5
9300
9320
9340
9360
9380
9400
Wavelength (Å)

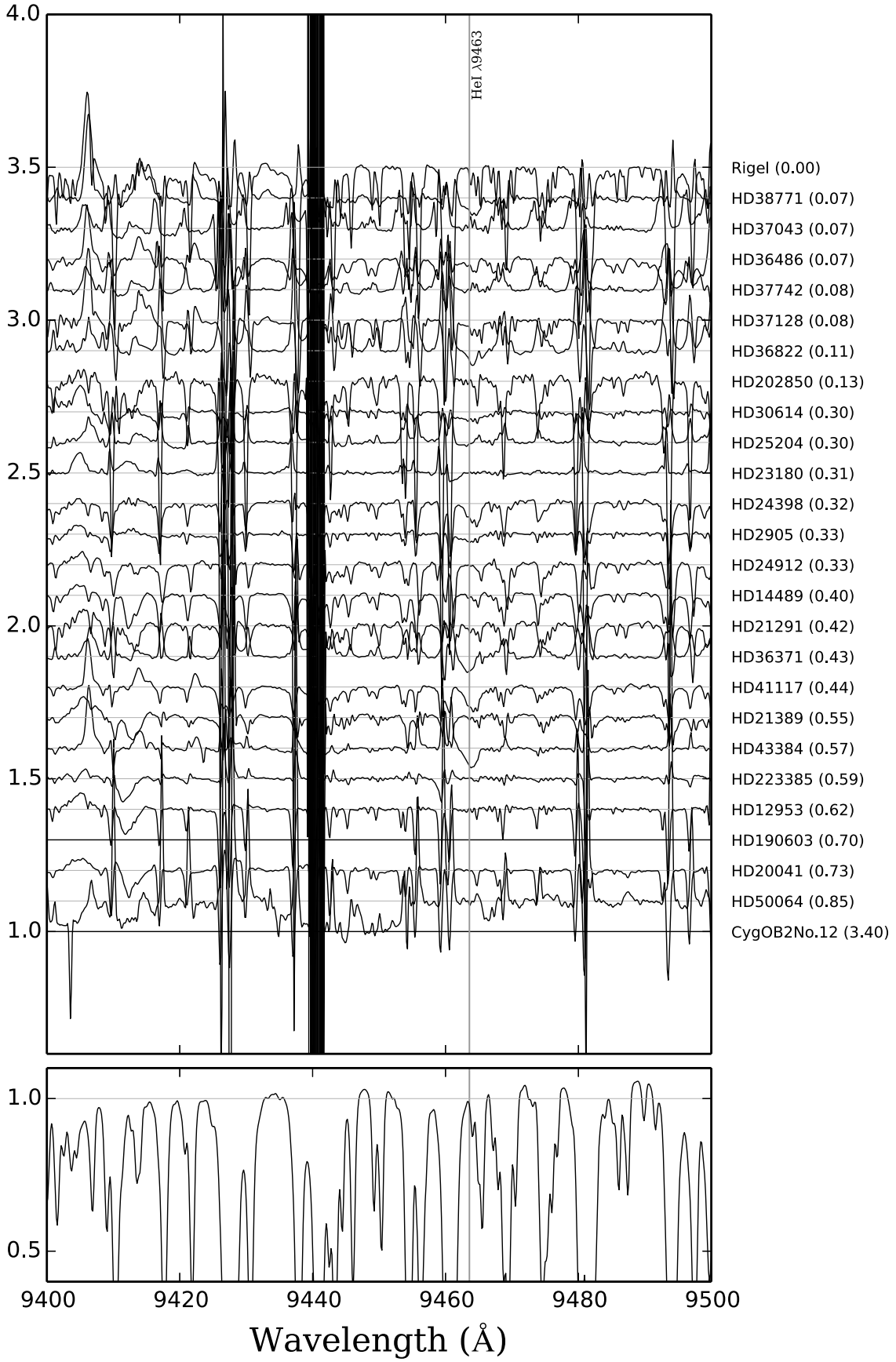
HeI λ9463
Rigel (0.00)
HD38771 (0.07)
HD37043 (0.07)
HD36486 (0.07)
HD37742 (0.08)
HD37128 (0.08)
HD36822 (0.11)
HD202850 (0.13)
HD30614 (0.30)
HD25204 (0.30)
HD23180 (0.31)
HD24398 (0.32)
HD2905 (0.33)
HD24912 (0.33)
HD14489 (0.40)
HD21291 (0.42)
HD36371 (0.43)
HD41117 (0.44)
HD21389 (0.55)
HD43384 (0.57)
HD223385 (0.59)
HD12953 (0.62)
HD190603 (0.70)
HD20041 (0.73)
HD50064 (0.85)
CygOB2No.12 (3.40)
4.0
3.5
3.0
2.5
2.0
1.5
1.0
1.0
0.5
9400
9420
9440
9460
9480
9500
Wavelength (Å)

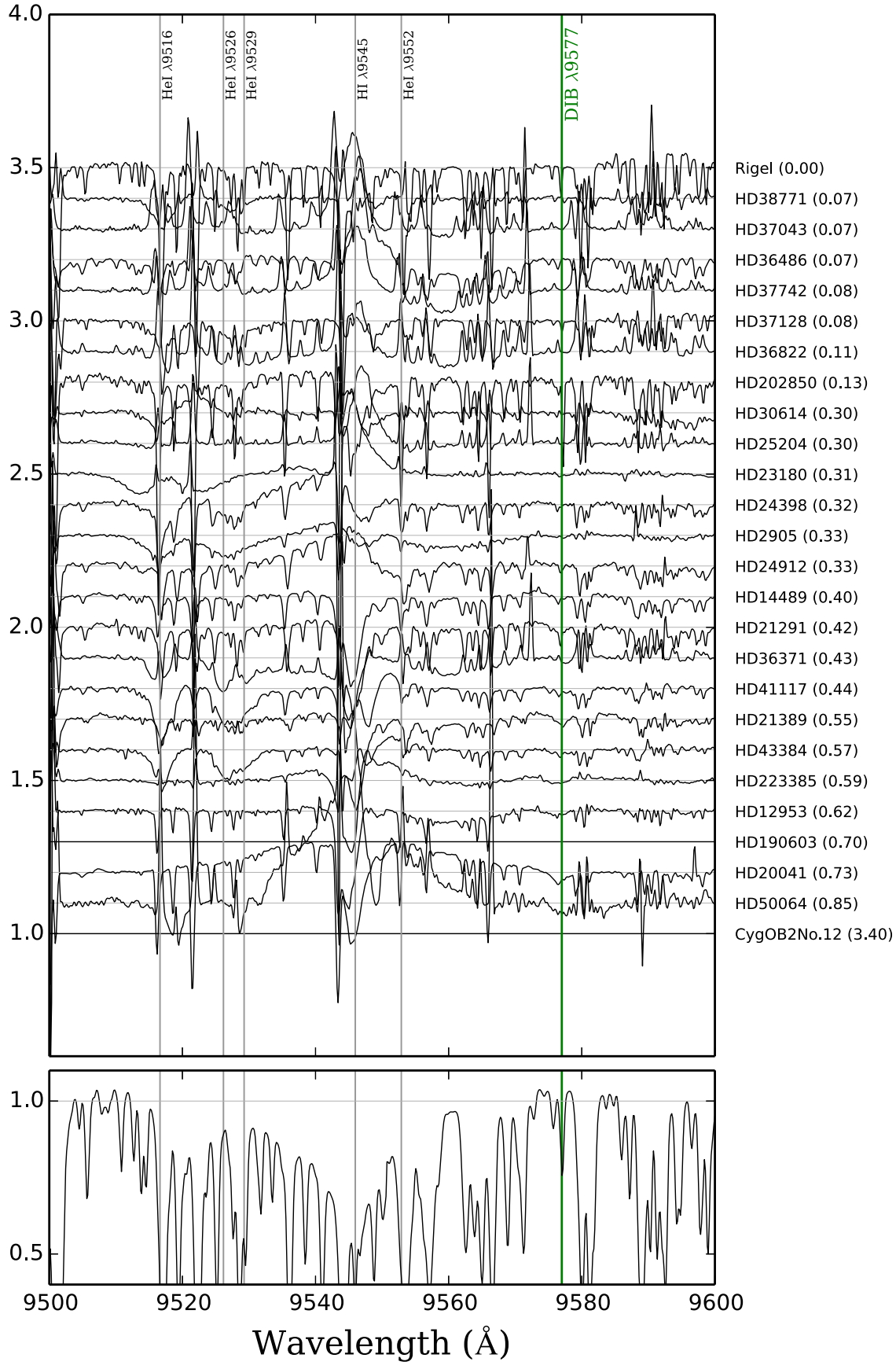
HeI λ9516
HeI λ9526
HeI λ9529
HI λ9545
HeI λ9552
DIB λ9577
Rigel (0.00)
HD38771 (0.07)
HD37043 (0.07)
HD36486 (0.07)
HD37742 (0.08)
HD37128 (0.08)
HD36822 (0.11)
HD202850 (0.13)
HD30614 (0.30)
HD25204 (0.30)
HD23180 (0.31)
HD24398 (0.32)
HD2905 (0.33)
HD24912 (0.33)
HD14489 (0.40)
HD21291 (0.42)
HD36371 (0.43)
HD41117 (0.44)
HD21389 (0.55)
HD43384 (0.57)
HD223385 (0.59)
HD12953 (0.62)
HD190603 (0.70)
HD20041 (0.73)
HD50064 (0.85)
CygOB2No.12 (3.40)
4.0
3.5
3.0
2.5
2.0
1.5
1.0
1.0
0.5
9500
9520
9540
9560
9580
9600
Wavelength (Å)

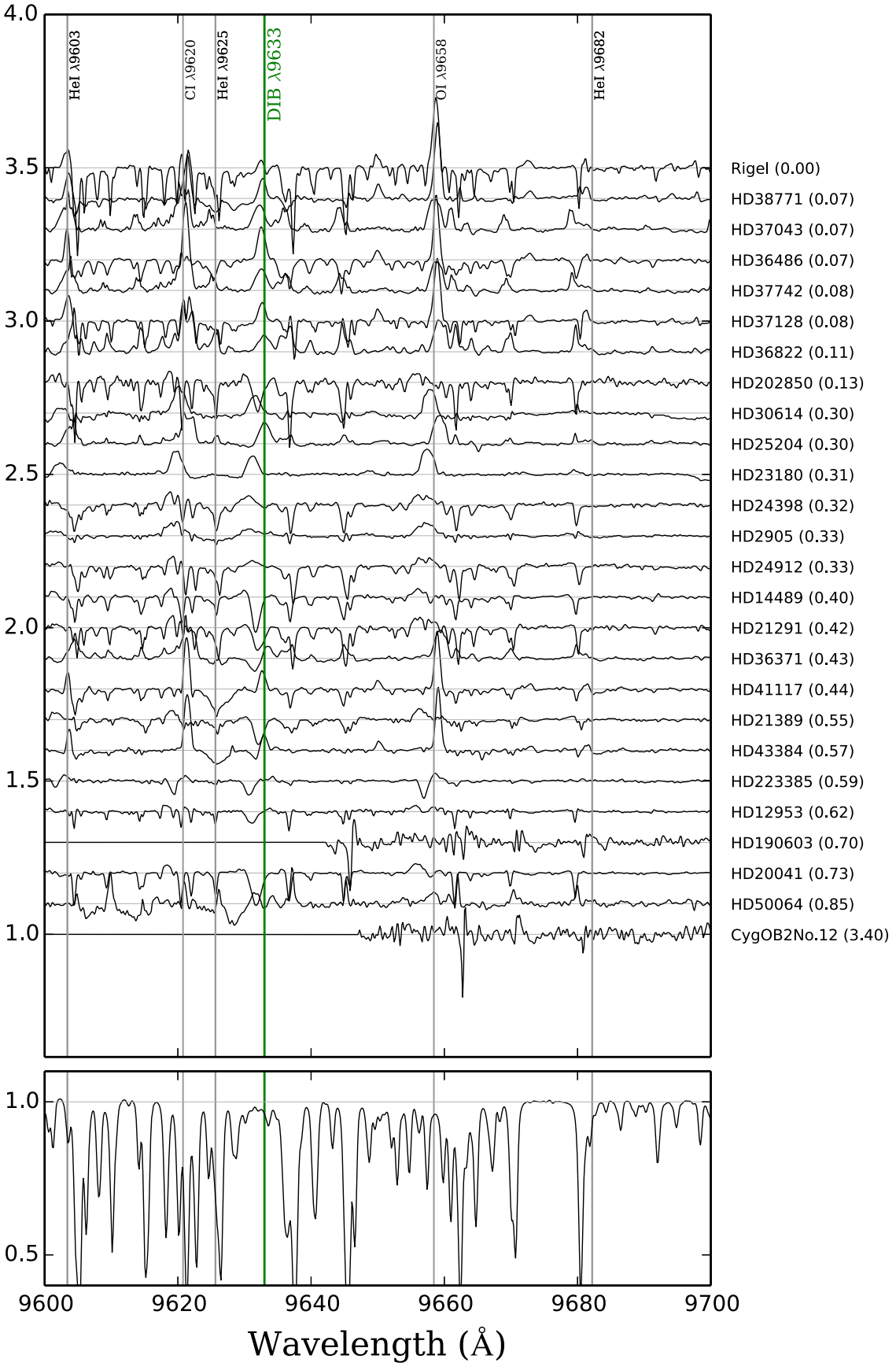
HeI λ9603
CI λ9620
HeI λ9625
DIB λ9633
OI λ9658
HeI λ9682
Rigel (0.00)
HD38771 (0.07)
HD37043 (0.07)
HD36486 (0.07)
HD37742 (0.08)
HD37128 (0.08)
HD36822 (0.11)
HD202850 (0.13)
HD30614 (0.30)
HD25204 (0.30)
HD23180 (0.31)
HD24398 (0.32)
HD2905 (0.33)
HD24912 (0.33)
HD14489 (0.40)
HD21291 (0.42)
HD36371 (0.43)
HD41117 (0.44)
HD21389 (0.55)
HD43384 (0.57)
HD223385 (0.59)
HD12953 (0.62)
HD190603 (0.70)
HD20041 (0.73)
HD50064 (0.85)
CygOB2No.12 (3.40)
4.0
3.5
3.0
2.5
2.0
1.5
1.0
1.0
0.5
9600
9620
9640
9660
9680
9700
Wavelength (Å)

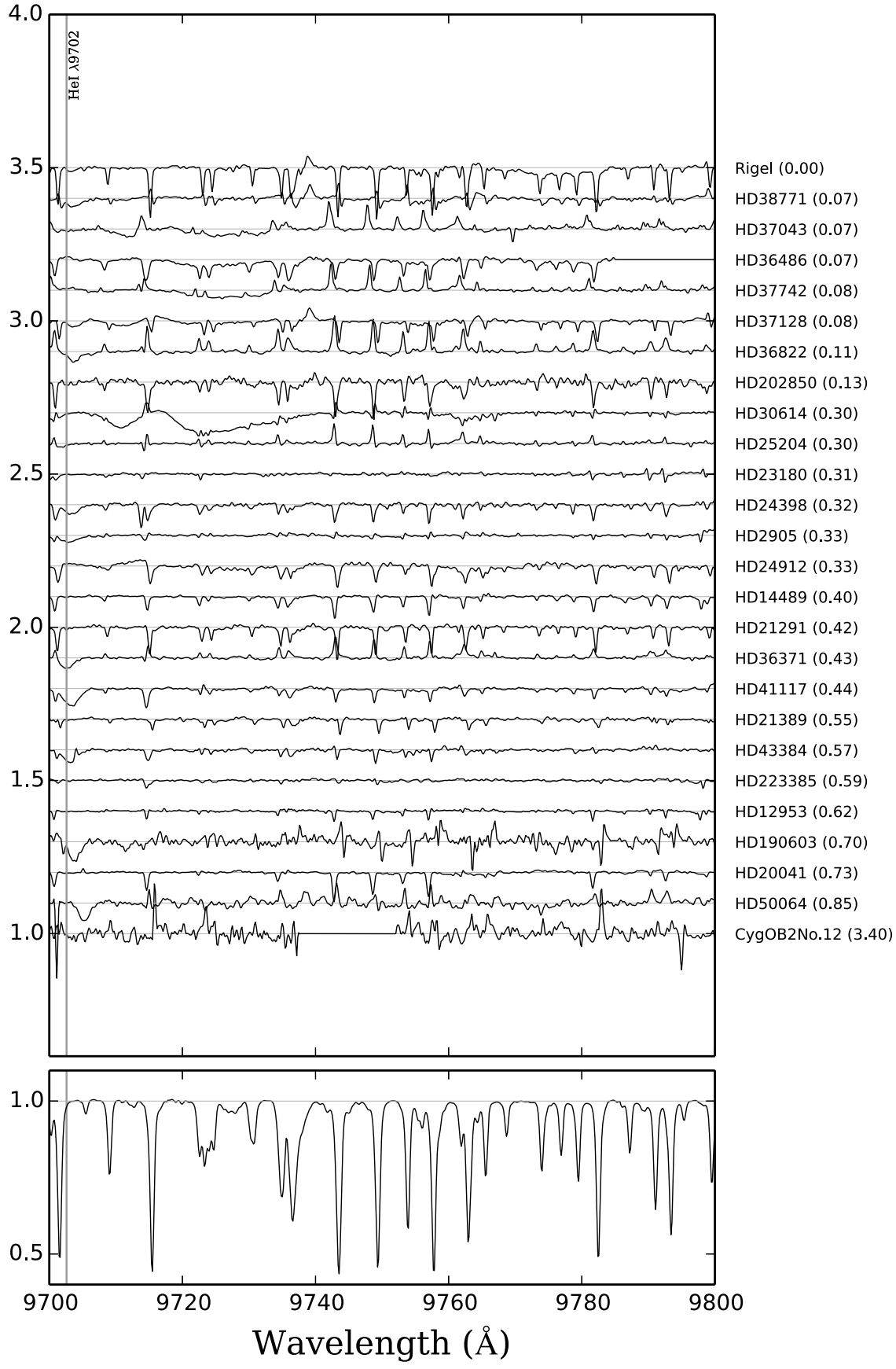
HeI λ9702
Rigel (0.00)
HD38771 (0.07)
HD37043 (0.07)
HD36486 (0.07)
HD37742 (0.08)
HD37128 (0.08)
HD36822 (0.11)
HD202850 (0.13)
HD30614 (0.30)
HD25204 (0.30)
HD23180 (0.31)
HD24398 (0.32)
HD2905 (0.33)
HD24912 (0.33)
HD14489 (0.40)
HD21291 (0.42)
HD36371 (0.43)
HD41117 (0.44)
HD21389 (0.55)
HD43384 (0.57)
HD223385 (0.59)
HD12953 (0.62)
HD190603 (0.70)
HD20041 (0.73)
HD50064 (0.85)
CygOB2No.12 (3.40)
4.0
3.5
3.0
2.5
2.0
1.5
1.0
1.0
0.5
9700
9720
9740
9760
9780
9800
Wavelength (Å)

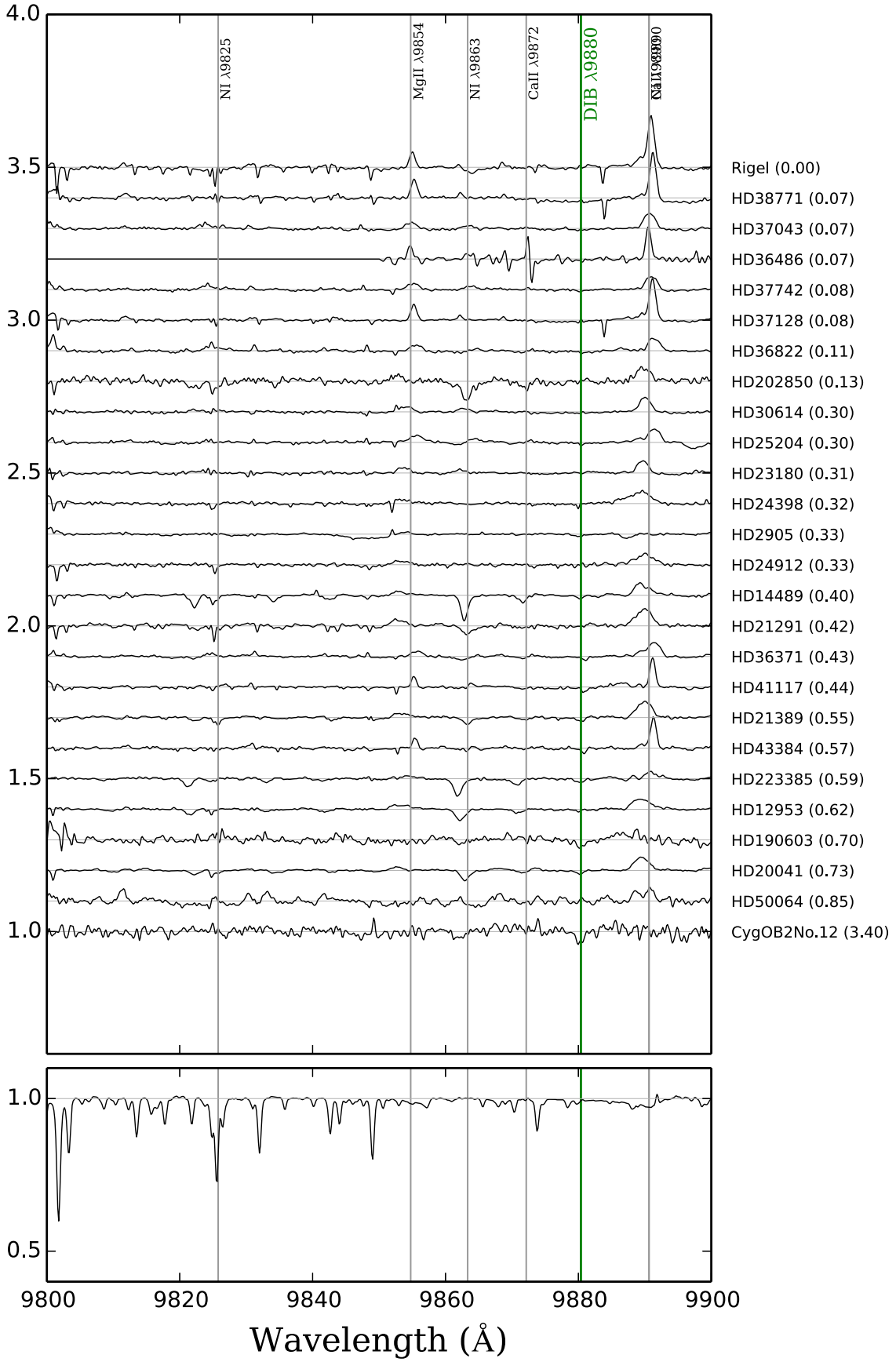
NI λ9825
MgII λ9854
NI λ9863
CaII λ9872
DIB λ9880
Rigel (0.00)
HD38771 (0.07)
HD37043 (0.07)
HD36486 (0.07)
HD37742 (0.08)
HD37128 (0.08)
HD36822 (0.11)
HD202850 (0.13)
HD30614 (0.30)
HD25204 (0.30)
HD23180 (0.31)
HD24398 (0.32)
HD2905 (0.33)
HD24912 (0.33)
HD14489 (0.40)
HD21291 (0.42)
HD36371 (0.43)
HD41117 (0.44)
HD21389 (0.55)
HD43384 (0.57)
HD223385 (0.59)
HD12953 (0.62)
HD190603 (0.70)
HD20041 (0.73)
HD50064 (0.85)
CygOB2No.12 (3.40)
4.0
3.5
3.0
2.5
2.0
1.5
1.0
1.0
0.5
9800
9820
9840
9860
9880
9900
Wavelength (Å)

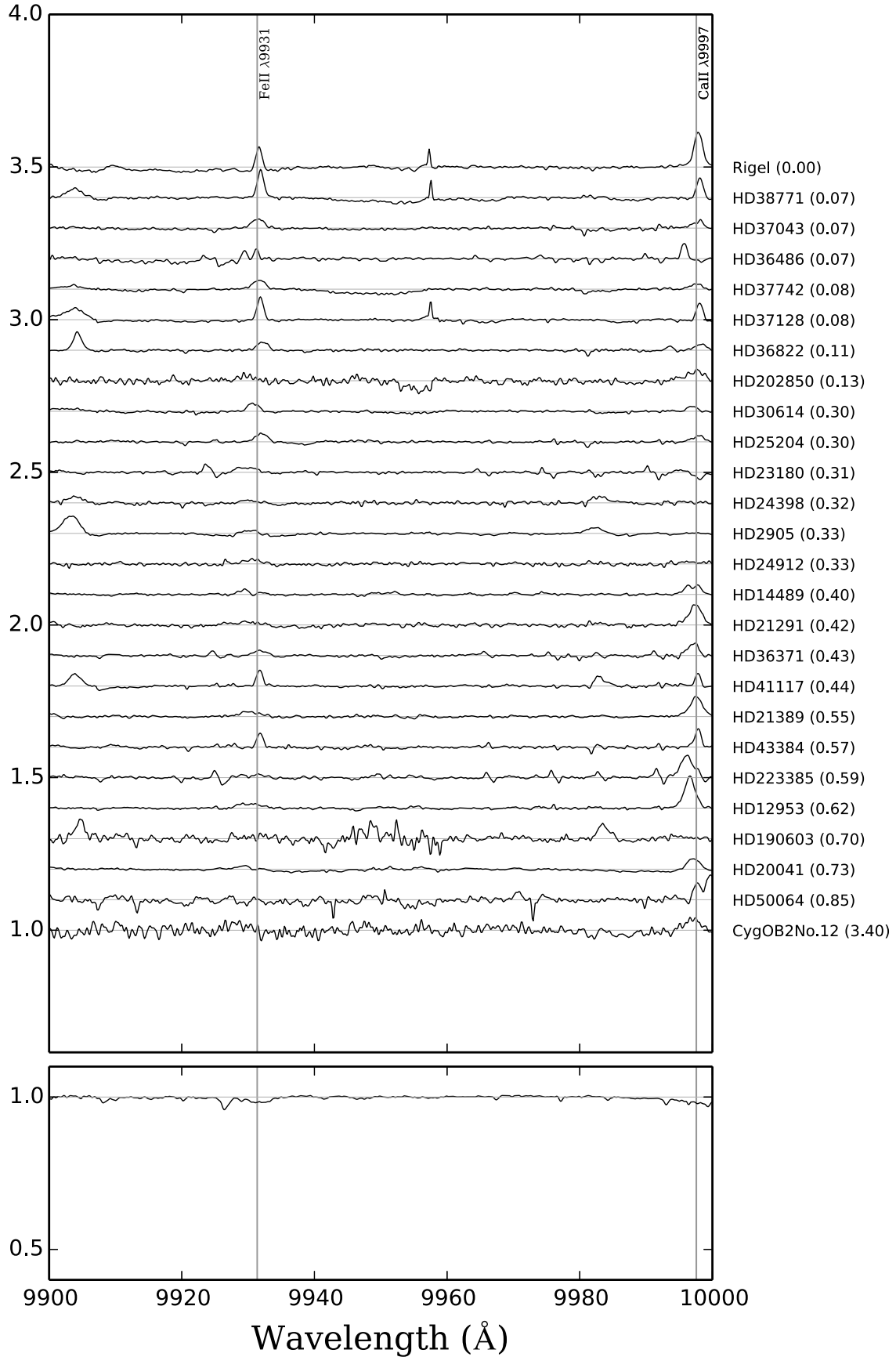
FeII λ9931
CaII λ9997
Rigel (0.00)
HD38771 (0.07)
HD37043 (0.07)
HD36486 (0.07)
HD37742 (0.08)
HD37128 (0.08)
HD36822 (0.11)
HD202850 (0.13)
HD30614 (0.30)
HD25204 (0.30)
HD23180 (0.31)
HD24398 (0.32)
HD2905 (0.33)
HD24912 (0.33)
HD14489 (0.40)
HD21291 (0.42)
HD36371 (0.43)
HD41117 (0.44)
HD21389 (0.55)
HD43384 (0.57)
HD223385 (0.59)
HD12953 (0.62)
HD190603 (0.70)
HD20041 (0.73)
HD50064 (0.85)
CygOB2No.12 (3.40)
4.0
3.5
3.0
2.5
2.0
1.5
1.0
1.0
0.5
9900
9920
9940
9960
9980
10000
Wavelength (Å)

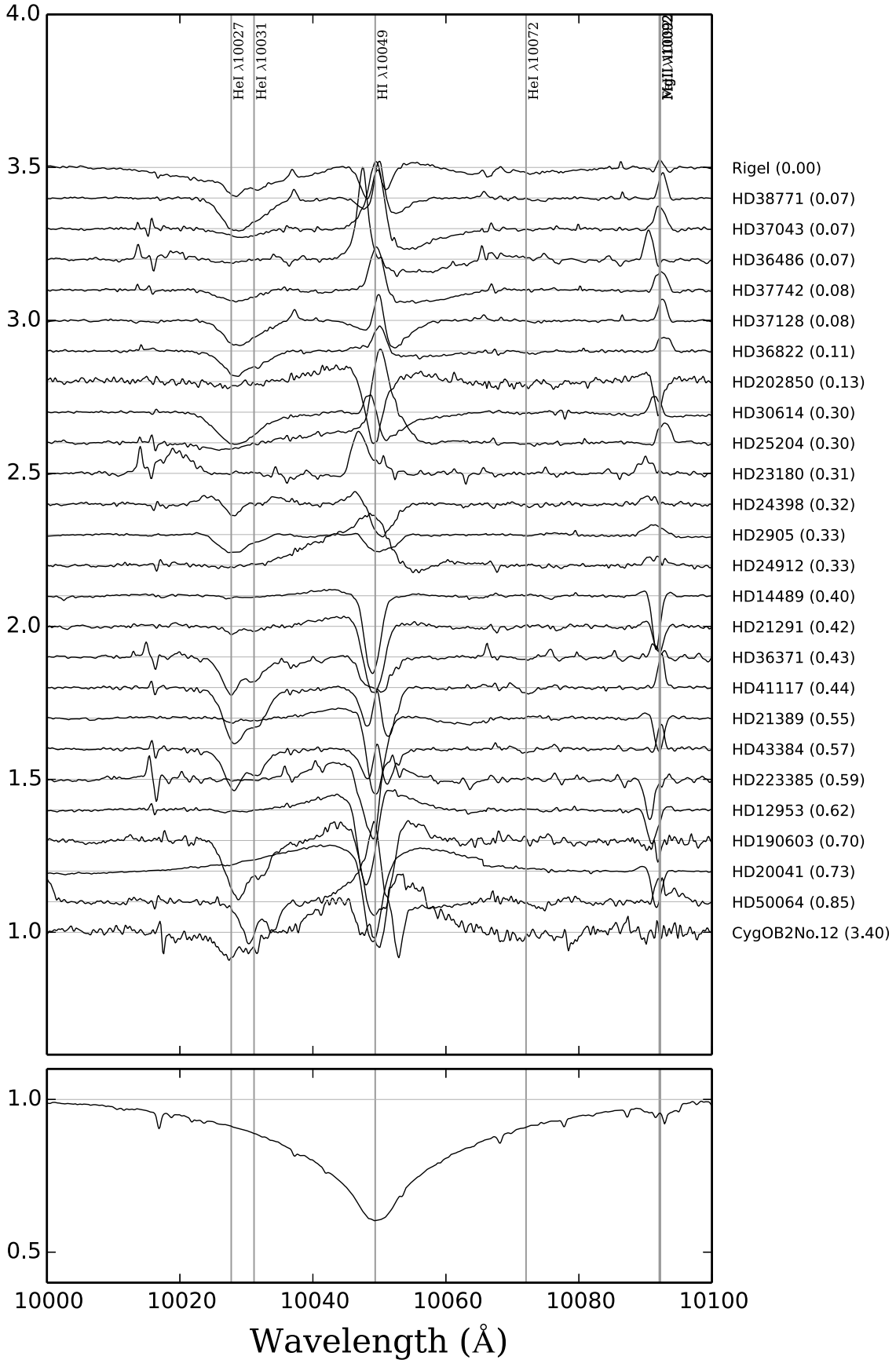
HeI λ10027
HeI λ10031
HI λ10049
HeI λ10072
MgII λ10092
Rigel (0.00)
HD38771 (0.07)
HD37043 (0.07)
HD36486 (0.07)
HD37742 (0.08)
HD37128 (0.08)
HD36822 (0.11)
HD202850 (0.13)
HD30614 (0.30)
HD25204 (0.30)
HD23180 (0.31)
HD24398 (0.32)
HD2905 (0.33)
HD24912 (0.33)
HD14489 (0.40)
HD21291 (0.42)
HD36371 (0.43)
HD41117 (0.44)
HD21389 (0.55)
HD43384 (0.57)
HD223385 (0.59)
HD12953 (0.62)
HD190603 (0.70)
HD20041 (0.73)
HD50064 (0.85)
CygOB2No.12 (3.40)
4.0
3.5
3.0
2.5
2.0
1.5
1.0
1.0
0.5
10000
10020
10040
10060
10080
10100
Wavelength (Å)

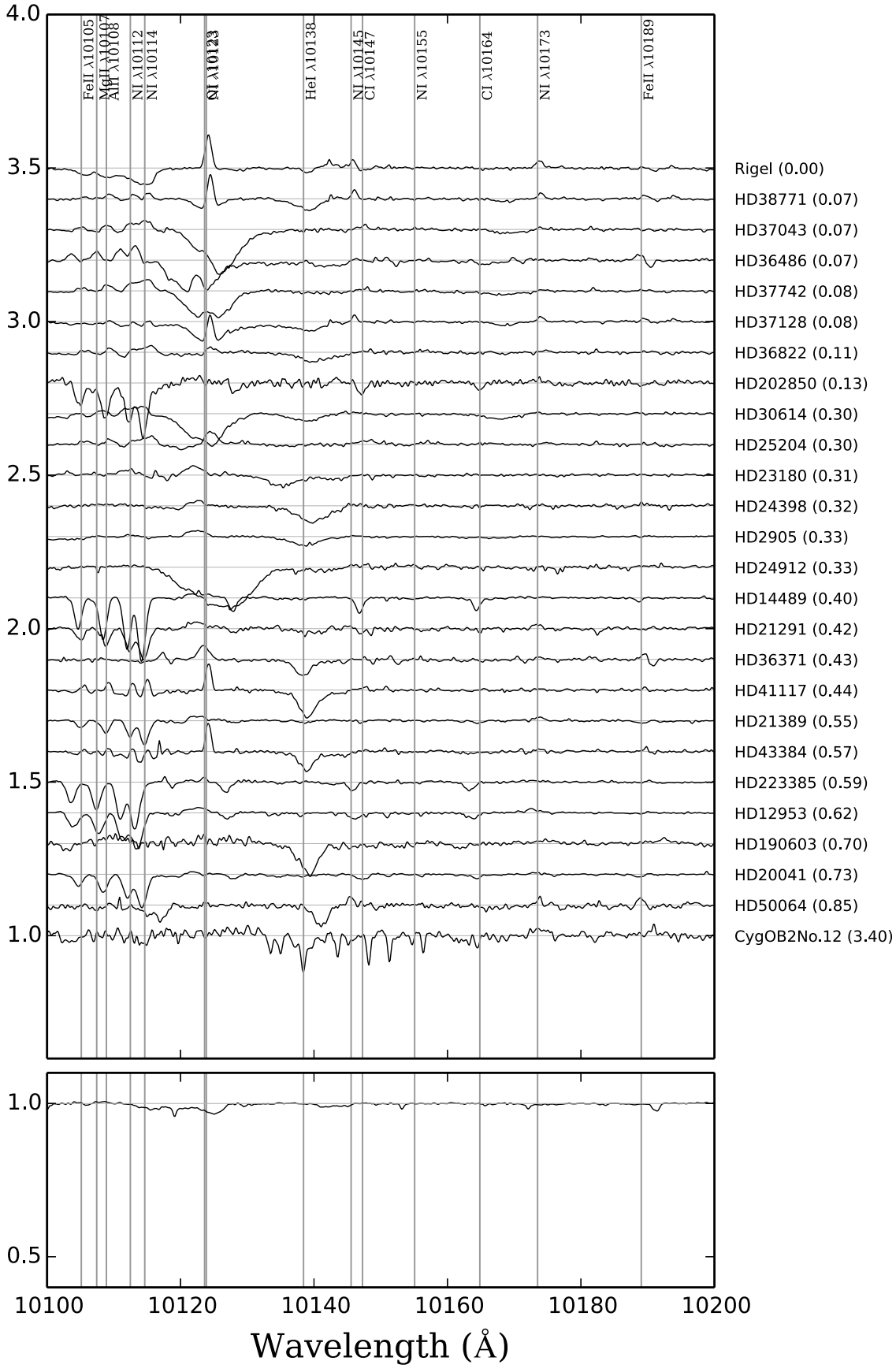
FeII λ10105
MgII λ10107
AlII λ10108
NI λ10112
NI λ10114
HeI λ10138
NI λ10145
CI λ10147
NI λ10155
CI λ10164
NI λ10173
FeII λ10189
Rigel (0.00)
HD38771 (0.07)
HD37043 (0.07)
HD36486 (0.07)
HD37742 (0.08)
HD37128 (0.08)
HD36822 (0.11)
HD202850 (0.13)
HD30614 (0.30)
HD25204 (0.30)
HD23180 (0.31)
HD24398 (0.32)
HD2905 (0.33)
HD24912 (0.33)
HD14489 (0.40)
HD21291 (0.42)
HD36371 (0.43)
HD41117 (0.44)
HD21389 (0.55)
HD43384 (0.57)
HD223385 (0.59)
HD12953 (0.62)
HD190603 (0.70)
HD20041 (0.73)
HD50064 (0.85)
CygOB2No.12 (3.40)
4.0
3.5
3.0
2.5
2.0
1.5
1.0
1.0
0.5
10100
10120
10140
10160
10180
10200
Wavelength (Å)

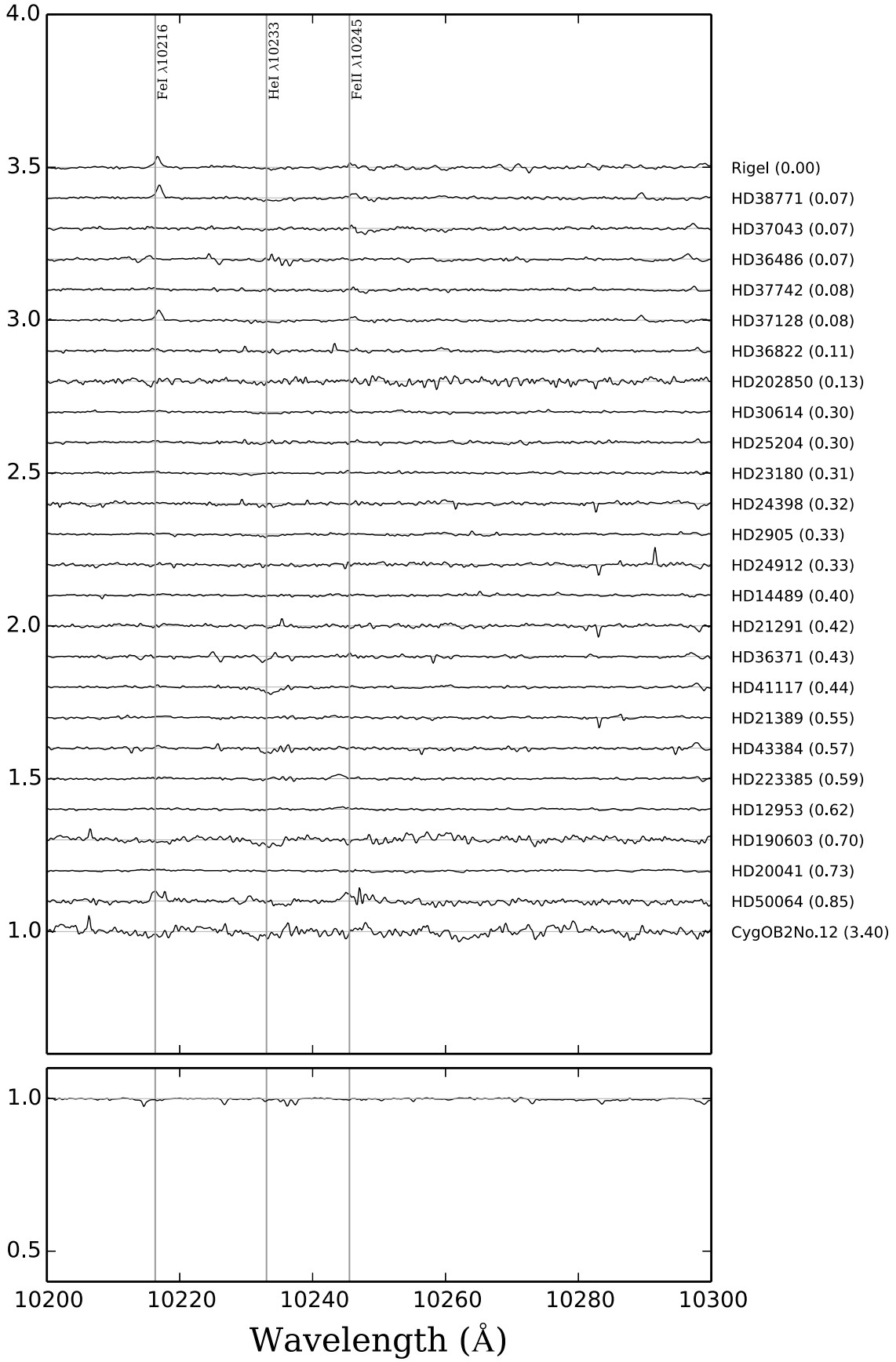
FeI λ10216
HeI λ10233
FeII λ10245
Rigel (0.00)
HD38771 (0.07)
HD37043 (0.07)
HD36486 (0.07)
HD37742 (0.08)
HD37128 (0.08)
HD36822 (0.11)
HD202850 (0.13)
HD30614 (0.30)
HD25204 (0.30)
HD23180 (0.31)
HD24398 (0.32)
HD2905 (0.33)
HD24912 (0.33)
HD14489 (0.40)
HD21291 (0.42)
HD36371 (0.43)
HD41117 (0.44)
HD21389 (0.55)
HD43384 (0.57)
HD223385 (0.59)
HD12953 (0.62)
HD190603 (0.70)
HD20041 (0.73)
HD50064 (0.85)
CygOB2No.12 (3.40)
4.0
3.5
3.0
2.5
2.0
1.5
1.0
1.0
0.5
10200
10220
10240
10260
10280
10300
Wavelength (Å)

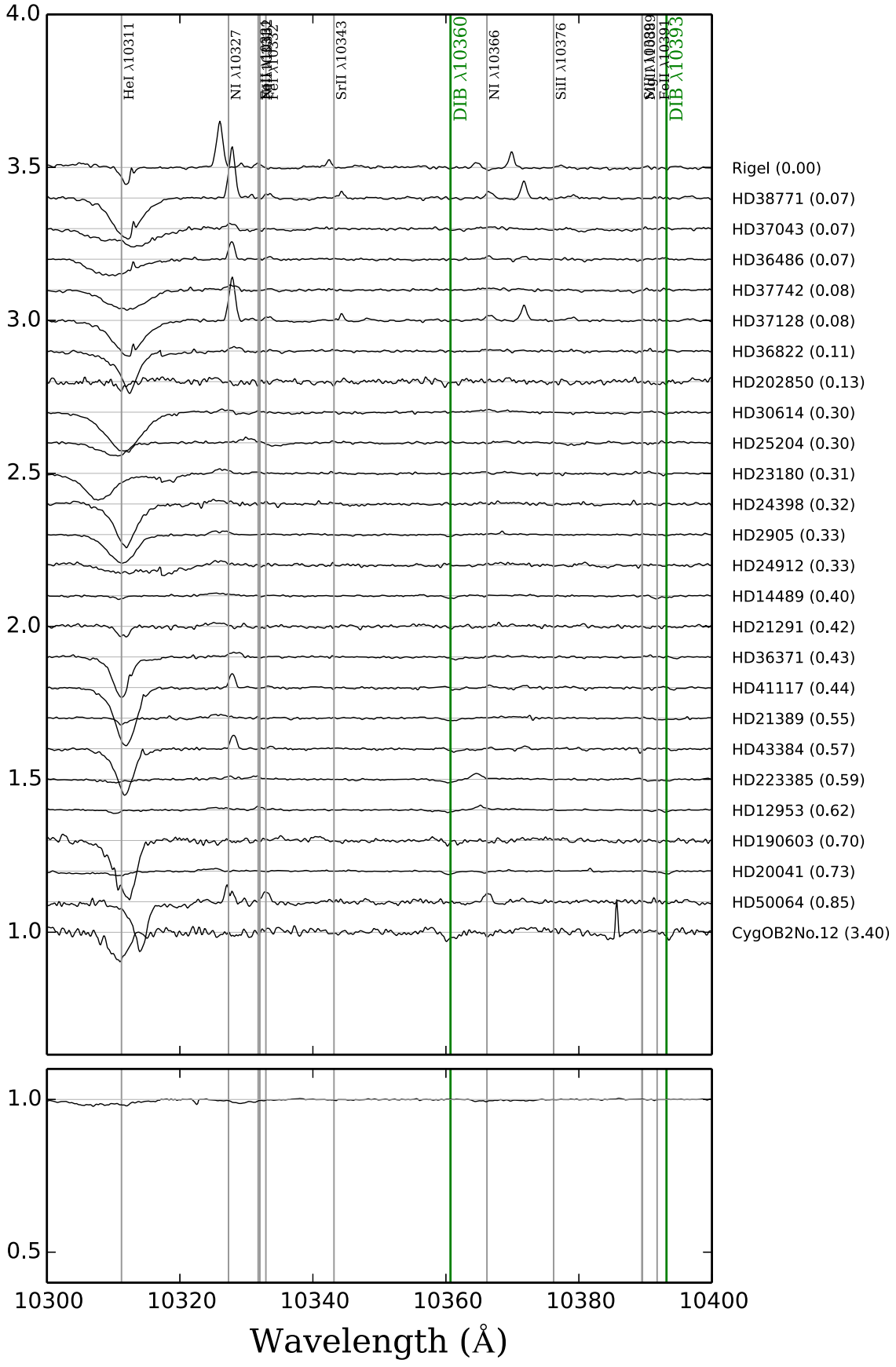
HeI λ10311
NI λ10327
SrII λ10343
DIB λ10360
NI λ10366
SiII λ10376
FeII λ10391
DIB λ10393
Rigel (0.00)
HD38771 (0.07)
HD37043 (0.07)
HD36486 (0.07)
HD37742 (0.08)
HD37128 (0.08)
HD36822 (0.11)
HD202850 (0.13)
HD30614 (0.30)
HD25204 (0.30)
HD23180 (0.31)
HD24398 (0.32)
HD2905 (0.33)
HD24912 (0.33)
HD14489 (0.40)
HD21291 (0.42)
HD36371 (0.43)
HD41117 (0.44)
HD21389 (0.55)
HD43384 (0.57)
HD223385 (0.59)
HD12953 (0.62)
HD190603 (0.70)
HD20041 (0.73)
HD50064 (0.85)
CygOB2No.12 (3.40)
4.0
3.5
3.0
2.5
2.0
1.5
1.0
1.0
0.5
10300
10320
10340
10360
10380
10400
Wavelength (Å)

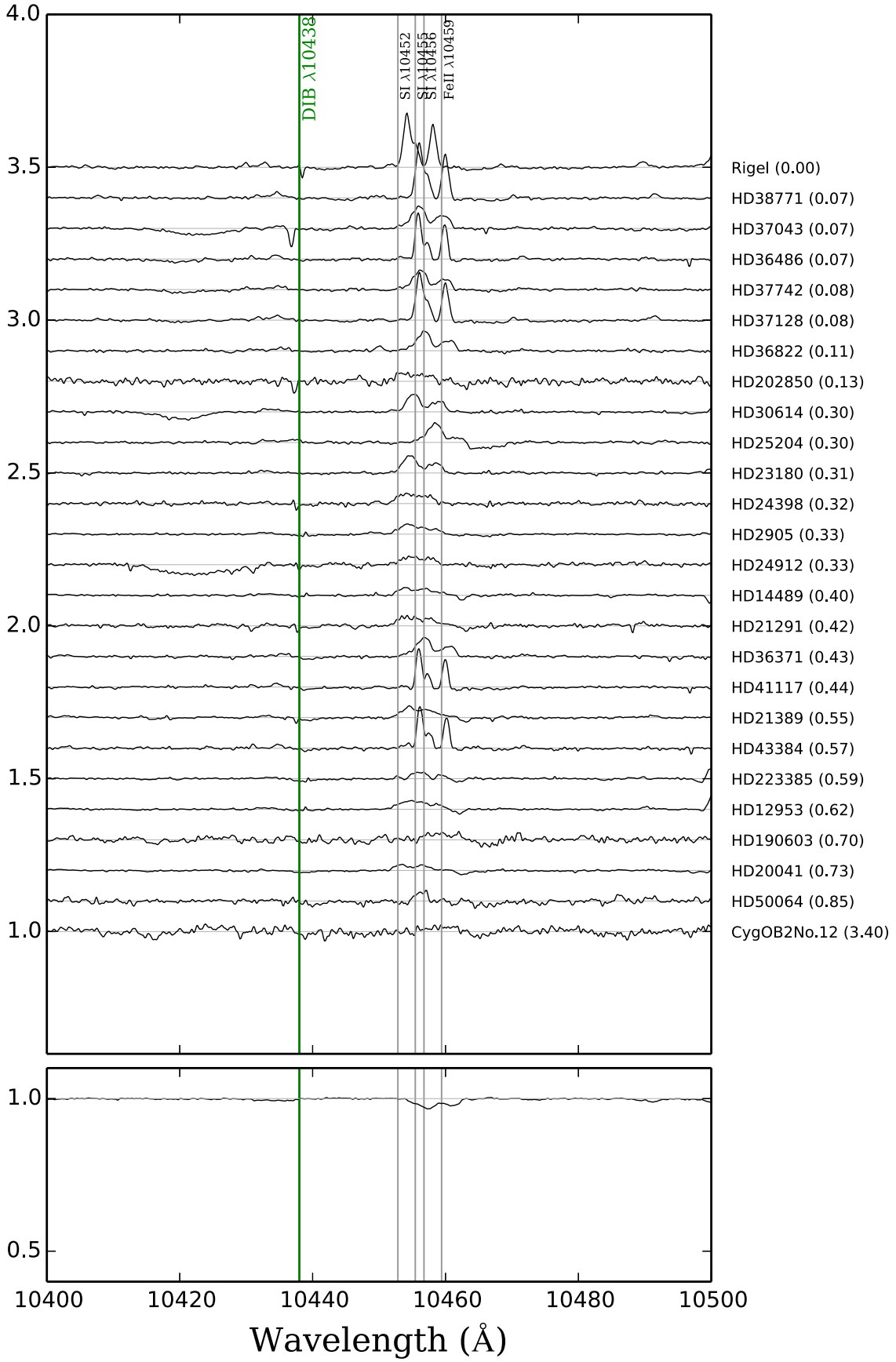
DIB λ10438
SI λ10452
SI λ10455
SI λ10456
FeII λ10459
Rigel (0.00)
HD38771 (0.07)
HD37043 (0.07)
HD36486 (0.07)
HD37742 (0.08)
HD37128 (0.08)
HD36822 (0.11)
HD202850 (0.13)
HD30614 (0.30)
HD25204 (0.30)
HD23180 (0.31)
HD24398 (0.32)
HD2905 (0.33)
HD24912 (0.33)
HD14489 (0.40)
HD21291 (0.42)
HD36371 (0.43)
HD41117 (0.44)
HD21389 (0.55)
HD43384 (0.57)
HD223385 (0.59)
HD12953 (0.62)
HD190603 (0.70)
HD20041 (0.73)
HD50064 (0.85)
CygOB2No.12 (3.40)
4.0
3.5
3.0
2.5
2.0
1.5
1.0
1.0
0.5
10400
10420
10440
10460
10480
10500
Wavelength (Å)

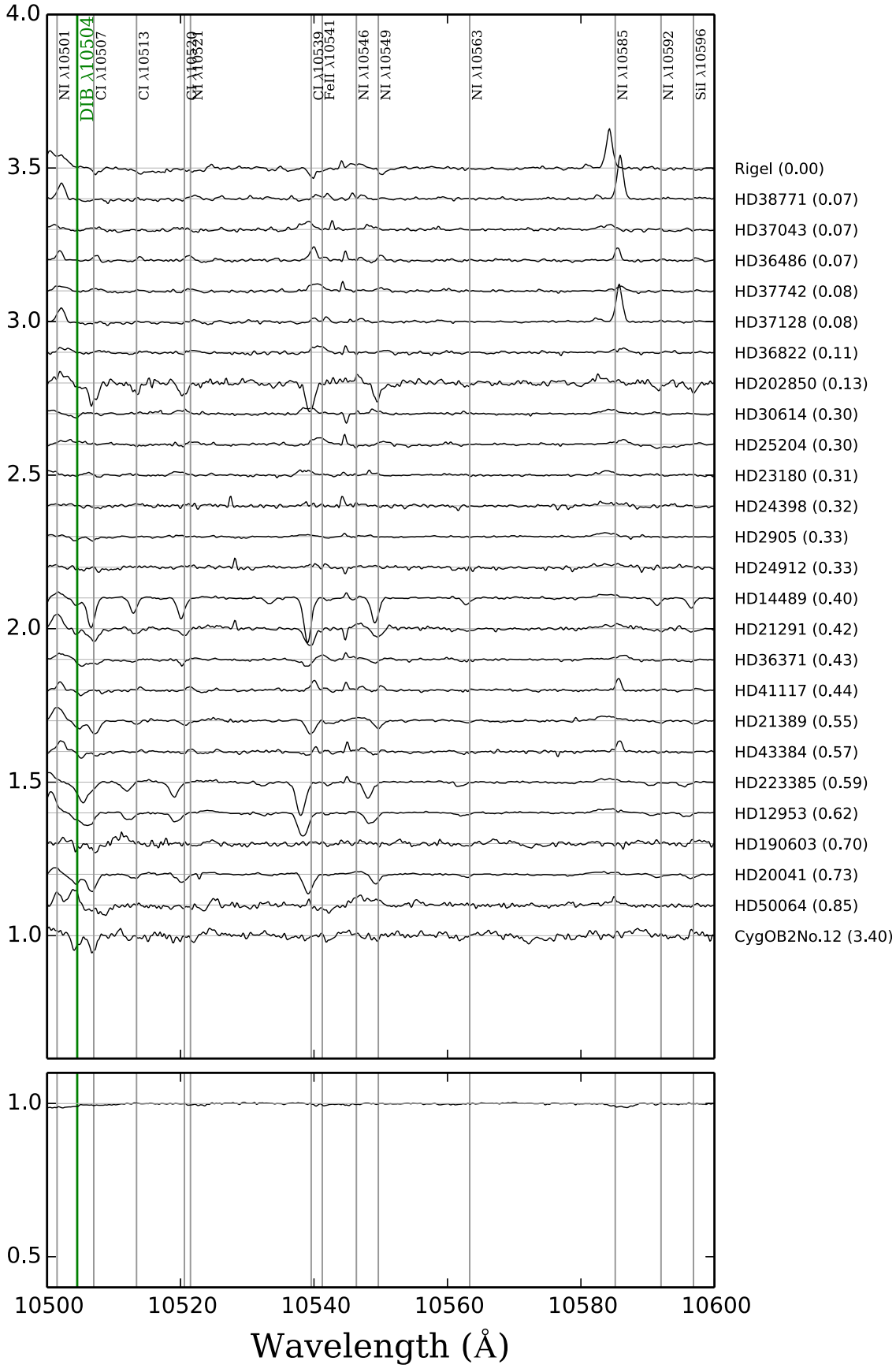
NI λ10501
DIB λ10504
CI λ10507
CI λ10513
CI λ10520
KI λ10521
CI λ10539
FeII λ10541
NI λ10546
NI λ10549
NI λ10563
NI λ10585
NI λ10592
SiI λ10596
Rigel (0.00)
HD38771 (0.07)
HD37043 (0.07)
HD36486 (0.07)
HD37742 (0.08)
HD37128 (0.08)
HD36822 (0.11)
HD202850 (0.13)
HD30614 (0.30)
HD25204 (0.30)
HD23180 (0.31)
HD24398 (0.32)
HD2905 (0.33)
HD24912 (0.33)
HD14489 (0.40)
HD21291 (0.42)
HD36371 (0.43)
HD41117 (0.44)
HD21389 (0.55)
HD43384 (0.57)
HD223385 (0.59)
HD12953 (0.62)
HD190603 (0.70)
HD20041 (0.73)
HD50064 (0.85)
CygOB2No.12 (3.40)
4.0
3.5
3.0
2.5
2.0
1.5
1.0
1.0
0.5
10500
10520
10540
10560
10580
10600
Wavelength (Å)

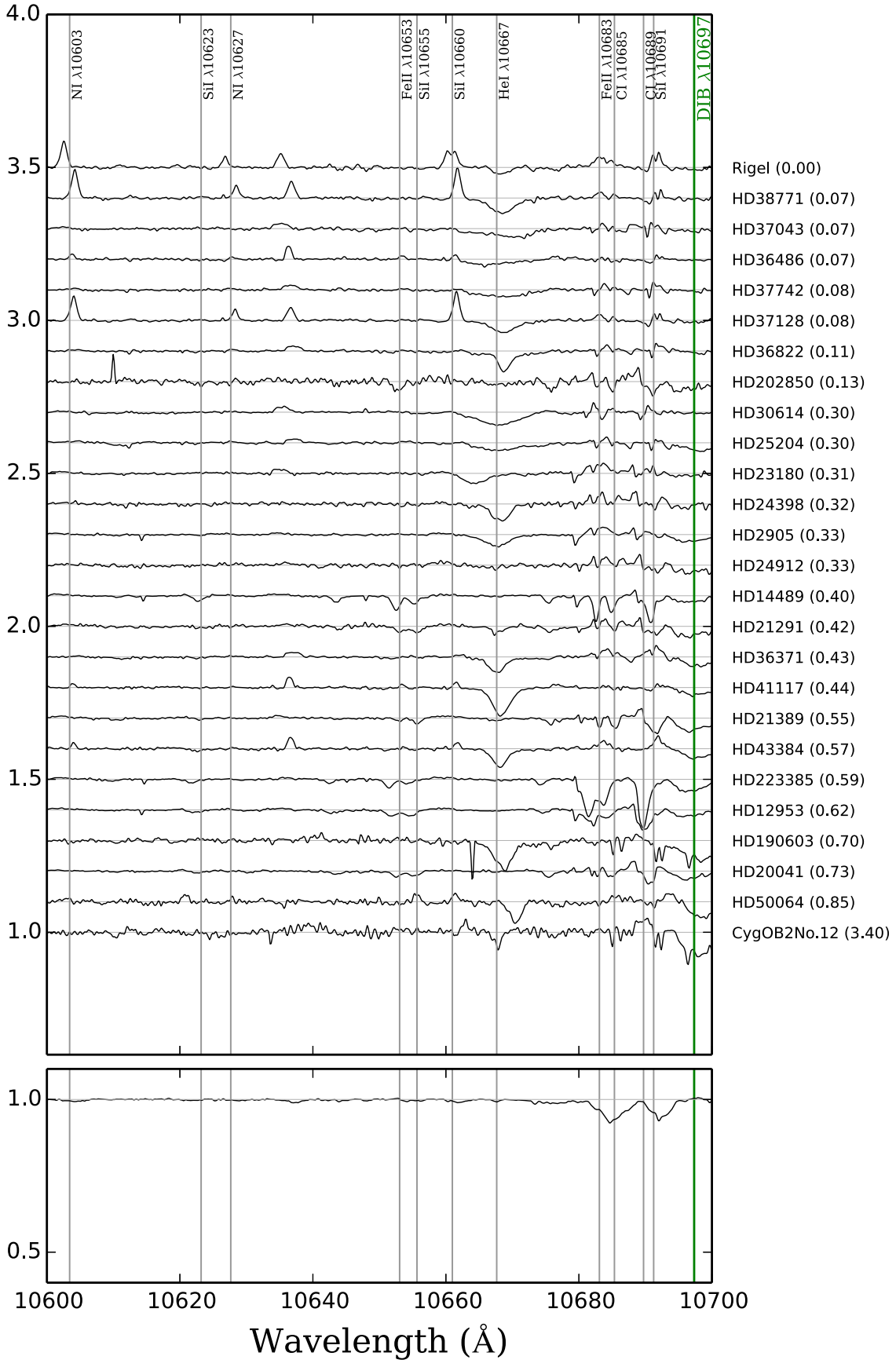
NI λ10603
SiI λ10623
NI λ10627
FeII λ10653
SiI λ10655
SiI λ10660
HeI λ10667
FeII λ10683
CI λ10685
CI λ10689
SiI λ10691
DIB λ10697
Rigel (0.00)
HD38771 (0.07)
HD37043 (0.07)
HD36486 (0.07)
HD37742 (0.08)
HD37128 (0.08)
HD36822 (0.11)
HD202850 (0.13)
HD30614 (0.30)
HD25204 (0.30)
HD23180 (0.31)
HD24398 (0.32)
HD2905 (0.33)
HD24912 (0.33)
HD14489 (0.40)
HD21291 (0.42)
HD36371 (0.43)
HD41117 (0.44)
HD21389 (0.55)
HD43384 (0.57)
HD223385 (0.59)
HD12953 (0.62)
HD190603 (0.70)
HD20041 (0.73)
HD50064 (0.85)
CygOB2No.12 (3.40)
4.0
3.5
3.0
2.5
2.0
1.5
1.0
1.0
0.5
10600
10620
10640
10660
10680
10700
Wavelength (Å)

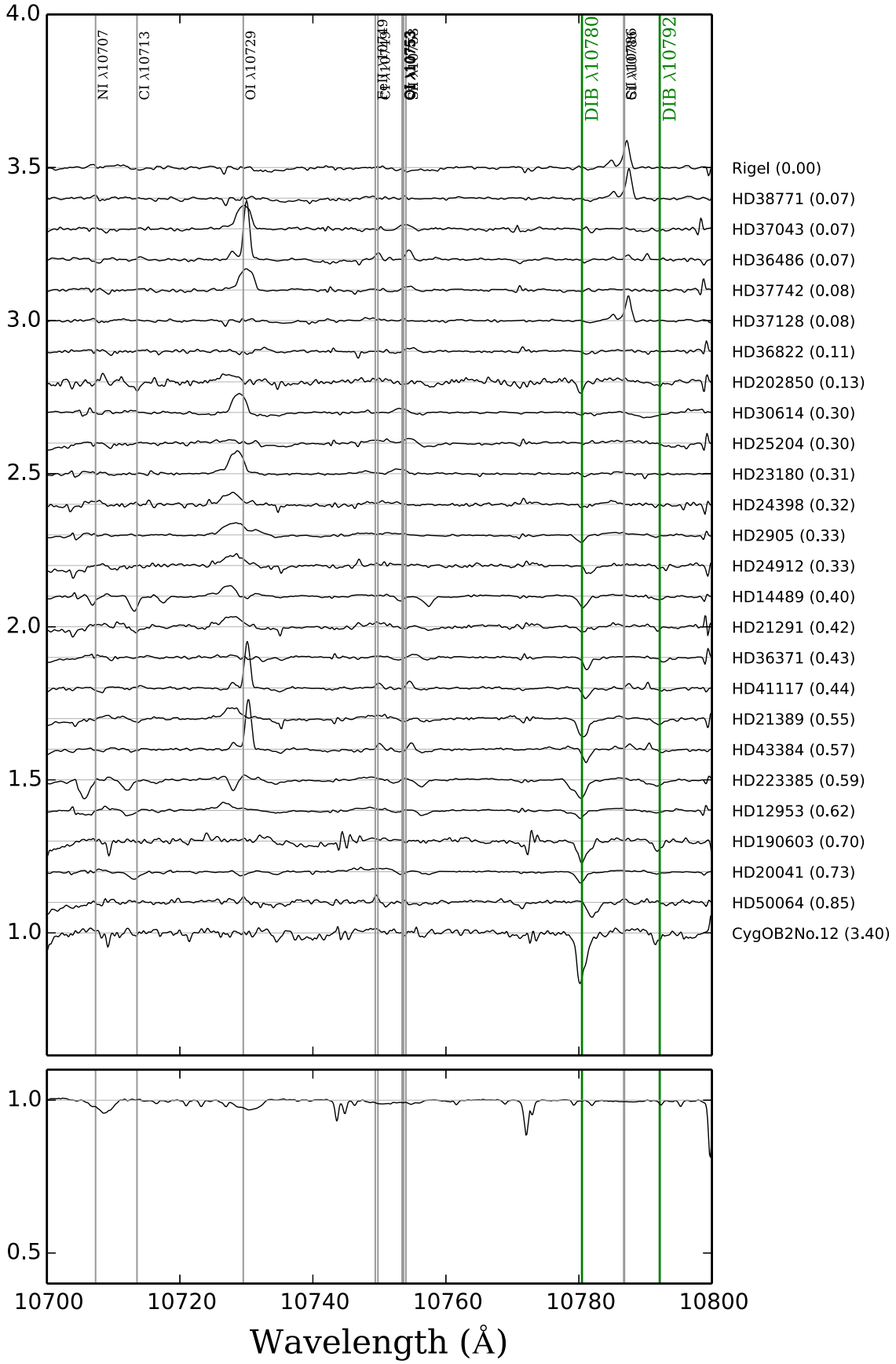
NI λ10707
CI λ10713
OI λ10729
DIB λ10780
DIB λ10792
Rigel (0.00)
HD38771 (0.07)
HD37043 (0.07)
HD36486 (0.07)
HD37742 (0.08)
HD37128 (0.08)
HD36822 (0.11)
HD202850 (0.13)
HD30614 (0.30)
HD25204 (0.30)
HD23180 (0.31)
HD24398 (0.32)
HD2905 (0.33)
HD24912 (0.33)
HD14489 (0.40)
HD21291 (0.42)
HD36371 (0.43)
HD41117 (0.44)
HD21389 (0.55)
HD43384 (0.57)
HD223385 (0.59)
HD12953 (0.62)
HD190603 (0.70)
HD20041 (0.73)
HD50064 (0.85)
CygOB2No.12 (3.40)
4.0
3.5
3.0
2.5
2.0
1.5
1.0
1.0
0.5
10700
10720
10740
10760
10780
10800
Wavelength (Å)

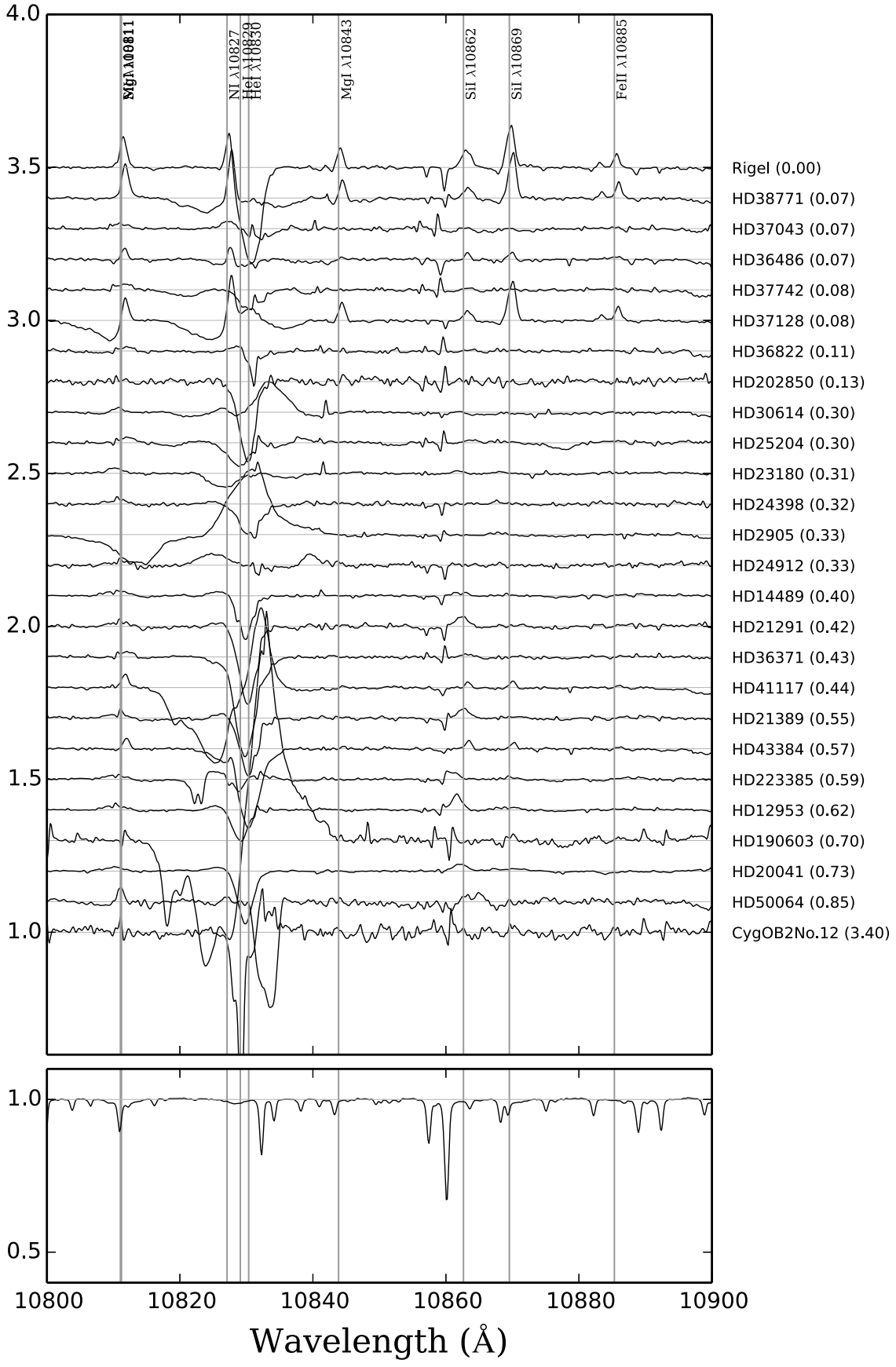
4.0
3.5
3.0
2.5
2.0
1.5
1.0
1.0
0.5
10800
10820
10840
10860
10880
10900
Wavelength (Å)
MgI λ10811
NI λ10827
HeI λ10830
MgI λ10843
SiI λ10862
SiI λ10869
FeII λ10885
Rigel (0.00)
HD38771 (0.07)
HD37043 (0.07)
HD36486 (0.07)
HD37742 (0.08)
HD37128 (0.08)
HD36822 (0.11)
HD202850 (0.13)
HD30614 (0.30)
HD25204 (0.30)
HD23180 (0.31)
HD24398 (0.32)
HD2905 (0.33)
HD24912 (0.33)
HD14489 (0.40)
HD21291 (0.42)
HD36371 (0.43)
HD41117 (0.44)
HD21389 (0.55)
HD43384 (0.57)
HD223385 (0.59)
HD12953 (0.62)
HD190603 (0.70)
HD20041 (0.73)
HD50064 (0.85)
CygOB2No.12 (3.40)

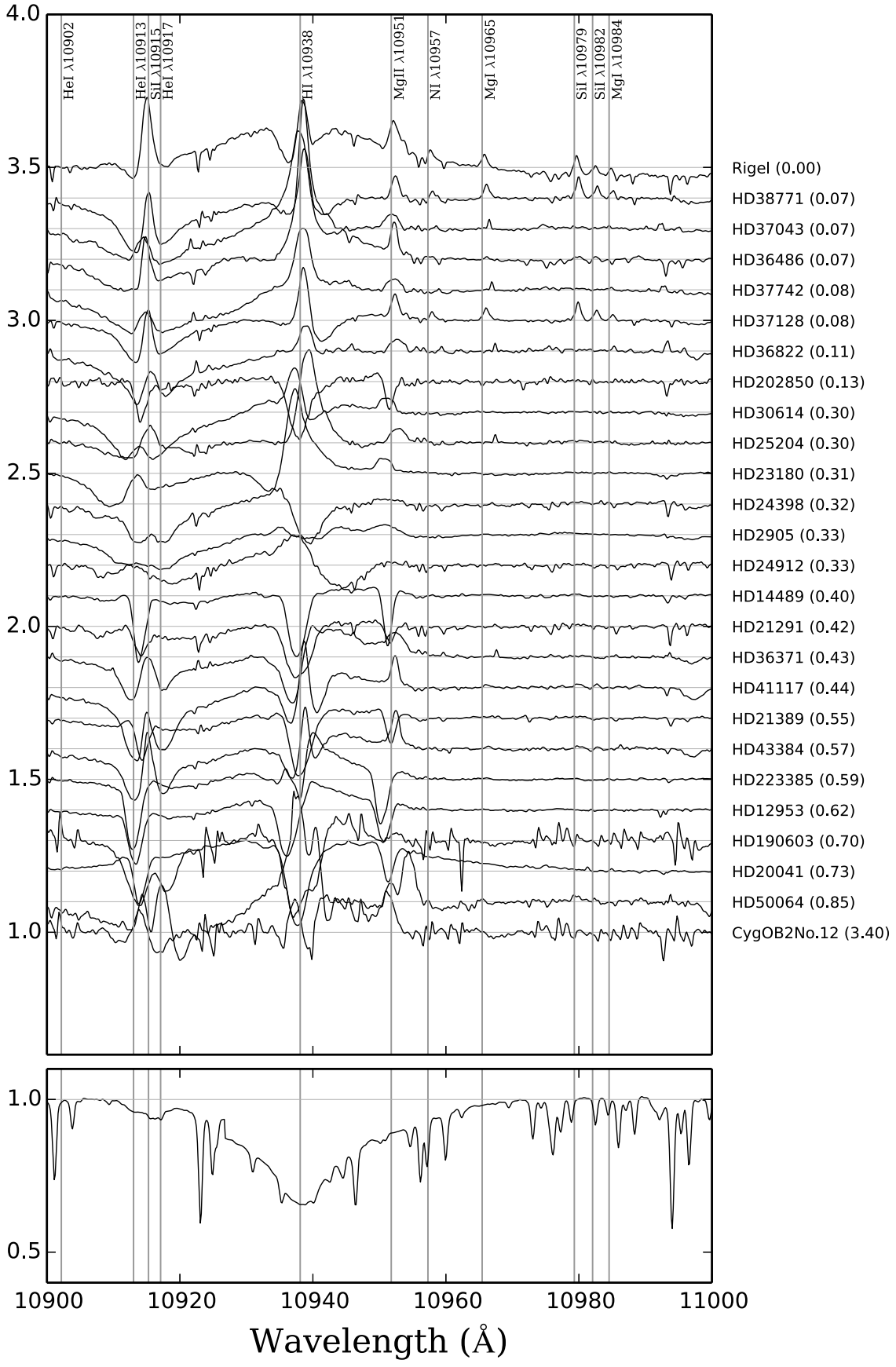
HeI λ10902
HeI λ10913
SiI λ10915
HeI λ10917
HI λ10938
MgII λ10951
NI λ10957
MgI λ10965
SiI λ10979
SiI λ10982
MgI λ10984
Rigel (0.00)
HD38771 (0.07)
HD37043 (0.07)
HD36486 (0.07)
HD37742 (0.08)
HD37128 (0.08)
HD36822 (0.11)
HD202850 (0.13)
HD30614 (0.30)
HD25204 (0.30)
HD23180 (0.31)
HD24398 (0.32)
HD2905 (0.33)
HD24912 (0.33)
HD14489 (0.40)
HD21291 (0.42)
HD36371 (0.43)
HD41117 (0.44)
HD21389 (0.55)
HD43384 (0.57)
HD223385 (0.59)
HD12953 (0.62)
HD190603 (0.70)
HD20041 (0.73)
HD50064 (0.85)
CygOB2No.12 (3.40)
4.0
3.5
3.0
2.5
2.0
1.5
1.0
1.0
0.5
10900
10920
10940
10960
10980
11000
Wavelength (Å)

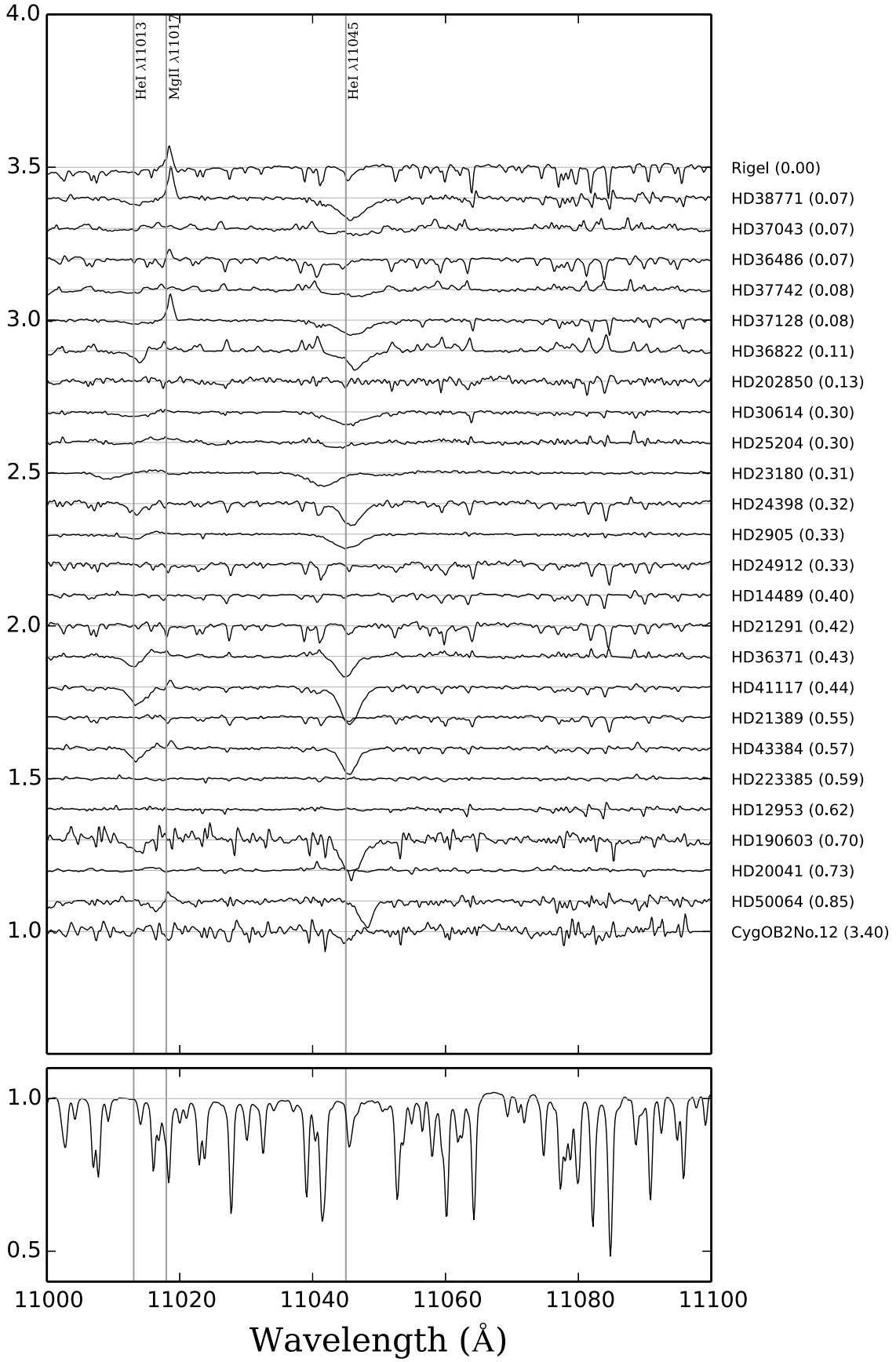
HeI λ11013
MgII λ11017
HeI λ11045
Rigel (0.00)
HD38771 (0.07)
HD37043 (0.07)
HD36486 (0.07)
HD37742 (0.08)
HD37128 (0.08)
HD36822 (0.11)
HD202850 (0.13)
HD30614 (0.30)
HD25204 (0.30)
HD23180 (0.31)
HD24398 (0.32)
HD2905 (0.33)
HD24912 (0.33)
HD14489 (0.40)
HD21291 (0.42)
HD36371 (0.43)
HD41117 (0.44)
HD21389 (0.55)
HD43384 (0.57)
HD223385 (0.59)
HD12953 (0.62)
HD190603 (0.70)
HD20041 (0.73)
HD50064 (0.85)
CygOB2No.12 (3.40)
4.0
3.5
3.0
2.5
2.0
1.5
1.0
1.0
0.5
11000
11020
11040
11060
11080
11100
Wavelength (Å)

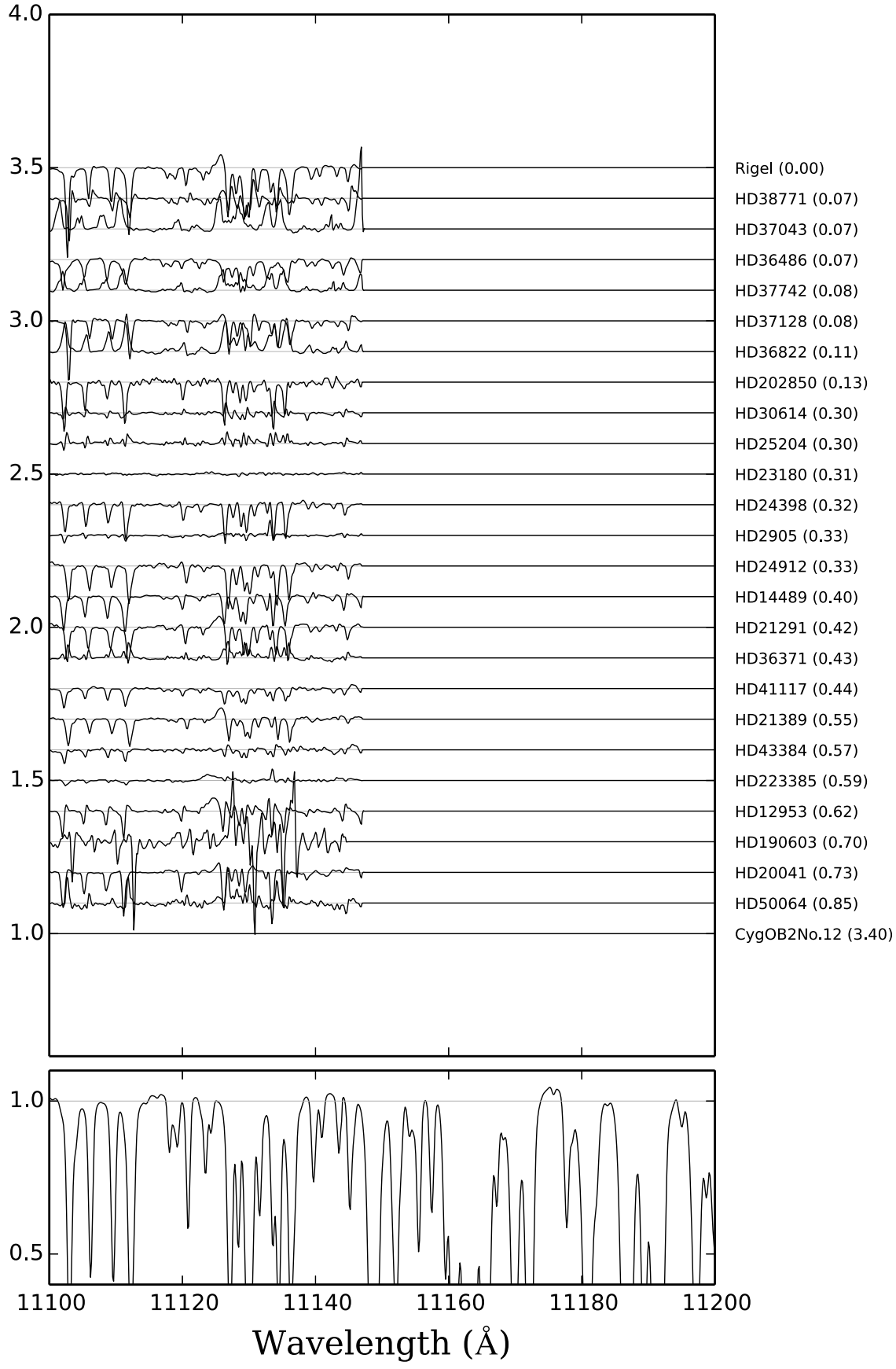
4.0
3.5
3.0
2.5
2.0
1.5
1.0
1.0
0.5
11100
11120
11140
11160
11180
11200
Wavelength (Å)
Rigel (0.00)
HD38771 (0.07)
HD37043 (0.07)
HD36486 (0.07)
HD37742 (0.08)
HD37128 (0.08)
HD36822 (0.11)
HD202850 (0.13)
HD30614 (0.30)
HD25204 (0.30)
HD23180 (0.31)
HD24398 (0.32)
HD2905 (0.33)
HD24912 (0.33)
HD14489 (0.40)
HD21291 (0.42)
HD36371 (0.43)
HD41117 (0.44)
HD21389 (0.55)
HD43384 (0.57)
HD223385 (0.59)
HD12953 (0.62)
HD190603 (0.70)
HD20041 (0.73)
HD50064 (0.85)
CygOB2No.12 (3.40)

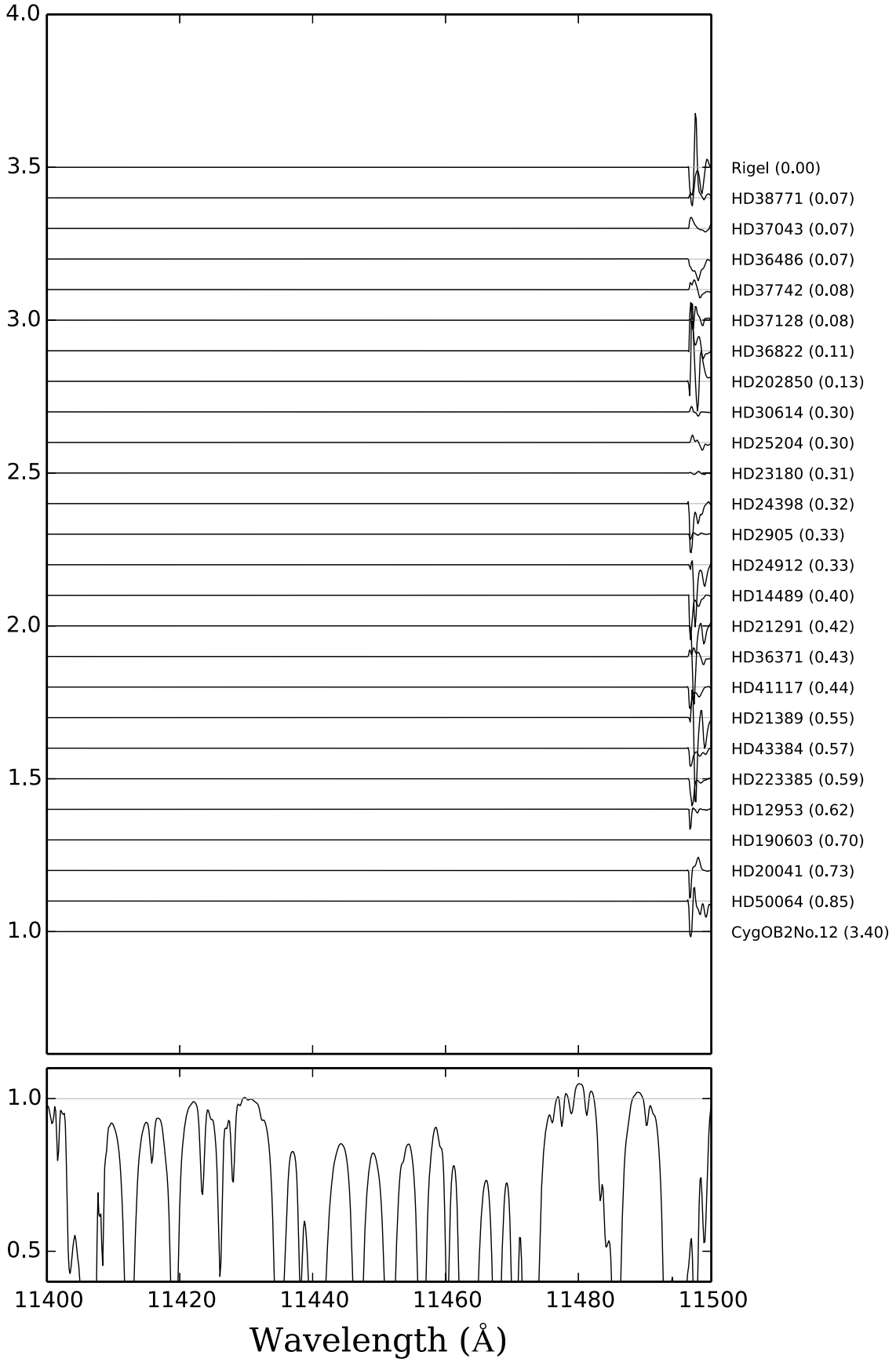
4.0
3.5
3.0
2.5
2.0
1.5
1.0
Rigel (0.00)
HD38771 (0.07)
HD37043 (0.07)
HD36486 (0.07)
HD37742 (0.08)
HD37128 (0.08)
HD36822 (0.11)
HD202850 (0.13)
HD30614 (0.30)
HD25204 (0.30)
HD23180 (0.31)
HD24398 (0.32)
HD2905 (0.33)
HD24912 (0.33)
HD14489 (0.40)
HD21291 (0.42)
HD36371 (0.43)
HD41117 (0.44)
HD21389 (0.55)
HD43384 (0.57)
HD223385 (0.59)
HD12953 (0.62)
HD190603 (0.70)
HD20041 (0.73)
HD50064 (0.85)
CygOB2No.12 (3.40)
1.0
0.5
11400
11420
11440
11460
11480
11500
Wavelength (Å)


4.0
3.5
3.0
2.5
2.0
1.5
1.0
1.0
0.5
11500
11520
11540
11560
11580
11600
Wavelength (Å)
Rigel (0.00)
HD38771 (0.07)
HD37043 (0.07)
HD36486 (0.07)
HD37742 (0.08)
HD37128 (0.08)
HD36822 (0.11)
HD202850 (0.13)
HD30614 (0.30)
HD25204 (0.30)
HD23180 (0.31)
HD24398 (0.32)
HD2905 (0.33)
HD24912 (0.33)
HD14489 (0.40)
HD21291 (0.42)
HD36371 (0.43)
HD41117 (0.44)
HD21389 (0.55)
HD43384 (0.57)
HD223385 (0.59)
HD12953 (0.62)
HD190603 (0.70)
HD20041 (0.73)
HD50064 (0.85)
CygOB2No.12 (3.40)

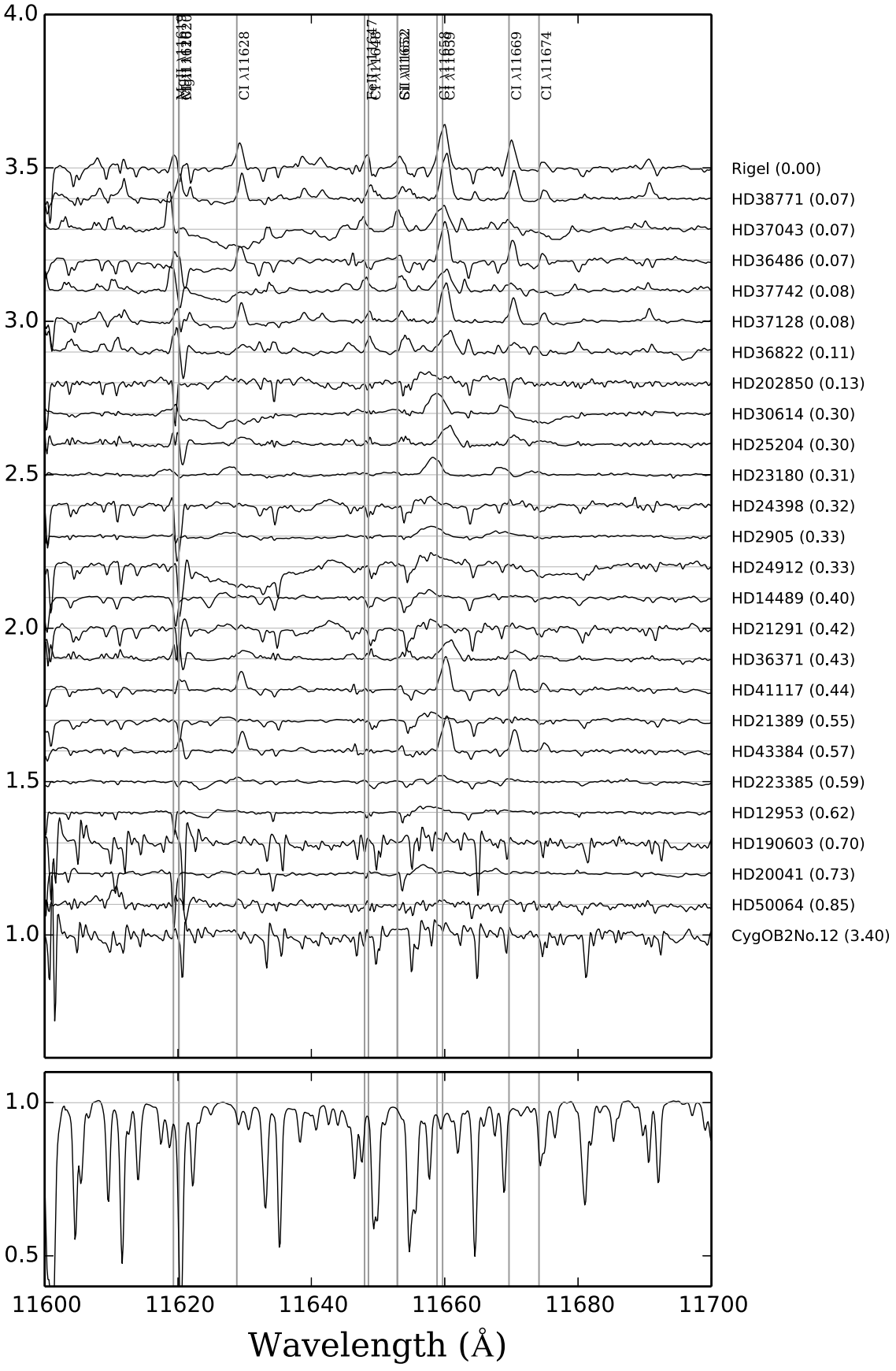
Cl λ11628
Cl λ11669
Cl λ11674
Rigel (0.00)
HD38771 (0.07)
HD37043 (0.07)
HD36486 (0.07)
HD37742 (0.08)
HD37128 (0.08)
HD36822 (0.11)
HD202850 (0.13)
HD30614 (0.30)
HD25204 (0.30)
HD23180 (0.31)
HD24398 (0.32)
HD2905 (0.33)
HD24912 (0.33)
HD14489 (0.40)
HD21291 (0.42)
HD36371 (0.43)
HD41117 (0.44)
HD21389 (0.55)
HD43384 (0.57)
HD223385 (0.59)
HD12953 (0.62)
HD190603 (0.70)
HD20041 (0.73)
HD50064 (0.85)
CygOB2No.12 (3.40)
4.0
3.5
3.0
2.5
2.0
1.5
1.0
0.5
11600
11620
11640
11660
11680
11700
Wavelength (Å)

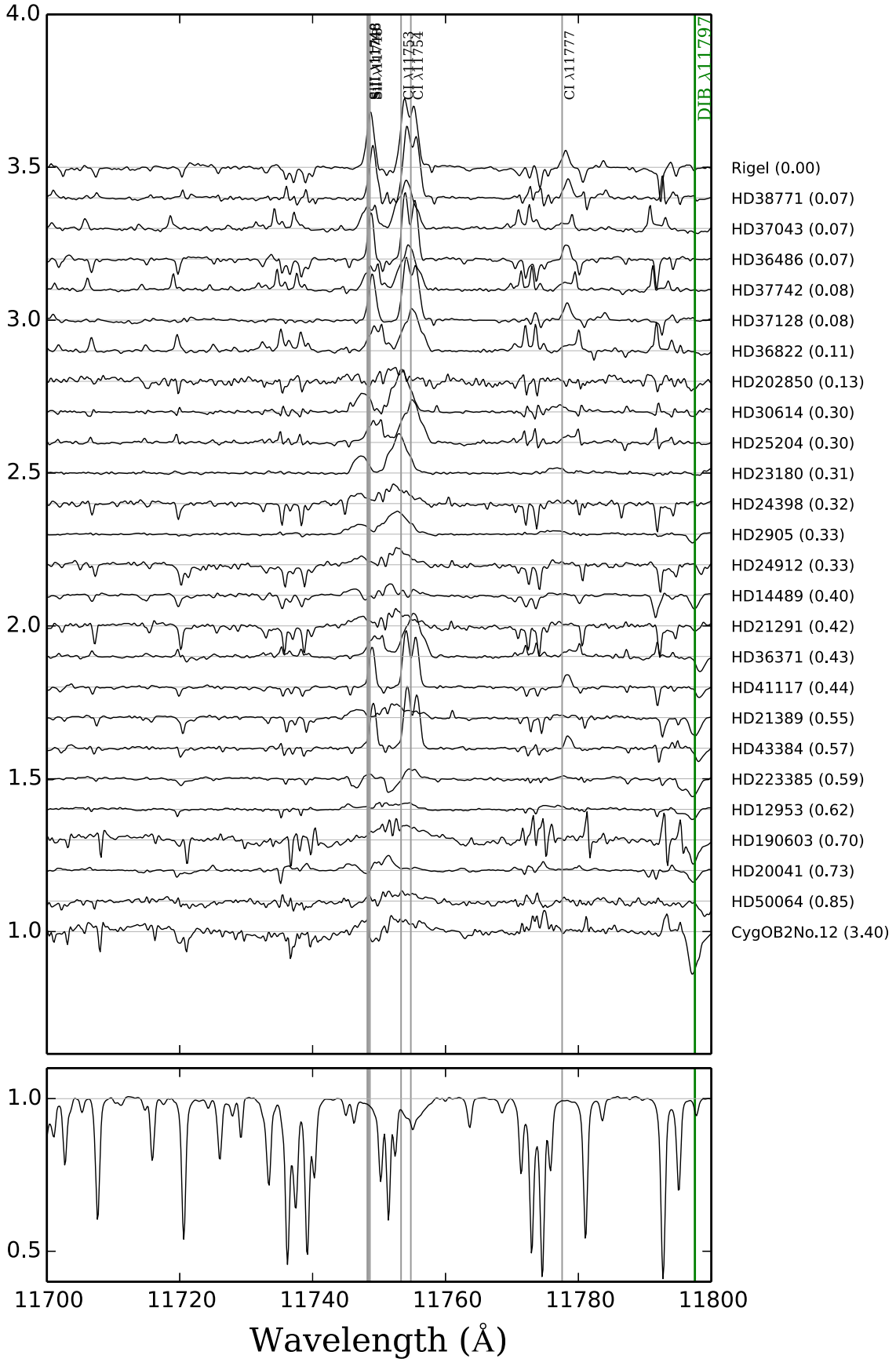
4.0
3.5
3.0
2.5
2.0
1.5
1.0
1.0
0.5
11700
11720
11740
11760
11780
11800
Wavelength (Å)
Si I λ11748
Si I λ11748
Si I λ11748
Cl I λ11753
Cl I λ11754
Cl I λ11777
DIB λ11797
Rigel (0.00)
HD38771 (0.07)
HD37043 (0.07)
HD36486 (0.07)
HD37742 (0.08)
HD37128 (0.08)
HD36822 (0.11)
HD202850 (0.13)
HD30614 (0.30)
HD25204 (0.30)
HD23180 (0.31)
HD24398 (0.32)
HD2905 (0.33)
HD24912 (0.33)
HD14489 (0.40)
HD21291 (0.42)
HD36371 (0.43)
HD41117 (0.44)
HD21389 (0.55)
HD43384 (0.57)
HD223385 (0.59)
HD12953 (0.62)
HD190603 (0.70)
HD20041 (0.73)
HD50064 (0.85)
CygOB2No.12 (3.40)

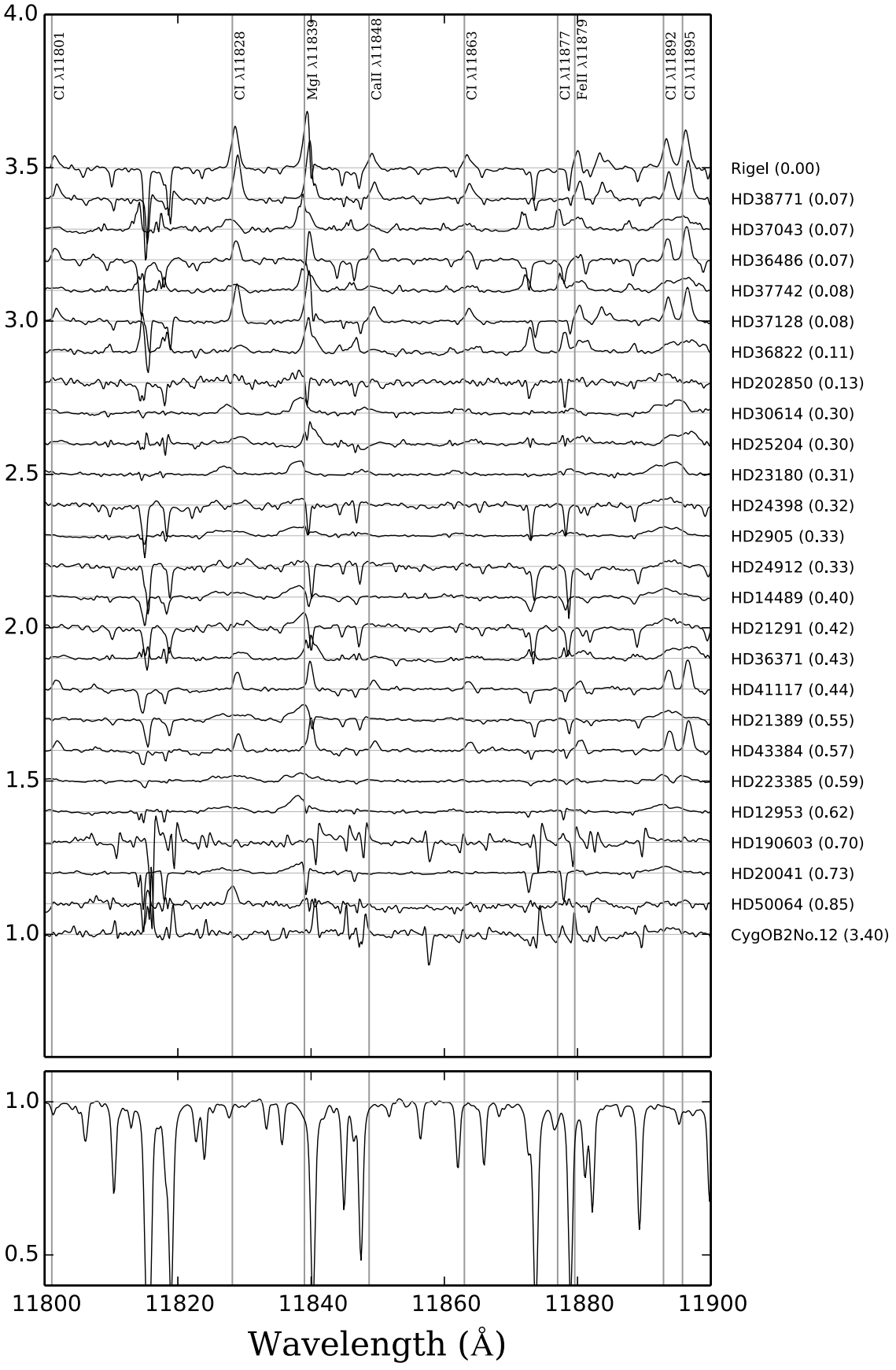
CI λ11801
CI λ11828
MgI λ11839
CaII λ11848
CI λ11863
CI λ11877
FeII λ11879
CI λ11892
CI λ11895
Rigel (0.00)
HD38771 (0.07)
HD37043 (0.07)
HD36486 (0.07)
HD37742 (0.08)
HD37128 (0.08)
HD36822 (0.11)
HD202850 (0.13)
HD30614 (0.30)
HD25204 (0.30)
HD23180 (0.31)
HD24398 (0.32)
HD2905 (0.33)
HD24912 (0.33)
HD14489 (0.40)
HD21291 (0.42)
HD36371 (0.43)
HD41117 (0.44)
HD21389 (0.55)
HD43384 (0.57)
HD223385 (0.59)
HD12953 (0.62)
HD190603 (0.70)
HD20041 (0.73)
HD50064 (0.85)
CygOB2No.12 (3.40)
4.0
3.5
3.0
2.5
2.0
1.5
1.0
1.0
0.5
11800
11820
11840
11860
11880
11900
Wavelength (Å)

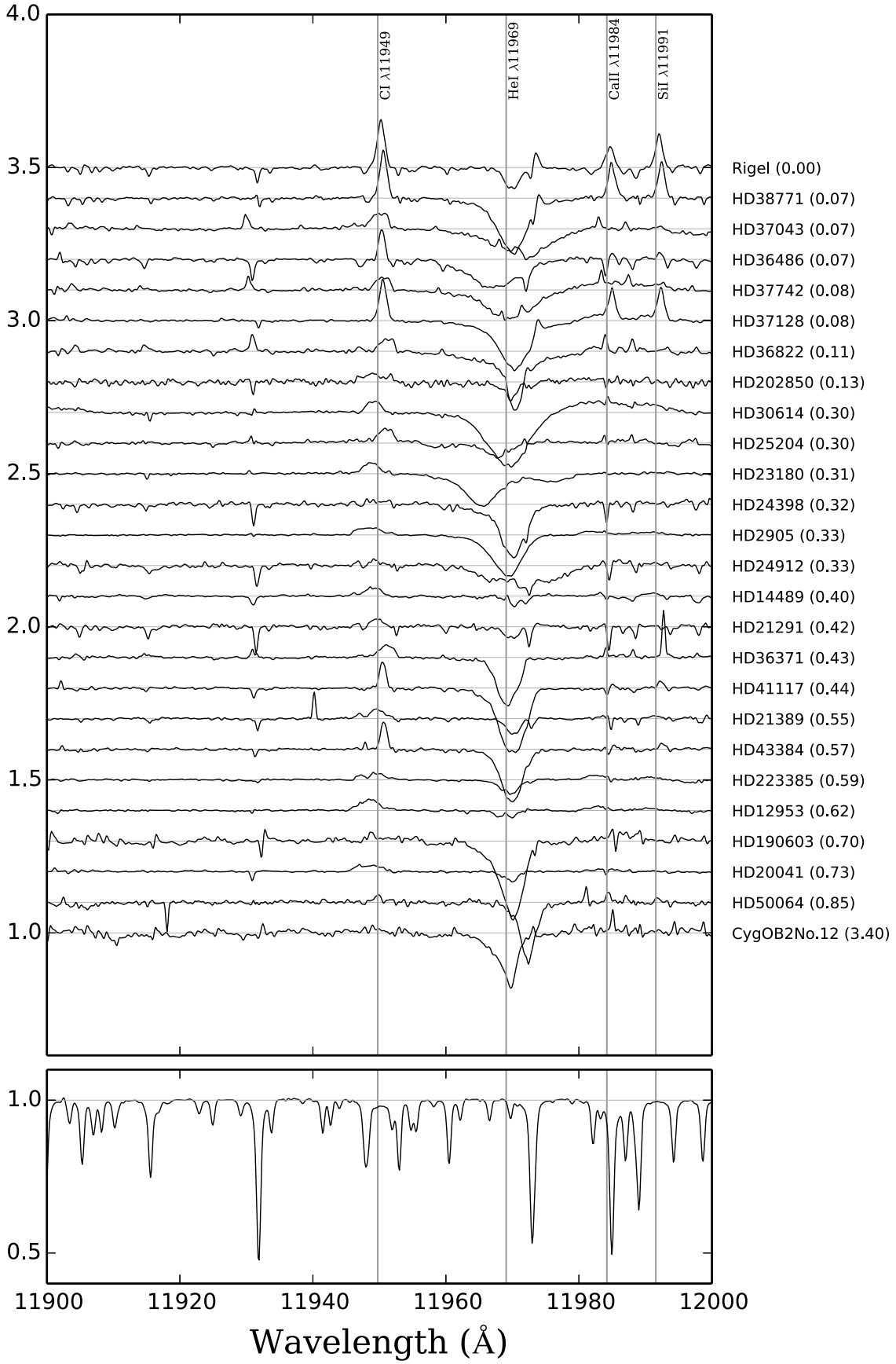
CI λ11949
HeI λ11969
CaII λ11984
SiI λ11991
Rigel (0.00)
HD38771 (0.07)
HD37043 (0.07)
HD36486 (0.07)
HD37742 (0.08)
HD37128 (0.08)
HD36822 (0.11)
HD202850 (0.13)
HD30614 (0.30)
HD25204 (0.30)
HD23180 (0.31)
HD24398 (0.32)
HD2905 (0.33)
HD24912 (0.33)
HD14489 (0.40)
HD21291 (0.42)
HD36371 (0.43)
HD41117 (0.44)
HD21389 (0.55)
HD43384 (0.57)
HD223385 (0.59)
HD12953 (0.62)
HD190603 (0.70)
HD20041 (0.73)
HD50064 (0.85)
CygOB2No.12 (3.40)
4.0
3.5
3.0
2.5
2.0
1.5
1.0
1.0
0.5
11900
11920
11940
11960
11980
12000
Wavelength (Å)

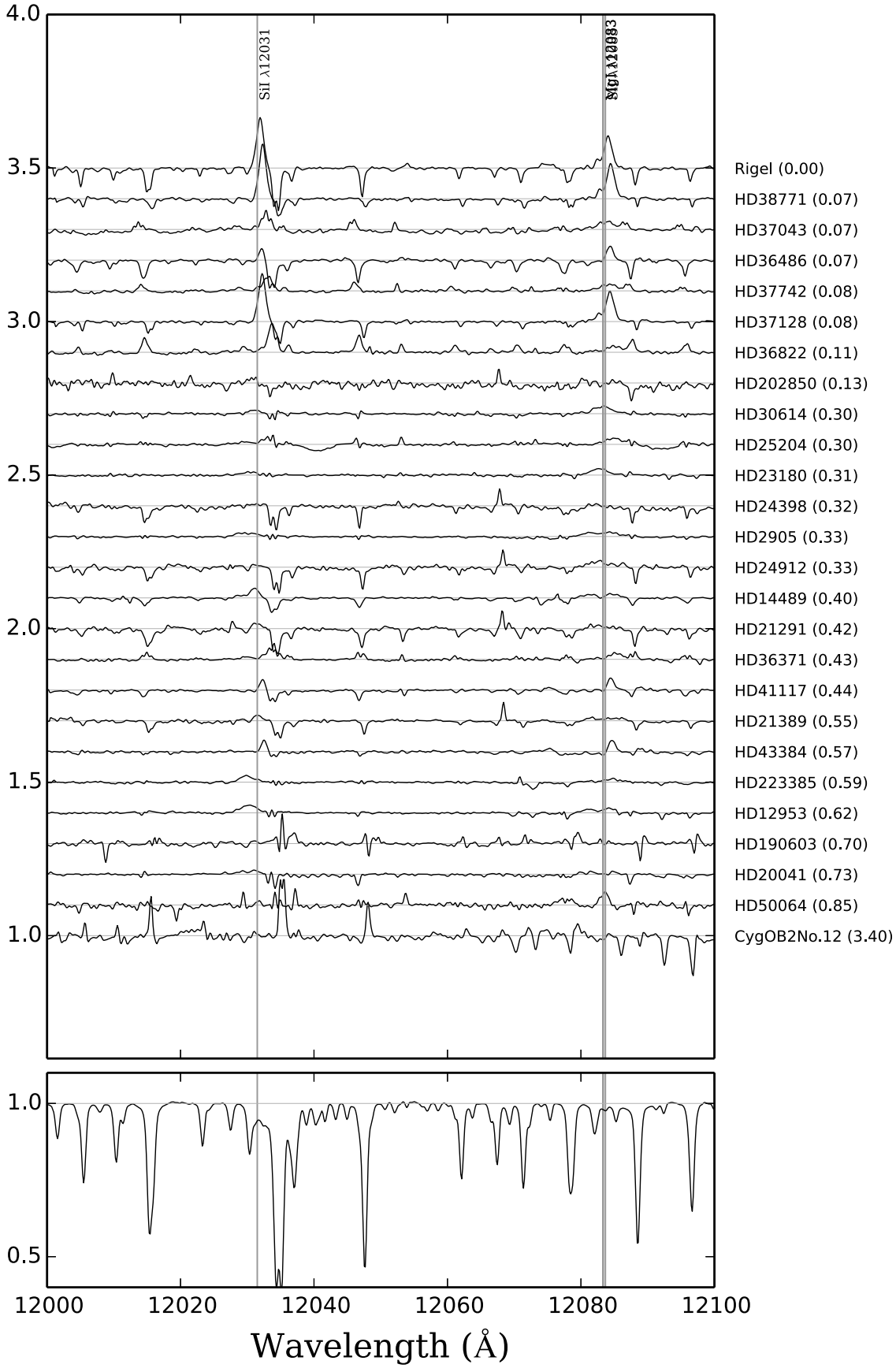
SiI λ12031
MgI λ12083
Rigel (0.00)
HD38771 (0.07)
HD37043 (0.07)
HD36486 (0.07)
HD37742 (0.08)
HD37128 (0.08)
HD36822 (0.11)
HD202850 (0.13)
HD30614 (0.30)
HD25204 (0.30)
HD23180 (0.31)
HD24398 (0.32)
HD2905 (0.33)
HD24912 (0.33)
HD14489 (0.40)
HD21291 (0.42)
HD36371 (0.43)
HD41117 (0.44)
HD21389 (0.55)
HD43384 (0.57)
HD223385 (0.59)
HD12953 (0.62)
HD190603 (0.70)
HD20041 (0.73)
HD50064 (0.85)
CygOB2No.12 (3.40)
4.0
3.5
3.0
2.5
2.0
1.5
1.0
1.0
0.5
12000
12020
12040
12060
12080
12100
Wavelength (Å)

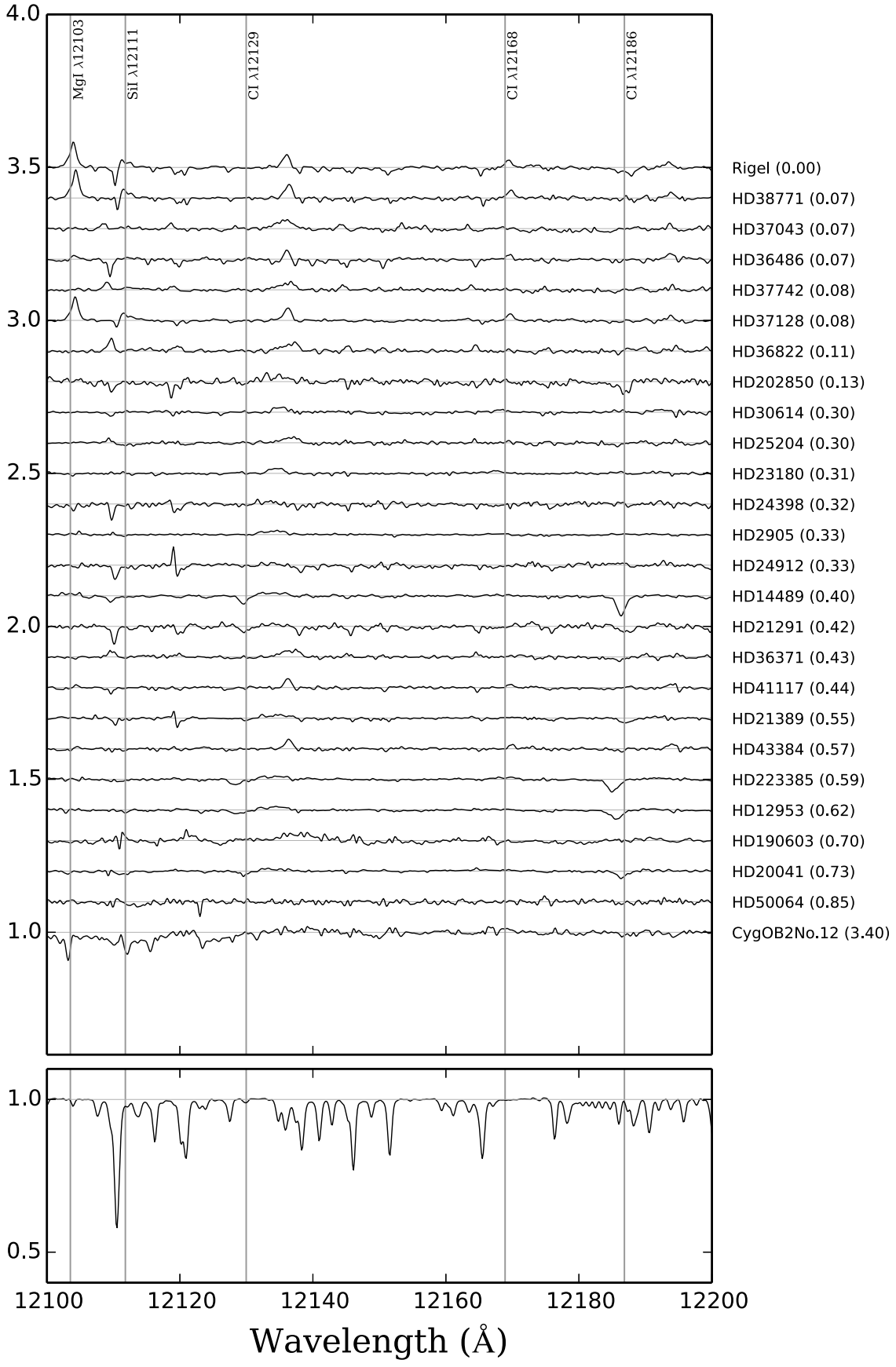
MgI λ12103
SiI λ12111
CI λ12129
CI λ12168
CI λ12186
Rigel (0.00)
HD38771 (0.07)
HD37043 (0.07)
HD36486 (0.07)
HD37742 (0.08)
HD37128 (0.08)
HD36822 (0.11)
HD202850 (0.13)
HD30614 (0.30)
HD25204 (0.30)
HD23180 (0.31)
HD24398 (0.32)
HD2905 (0.33)
HD24912 (0.33)
HD14489 (0.40)
HD21291 (0.42)
HD36371 (0.43)
HD41117 (0.44)
HD21389 (0.55)
HD43384 (0.57)
HD223385 (0.59)
HD12953 (0.62)
HD190603 (0.70)
HD20041 (0.73)
HD50064 (0.85)
CygOB2No.12 (3.40)
4.0
3.5
3.0
2.5
2.0
1.5
1.0
1.0
0.5
12100
12120
12140
12160
12180
12200
Wavelength (Å)

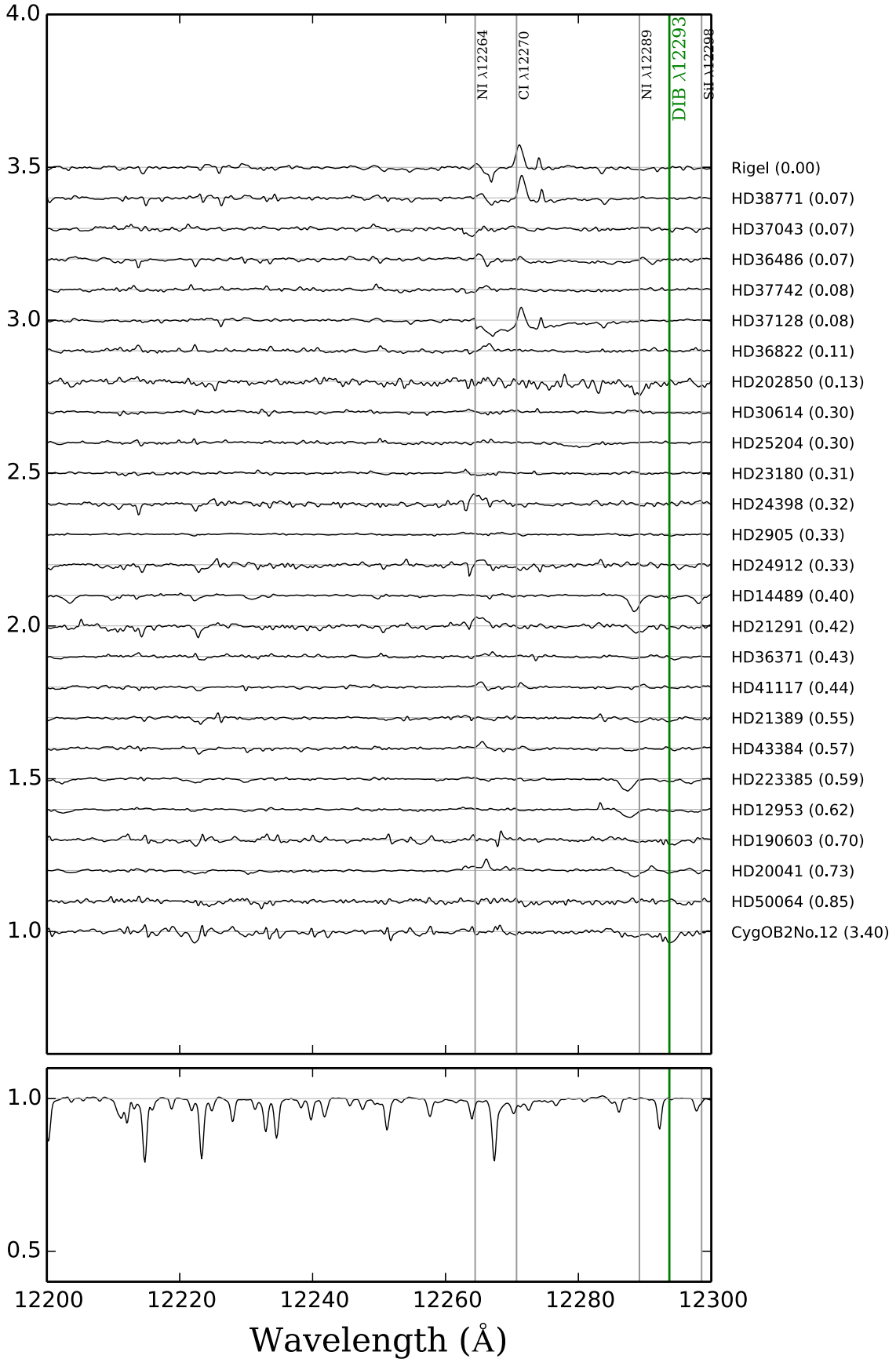
NI λ12264
CI λ12270
NI λ12289
DIB λ12293
SiI λ12308
Rigel (0.00)
HD38771 (0.07)
HD37043 (0.07)
HD36486 (0.07)
HD37742 (0.08)
HD37128 (0.08)
HD36822 (0.11)
HD202850 (0.13)
HD30614 (0.30)
HD25204 (0.30)
HD23180 (0.31)
HD24398 (0.32)
HD2905 (0.33)
HD24912 (0.33)
HD14489 (0.40)
HD21291 (0.42)
HD36371 (0.43)
HD41117 (0.44)
HD21389 (0.55)
HD43384 (0.57)
HD223385 (0.59)
HD12953 (0.62)
HD190603 (0.70)
HD20041 (0.73)
HD50064 (0.85)
CygOB2No.12 (3.40)
4.0
3.5
3.0
2.5
2.0
1.5
1.0
1.0
0.5
12200
12220
12240
12260
12280
12300
Wavelength (Å)

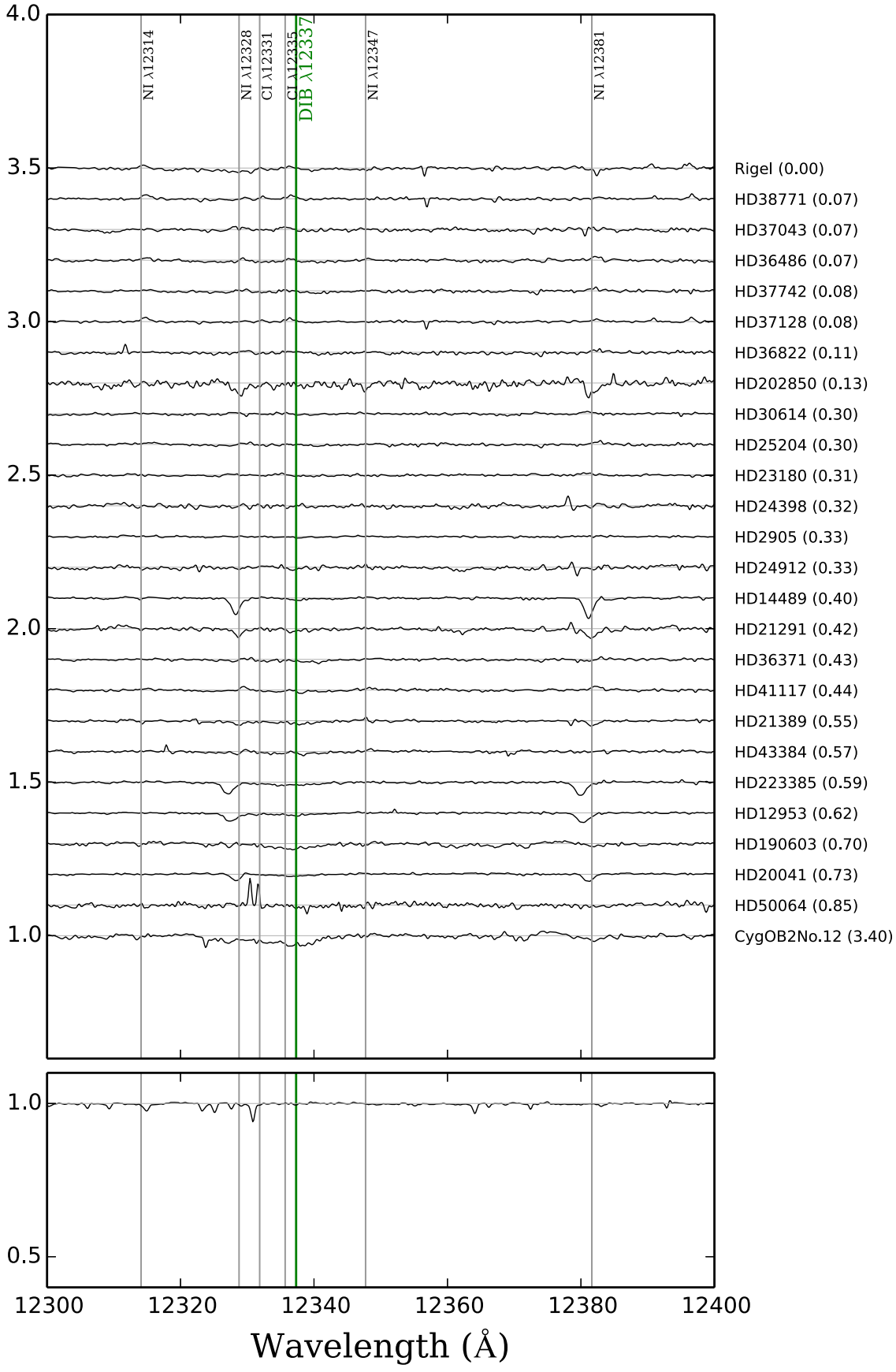
NI λ12314
NI λ12328
CI λ12331
CI λ12335
DIB λ12337
NI λ12347
NI λ12381
Rigel (0.00)
HD38771 (0.07)
HD37043 (0.07)
HD36486 (0.07)
HD37742 (0.08)
HD37128 (0.08)
HD36822 (0.11)
HD202850 (0.13)
HD30614 (0.30)
HD25204 (0.30)
HD23180 (0.31)
HD24398 (0.32)
HD2905 (0.33)
HD24912 (0.33)
HD14489 (0.40)
HD21291 (0.42)
HD36371 (0.43)
HD41117 (0.44)
HD21389 (0.55)
HD43384 (0.57)
HD223385 (0.59)
HD12953 (0.62)
HD190603 (0.70)
HD20041 (0.73)
HD50064 (0.85)
CygOB2No.12 (3.40)
4.0
3.5
3.0
2.5
2.0
1.5
1.0
1.0
0.5
12300
12320
12340
12360
12380
12400
Wavelength (Å)

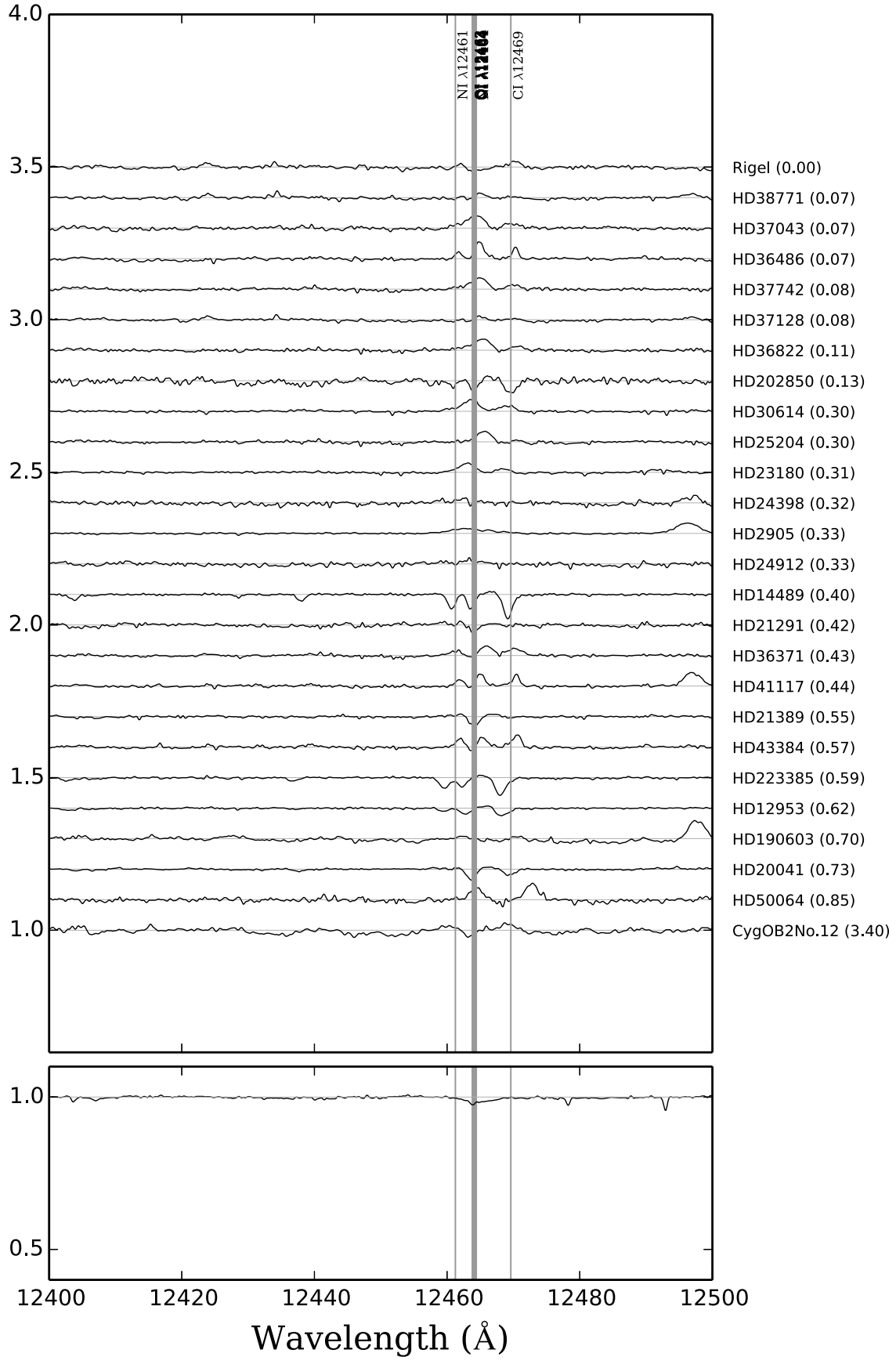
NI λ12461
CI λ12469
Rigel (0.00)
HD38771 (0.07)
HD37043 (0.07)
HD36486 (0.07)
HD37742 (0.08)
HD37128 (0.08)
HD36822 (0.11)
HD202850 (0.13)
HD30614 (0.30)
HD25204 (0.30)
HD23180 (0.31)
HD24398 (0.32)
HD2905 (0.33)
HD24912 (0.33)
HD14489 (0.40)
HD21291 (0.42)
HD36371 (0.43)
HD41117 (0.44)
HD21389 (0.55)
HD43384 (0.57)
HD223385 (0.59)
HD12953 (0.62)
HD190603 (0.70)
HD20041 (0.73)
HD50064 (0.85)
CygOB2No.12 (3.40)
4.0
3.5
3.0
2.5
2.0
1.5
1.0
1.0
0.5
12400
12420
12440
12460
12480
12500
Wavelength (Å)

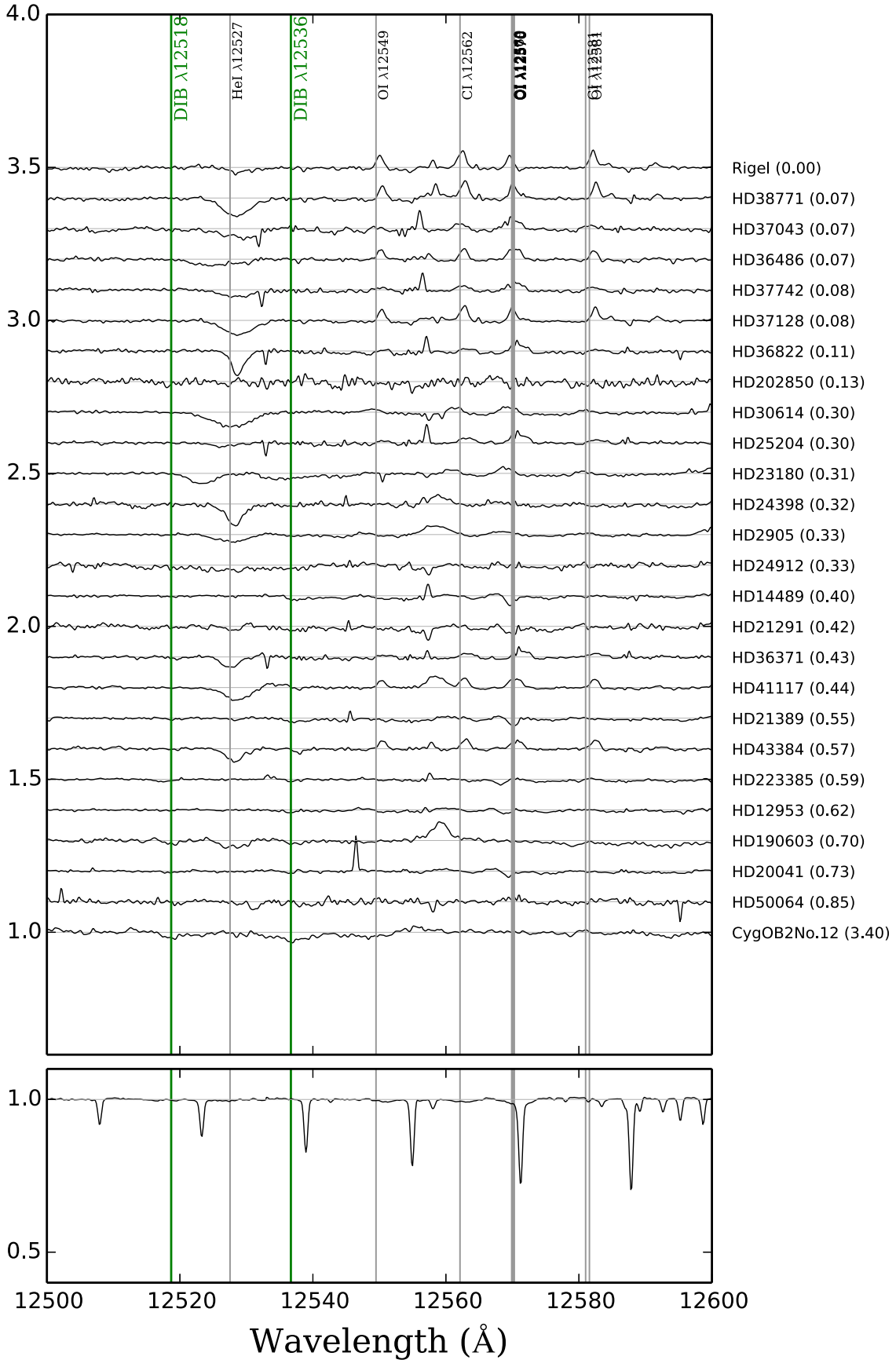
DIB λ12518
HeI λ12527
DIB λ12536
OI λ12549
CI λ12562
OI λ12581
Rigel (0.00)
HD38771 (0.07)
HD37043 (0.07)
HD36486 (0.07)
HD37742 (0.08)
HD37128 (0.08)
HD36822 (0.11)
HD202850 (0.13)
HD30614 (0.30)
HD25204 (0.30)
HD23180 (0.31)
HD24398 (0.32)
HD2905 (0.33)
HD24912 (0.33)
HD14489 (0.40)
HD21291 (0.42)
HD36371 (0.43)
HD41117 (0.44)
HD21389 (0.55)
HD43384 (0.57)
HD223385 (0.59)
HD12953 (0.62)
HD190603 (0.70)
HD20041 (0.73)
HD50064 (0.85)
CygOB2No.12 (3.40)
4.0
3.5
3.0
2.5
2.0
1.5
1.0
1.0
0.5
12500
12520
12540
12560
12580
12600
Wavelength (Å)

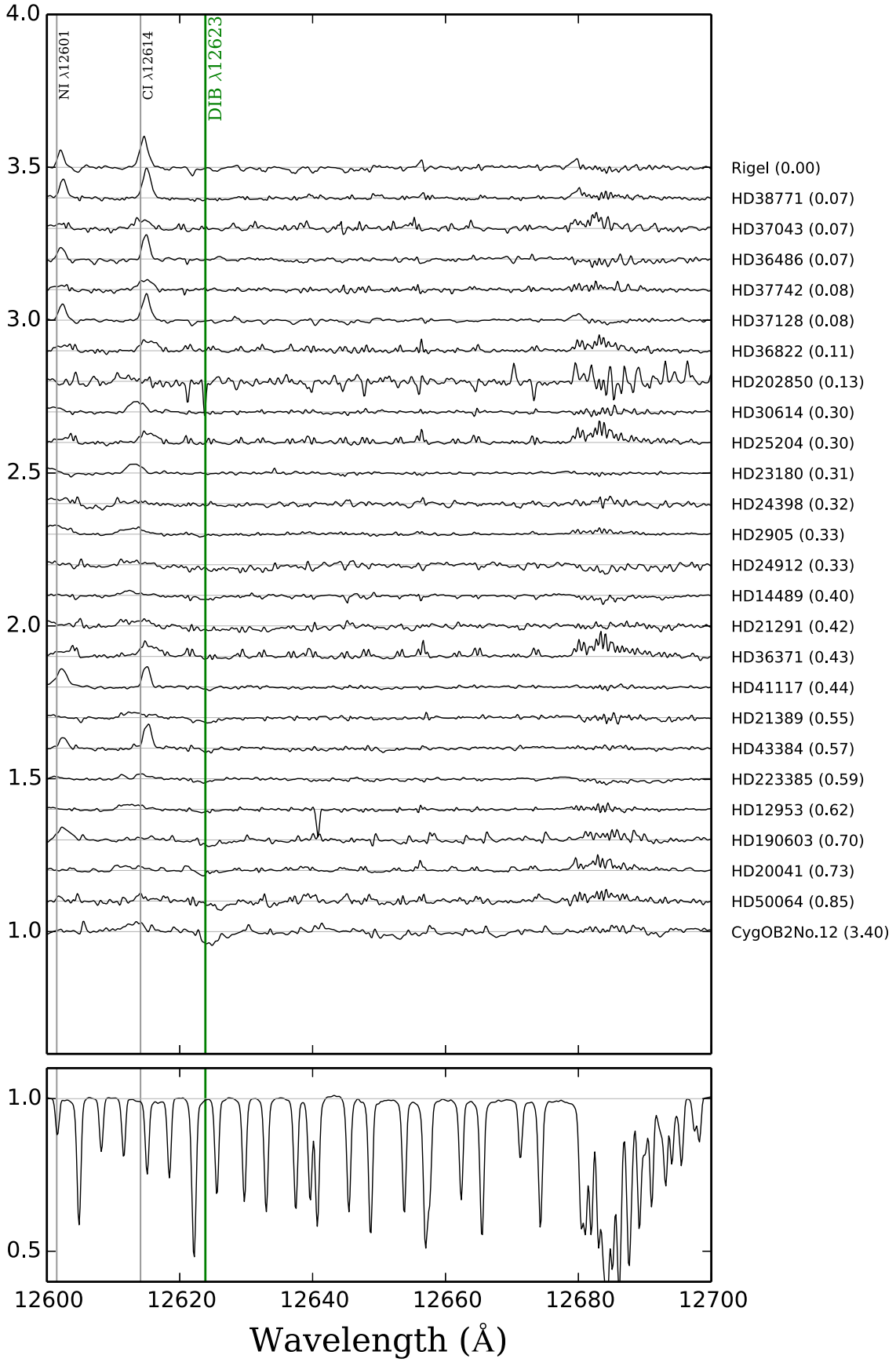
NI λ12601
CI λ12614
DIB λ12623
Rigel (0.00)
HD38771 (0.07)
HD37043 (0.07)
HD36486 (0.07)
HD37742 (0.08)
HD37128 (0.08)
HD36822 (0.11)
HD202850 (0.13)
HD30614 (0.30)
HD25204 (0.30)
HD23180 (0.31)
HD24398 (0.32)
HD2905 (0.33)
HD24912 (0.33)
HD14489 (0.40)
HD21291 (0.42)
HD36371 (0.43)
HD41117 (0.44)
HD21389 (0.55)
HD43384 (0.57)
HD223385 (0.59)
HD12953 (0.62)
HD190603 (0.70)
HD20041 (0.73)
HD50064 (0.85)
CygOB2No.12 (3.40)
4.0
3.5
3.0
2.5
2.0
1.5
1.0
1.0
0.5
12600
12620
12640
12660
12680
12700
Wavelength (Å)

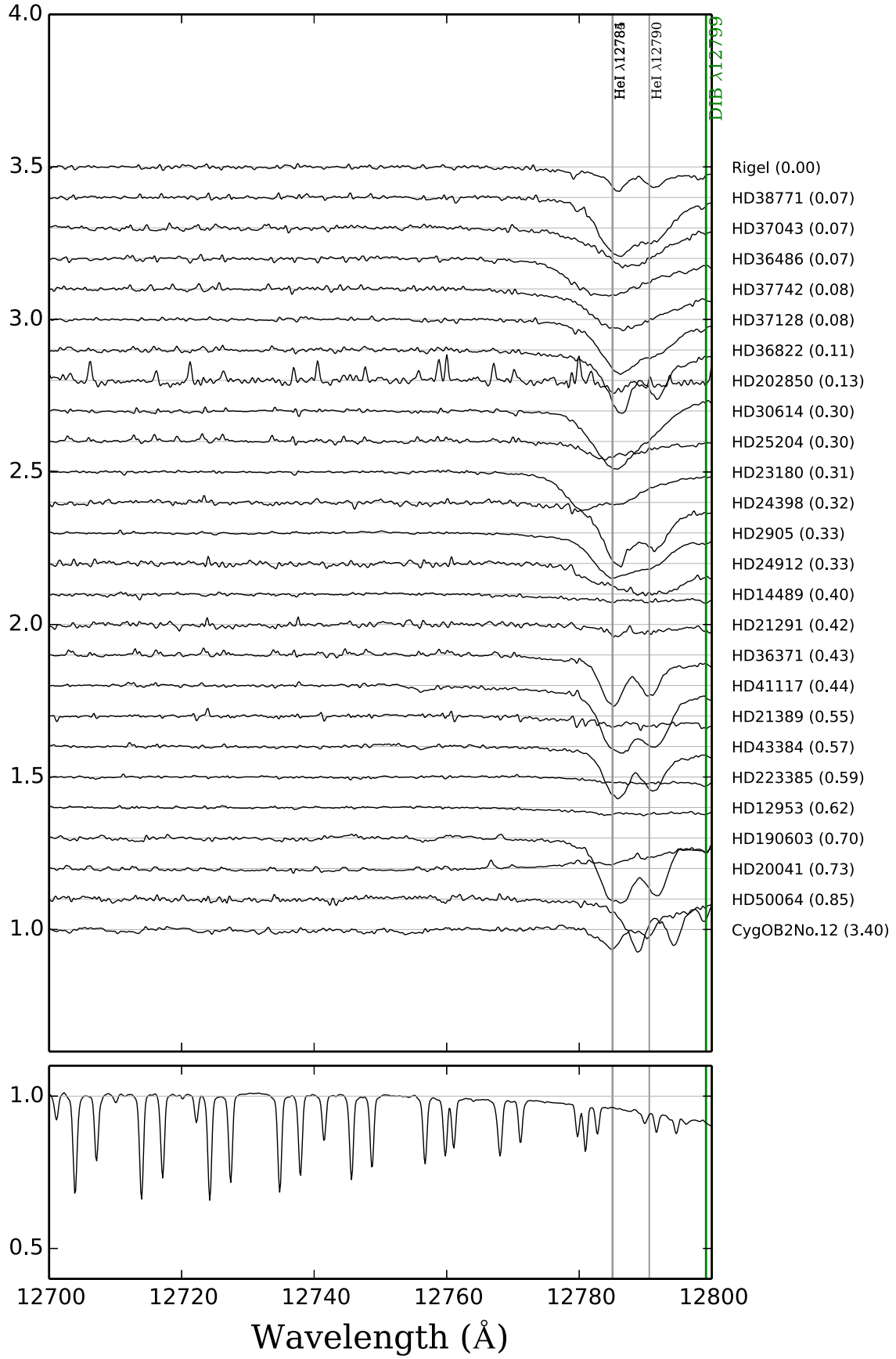
HeI λ12784
HeI λ12790
DIB λ12799
Rigel (0.00)
HD38771 (0.07)
HD37043 (0.07)
HD36486 (0.07)
HD37742 (0.08)
HD37128 (0.08)
HD36822 (0.11)
HD202850 (0.13)
HD30614 (0.30)
HD25204 (0.30)
HD23180 (0.31)
HD24398 (0.32)
HD2905 (0.33)
HD24912 (0.33)
HD14489 (0.40)
HD21291 (0.42)
HD36371 (0.43)
HD41117 (0.44)
HD21389 (0.55)
HD43384 (0.57)
HD223385 (0.59)
HD12953 (0.62)
HD190603 (0.70)
HD20041 (0.73)
HD50064 (0.85)
CygOB2No.12 (3.40)
4.0
3.5
3.0
2.5
2.0
1.5
1.0
1.0
0.5
12700
12720
12740
12760
12780
12800
Wavelength (Å)

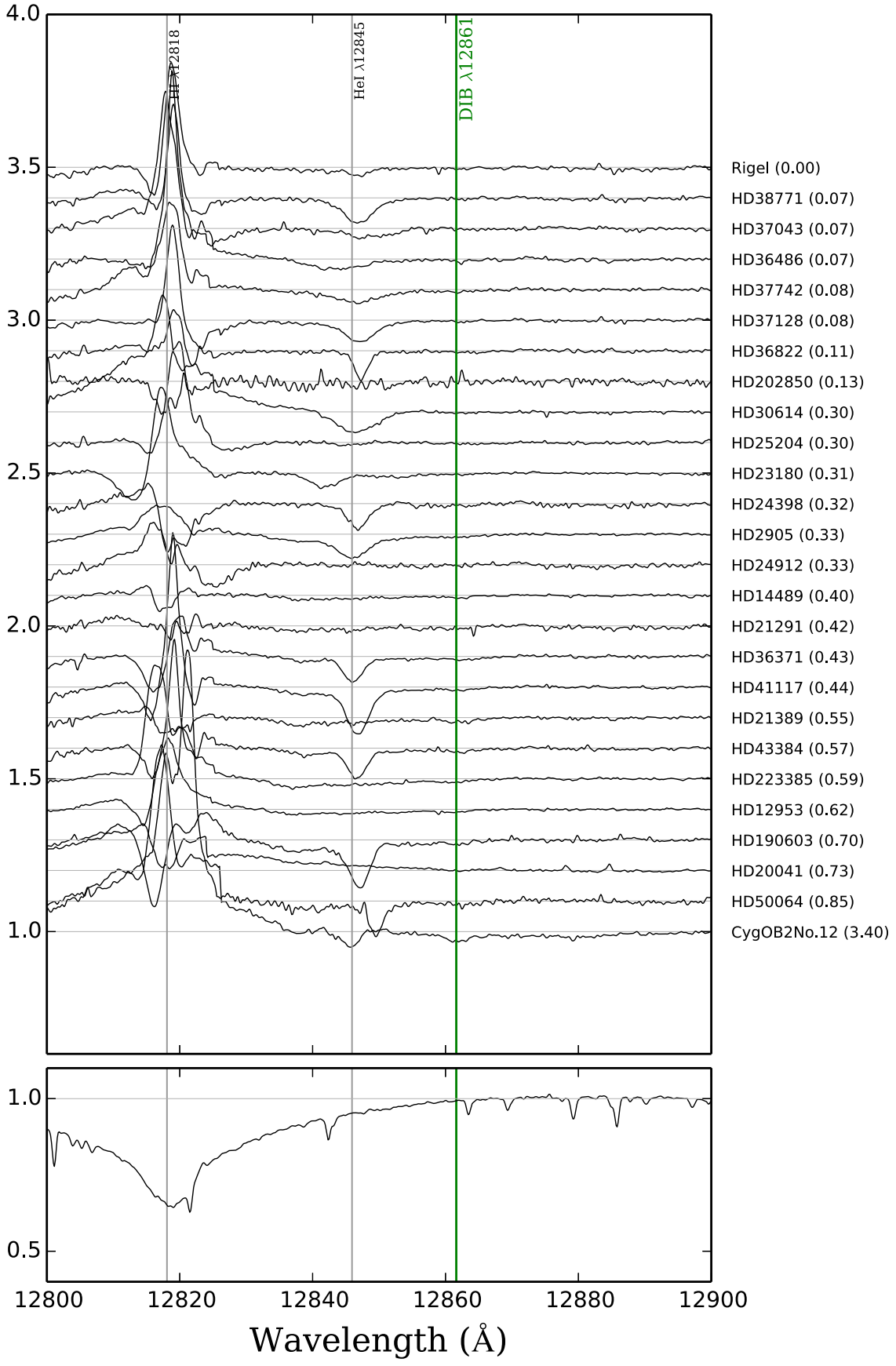
HI λ12818
HeI λ12845
DIB λ12861
Rigel (0.00)
HD38771 (0.07)
HD37043 (0.07)
HD36486 (0.07)
HD37742 (0.08)
HD37128 (0.08)
HD36822 (0.11)
HD202850 (0.13)
HD30614 (0.30)
HD25204 (0.30)
HD23180 (0.31)
HD24398 (0.32)
HD2905 (0.33)
HD24912 (0.33)
HD14489 (0.40)
HD21291 (0.42)
HD36371 (0.43)
HD41117 (0.44)
HD21389 (0.55)
HD43384 (0.57)
HD223385 (0.59)
HD12953 (0.62)
HD190603 (0.70)
HD20041 (0.73)
HD50064 (0.85)
CygOB2No.12 (3.40)
4.0
3.5
3.0
2.5
2.0
1.5
1.0
1.0
0.5
12800
12820
12840
12860
12880
12900
Wavelength (Å)

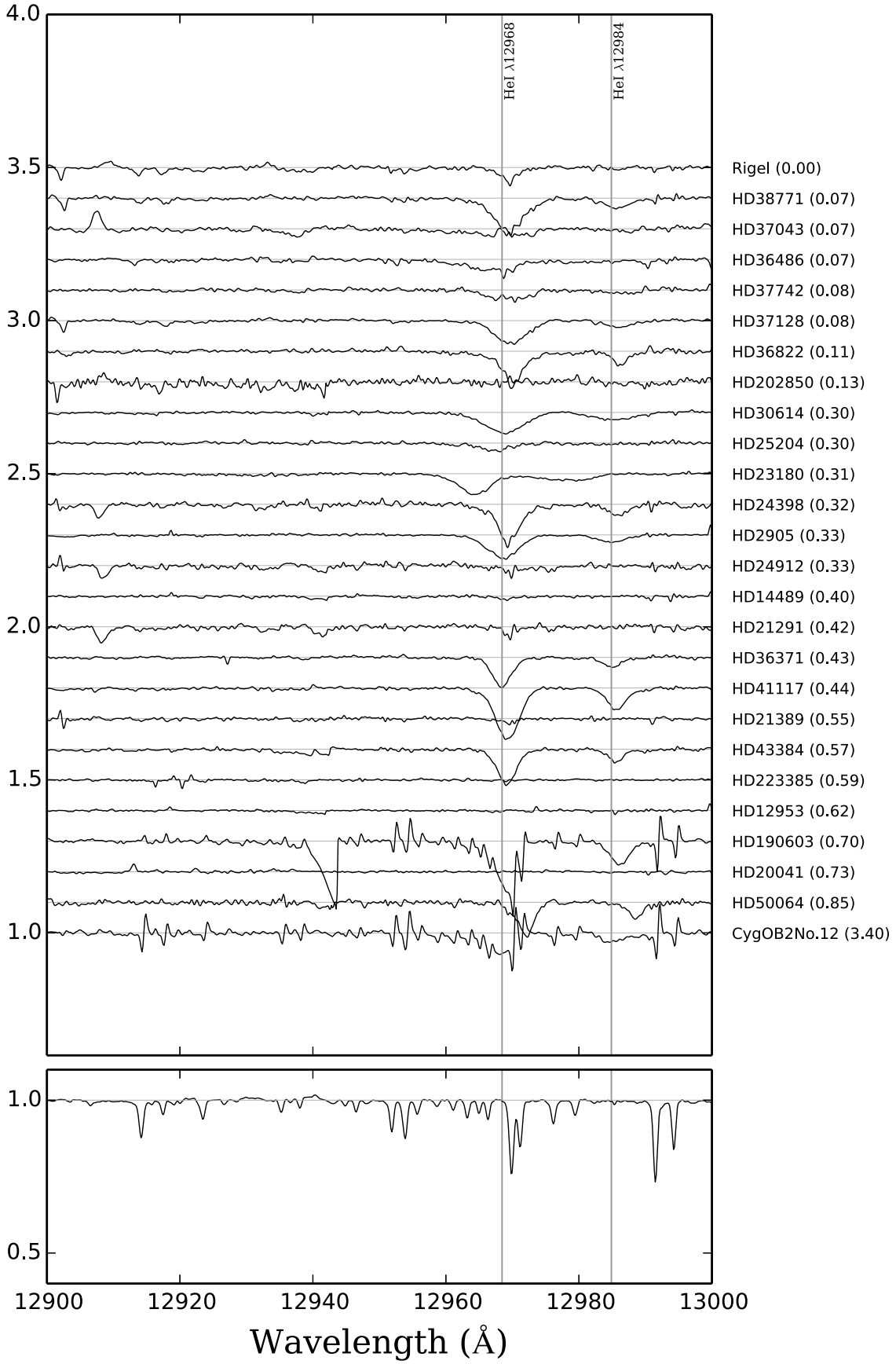
HeI λ12968
HeI λ12984
Rigel (0.00)
HD38771 (0.07)
HD37043 (0.07)
HD36486 (0.07)
HD37742 (0.08)
HD37128 (0.08)
HD36822 (0.11)
HD202850 (0.13)
HD30614 (0.30)
HD25204 (0.30)
HD23180 (0.31)
HD24398 (0.32)
HD2905 (0.33)
HD24912 (0.33)
HD14489 (0.40)
HD21291 (0.42)
HD36371 (0.43)
HD41117 (0.44)
HD21389 (0.55)
HD43384 (0.57)
HD223385 (0.59)
HD12953 (0.62)
HD190603 (0.70)
HD20041 (0.73)
HD50064 (0.85)
CygOB2No.12 (3.40)
4.0
3.5
3.0
2.5
2.0
1.5
1.0
1.0
0.5
12900
12920
12940
12960
12980
13000
Wavelength (Å)

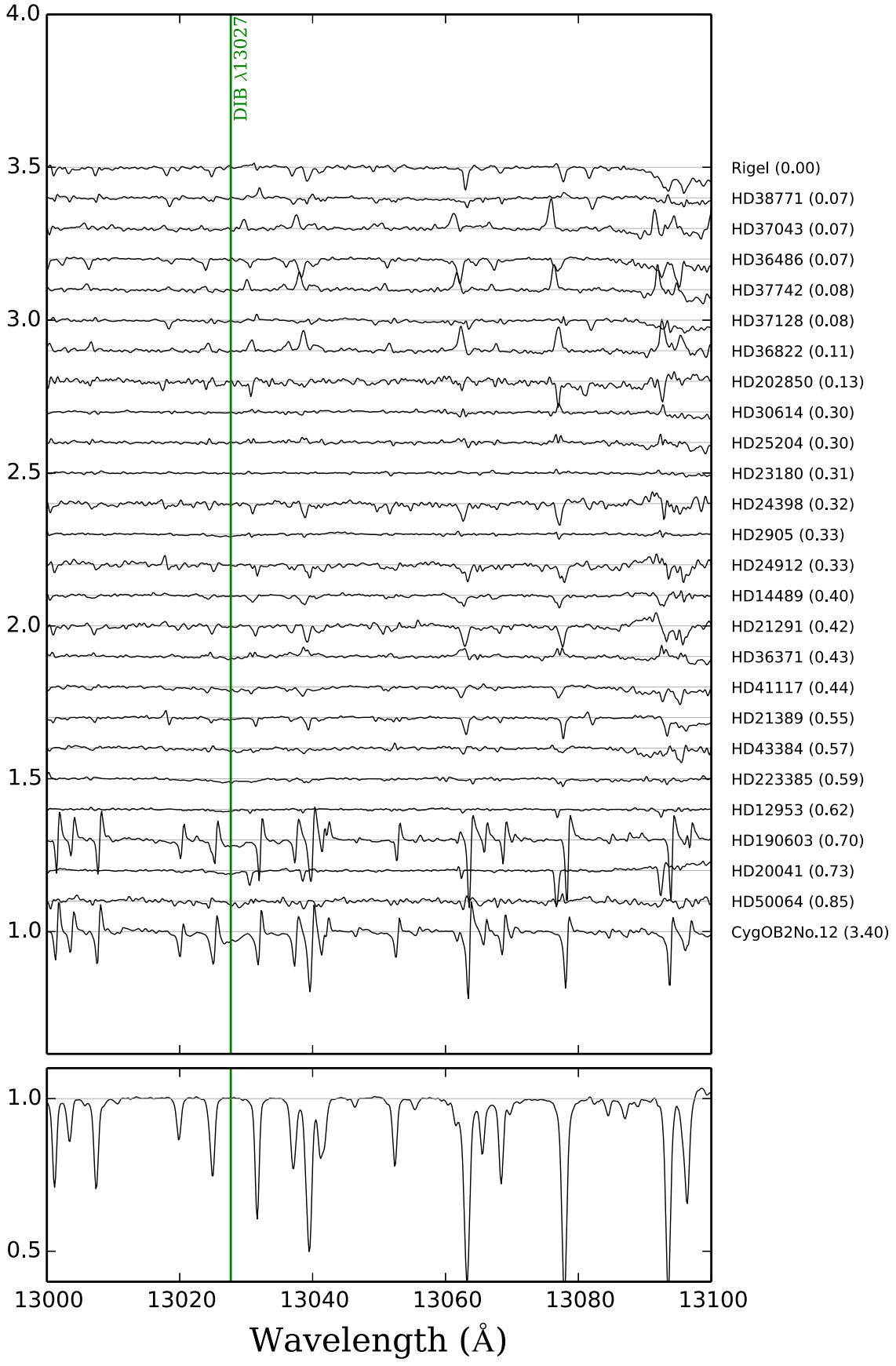
DIB λ13027
Rigel (0.00)
HD38771 (0.07)
HD37043 (0.07)
HD36486 (0.07)
HD37742 (0.08)
HD37128 (0.08)
HD36822 (0.11)
HD202850 (0.13)
HD30614 (0.30)
HD25204 (0.30)
HD23180 (0.31)
HD24398 (0.32)
HD2905 (0.33)
HD24912 (0.33)
HD14489 (0.40)
HD21291 (0.42)
HD36371 (0.43)
HD41117 (0.44)
HD21389 (0.55)
HD43384 (0.57)
HD223385 (0.59)
HD12953 (0.62)
HD190603 (0.70)
HD20041 (0.73)
HD50064 (0.85)
CygOB2No.12 (3.40)
4.0
3.5
3.0
2.5
2.0
1.5
1.0
1.0
0.5
13000
13020
13040
13060
13080
13100
Wavelength (Å)

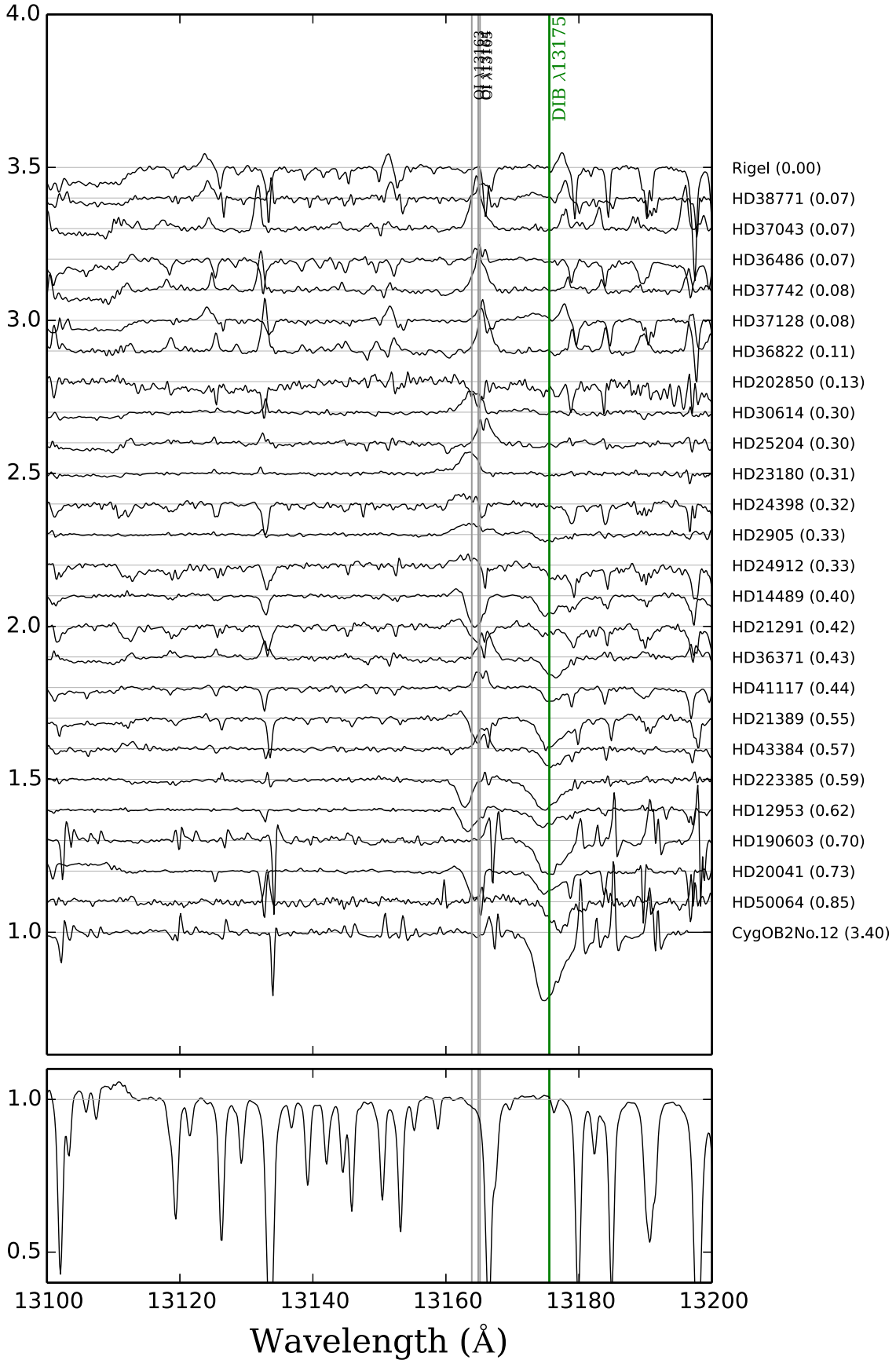
4.0
3.5
3.0
2.5
2.0
1.5
1.0
1.0
0.5
13100
13120
13140
13160
13180
13200
Wavelength (Å)
O I λ13162
O I λ13165
DIB λ13175
Rigel (0.00)
HD38771 (0.07)
HD37043 (0.07)
HD36486 (0.07)
HD37742 (0.08)
HD37128 (0.08)
HD36822 (0.11)
HD202850 (0.13)
HD30614 (0.30)
HD25204 (0.30)
HD23180 (0.31)
HD24398 (0.32)
HD2905 (0.33)
HD24912 (0.33)
HD14489 (0.40)
HD21291 (0.42)
HD36371 (0.43)
HD41117 (0.44)
HD21389 (0.55)
HD43384 (0.57)
HD223385 (0.59)
HD12953 (0.62)
HD190603 (0.70)
HD20041 (0.73)
HD50064 (0.85)
CygOB2No.12 (3.40)

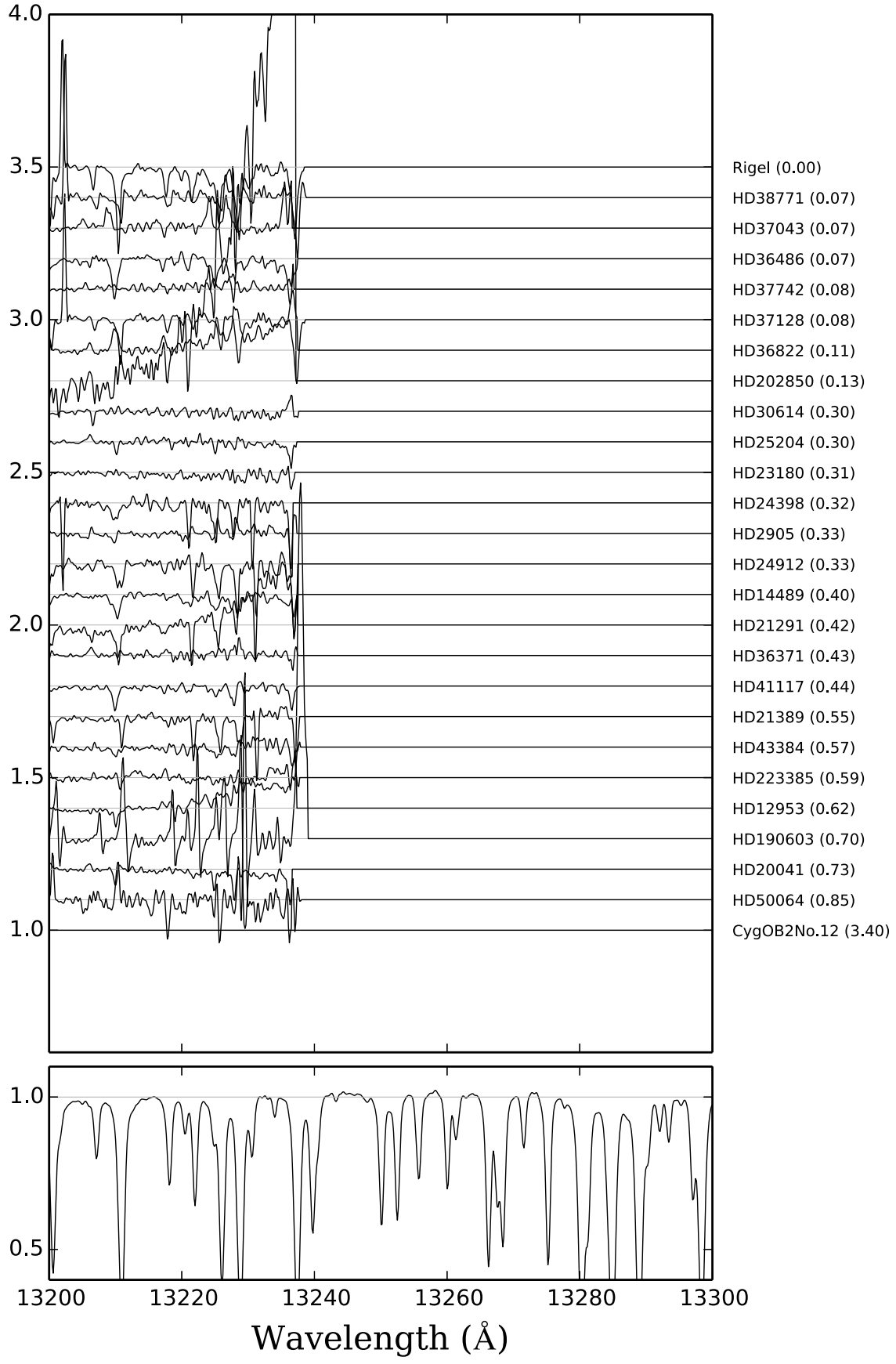
4.0
3.5
3.0
2.5
2.0
1.5
1.0
Rigel (0.00)
HD38771 (0.07)
HD37043 (0.07)
HD36486 (0.07)
HD37742 (0.08)
HD37128 (0.08)
HD36822 (0.11)
HD202850 (0.13)
HD30614 (0.30)
HD25204 (0.30)
HD23180 (0.31)
HD24398 (0.32)
HD2905 (0.33)
HD24912 (0.33)
HD14489 (0.40)
HD21291 (0.42)
HD36371 (0.43)
HD41117 (0.44)
HD21389 (0.55)
HD43384 (0.57)
HD223385 (0.59)
HD12953 (0.62)
HD190603 (0.70)
HD20041 (0.73)
HD50064 (0.85)
CygOB2No.12 (3.40)
1.0
0.5
13200
13220
13240
13260
13280
13300
Wavelength (Å)

Appendix B

Correlations of NIR DIBs

Correlations among 18 NIR DIBs from the survey data (black circles; Chapter 4) and the data of the Cyg OB2 association (red circles; Chapter 8) are shown. The black lines show the linear function fitted to the all points in each plot.

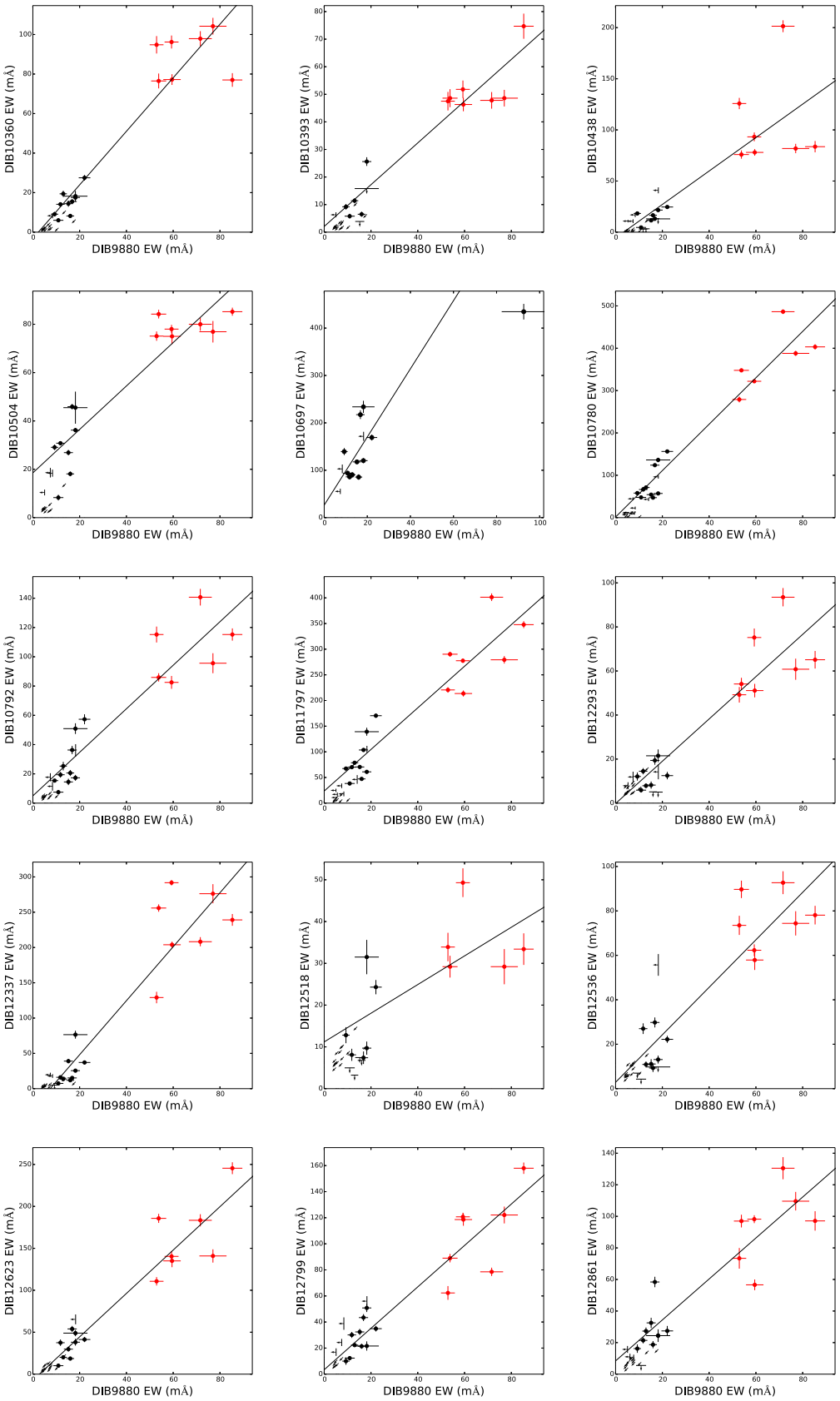
DIB10360 EW (mÅ)
DIB10393 EW (mÅ)
DIB10438 EW (mÅ)
DIB10504 EW (mÅ)
DIB10697 EW (mÅ)
DIB10780 EW (mÅ)
DIB10792 EW (mÅ)
DIB11797 EW (mÅ)
DIB12293 EW (mÅ)
DIB12337 EW (mÅ)
DIB12518 EW (mÅ)
DIB12536 EW (mÅ)
DIB12623 EW (mÅ)
DIB12799 EW (mÅ)
DIB12861 EW (mÅ)
DIB9880 EW (mÅ)

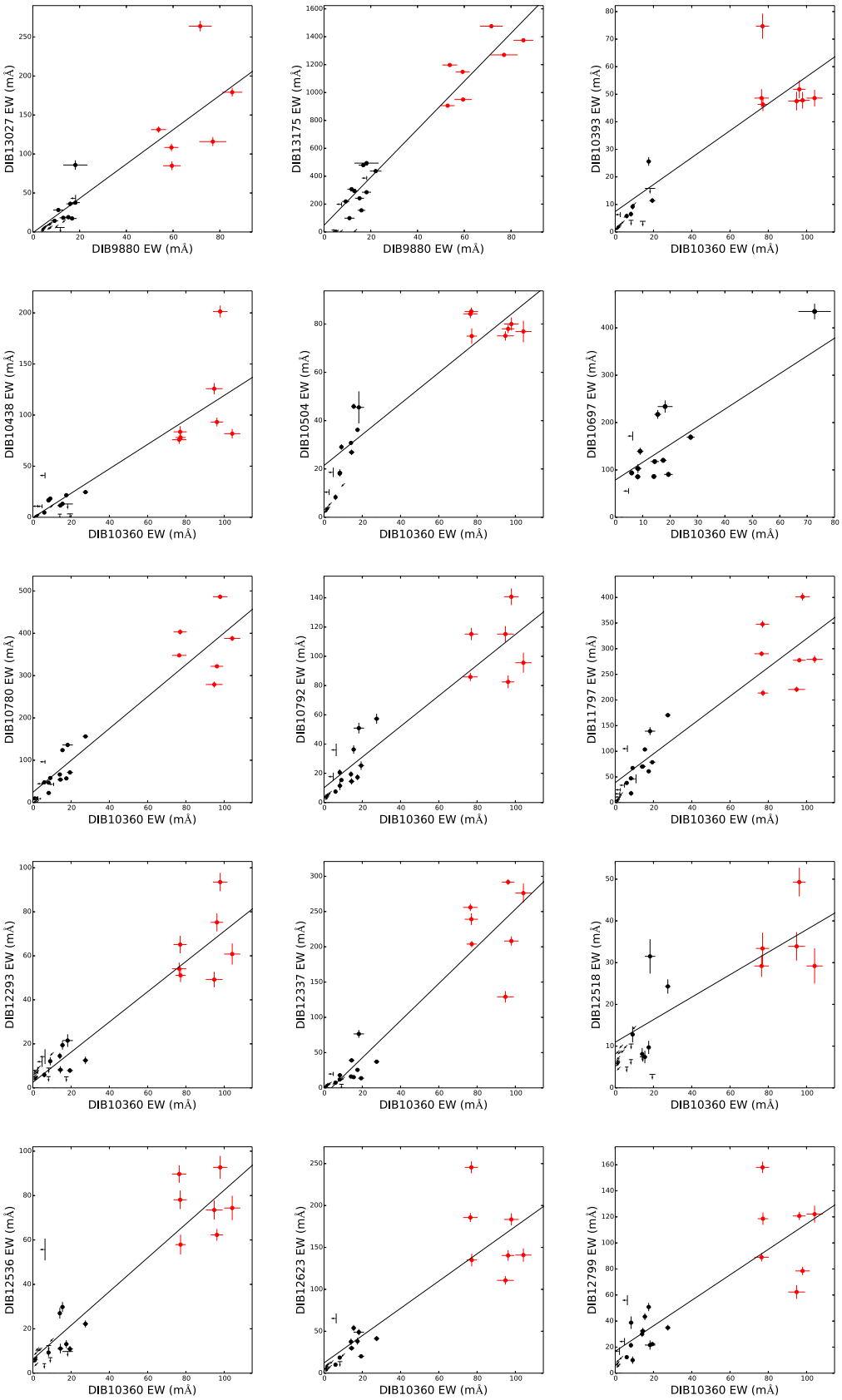
DIB13027 EW (mÅ)
DIB9880 EW (mÅ)
DIB13175 EW (mÅ)
DIB9880 EW (mÅ)
DIB10393 EW (mÅ)
DIB10360 EW (mÅ)
DIB10438 EW (mÅ)
DIB10360 EW (mÅ)
DIB10504 EW (mÅ)
DIB10360 EW (mÅ)
DIB10697 EW (mÅ)
DIB10360 EW (mÅ)
DIB10780 EW (mÅ)
DIB10360 EW (mÅ)
DIB10792 EW (mÅ)
DIB10360 EW (mÅ)
DIB11797 EW (mÅ)
DIB10360 EW (mÅ)
DIB12293 EW (mÅ)
DIB10360 EW (mÅ)
DIB12337 EW (mÅ)
DIB10360 EW (mÅ)
DIB12518 EW (mÅ)
DIB10360 EW (mÅ)
DIB12536 EW (mÅ)
DIB10360 EW (mÅ)
DIB12623 EW (mÅ)
DIB10360 EW (mÅ)
DIB12799 EW (mÅ)
DIB10360 EW (mÅ)

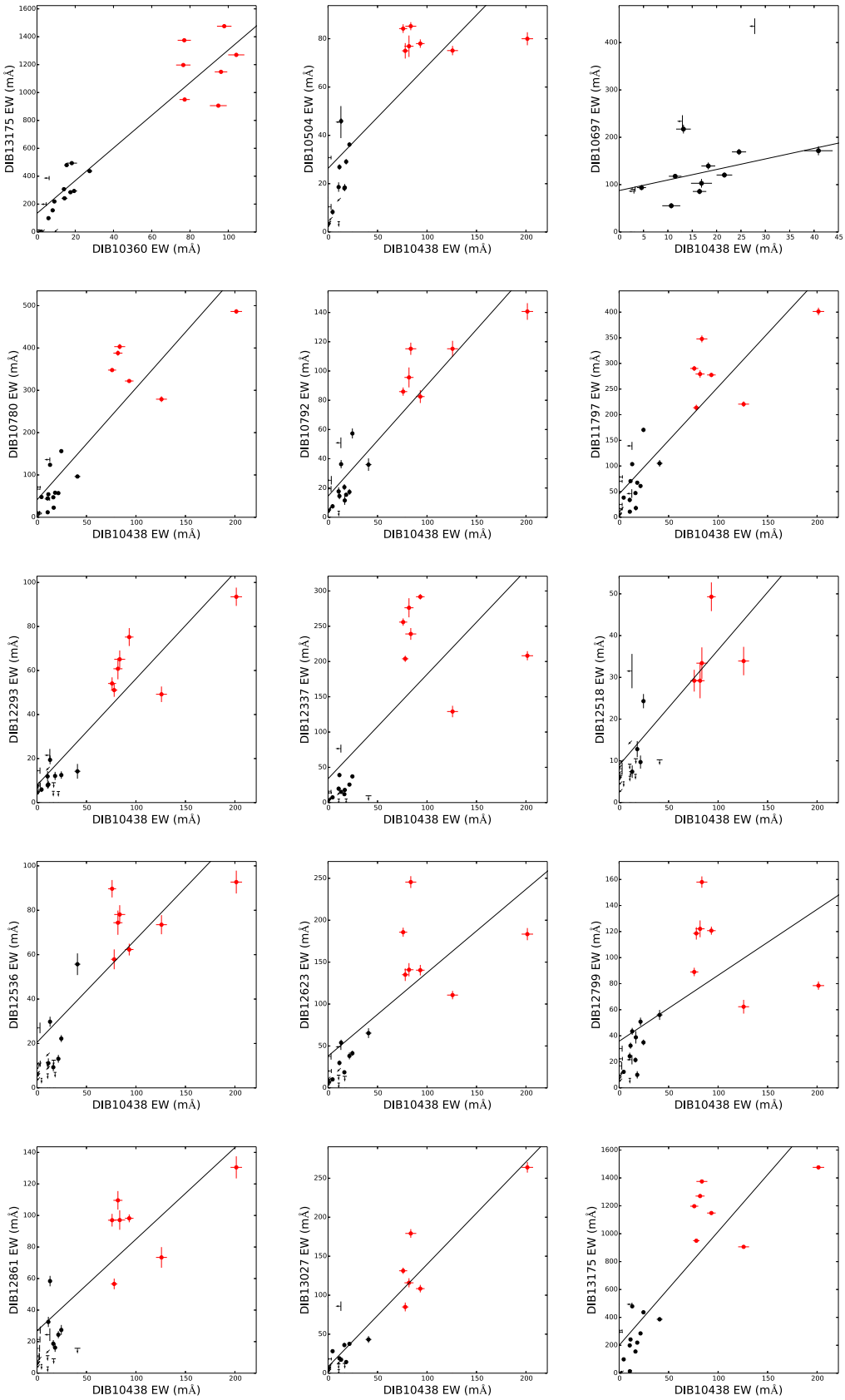
DIB13175 EW (mÅ)
DIB10360 EW (mÅ)
DIB10504 EW (mÅ)
DIB10438 EW (mÅ)
DIB10697 EW (mÅ)
DIB10438 EW (mÅ)
DIB10780 EW (mÅ)
DIB10438 EW (mÅ)
DIB10792 EW (mÅ)
DIB10438 EW (mÅ)
DIB11797 EW (mÅ)
DIB10438 EW (mÅ)
DIB12293 EW (mÅ)
DIB10438 EW (mÅ)
DIB12337 EW (mÅ)
DIB10438 EW (mÅ)
DIB12518 EW (mÅ)
DIB10438 EW (mÅ)
DIB12536 EW (mÅ)
DIB10438 EW (mÅ)
DIB12623 EW (mÅ)
DIB10438 EW (mÅ)
DIB12799 EW (mÅ)
DIB10438 EW (mÅ)
DIB12861 EW (mÅ)
DIB10438 EW (mÅ)
DIB13027 EW (mÅ)
DIB10438 EW (mÅ)
DIB13175 EW (mÅ)
DIB10438 EW (mÅ)

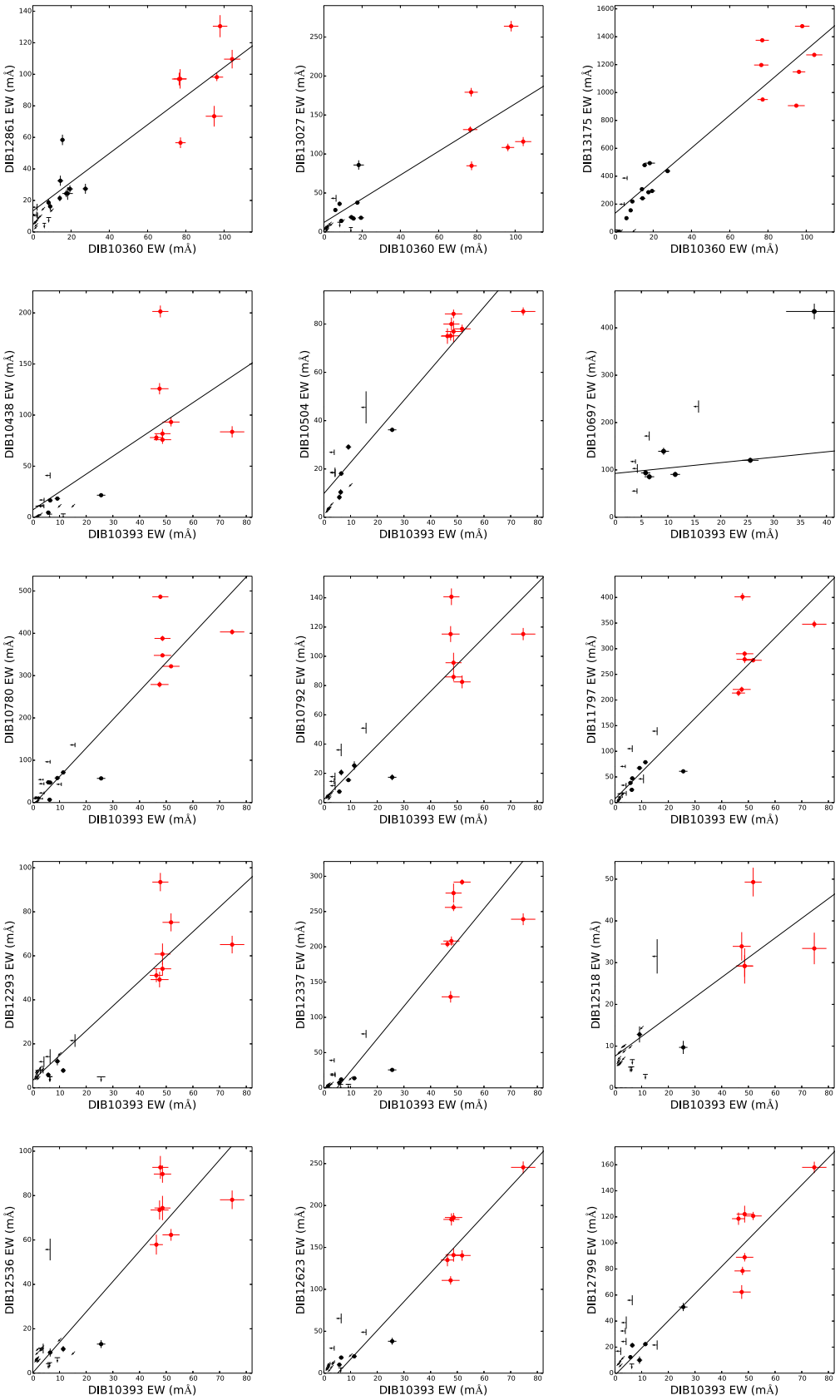
DIB12861 EW (mÅ)
DIB10360 EW (mÅ)
DIB13027 EW (mÅ)
DIB10360 EW (mÅ)
DIB13175 EW (mÅ)
DIB10360 EW (mÅ)
DIB10438 EW (mÅ)
DIB10393 EW (mÅ)
DIB10504 EW (mÅ)
DIB10393 EW (mÅ)
DIB10697 EW (mÅ)
DIB10393 EW (mÅ)
DIB10780 EW (mÅ)
DIB10393 EW (mÅ)
DIB10792 EW (mÅ)
DIB10393 EW (mÅ)
DIB11797 EW (mÅ)
DIB10393 EW (mÅ)
DIB12293 EW (mÅ)
DIB10393 EW (mÅ)
DIB12337 EW (mÅ)
DIB10393 EW (mÅ)
DIB12518 EW (mÅ)
DIB10393 EW (mÅ)
DIB12536 EW (mÅ)
DIB10393 EW (mÅ)
DIB12623 EW (mÅ)
DIB10393 EW (mÅ)
DIB12799 EW (mÅ)
DIB10393 EW (mÅ)

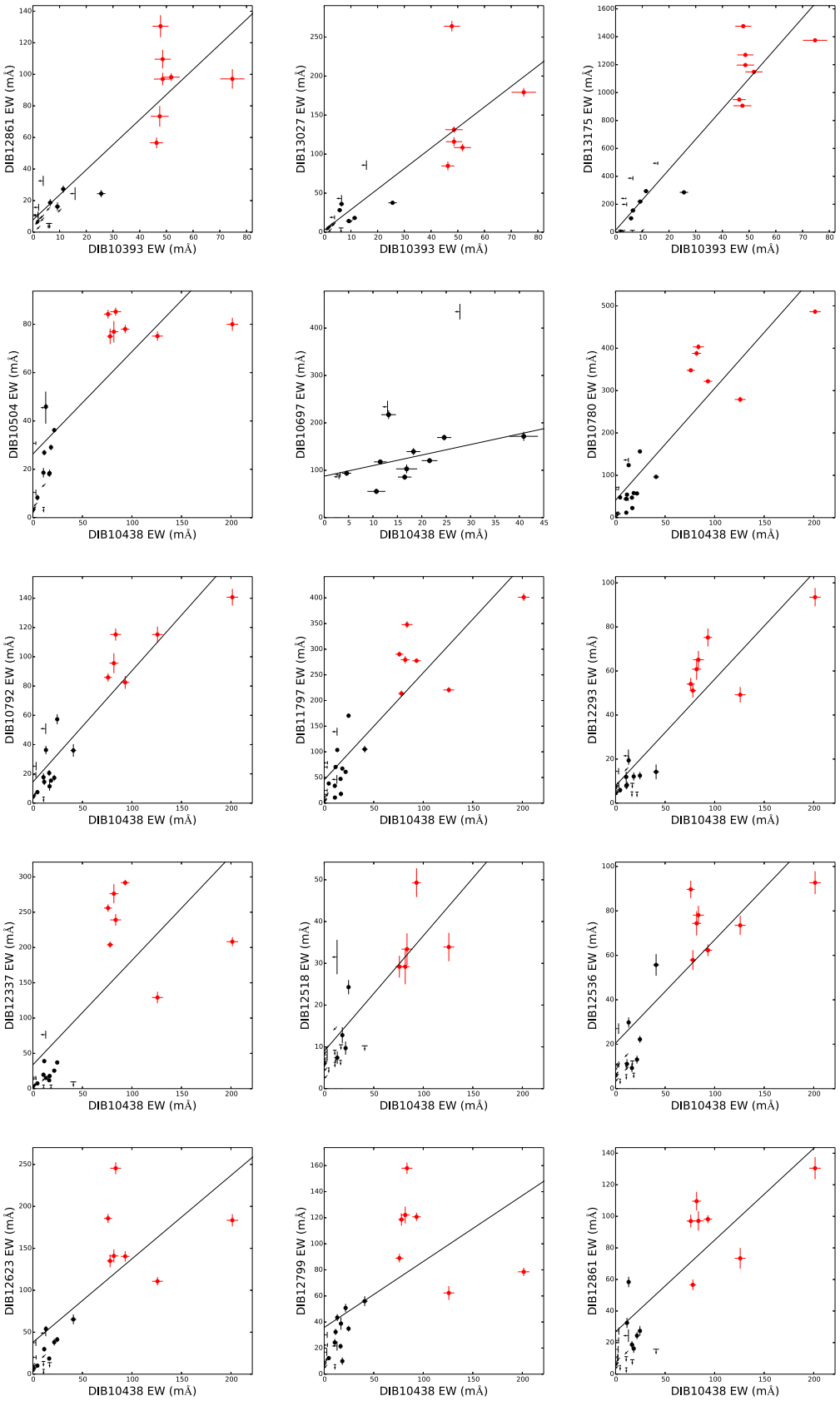
DIB12861 EW (mÅ)
DIB10393 EW (mÅ)
DIB13027 EW (mÅ)
DIB10393 EW (mÅ)
DIB13175 EW (mÅ)
DIB10393 EW (mÅ)
DIB10504 EW (mÅ)
DIB10438 EW (mÅ)
DIB10697 EW (mÅ)
DIB10438 EW (mÅ)
DIB10780 EW (mÅ)
DIB10438 EW (mÅ)
DIB10792 EW (mÅ)
DIB10438 EW (mÅ)
DIB11797 EW (mÅ)
DIB10438 EW (mÅ)
DIB12293 EW (mÅ)
DIB10438 EW (mÅ)
DIB12337 EW (mÅ)
DIB10438 EW (mÅ)
DIB12518 EW (mÅ)
DIB10438 EW (mÅ)
DIB12536 EW (mÅ)
DIB10438 EW (mÅ)
DIB12623 EW (mÅ)
DIB10438 EW (mÅ)
DIB12799 EW (mÅ)
DIB10438 EW (mÅ)
DIB12861 EW (mÅ)
DIB10438 EW (mÅ)

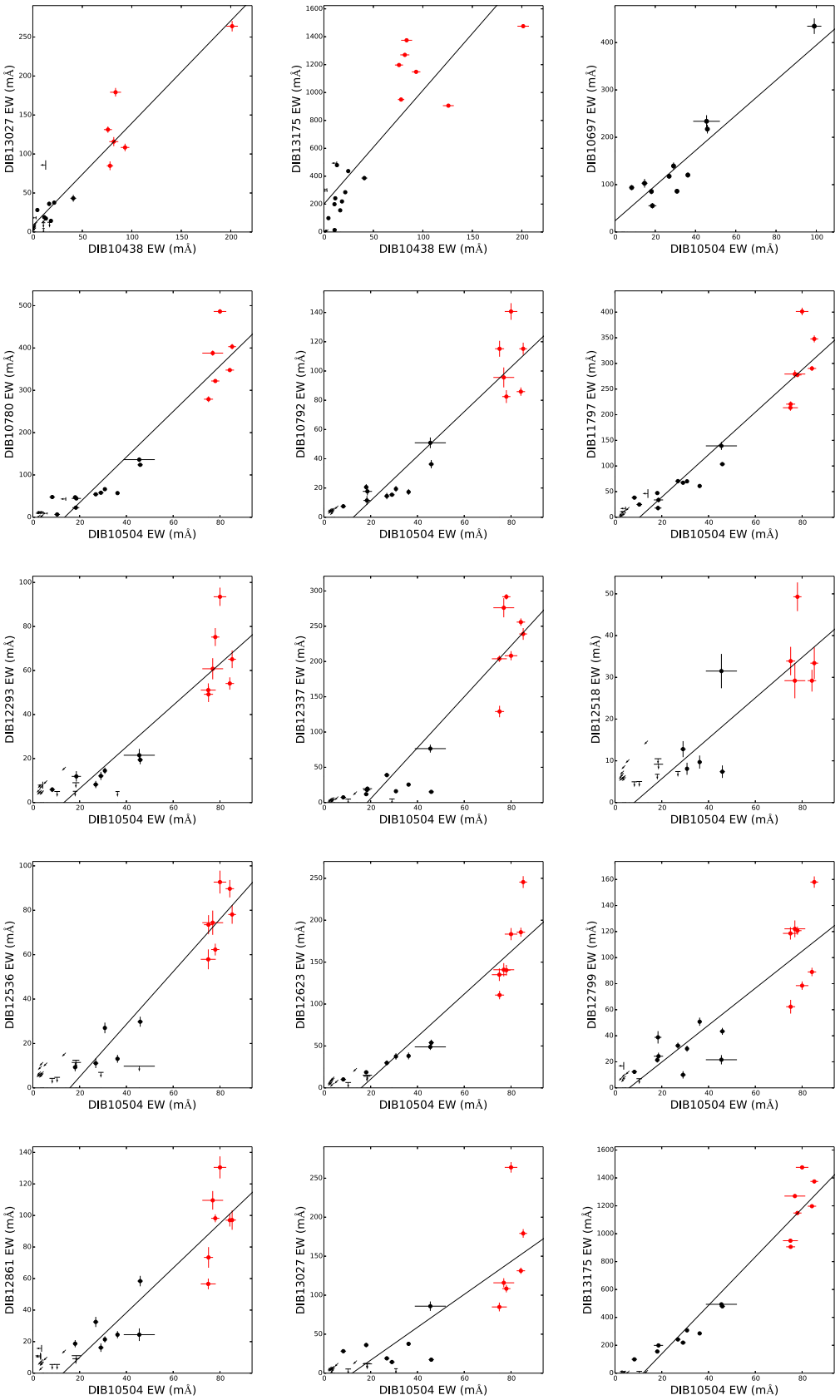
DIB13027 EW (mÅ)
DIB10438 EW (mÅ)
DIB13175 EW (mÅ)
DIB10438 EW (mÅ)
DIB10697 EW (mÅ)
DIB10504 EW (mÅ)
DIB10780 EW (mÅ)
DIB10504 EW (mÅ)
DIB10792 EW (mÅ)
DIB10504 EW (mÅ)
DIB11797 EW (mÅ)
DIB10504 EW (mÅ)
DIB12293 EW (mÅ)
DIB10504 EW (mÅ)
DIB12337 EW (mÅ)
DIB10504 EW (mÅ)
DIB12518 EW (mÅ)
DIB10504 EW (mÅ)
DIB12536 EW (mÅ)
DIB10504 EW (mÅ)
DIB12623 EW (mÅ)
DIB10504 EW (mÅ)
DIB12799 EW (mÅ)
DIB10504 EW (mÅ)
DIB12861 EW (mÅ)
DIB10504 EW (mÅ)
DIB13027 EW (mÅ)
DIB10504 EW (mÅ)
DIB13175 EW (mÅ)
DIB10504 EW (mÅ)

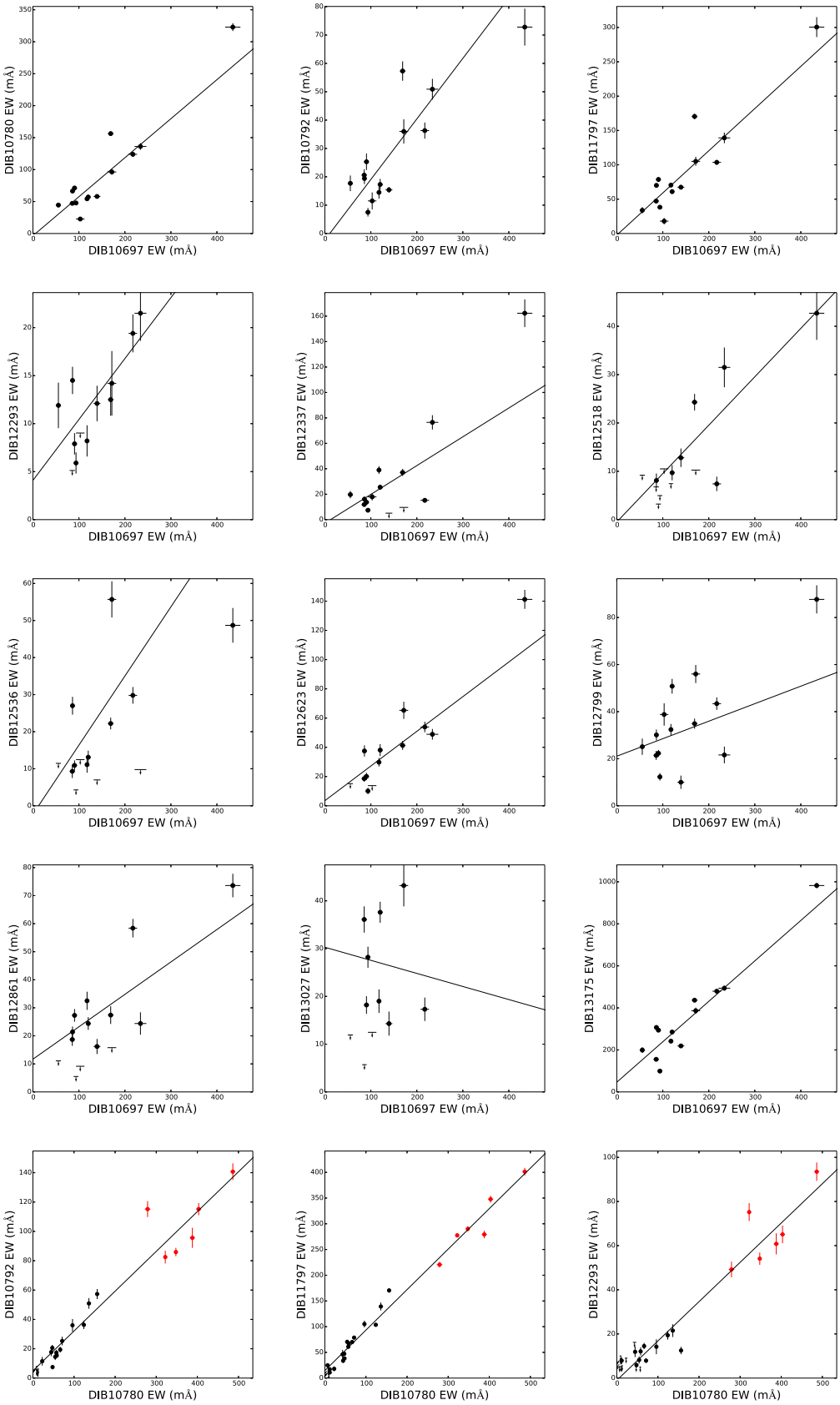
DIB10780 EW (mÅ)
DIB10697 EW (mÅ)
DIB10792 EW (mÅ)
DIB10697 EW (mÅ)
DIB11797 EW (mÅ)
DIB10697 EW (mÅ)
DIB12293 EW (mÅ)
DIB10697 EW (mÅ)
DIB12337 EW (mÅ)
DIB10697 EW (mÅ)
DIB12518 EW (mÅ)
DIB10697 EW (mÅ)
DIB12536 EW (mÅ)
DIB10697 EW (mÅ)
DIB12623 EW (mÅ)
DIB10697 EW (mÅ)
DIB12799 EW (mÅ)
DIB10697 EW (mÅ)
DIB12861 EW (mÅ)
DIB10697 EW (mÅ)
DIB13027 EW (mÅ)
DIB10697 EW (mÅ)
DIB13175 EW (mÅ)
DIB10697 EW (mÅ)
DIB10792 EW (mÅ)
DIB10780 EW (mÅ)
DIB11797 EW (mÅ)
DIB10780 EW (mÅ)
DIB12293 EW (mÅ)
DIB10780 EW (mÅ)

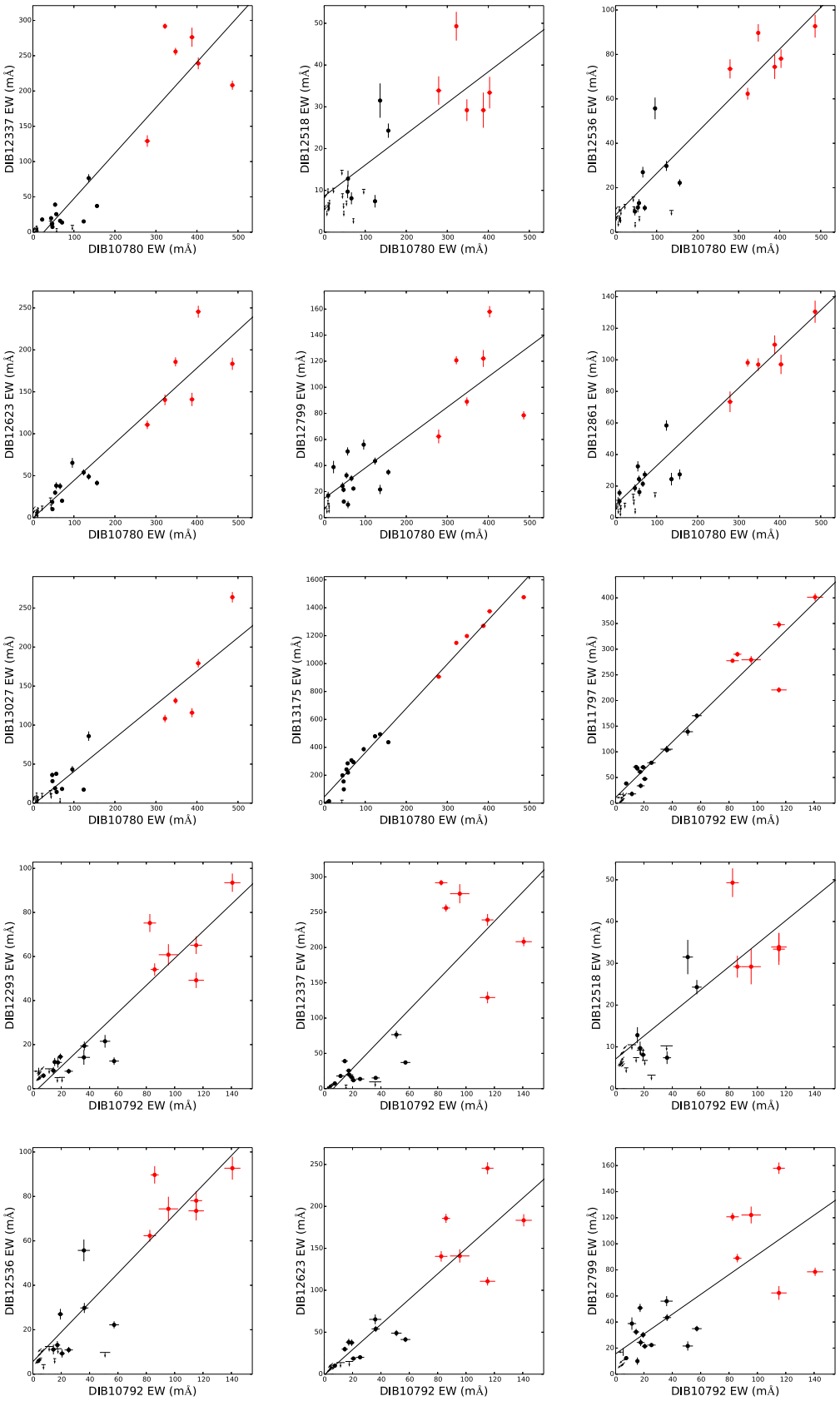
DIB12337 EW (mÅ)
DIB10780 EW (mÅ)
DIB12518 EW (mÅ)
DIB10780 EW (mÅ)
DIB12536 EW (mÅ)
DIB10780 EW (mÅ)
DIB12623 EW (mÅ)
DIB10780 EW (mÅ)
DIB12799 EW (mÅ)
DIB10780 EW (mÅ)
DIB12861 EW (mÅ)
DIB10780 EW (mÅ)
DIB13027 EW (mÅ)
DIB10780 EW (mÅ)
DIB13175 EW (mÅ)
DIB10780 EW (mÅ)
DIB11797 EW (mÅ)
DIB10792 EW (mÅ)
DIB12293 EW (mÅ)
DIB10792 EW (mÅ)
DIB12337 EW (mÅ)
DIB10792 EW (mÅ)
DIB12518 EW (mÅ)
DIB10792 EW (mÅ)
DIB12536 EW (mÅ)
DIB10792 EW (mÅ)
DIB12623 EW (mÅ)
DIB10792 EW (mÅ)
DIB12799 EW (mÅ)
DIB10792 EW (mÅ)

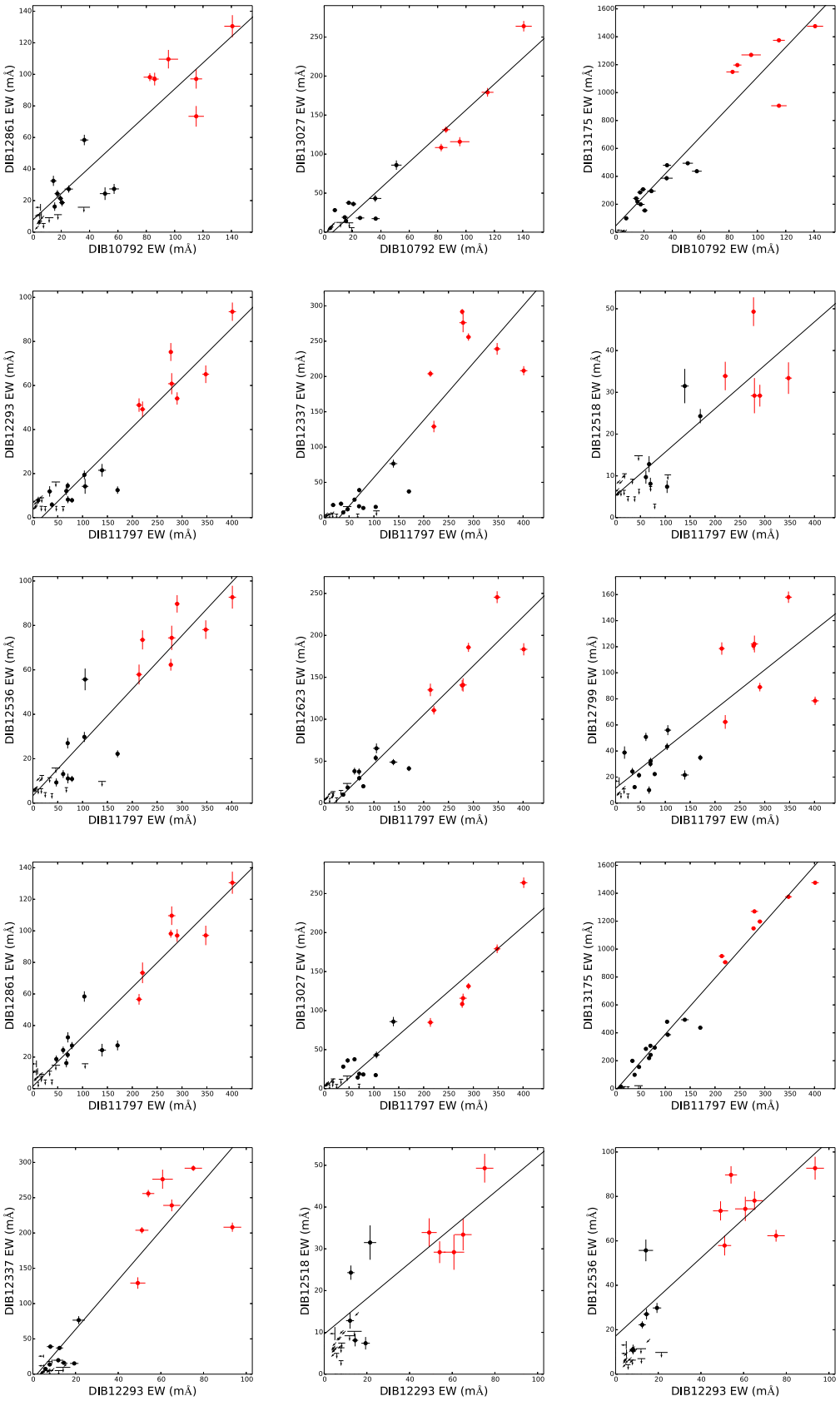
DIB12861 EW (mÅ)
DIB10792 EW (mÅ)
DIB13027 EW (mÅ)
DIB10792 EW (mÅ)
DIB13175 EW (mÅ)
DIB10792 EW (mÅ)
DIB12293 EW (mÅ)
DIB11797 EW (mÅ)
DIB12337 EW (mÅ)
DIB11797 EW (mÅ)
DIB12518 EW (mÅ)
DIB11797 EW (mÅ)
DIB12536 EW (mÅ)
DIB11797 EW (mÅ)
DIB12623 EW (mÅ)
DIB11797 EW (mÅ)
DIB12799 EW (mÅ)
DIB11797 EW (mÅ)
DIB12861 EW (mÅ)
DIB11797 EW (mÅ)
DIB13027 EW (mÅ)
DIB11797 EW (mÅ)
DIB13175 EW (mÅ)
DIB11797 EW (mÅ)
DIB12337 EW (mÅ)
DIB12293 EW (mÅ)
DIB12518 EW (mÅ)
DIB12293 EW (mÅ)
DIB12536 EW (mÅ)
DIB12293 EW (mÅ)

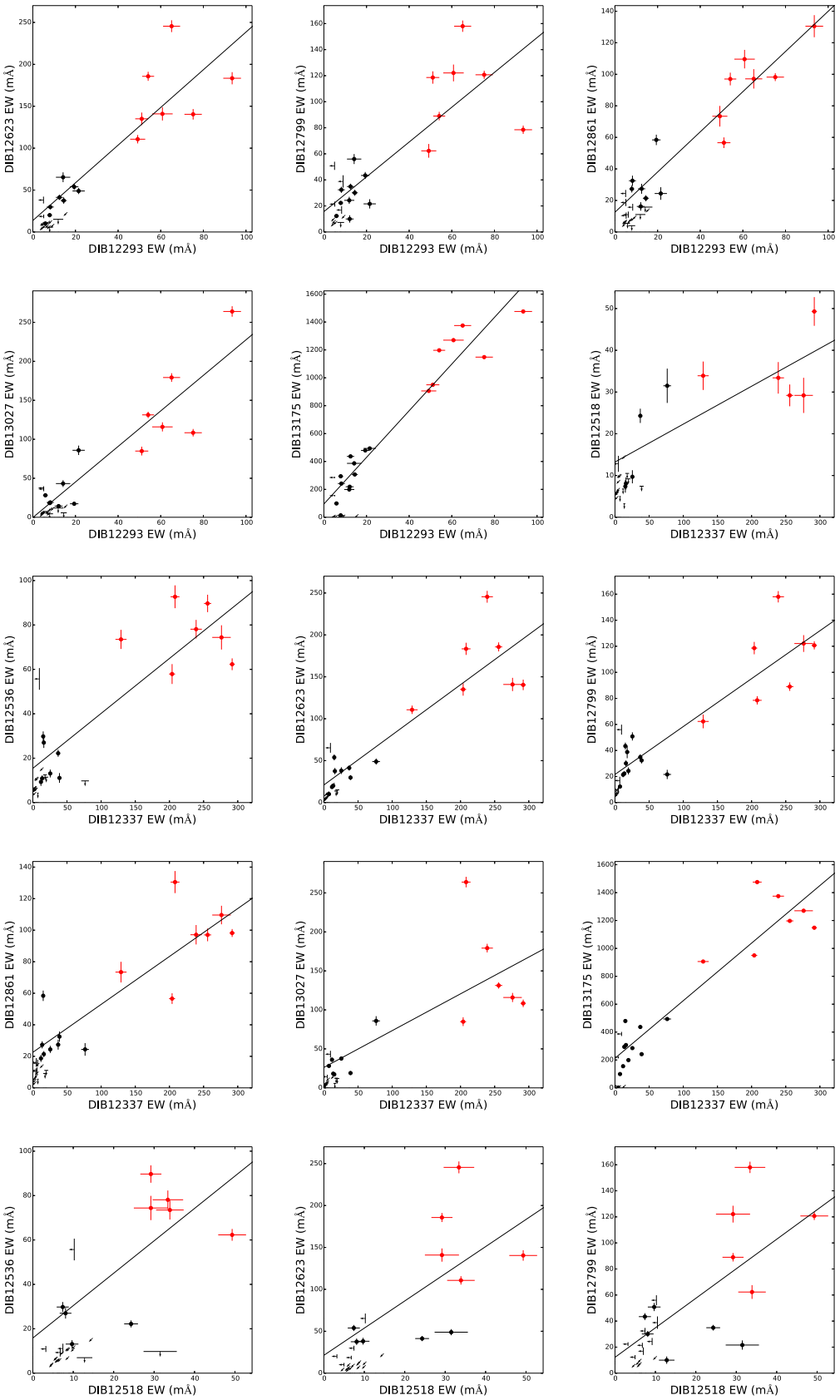
DIB12623 EW (mÅ)
DIB12293 EW (mÅ)
DIB12799 EW (mÅ)
DIB12293 EW (mÅ)
DIB12861 EW (mÅ)
DIB12293 EW (mÅ)
DIB13027 EW (mÅ)
DIB12293 EW (mÅ)
DIB13175 EW (mÅ)
DIB12293 EW (mÅ)
DIB12518 EW (mÅ)
DIB12337 EW (mÅ)
DIB12536 EW (mÅ)
DIB12337 EW (mÅ)
DIB12623 EW (mÅ)
DIB12337 EW (mÅ)
DIB12799 EW (mÅ)
DIB12337 EW (mÅ)
DIB12861 EW (mÅ)
DIB12337 EW (mÅ)
DIB13027 EW (mÅ)
DIB12337 EW (mÅ)
DIB13175 EW (mÅ)
DIB12337 EW (mÅ)
DIB12536 EW (mÅ)
DIB12518 EW (mÅ)
DIB12623 EW (mÅ)
DIB12518 EW (mÅ)
DIB12799 EW (mÅ)
DIB12518 EW (mÅ)

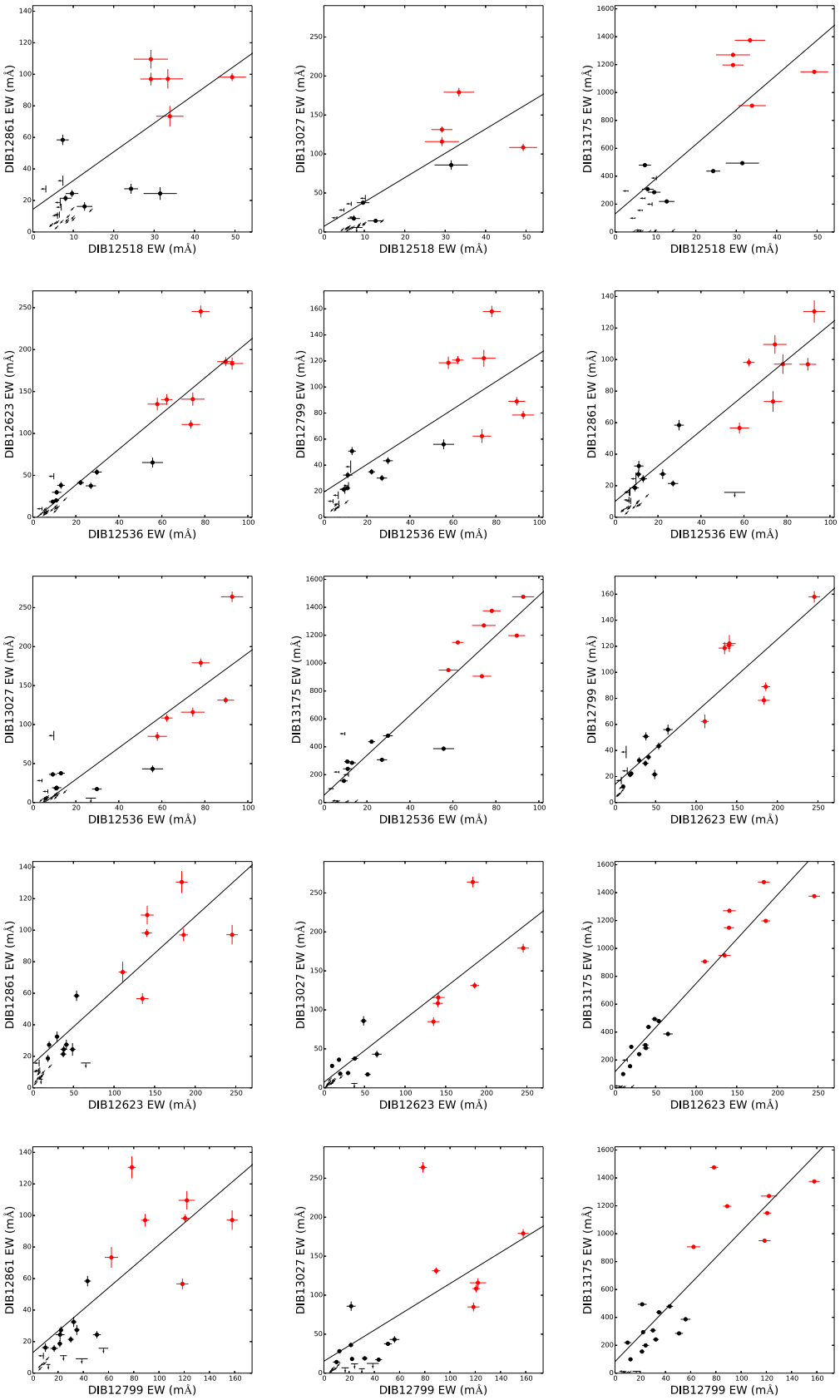
DIB12861 EW (mÅ)
DIB12518 EW (mÅ)
DIB13027 EW (mÅ)
DIB12518 EW (mÅ)
DIB13175 EW (mÅ)
DIB12518 EW (mÅ)
DIB12623 EW (mÅ)
DIB12536 EW (mÅ)
DIB12799 EW (mÅ)
DIB12536 EW (mÅ)
DIB12861 EW (mÅ)
DIB12536 EW (mÅ)
DIB13027 EW (mÅ)
DIB12536 EW (mÅ)
DIB13175 EW (mÅ)
DIB12536 EW (mÅ)
DIB12799 EW (mÅ)
DIB12623 EW (mÅ)
DIB12861 EW (mÅ)
DIB12623 EW (mÅ)
DIB13027 EW (mÅ)
DIB12623 EW (mÅ)
DIB13175 EW (mÅ)
DIB12623 EW (mÅ)
DIB12861 EW (mÅ)
DIB12799 EW (mÅ)
DIB13027 EW (mÅ)
DIB12799 EW (mÅ)
DIB13175 EW (mÅ)
DIB12799 EW (mÅ)

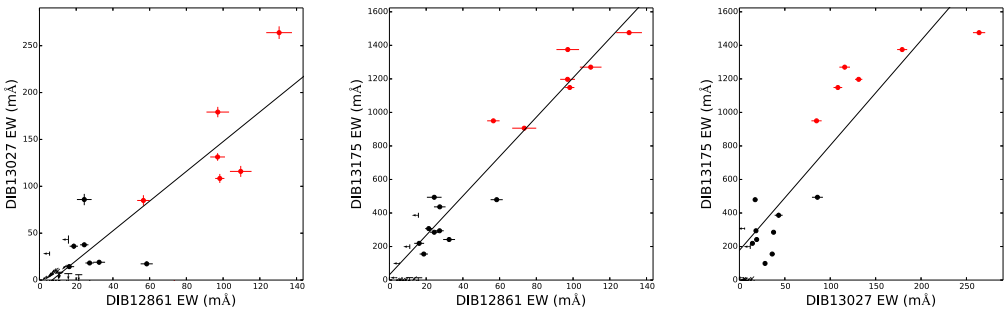
DIB13027 EW (mÅ)
DIB12861 EW (mÅ)
DIB13175 EW (mÅ)
DIB12861 EW (mÅ)
DIB13175 EW (mÅ)
DIB13027 EW (mÅ)

Appendix C

Correlations between NIR DIBs and optical DIBs

Correlations between four NIR DIBs ($\lambda\lambda$10438, 10780, 11797, and 13175) and two representative optical DIBs ($\lambda\lambda$5780.5 and 5797.1) from the survey data (black circles; Chapter 4) and the data from Cox et al. (2014) (blue circles) are shown in this appendix. The black points show the DIBs toward the target stars of the survey. The blue points show the DIBs detected by Cox et al. (2014). The black line shows the linear function fitted to the black points.

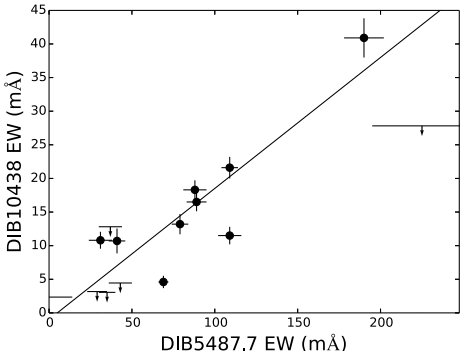
DIB10438 EW (mÅ)
DIB5487.7 EW (mÅ)

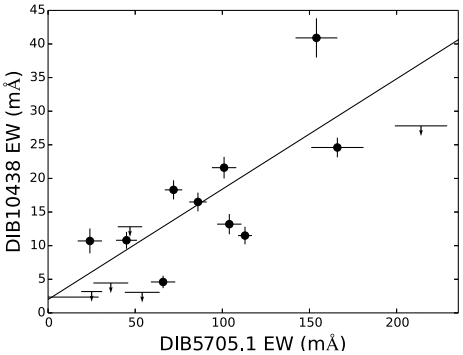
DIB10438 EW (mÅ)
DIB5705.1 EW (mÅ)

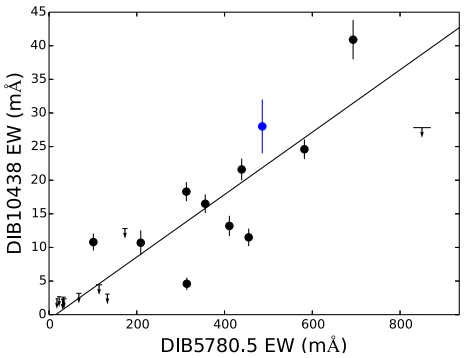
DIB10438 EW (mÅ)
DIB5780.5 EW (mÅ)

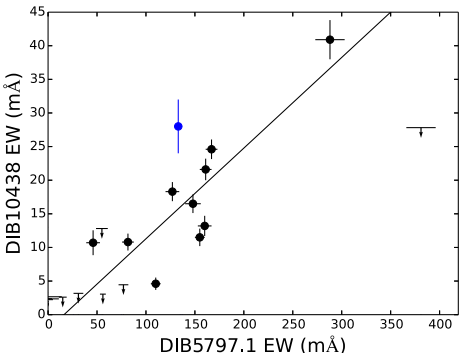
DIB10438 EW (mÅ)
DIB5797.1 EW (mÅ)

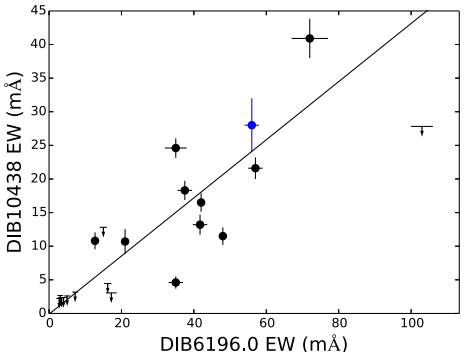
DIB10438 EW (mÅ)
DIB6196.0 EW (mÅ)

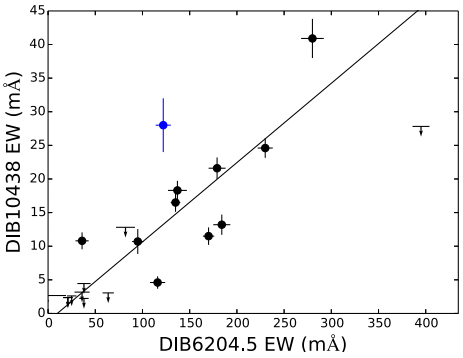
DIB10438 EW (mÅ)
DIB6204.5 EW (mÅ)

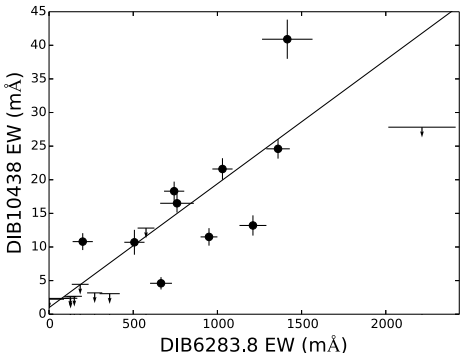
DIB10438 EW (mÅ)
DIB6283.8 EW (mÅ)

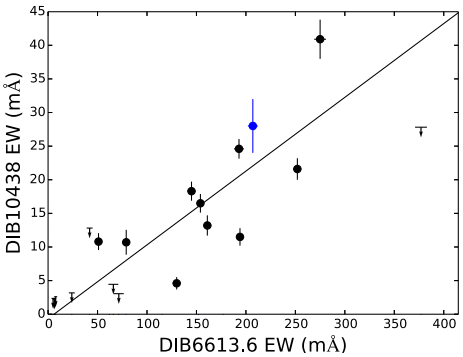
DIB10438 EW (mÅ)
DIB6613.6 EW (mÅ)

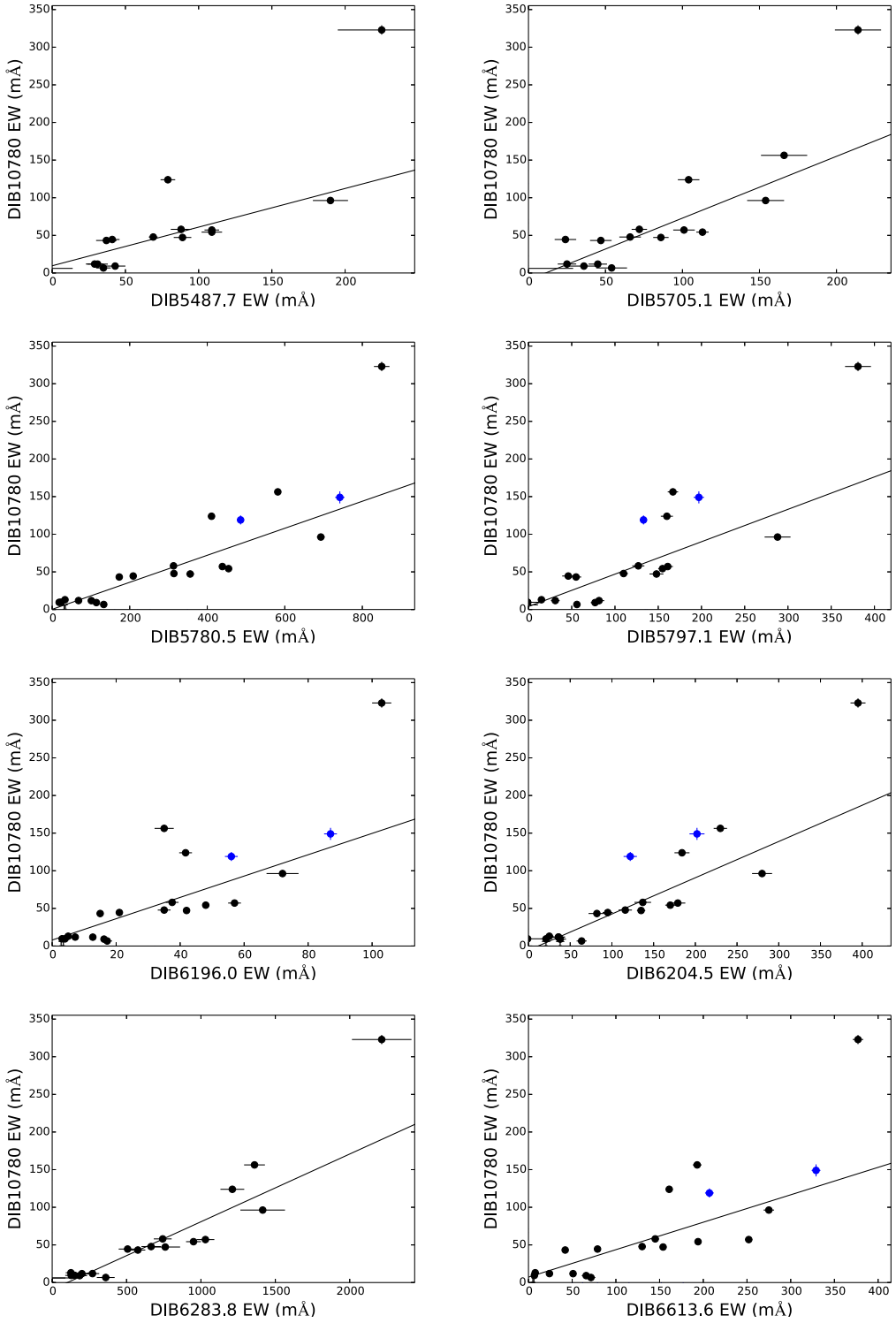
DIB10780 EW (mÅ)
DIB5487.7 EW (mÅ)
DIB10780 EW (mÅ)
DIB5705.1 EW (mÅ)
DIB10780 EW (mÅ)
DIB5780.5 EW (mÅ)
DIB10780 EW (mÅ)
DIB5797.1 EW (mÅ)
DIB10780 EW (mÅ)
DIB6196.0 EW (mÅ)
DIB10780 EW (mÅ)
DIB6204.5 EW (mÅ)
DIB10780 EW (mÅ)
DIB6283.8 EW (mÅ)
DIB10780 EW (mÅ)
DIB6613.6 EW (mÅ)

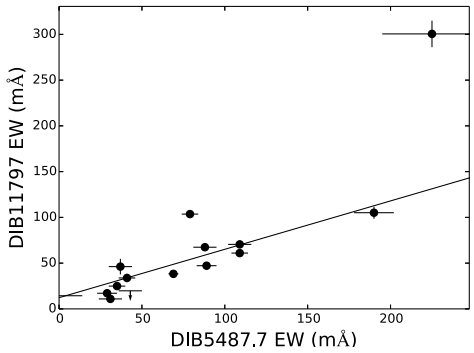
DIB11797 EW (mÅ)
DIB5487.7 EW (mÅ)

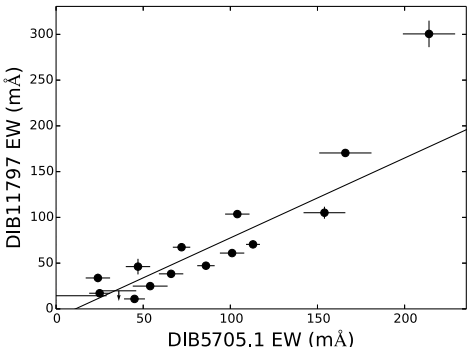
DIB11797 EW (mÅ)
DIB5705.1 EW (mÅ)

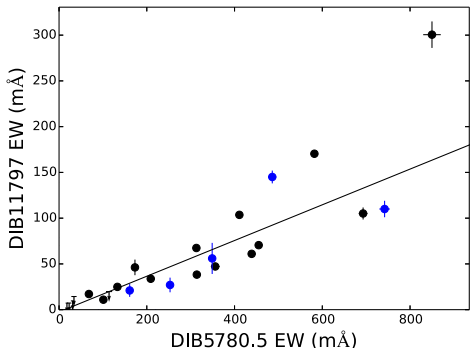
DIB11797 EW (mÅ)
DIB5780.5 EW (mÅ)

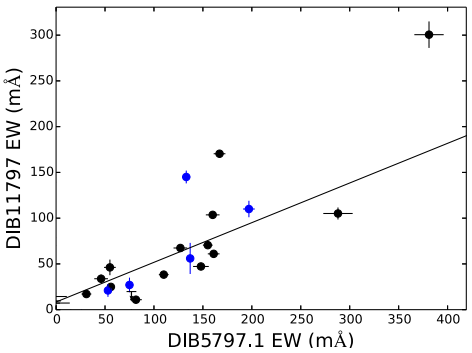
DIB11797 EW (mÅ)
DIB5797.1 EW (mÅ)

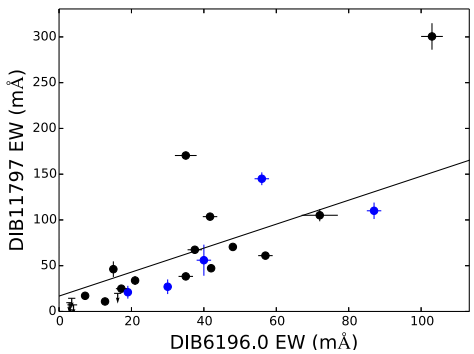
DIB11797 EW (mÅ)
DIB6196.0 EW (mÅ)

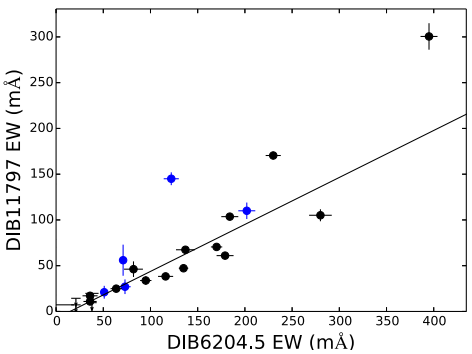
DIB11797 EW (mÅ)
DIB6204.5 EW (mÅ)

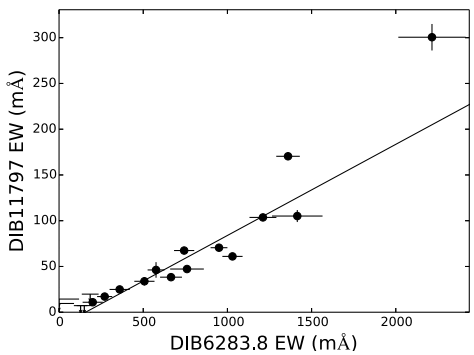
DIB11797 EW (mÅ)
DIB6283.8 EW (mÅ)

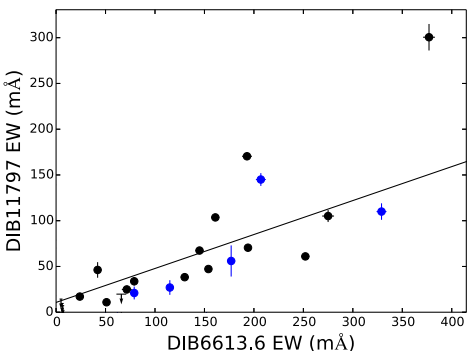
DIB11797 EW (mÅ)
DIB6613.6 EW (mÅ)

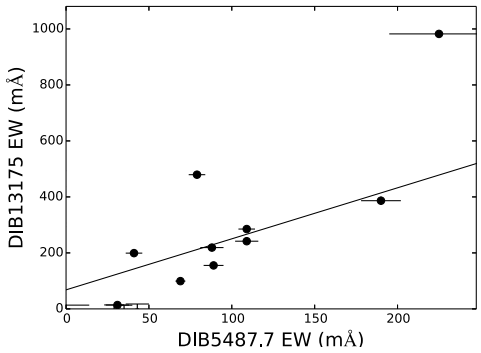
DIB13175 EW (mÅ)
DIB5487.7 EW (mÅ)

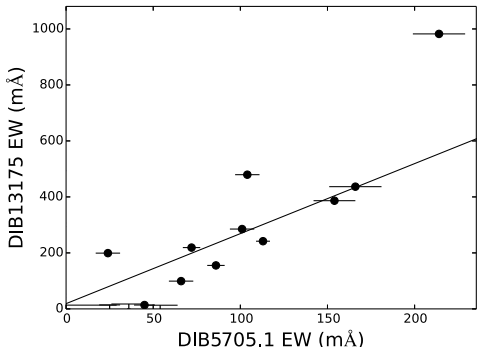
DIB13175 EW (mÅ)
DIB5705.1 EW (mÅ)

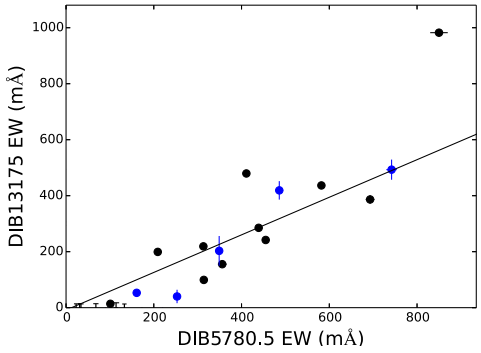
DIB13175 EW (mÅ)
DIB5780.5 EW (mÅ)

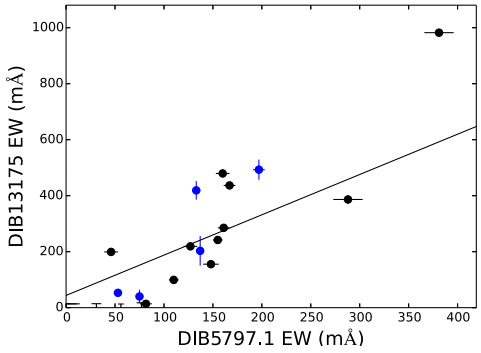
DIB13175 EW (mÅ)
DIB5797.1 EW (mÅ)

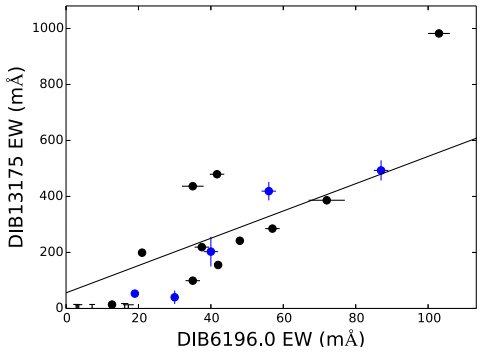
DIB13175 EW (mÅ)
DIB6196.0 EW (mÅ)

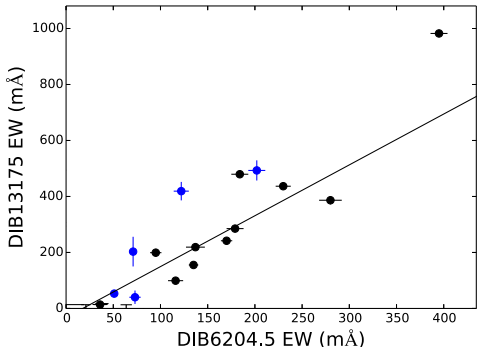
DIB13175 EW (mÅ)
DIB6204.5 EW (mÅ)

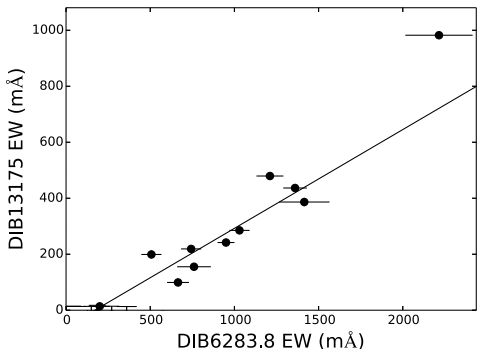
DIB13175 EW (mÅ)
DIB6283.8 EW (mÅ)

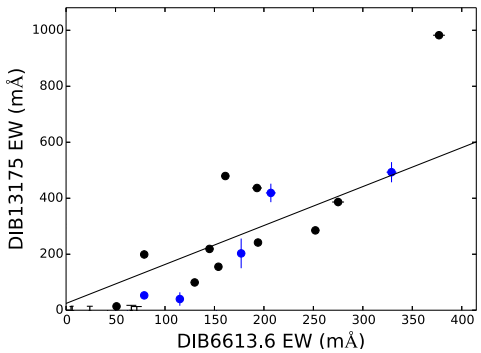
DIB13175 EW (mÅ)
DIB6613.6 EW (mÅ)